To the Graduate Council:

I am submitting herewith a dissertation written by Stephen Jesse entitled "A study of the evolution of laser-induced periodic surface microstructures on silicon and electronic transport in composite carbon nanotube networks." I have examined the final electronic copy of this dissertation for form and content and recommend that it be accepted in partial fulfillment of the requirements for the degree of Doctor of Philosophy, with a major in Materials Science and Engineering.

Dr. A.J. Pedraza
Major Professor

We have read this dissertation
and recommend its acceptance:

Dr. E.P. George

Dr. M.L. Simpson

Dr. R.N. Compton

Dr. D.B. Geohegan

Acceptance for the Council:

Dr. A. Mayhew
Vice Chancellor and Dean of
Graduate Studies

(Original signatures are on file with official student records)

A STUDY OF THE EVOLUTION OF LASER-INDUCED PERIODIC SURFACE MICROSTRUCTURES ON SILICON AND ELECTRONIC TRANSPORT IN COMPOSITE CARBON NANOTUBE NETWORKS

A dissertation

Presented for the

Doctor of Philosophy Degree

The University of Tennessee, Knoxville

Stephen Jesse

December 2004

Copyright © by Stephen Jesse
All rights reserved

Copies of this document may be printed from this website
for personal use without permission

Dedication

I dedicate this to Reinhardt, Ursula, and Lisa.

Acknowledgements

This work would not have been possible without the assistance of numerous trusted teachers, scientists, fellow students, and friends. I would like to thank Dr. Anthony Pedraza for his guidance in my investigation in laser-matter interactions and especially his patience and willingness to grant me time and freedom to find the answers I sought. I would also like to thank Dr. David Geohegan for the opportunity to work with him and his group at ORNL and for his ever-present help in investigating new realms of nano-science. I greatly appreciate the extensive time and help that Dr. Jason Fowlkes and Dr. Michael Guillorn offered as fellow students in teaching me to use experimental equipment as well as joining me in endless discussions of deep and significant theoretical matters. Much of credit for the work using scanning impedance microscopy should go to Dr. Sergei Kalinin as he performed many of the measurements and used his vast expertise in this area to bring clarity and understanding to the experimental results. I would also like to thank my committee members for their thoughtfulness and helpful advice in their review of this dissertation. I owe a debt of gratitude to Doug Fielden and Hank McClich for the quality craftsmanship they invested in constructing custom experimental equipment.

I would like to thank my family for providing a constant source of encouragement, and I want to thank my friends for providing a constant source of encouragement and distraction. Finally, I would like to thank the Buddha, the Dhamma, and the Sangha for being the greatest teachers of all.

Research of laser matter interactions was sponsored by the National Science Foundation Grant N° DMR-9901238 and by the Oak Ridge National Laboratory, managed by UT-Battelle, LLC, for the U.S. Department of Energy under contract DE-AC05-00OR22725. Research of nanotube composites was sponsored by NASA-Langley Research Center and the Laboratory-Directed Research and Development Program at ORNL, and the U.S. Department of Energy under contract DE-AC05-00OR22725 with the Oak Ridge National Laboratory, managed by UT-Battelle, LLC.

Abstract

This dissertation addresses two main topics, the formation of micron-scale surface structures on single crystal silicon by irradiation with a KrF (248 nm) pulsed excimer laser source, and an investigation into electronic transport through composites of polymer (PMMA) and single-walled carbon nanotubes. It is shown that the spacing between laser-generated surface structures is determined primarily by the melt time and that the crystal orientation of the substrate can determine whether surface structures will form at all and also influence the shape of individual surface structures. During the melt/solidification cycle, the shape of liquid-vapor interface in modified by surface tension, and the shape of the solid-liquid interface is modified by a combination of thermal diffusion and faceting processes. At the last stages of solidification, the two interfaces converge but will be shaped differently resulting in an incongruity and isolated pools of molten material on the solid surface. The shape, and more importantly the final height, that these molten pools assume after they solidify depends the surface atomic density of the advancing solid interface (κ_s) compared to the surface atomic density of the liquid (κ_l). If $\kappa_s > \kappa_l$, as in the (110) face, the final height of the solid will be lower than the initial height of the liquid pool and surface structures will not form. If $\kappa_s < \kappa_l$, then perturbations with the correct periodicity will evolve into surface structures. Micro-cone structures form during irradiation in the presence of an SF_6 atmosphere due to multiple reflections of the incident light on a sufficiently rough surface. Electronic transport studies were performed on nanotube polymer composites using scanning electron microscopy and scanning impedance microscopy. These techniques have been used to map potential distribution within embedded networks and image paths for current flow.

Table of Contents

CHAPTER 1 REVIEW OF THE LITERATURE 1.1

1.1 INTRODUCTION 1.1

1.2 LASER INDUCED EVOLUTION OF SURFACE STRUCTURE 1.2

1.2.1 Preview of Experimental Conditions 1.2

1.2.2 Preview of Results 1.2

1.2.3 Review of Literature on Laser Patterning 1.5

Laser Induce Instabilities at the Vapor Interface 1.6

Instabilities at the Solid-Liquid Interface 1.17

1.3 LITERATURE REVIEW OF ELECTRONIC TRANSPORT IN SWNT'S 1.19

1.3.1 Electronic Properties of Individual SWNT's 1.20

Band Structure 1.20

Ballistic Transport in Nanotubes 1.22

1.3.2 Nanotube Heterojunctions 1.22

1.3.3 Nanotube Y-Junctions 1.26

1.3.4 Nanotube Crossing Junctions 1.28

1.3.5 Transport through Nanotube Composites 1.31

Geometric Considerations in Percolation 1.31

Interconnections in Percolation 1.35

CHAPTER 2 EXPERIMENTAL METHODS FOR LASER-INDUCED SURFACE STRUCTURING STUDIES 2.37

2.1 SURFACE LASER IRRADIATION EXPERIMENTAL SETUP 2.37

2.2 IN-SITU IMAGING OF THE SURFACE AND ABLATION PLUME 2.41

2.2.1 Description of Continuous Mode Imaging 2.41

2.2.2 Description of Sequential Mode Imaging 2.42

2.3 SURFACE CHARACTERIZATION TECHNIQUES 2.42

CHAPTER 3 EXPERIMENTAL RESULTS OF LASER INDUCED SURFACE MICROSTRUCTURING 3.44

3.1 RESULTS OF PROFILOMETRY 3.44

3.2 RESULTS OF ATOMIC FORCE MICROSCOPY 3.50

3.3 THE EFFECT OF TEMPERATURE AND ENERGY ON FEATURE SPACING 3.53

3.4 IN-SITU OPTICAL MICROSCOPY OF SURFACE EVOLUTION 3.53

3.4.1 Plan view of the substrate 3.56

3.4.2 Cross-Sectional view of the substrate 3.56

3.5 In-Situ Imaging of Plume Motion 3.58
3.6 Crystallography and the Morphology Surface Structure 3.61
3.7 Micro-cone Evolution on (110) Crystal Faces 3.61
3.8 The Induced Organization of Surface Structure 3.64
3.9 Liquid Chemical Etching of Micro-cone Structures 3.66

CHAPTER 4 DISCUSSION OF RESULTS AND MODELING OF LASER-INDUCED SURFACE MICROSTRUCTURING 4.68

4.1 A Model of Laser Induced Melting 4.68
4.2 The Role of Thermal Diffusion and Capillary Wave Motion in Establishing Surface Structure Spacing 4.70
4.2.1 The Role of Lateral Heat Diffusion in the Evolution of the SL Interface 4.70
4.2.2 The Role of Surface Tension in the Evolution of the LV Interface 4.72
4.2.3 Convergence of the Solid-liquid and Liquid-Vapor Interfaces 4.73
4.3 The Last Stage of Solidification and the Role of Crystallography 4.77
4.3.1 Discussion of Atomic Densities 4.78
4.3.2 General Method for Calculating Surface Atomic Densities for all Crystal Orientations 4.81
4.3.3 Surface Atomic Density of Molten Silicon 4.84
4.3.4 Accounting of Atoms at the Solid-Liquid Interface 4.85
4.3.5 A Continuum Model for Solidification 4.88
4.3.6 The Solidification of General Shapes 4.95
4.3.7 Faceting of the (111) Interface During Solidification 4.96
4.3.8 Thermal Diffusion and Capillary Wave Motion Acting on 2-D Interfaces 4.100
4.3.9 Results of Including Faceting Effects and Surface Symmetry 4.101
4.3.10 The Expression of Crystallography in the Surface Structure 4.101
4.4 The Evolution of the Micro-Cone Surface Structure 4.107
4.4.1 The Transition from Waves to Cones and the Interaction of Surface and Light 4.107
Experimental Evidence of Critical Roughness 4.107
Ray-Tracing of Reflected Light 4.108
Multiple Surface Reflections 4.111
4.4.2 The Continued Evolution of the Black Silicon Surface Structure 4.112
4.4.3 Ablation Plume Analysis as Related to the Evolution of Micro-cones 4.115
The Role of the Plume over Multiple Laser Pulses 4.115
Plume Motion During a Single Pulse 4.116

CHAPTER 5 EXPERIMENTAL METHODS FOR SWNT TRANSPORT STUDIES 5.118

5.1 Sample Preparation 5.118

5.2 CURRENT-VOLTAGE MEASUREMENTS 5.118
5.3 TRANSMISSION ELECTRON MICROSCOPY OF COMPOSITES 5.118
5.4 SCANNING ELECTRON MICROSCOPY OF COMPOSITE NETWORKS 5.119
5.4.1 SEM Sample Stage 5.119
5.4.2 Imaging while Applying Bias to the Sample Surface 5.120
5.4.3 Specimen Current Imaging 5.120
5.5 MEASUREMENTS USING THE SCANNING PROBE MICROSCOPE 5.121

CHAPTER 6 EXPERIMENTAL RESULTS 0F SWNT TRANSPORT STUDIES 6.124

6.1 RESULTS OF TEM STUDIES 6.124
6.2 RESULTS OF SEM STUDIES 6.124
6.2.1 Variations of the Incident Beam Excitation Energy 6.124
6.2.2 Variation of the Applied Surface Bias 6.126
6.2.3 Specimen Current Imaging 6.129
6.3 RESULTS OF SCANNING PROBE MICROSCOPY STUDIES 6.129

CHAPTER 7 DISCUSSION OF RESULTS AND MODELING FOR NANOTUBE-COMPOSITE TRANSPORT STUDIES 134

7.1 DISCUSSION OF NON-LINEARITY AND RECTIFYING BEHAVIOR IN CURRENT-VOLTAGE MEASUREMENTS 134
7.2 DISCUSSION OF SEM BASED TRANSPORT STUDIES 138
7.2.1 Electric Field Induced Contrast 139
Types of Voltage Induced Contrast 139
Electric Field Induced Contrast 141
7.2.2 Relationship Between Image Contrast and Electron Beam Excitation Voltage 145
Discussion of SEM Imaging 145
Discussion of Specimen Current Imaging 145
7.3 DISCUSSION OF SIM BASED TRANSPORT STUDIES 146
7.3.1 Imaging at Low Frequency and Determination of Potential Distribution 146
7.3.2 High Frequency Transport and the Line Transmission Model 147

CHAPTER 8 CONCLUSION 151

BIBLIOGRAPHY 152

APPENDIX 156

1.1 DESCRIPTION OF EVAPORATION INSTABILITY 157
1.2 DESCRIPTION OF PLUME-WAVE INTERACTION 161

1.3 Fowler-Nordheim Equation 162
1.4 Cone Solidification Derivation 164
1.5 Derivation of a Sinusoid Solidifying 171
1.6 Description of Laser Melting Simulation 178
1.7 FlexPDE Code for Laser Melting 182
1.8 Matlab Code for Model for Surface Structure Evolution 184
1.9 Function for Simulating Thermal and Capillary Effects 187
1.10 Function for Determining Faceting Effects 190
1.11 Function for Modeling End-Stage Solidification 193
1.12 Function for Determining the Atomic Density of Silicon 197
1.13 Matlab Ray-Tracing Program 199
1.14 Function Used in Ray-Tracing Program 205

VITA 207

List of Figures

Figure 1.1. Overview of experimental results. *1.3*
Figure 1.2. AFM images of LIPPS structures *1.8*
Figure 1.3. Diagram of evaporation instability. *1.9*
Figure 1.4. Diagram of the possible effects that surface shape may have on plume dynamics. *1.11*
Figure 1.5. SEM micrographs of femto-second laser generated micro-cones *1.13*
Figure 1.6. Optical micrographs of laser irradiated silica coated single crystal silicon *1.15*
Figure 1.7. Diagram illustrating the formation of laser induced waves by buckling silica *1.16*
Figure 1.8. Optical micrographs of organized patterns formed by laser irradiation *1.17*
Figure 1.9. Types of nanotubes *1.20*
Figure 1.10. Diagram of nanotube Brillouin zones and k-vector alignment. *1.21*
Figure 1.11. STM image of nanotube hetero-junction *1.23*
Figure 1.12. TEM image of multi-wall nanotube hetero-junction. *1.23*
Figure 1.13. Nanotube junctions using tangent heptagon and hexagon rings *1.25*
Figure 1.14. First Brillouin zone with allowable k-vectors for various nanotubes *1.25*
Figure 1.15. Diagram of carbon nanotube on a HOPG substrate *1.29*
Figure 1.16. Measurement of conduction between crossed nanotubes. *1.30*
Figure 1.17. Results of theoretical study of nanotube-nanotube junctions *1.32*
Figure 1.18. Examples of excluded volumes fillers of dimension and degrees of freedom. *1.34*
Figure 2.1. View of surface treatment and diagnostic experimental setup *2.38*
Figure 2.2. Close-up views of surface treatment and diagnostic experimental setup. *2.39*
Figure 2.3. Diagram of setup used for in-situ surface irradiation imaging. *2.42*
Figure 3.1. Plots of results from profilometric measurements of laser induced surface roughness *3.45*
Figure 3.2. Profilometry measurements material loss due to laser irradiation *3.46*
Figure 3.3. Profilometry measurements of Si substrates irradiated with varying number of pulses *3.48*
Figure 3.4. Profilometry measurements of Si substrates irradiated with varying background pressures *3.49*
Figure 3.5. Profilometry of Si substrates irradiated with varying partial pressures of SF_6. ..... *3.50*
Figure 3.6. AFM images of early stages of laser induced surface structuring *3.51*
Figure 3.7. Plots of AFM measurements of surface structure amplitude and grade *3.52*
Figure 3.8. Results of the effect of substrate temperature on feature spacing *3.54*
Figure 3.9. Plots of the effect of incident energy and substrate temperature on feature spacing *3.55*
Figure 3.10. In-situ images of the profile of the evolving surface captured in continuous mode *3.57*
Figure 3.11. In-situ images of the profile of the evolving plume captured in sequential mode *3.59*
Figure 3.12. Plots of plume propagation as a function of time and ambient pressure *3.60*
Figure 3.13. Micrographs showing the role of crystallographic orientation on structure morphology. *3.62*
Figure 3.14. SEM images of micro-cone growth on (110) silicon surface *3.63*

Figure 3.15. SEM micrographs of patterns imposed placing a coarse wire mesh in the beam path 3.65
Figure 3.16. SEM micrographs of micro-cones on a (100) surface after etching in KOH. 3.67
Figure 4.1. 3-D plot of results of melt time calculations vs. incident energy and substrate temperature. .4.69
Figure 4.2. Diagram showing lateral thermal diffusion within an irradiated corrugated substrate 4.71
Figure 4.3. Diagrams illustrating the cause for SL and LV interface mismatch.....4.74
Figure 4.4 Plot of surface feature spacing as a function of melt time.....4.77
Figure 4.5. Illustration of the geometry of liquid and solid regions at the last stage of solidification 4.78
Figure 4.6 Crystal structures, surface atomic densities, and the volume elements for three crystal faces 4.80
Figure 4.7. Configuration of the silicon tetravalent bonding relative to various surface orientations.....4.82
Figure 4.8. Diagram and equations of Euler rotation angles 4.83
Figure 4.9. Surface atomic density map of crystalline silicon for all crystal orientations.....4.84
Figure 4.10. Volume element representation of epitaxial solidification on a (110) surface 4.86
Figure 4.11.Volume element epitaxial growth for two different initial liquid shapes 4.87
Figure 4.12. Initial shape of a liquid cone on a flat, solid surface.....4.88
Figure 4.13. Solidification of the first infinitesimal layer 4.89
Figure 4.14. Change in the volume and shape of the liquid due to SL interfacial advance 4.91
Figure 4.15. Results of applying equation 4.19 to a liquid silicon cone solidification. 4.93
Figure 4.16. Solidification process of a liquid cone on a crystalline surface 4.94
Figure 4.17. Results of modeling growth of sinusoidal surface perturbations.....4.95
Figure 4.18. Plots of the velocity of the interface velocity as a function of undercooling 4.97
Figure 4.19. Illustrations of the effect of (111) faceting during solidification in a wavy thermal field 4.99
Figure 4.20. Illustrations of surfaces approximating the shape of (111) and (100) surface structures ...4.102
Figure 4.21. Results of modeling the evolution of surface structures includes faceting effects 4.103
Figure 4.22. Illustration highlighting varying surface orientations at the last stage of solidification.....4.103
Figure 4.23. Surface density mapped onto sinusoidal perturbations on (100) and (111) surfaces.....4.105
Figure 4.24 Surface density mapped onto sinusoidal perturbations on (211) and (110) surfaces.....4.106
Figure 4.25. Measured amplitude of surface waves as a function of the number of pulses. 4.108
Figure 4.26. Results of modeling the distribution of reflected light above a sinusoidal surface.....4.109
Figure 4.27. Multiple surface reflections on a sinusoidal surface 4.111
Figure 4.28. Analysis of multiple reflections in micro-holes.....4.113
Figure 5.1. Photographs of the SEM stage 5.119
Figure 5.2. Diagram of setup for specimen current imaging.....5.120
Figure 5.3. Diagram of SIM technique 5.122
Figure 6.1. TEM images of SWNT's in PMMA 6.125
Figure 6.2. SEM image of SWNT bundles at two different primary beam excitation voltages.....6.125
Figure 6.3. Results of measuring the effects of applied bias in the SEM 6.127

Figure 6.4. SEM images of nanotube/polymer composites under various bias conditions. 6.128
Figure 6.5. A series of SC images taken at different incident beam voltages.....6.130
Figure 6.6. SC images taken illustrating a gradient in current flow across the network.....6.130
Figure 6.7. AFM, SIM, and SEM images of nanotube polymer composites.....6.131
Figure 6.8. SIM images of phase and amplitude data for three different bias conditions.....6.132
Figure 6.9. Plot of phase lag as a function of driving frequency 6.133
Figure 7.1. Illustration of a sample substrate 135
Figure 7.2. Rectifying behavior in nanotube composite experiments.....137
Figure 7.3. Plot of secondary yield as a function of primary electron energy 139
Figure 7.4. Voltage induced shift in the energy spectrum of secondary electrons 140
Figure 7.5. Illustration of a cross-sectional view of a biased test sample.....141
Figure 7.6. Plots of the SE emission spectra with the Schottky effect considered.....142
Figure 7.7. Comparison of EFIC model and experimental measurements of brightness.....143
Figure 7.8. Surface potential maps of nanotube composites.....144
Figure 7.9. SIM amplitude images and maps of potential distribution throughout a composite network...148
Figure 7.10. Predicted voltage and phase lag distribution at high frequencies.....149

CHAPTER 1 REVIEW OF THE LITERATURE

1.1 Introduction

This thesis covers two main topics. The first is a study of self-organization on the micron scale. Laser-induced surface structures on single crystal silicon are experimentally studied and a detailed model is constructed describing their formation and evolution. This model is able to predict the growth rate and spacing of the surface structure as a function of initial substrate temperature, laser intensity, and surface orientation. This study is extended to investigate micro-hole/micro-cone formation which occurs when the laser surface treatment is performed in the presence of a reactive atmosphere. The importance of thermal transport through the substrate, capillary fluid motion of melted substrate surface, and epitaxial crystal growth are important factors in defining the growth and shape of perturbations will be analyzed. The inhomogeneous distribution of reflected light from a perturbed and uneven substrate surface will be examined. This redistribution of incident energy can interact with surrounding atmosphere to cause highly localized etching of the surface. This etching results in the formation of high aspect ratio micro-holes in the substrate. Some of this material removed from the holes is re-deposited on the surface to form micro-cones. The ultimate height of the micro-cones above the original surface is governed by the dynamics of the ablation plume. The mechanisms where by large scale experimental conditions, such as ambient temperature, pressure, and atmosphere, influence the mass formation of regular micron sized surface structures will be studied. The correlation between the gross growth conditions and final micro-structuring will be established with the expectations of using these techniques to set growth conditions necessary to obtain the desired, self-organized fine structure.

The second of the main topics deals with study of electronic transport through carbon nanotube-polymer composites. Understanding transport at the nano-scale is critical to engineering nano-composites with desired properties. The experimental and analysis techniques described here are applicable to many other composite systems and may be key to understanding fundamentals of filler/matrix interaction of nano-composites used in polymer based light emitters and photovoltaics. Scanning electron microscopy as well as scanning probe microscopy techniques have been developed and applied to the imaging of transport through nanotube composites on the sub-micron scale. In addition, computer models based on circuit analysis of networks of non-linear elements will be developed to determine the nature of conduction through the composite.

1.2 Laser Induced Evolution of Surface Structure

1.2.1 Preview of Experimental Conditions

Pulsed lasers can be used to deposit a large amount of energy onto a solid surface in very short periods of time. While the total energy of the laser pulse is relatively small in most cases (0.1 to 10 J/cm^2), the time in which this deposition occurs is so short that the incident power becomes significant. For instance, the typical range of incident flux for the experiments studied here is a 2 J/cm^2 laser pulse lasting 20 ns. Under such conditions, the incident power is 100 MW/cm^2. Such large power densities are unique to pulsed laser systems and avail opportunities for interesting materials processing techniques. The fact that the distribution of wavelengths, polarization, and phase of light within the beam is very narrow provides additional tools for materials processing.

Pulsed laser processing of materials falls into two categories, pulsed laser deposition and surface modification. The first involves removing material from a target by ablation with the high power beam to expel material from this target onto another substrate in order to form a thin layer of this material on that substrate. By doing this, very thin layers of materials with precisely controlled composition and crystallography can be engineered. Although laser deposition plays some role in the work presented here, it is not the focus of this investigation. Instead, the effect that laser-matter interaction has on the target will be studied.

It is well know that intense beams of energy can modify surfaces in extraordinary ways. The high power generates conditions where the target and surrounding gas are pushed abruptly away from equilibrium. Intense thermal gradients give rise to high speed phase changes. These processes take place on time and length scales that dictate which physical processes play dominant roles while the system races back to equilibrium. Often the forces that are dominant on long time scales, like gravity, are negligible, while other normally unimportant forces, like those due to surface tension, can dominate. Understanding the transport of material, thermal energy, and vibrational energy is vital to achieving an understanding of the surface modifications process. The time for these processes is so severely limited that the distances over which they can have an effect is in turn severely limited.

1.2.2 Preview of Results

A brief overview of important experimental results can provide some perspective on previously published work to be presented in the literature review. These experiments involved irradiating polished, single crystal silicon wafers of various crystal orientations in either Ar or SF_6 atmospheres at power densities (2 – 3 J/cm^2) high enough to induce melting of the substrate. The longest time that any portion of the substrate remains molten is on the order of tenths of a microsecond, which is much shorter than the 25 ms between successive laser pulses. Figure 1.1 is a compilation of images illustrating key results.

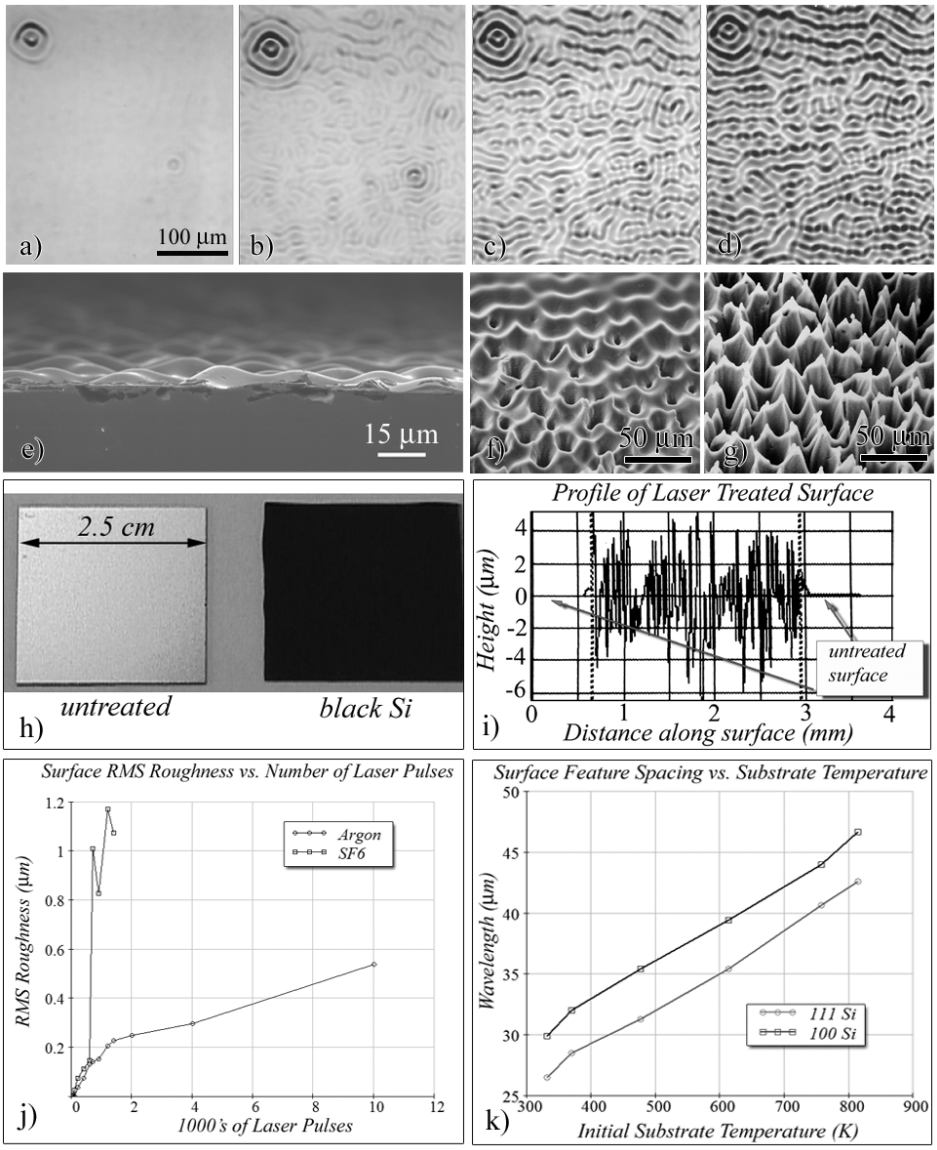

Figure 1.1. Overview of experimental results.

(a-d) In-situ optical micrographs of laser ablated silicon showing increasing amplitude of surface structure at 50, 100, 150, and 200 pulses, (e) side view of cross-section laser treated substrate, (f) SEM image taken at 45° showing transition of surface morphology from waves to cones, 500 pulses, (g) SEM image taken at 45° of developed cones, (h) photograph showing macro appearance of laser treatment in SF_6 atmosphere, (i) profilometric data of surface roughness showing waves extending above original substrate surface, (j) Plot of RMS surface roughness vs. increasing number of laser pulses for Ar and SF_6 atmospheres, (k) plot of change in surface feature spacing over a range of samples prepared with different initial substrate temperature.

Figure 1.1(a-d) are a series of micrographs illustrating the evolution of surface relief at increasing number of successive incident laser pulses of 50, 100, 150, and 200 pulses respectively. Note that first indications of the final surface topography are visible after 50 pulses. Profilometry of the surface indicates a measurable relief with a peak to valley distance of about 40 nm after only 5 shots. As the number of pulses increases, the position of the emerging peaks and valleys of the relief do not change. Rather, it is only the amplitude of the relief that increases with the number of pulses. Note also that the spacing of surface features is quite regular. Figure 1.1(e) is a side view of a cross-sectioned substrate of well developed wave surface structure resulting from 1000 pulses in an 500 mbar Ar atmosphere. If this same process is done in an SF_6 atmosphere, the same wave shape results through the first ~400 shots, but then the surface morphology quickly deviates into high aspect ratio micro-holes and micro-cones that reach above the substrate surface. This transition is illustrated in Figure 1.1(f) in which waves populate the top of the image, deepening micro-holes are clearly visible toward the middle of the image, and the first indications of growing micro-cones can be seen toward the bottom of the image. Presumably, this gradient in growth rate is due to a gradient in incident energy density. Note that the micro-holes form in the valleys of the waves and the cones grow from the crests. This means that the eventual map of the micro-cone structure is also established within the first few laser pulses. It will be shown later that this provides a means to deterministically set a final desired ordering of the cone structure by adjusting experimental conditions early in the growth process. Figure 1.1(g) shows the micro-cone/micro-hole morphology formed after 800 laser pulses in an SF_6 atmosphere. The vast majority of the once mirror like surface is angled 70° to 85° from the original plane of the surface after laser treatment. One might expect that a speckled, rough appearance would result since incident light would presumably be scattered away from the surface. Instead, nearly all incident visible light (~98%) is reflect back multiple times onto the substrate and eventually absorbed[1,2]. The SF_6-laser treated surface takes on a velvety black appearance as a result and has been termed '*black silicon*'. A photograph comparing untreated Si to laser treated Si is shown in Figure 1.1(h). The black appearance is not due to a coating on the silicon. On the micron scale, the silicon surface is still clean, smooth and mono-crystalline. The high absorbency is due to multiple reflections of incident light within the micro-holes that, ironically, were forged by multiple reflections of incident laser light.

Along with extensive work on charting the growth of laser induced surface structure by SEM and light microscope imaging, profilometric data was recorded as well. Figure 1.1(i) is the surface profile of silicon treated with 4000 pulses at 3.0 J/cm^2 in an Ar atmosphere. Since the silicon was treated in an inert atmosphere, the surface is composed of waves instead of micro-cones. It is clearly visible in this plot that the peaks of the waves extend above the original surface of the silicon. Figure 1.1(j) compares the development of root mean squared (RMS) roughness as a function of the number of laser pulses for treatment of silicon in two different atmospheres. Note that there is no significant difference in the development of surface structure in the early stages of wave growth. This indicates that the reactive atmosphere does not play a role in early surface structure development. After approximately 600 pulses

though, a striking deviation takes place. Micro-hole/micro-cone structure begins to develop in the SF_6 case, while the wave structure in the Ar case continues to increase in amplitude steadily up to 10,000 pulses. These same experiments were run in vacuum ($5 \bullet 10^{-6}$ Torr) yielding the same results as the Ar atmosphere. Early attempts in this project to understand the mechanisms that establish the wavelength of the surface structure resulted in a model that predicted that the spacing of surface features should be highly dependent on the time that the top layer of the substrate is in a molten state, termed '*melt time*'. Changing the melt time can be done either by changing the incident laser energy density or the initial substrate temperature prior irradiation. Changing incident energy does not alter melt time significantly and is usually associated with other affects such as increased evaporation. Initial substrate temperature could be varied experimentally over a range of about 500K and does strongly influence melt time. The results of measurements of average feature spacing for different substrate temperatures are shown in Figure 1.1(k). Wave spacing is shown to increase with substrate temperature as the model predicted. One other result which is apparent in this plot is that wave spacing is also influenced by the crystallographic orientation of the substrate. Other important results include the finding that the crystallographic orientation is weakly represented in the morphology of the waves, and more remarkably, that under the same experimental conditions, waves do not form on (110) crystal faces at all.

A summary of the important experimental results is listed below:

1. The position of the peaks and valleys of the surface structure is establish within the first few laser pulses.
2. Subsequent laser pulses steadily increase the amplitude of the surface undulations.
3. If the laser processing is performed in an inert atmosphere such as Ar or vacuum, the waves continue to increase in height steadily up to at least 10,000 pulses.
4. If laser processing is performed in a potentially reactive atmosphere such as SF_6, then the surface waves develop in the same way as in Ar up to a certain number of pulses beyond which micro-holes form.
5. The maximum height of the surface waves extends above the original surface of the silicon.
6. Increasing the initial temperature of the substrate results in increased spacing between surface features.
7. Crystallography plays an important role in the shape and spacing of surface waves and in at least one case can preclude the growth of surface structure.

1.2.3 Review of Literature on Laser Patterning

Very often, perturbations form and evolve as a surface is irradiated by intense laser light and more interestingly, these perturbations tend form into regular surface patterns. A large amount of theoretical work has been focused on understanding the reasons for pattern formation on laser treated surfaces. Generally, the term 'instability' is used to describe the means by which the initially flat surface of the target develops an organized surface structure. Under non-equilibrium conditions that exist during irradiation,

forces that tend to flatten surfaces are overcome and small perturbations can increase in amplitude if positive feedback is established. In some cases, the simple presence of small surface perturbations is enough to initiate a positive feedback cycle. The interaction between surface perturbations and surrounding conditions will cause some perturbations to grow and others to diminish in time or with successive laser pulses depending on their wavelength. Instability theory seeks to determine which wavelengths promote growth and which ones do not.

The existence of surface structure on a previously flat surface indicates that, at some point in the process, material transport must have taken place. For organized surface patterns to form, this transport would need to be done in some orderly fashion. Phase transformation acting alone is usually not a means by which material transport occurs. Instabilities can provide the means for excess energy at the surface to be channeled into material transport.

Laser induced phase change within the target creates phase boundaries. Previous theoretical analysis of laser induced instabilities can be divided into three main categories based on the interfaces upon which these instabilities act. Some models focus on the interface between condensed matter (either liquid or solid) and the vapor phase. This includes either studying the advance of an evaporation front as it proceeds into the substrate or studying the motion of a free liquid surface. Other research focuses on the solid-liquid interface during re-solidification. This includes investigating the effects of thermal gradients on growth and interface energy anisotropy related to crystal orientation. The third category focuses on actions present at the interface of the solid, liquid, and vapor phases. Much of the research in this area has been directed to optimizing growth processes of large single crystals such as in Czochralski and ribbon growth of silicon. Unbalanced forces can be generated at this triple point and potentially cause mass transport.

Laser Induce Instabilities at the Vapor Interface

Laser matter interaction can be resonant or non-resonant in nature[3]. In resonant phenomena, considerations of the electromagnetic wave nature of the incident light (such as polarization, coherence, and spectral information) need to be made. In non-resonant phenomena, the laser serves only as an energy source and the resulting mechanisms are driven by thermo-physical or thermo-chemical effects. Fluence, pulse width and shape, and focusing are important factors in this regime. The latter is of interest in this study, but the former deserves mentioning.

LIPSS

There is no consensus in the literature for labeling the different surface structures that result from laser irradiation. The non-specific term ‘Laser Induced Periodic Surface Structures’ (LIPSS) has been coined by one group of researches[4-6] to describe one specific type of surface structure even though the name could be used to accurately describe others. LIPSS refers to a resonant phenomenon in which the incident light interacts with light that is reflected parallel to the surface to form an interference pattern. The maxima and minima of energy density of the interference pattern straddle the threshold for melting so that

highly localized melting occurs at locations of interference pattern maxima. Marangoni flows are initiated in the liquid due to the temperature gradients parallel to the surface and transport material. Figure 1.2 illustrates typical LIPPS patterns[7]. If the angle of incidence of the beam is perpendicular to the surface, the periodicity of the surface structure will match the wavelength of the laser. Adjustments in the spacing of the surface structure can be accomplished by changing the angle of incidence and polarization direction.

Evaporation Front Instabilities

The bulk of theoretical work on evaporation front instability was performed by scientists in the former Soviet Union from the late 1970's through the 1990's some of which is summarized by Anisimov[3]. The basic premise of this work is that the absorption of incident power on the substrate is limited by the thermal diffusion. Heat build-up is so rapid that the solid to liquid phase transition does not occur over a large enough volume in a short enough time to sufficiently contain or dissipate the heat. If temperature of the molten material becomes high enough, significant evaporation will occur. Evaporation can occur at any temperature above 0 K for any solid or liquid, but the evaporation rate, given in equation 1.1, is exponentially dependent on temperature and increases quickly near the boiling point.

$$V_s = V_o \cdot exp\left(-\frac{M \cdot L_v}{k_b \cdot T_s}\right)$$

equation 1.1

In this equation, V_s is the normal component of the evaporation front velocity, V_o is a constant on the order of the speed of sound in the condensed phase, M is the atomic mass, L_v is the latent heat of vaporization, k_b is Boltzmann's constant, and T_s is the surface temperature. The high power densities necessary to produce boiling are rarely of practical use outside of drilling holes. For energy densities low enough to avoid explosive boiling but still high compared to thermal diffusion rates, substrates remain in tact and temperatures in the molten substrate can rise enough for evaporation to be appreciable.

One class of evaporation front instabilities that has been investigated is due to a generation of negative temperature gradients within the liquid in close vicinity to the evaporation front, in accordance with the coordinate system in Figure 1.3. This means that over at least a small region, the temperature of the liquid increases at increasing distances from the liquid-vapor interface. Numerical modeling has demonstrated that for a given substrate, certain laser parameters can yield such conditions[3]. Figure 1.3(a-b) illustrates this. A small perturbation, $\eta(x)$, from the originally flat interface in the form of a displacement into the substrate would cause that region of the front to be at a higher temperature (Figure 1.3 (d)).

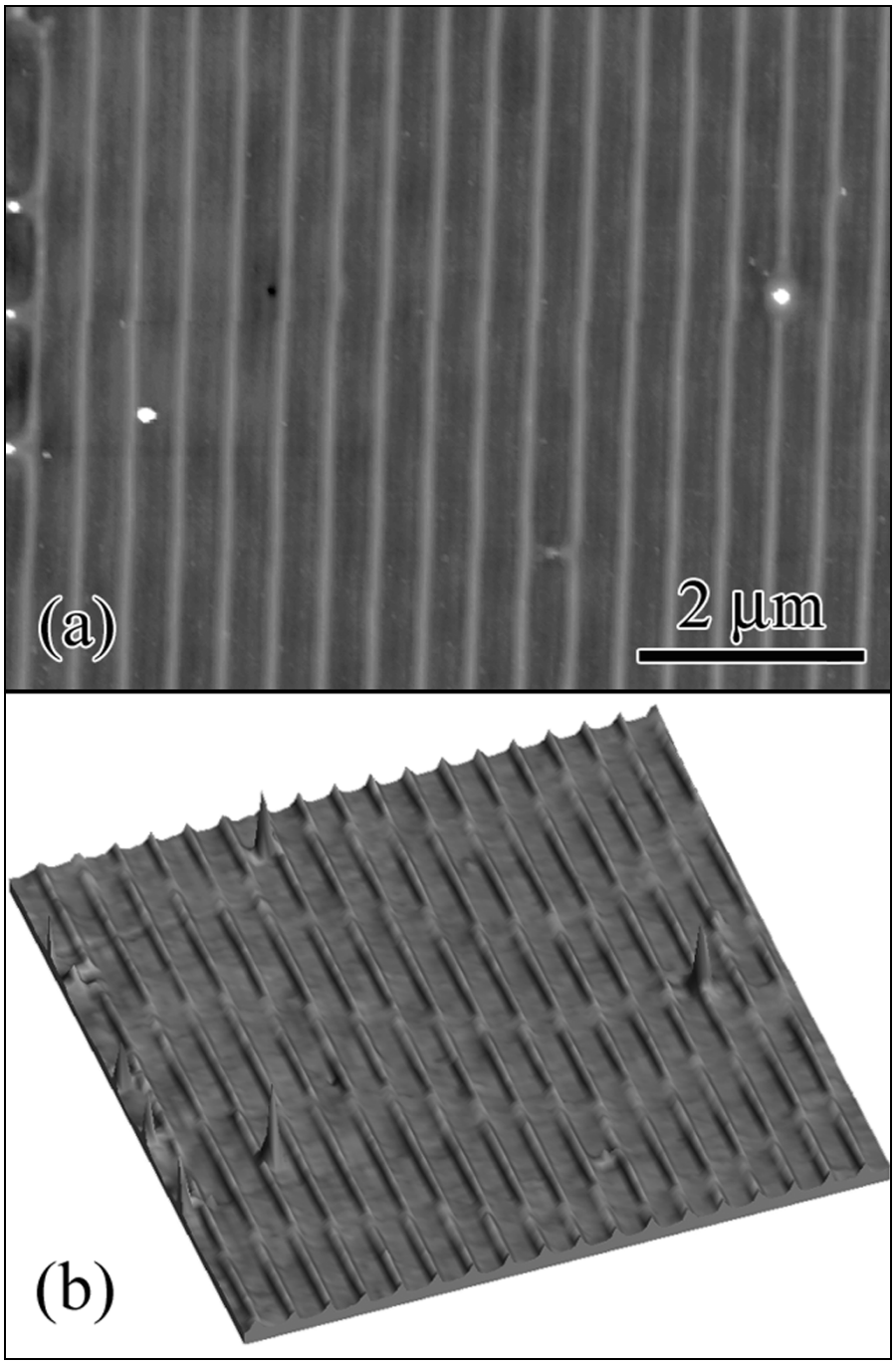

Figure 1.2. AFM images of LIPPS structures

AFM micrographs of LIPSS structures generated using KrF laser light (248 nm) at an angle of incidence 65° from normal. The average spacing between ripples is 440 nm. (a) a plan view of surface structure, (b) angled view of surface structure.

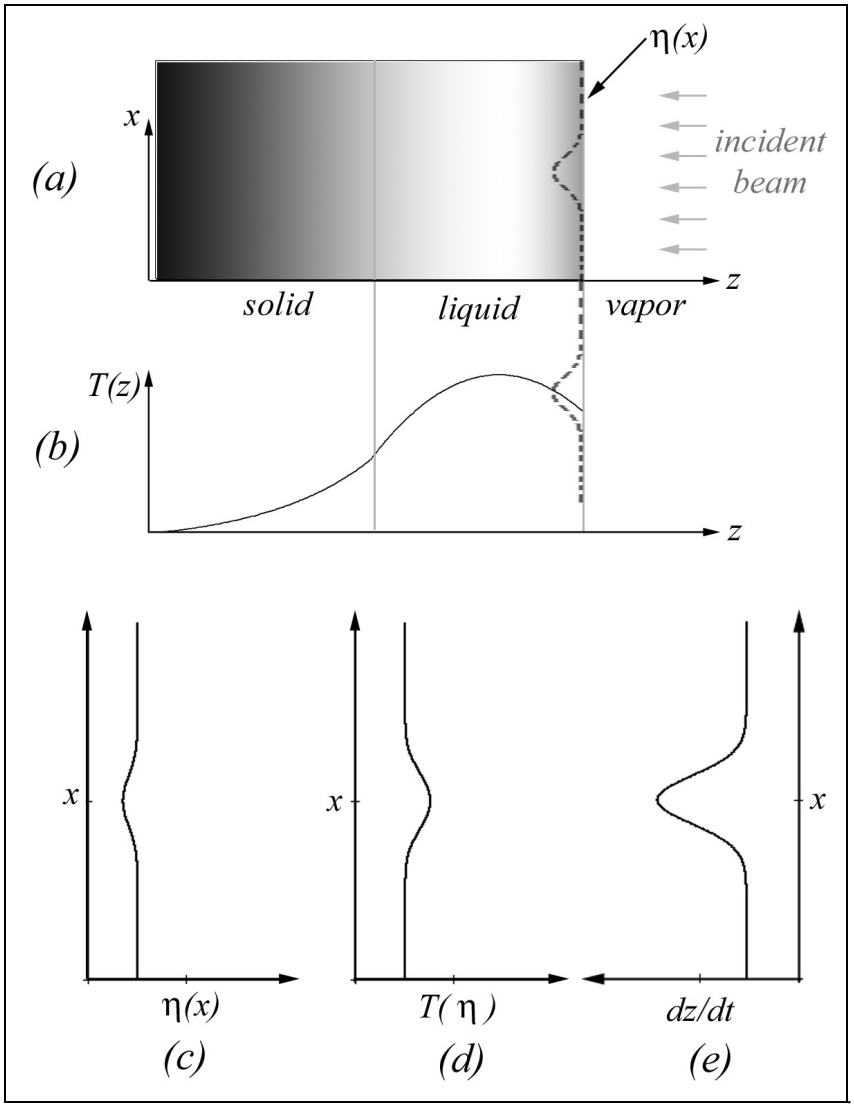

Figure 1.3. Diagram of evaporation instability.

(a) substrate cross-section during irradiation showing phase boundaries. The shading represents temperature - dark for low temperatures and light for high temperatures. The perturbations η is superimposed on the liquid-vapor interface. (b) plot of the temperature as a function of depth into the substrate corresponding to shading in (a). Note the negative temperature gradient at the liquid-vapor interface and that the peak of the perturbation is the location of highest temperature on the interface. (c) plot of perturbation height across interface. (d) plot of temperature across the interface. (e) plot of interface velocity due to temperature variation along the interface.

Since evaporation rate is related exponentially to interface temperature (equation 1.1), that perturbed region will acquire a larger velocity than the rest of the interface (Figure 1.3 (e)) and will increase in amplitude. Perturbations of different widths will not necessarily grow at the same rates however. Interface curvature can effectively change the heat of vaporization and subsequently change the rate of evaporation thus preventing perturbations below a certain size from growing. At the other extreme, large wavelength perturbation growth is suppressed by the depth over which the liquid temperature gradient is positive. These two boundaries help define a narrow wavelength range over which perturbations are unstable.

A model based on this idea has been developed using several simplifying assumptions such as: evaporation occurs in a vacuum, the evaporated material does not interfere with the incident beam, radiant heat loss is negligible, and the temperature profile in the liquid can be solved by the 1-D diffusion equation with allowances made for phase change. Further analysis yields equations that determine the most unstable and fastest growing perturbations.

The evaporation front instability theory described above has been applied to the experimental conditions used in this thesis project. The details of this are given in Appendix 1. The results indicate that 2-3 J/cm^2 energy densities are too low to initiate appreciable evaporation much less generate surface structure. This theory does predict that if the same laser energy were compressed into a 0.5 ns instead of 20 ns pulse, significant evaporation and instability growth in the evaporation front would be evident and surface structure with wavelengths of around 100 nm would be present. For the laser conditions used however, the thermal conductivity of silicon is simply too high compared to the rate of energy deposition for this model to be applicable. Furthermore, from Figure 1.1(i),we see that the profile of the surface perturbations protrude above the original surface. This excludes the possibility that evaporation alone is the cause for perturbation growth. Other experimental measurements found the rate of material loss prior to the formation of micro-holes to be on the order of a few angstroms per pulse. This is further indication that evaporation is not a factor in generating the surface structures in this project.

Plume – Melt Interaction

Another possible instability mechanism has been put forth by Brailovsky et. al.[8] who investigated the possible effect that a corrugated liquid surface may have on the pressure distribution within the ablation plume and the effect that this uneven pressure may have on reshaping the liquid surface. The process is simple in concept and is illustrated in Figure 1.4. The material ejected from the surface is propelled perpendicular to the surface. Above concave regions of the surface, the ablation plume will interfere with itself to produce higher pressure zones. In contrast, the plume can expand more easily above convex regions and create zones of lower pressure. The uneven distribution of pressure will act to push liquid from the valleys to the peaks. There is a competition between capillary forces which seek to flatten the liquid and pressure forces which seek to roughen it. A dispersion relation has been derived to determine the wavelengths for which pressure forces are dominant. To test this, the authors irradiated metallic targets of brass, bronze, Ni, Ge, Sn, and other materials. Trains of laser pulses with pulse widths of 30 ns and power

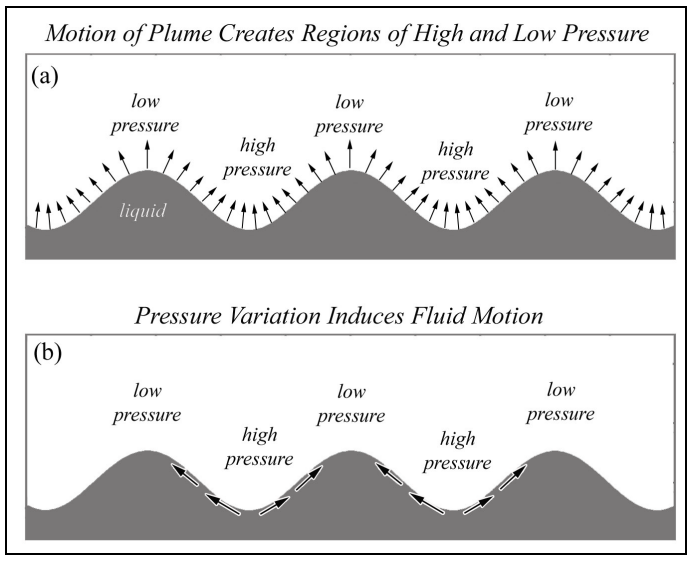

Figure 1.4. Diagram of the possible effects that surface shape may have on plume dynamics.

(a) The products of ablation are emitted normal to the substrate surface. If the surface is corrugated, oscillations in plume pressure can result as the ablation products interact. (b) The regions of high and low pressure in close proximity to the liquid surface can act to reshape the liquid surface.

densities on the order of $9 \cdot 10^8$ W/cm^2 were directed at the targets. This is equivalent to 27 J/cm^2, an energy density about 10 times larger than that used in experiments in this thesis. The background pressure was varied from between 10^{-3} Pa to 10^5 Pa. Laser irradiation generated surface patterns with wavelengths between 20μm and 30μm. Their experimental results show that the ultimate height of the surface perturbation decreases with increasing background pressure. It is also shown that surface structure wavelength increases and surface morphology changes somewhat with increasing angle of incidence (measured from the surface normal). Unfortunately, the derivation and equations presented in support of this concept contain errors, so it is not possible to compare the Brailovsky model against the results in this thesis. The authors claim that the wavelength predicted by their model is 10μm in agreement with their experimental results.

Although ablation plume confinement caused by surface structure is apparent in later stages of micro-hole and micro-cone development, it does not appear that the Brailovsky model is adequate to explain the experimental results in this thesis for early stages of wave growth. In contrast to the conditions and results he presents, in this thesis project the power densities are much lower, surface structure wavelength is independent of the angle of incidence, and variation in background pressure has no effect on wavelength. Furthermore, profilometry indicates that the first detectable surface waves have an amplitude

of ~2nm over a wavelength of 20μm. This is still a very flat surface and it is not likely that such a smooth surface could generate significant variations in pressure in the plume to move liquid over distances of several microns.

Capillary Wave Resonance

In recent years several attempts have been made determine the role that wave motion in the short lived liquid layer may have in the growth process of surface structure. Images of the surfaces have the appearance of liquid waves frozen in place and simple fluid wave motion intuitively seems to be a reasonable means for transporting material. Equation 1.2 gives the dispersion relation for fluid surface waves[9].

$$\omega = \sqrt{\left(g \cdot k + \frac{\sigma \cdot k^3}{\rho} \right) tanh(k \cdot h)}$$

Equation 1.2

This equation was derived assuming fluid incompressibility, irrotational fluid motion, a fluid depth much larger than wave amplitude, an infinite interface area, and does not take into account fluid viscosity. In this, ω is the wave oscillation frequency, g is the acceleration due to gravity, σ is liquid surface tension, ρ is liquid mass density, k is the wave number equal to $2\pi/\lambda$, λ is wavelength, and h is the liquid depth. Because of the short time periods and the small length scales associated with this process, gravity has a negligible effect on the molten metal. Fluid motion is dictated by surface tension forces and g can be set to 0. The maximum melt depth is small compared to wavelength so $tanh(h \cdot k)$ is often approximated as $h \cdot k$.

Dolgaev et. al.[10] have preformed nearly identical experiments as in this thesis and record similar results to the ones presented in this thesis. In their experiments, single crystal silicon wafers were irradiated with a 248nm pulsed laser source having a 20 ns pulse widths and energy density of 2 J/cm^2. The surface structure that forms is nearly indistinguishable from those shown in Figure 1.1. The experimental conditions differ in that they have used a 40 μm spot size and raster scan the substrate to form large areas of waves and micro-cones. They argue that the formation of surface structure is due to surface waves entering a state of resonance within the small spot size. The discussion begins by considering the cycle time for fluid motion. The assumption is made that the melt time is equivalent to the 20 ns pulse duration. In actuality, the melt time is 10 to 50 times longer than the pulse width for silicon at the fluences used.[11] A further assumption is made that the surface oscillation will undergo exactly one cycle during the melt time. If the melt depth is assumed to be 1 μm, which is accurate estimate, then Equation 1.2 gives λ equal to 1 μm. This value is much shorter than the actual measured wavelength. It is then argued that the capillary equation is not valid for this situation since it assumes an infinite surface extent. The actual spot size is finite and so the spectrum of wave vectors should be discretized thus giving the following equation for allowable wave numbers,

$$k = \sqrt{\pi^2 \cdot \left(\frac{m^2}{a^2} + \frac{n^2}{b^2} \right)}$$

Equation 1.3.

m and *n* are integer eigenvalues and *a* and *b* are spot size dimensions. Experiments performed as part of this thesis resulted in surface features with the same wavelength as reported by Dolgaev, but wavelength was found to spot size independent. It appears that the similarity between spot size and feature spacing could be coincidental in the Dolgaev study.

Another group of researchers[12] report results for roughly the same experiments, laser irradiation of Si substrates above the melting threshold. This group used femto-second lasers instead of nanosecond lasers and masked the silicon surface in some cases with TEM grids of varying grid sizes. This was done by attaching TEM grids with conductive tape flat against the surface of the silicon substrate and irradiating both the grid and the substrate with multiple laser pulses. The holes in the TEM grids act as small apertures for the laser light. They have presented experimental results, shown in Figure 1.5, consistent with ones in this thesis. Namely, feature spacing increased with increasing melt time, as modulated by intensity in their case, spacing was independent of spot size, and silicon cones formed one the crests of waves. They

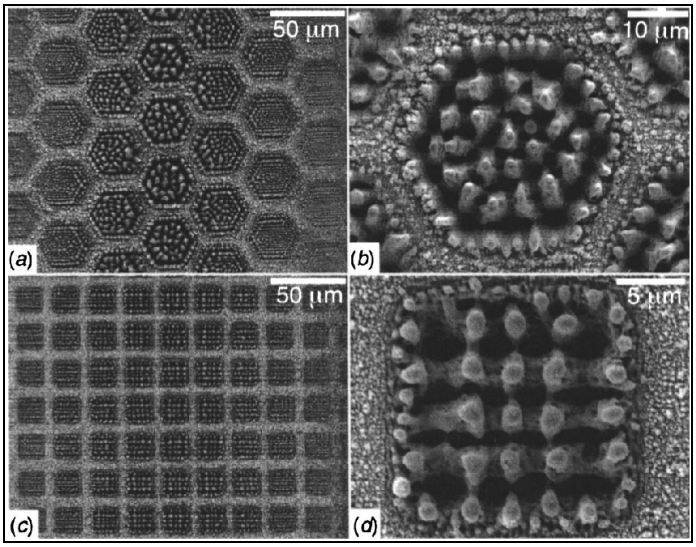

Figure 1.5. SEM micrographs of femto-second laser generated micro-cones

TEM grids were used as partial masks for substrate. The conical structures formed where laser light could pass through the holes of the TEM grids. Note in (a) and (c) that the cone spacing varies across the substrate even though the aperture size is constant.

measured a feature spacings of around 5 μm. In their analysis they conclude that discretized liquid vibrations modes is not a likely means for establishing the surface periodicity. This is apparent in Figure 1.5(a and c) in which spot size is fixed by the TEM grid spacing but micro-cone spacing varies throughout the irradiated region. They also conclude that action of the plume likewise does not play a role in wave formation. The authors do advocate capillary wave mechanics, of the continuum variety as in Equation 1.2, as a likely important factor in wavelength selection, but that other mechanisms must also play a role. They use a similar argument as given by Dolgaev that the time for a single wave oscillation cycle is set to be equal to the melt time and no wave with a longer wavelength should exist. Since they are using a femto-second laser, the melt time can be shorter and still maintain an appreciable melt depth as compared to melt times for nanosecond lasers. Calculations assuming a range of melt times between 75 ns and 600 ns and melt depths of between 100 nm and 10 μm yields estimates for the range of possible wavelengths between 2 μm and 20 μm. This range spans the 5 μm spacing for their results using TEM grids as masks and the ~15 μm spacing which results from no mask being used. The lower estimates of melt time and depth are probably closer to the actual values since they were measured by another group experimentally under similar conditions[13]. The upper estimate for melt depth that was used is about 100 times greater than the actual melt depth and is quite unrealistic. So this model can not adequately explain the formation of the longer wavelength surface structures.

The restriction that the wavelength is limited by the time needed for that wave to complete an entire cycle during the melt time originates from the idea that if the wavelength were any longer, and oscillated at a lower frequency, then the wave amplitude would necessarily be smaller at the end of a melt-solidification cycle because the wave would solidify before it returned to its original height. The model presented as part of this thesis does not assume this restriction. The capillary wave equation describes how an uneven liquid will move due to surface tension. There is no reason why a surface wave could not move through just a half, or a tenth, or less of a cycle in the given melt time. It will be shown that if capillary wave moves through only a small fraction of a cycle then most of its original amplitude can be maintained while other mechanisms work to increase the amplitude from pulse to pulse. If the presumably more accurate estimates of a melt time of 75 ns and a melt depth of 100 nm are used in the model to be presented later as part of this thesis, a spacing of 4.5 μm is predicted in good agreement with the experimentally measured value.

Laser Induced Waves on Silica Coated Silicon Wafers

Several research groups[13-15] have been investigating another way to induce wave growth on silicon surfaces irradiating wafers coated with silicon oxide. The resulting surface structure looks very similar to the ones studied in this thesis except that the wavelength is often much smaller. Compare Figure 1.1(a-d) and Figure 1.6 and note the difference in scale. Oxide layers of different thickness are thermally grown onto single crystal silicon substrates that are then irradiated with between 1 and 10 laser pulses. The top

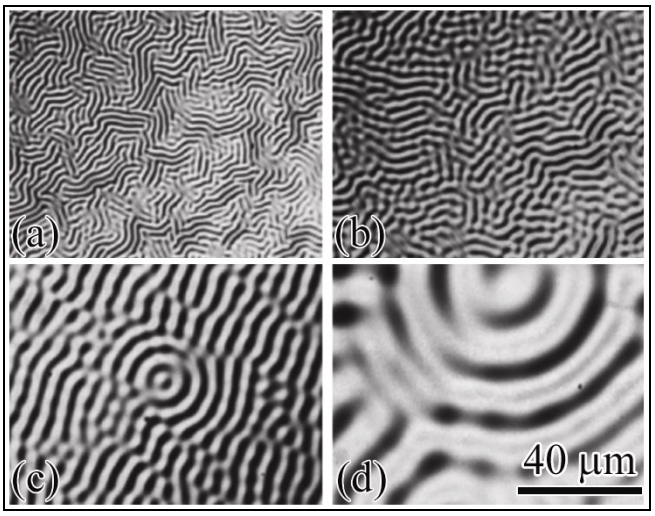

Figure 1.6. Optical micrographs of laser irradiated silica coated single crystal silicon

The periodicity of the surface structure is a function of silica thickness where the oxide is (a) 36 nm, (b) 92 nm, (c) 178 nm, and (d) 440 nm.

silica layer is transparent to the incident beam, so nearly all absorption takes place in the silicon. Laser is fluence high enough to induce melting in the silicon while the oxide layer remains solid. Evaporation of the silicon is carefully avoided since this would cause the oxide layer to separate from the melt below.

A residual compressive stress of approximately 300 Mpa is always present in the thermally grown oxide layer when at room temperature. The oxidition process itself is not the root cause of stress. Rather, the stress is due to the two materials having different coefficients of thermal expansion. Though there is no stress at the film growth temperature, the 800 K drop to room temperature after processing results in a mismatch in contraction and induces strain. The coefficient of thermal expansion for Si is about ten times that for SiO_2, so the silica is under compressive stress at room temperature. Sokolowski-Tinten et.al.[13] have proposed a model in which surface structure formation is driven by compressive residual stress in the silica causing it to buckle while the silicon layer below is molten. See Figure 1.7. Buckling of free columns and plates is well understood[16,17], but the nature of the briefly formed boundary conditions at the silica-melt interface is somewhat more complicated since the allowed modes of buckling are determined in large part by the fluid mechanics of the molten silicon. One restriction at the boundary is that the volume of the fluid must be conserved. No such restriction is present in the buckling of free columns or plates and so these structures are prone to fail in the lowest energy, half-sine-wave buckling mode (Figure 1.7(d)). Conservation of liquid volume does not allow this mode so that the second mode of buckling, the full sine-

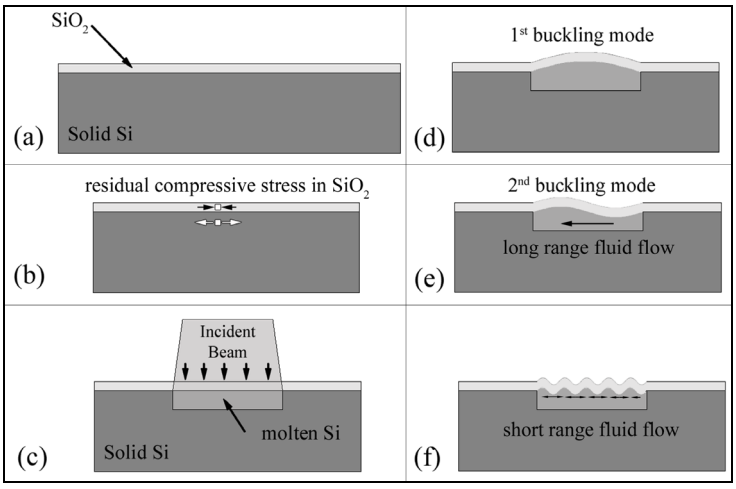

Figure 1.7. Diagram illustrating the formation of laser induced waves by buckling silica

(a) growth of oxide layer takes place at elevated temperatures. (b) as the processed wafer cools to room temperature the silicon contracts more than the silica which generates compressive stress in the silica. (c) laser irradiation passes through the oxide layer but melts the silicon beneath, thus freeing oxide to buckle. (d) the first (half sin wave) buckling mode is not permitted because fluid volume is not conserved.(e) the second mode of buckling is permitted by volume constraints, but requires long range fluid transport in order to occur. (f) high order buckling mode which results due to a balance between minimizing fluid transport and oxide stress.

wave, is the lowest energy mode of failure permitted (Figure 1.7(e)). However, for the second mode of buckling to occur, a significant volume of liquid must be transported laterally across the substrate.

Fluid mechanics dictates how fast this liquid transport can occur for a given the amount of force provided by strain. Since the melt time is on the order of 10 ns – 100 ns, flow rates are important. The spacing of the surface structure is therefore determined by a balance between the oxide layer seeking a low energy, long wavelength mode of buckling and the fluid inertia and viscosity that tends to avoid high velocity transport. The Sokolowski-Tinten model correctly predicts the wave spacing for 50 nm and 100 nm thick oxide layers.

Some related experiments have been carried out in an attempt to exploit this stress induced surface structuring to generate controlled surface patterns[14]. This was done by lithographically pre-patterning gold features on the oxide surface in order to protect selected regions of silicon from the laser and from melting. During irradiation, the oxide is effectively pinned at the locations beneath the gold thus modifying the way the stress field in the silica can relax and the way subsequent wave pattern forms. A goal of this work

would be to use standard lithographic processes combined with laser treatment to create surface patterns with resolution greater than that currently permitted by lithography alone. Figure 1.8 shows results of this work.

Instabilities at the Solid-Liquid Interface

Nearly all studies of laser induced surface modification are concerned with action at the interface between vapor and either solid or liquid. However, the instabilities that are known to occur at the solid-liquid interface during solidification should be explored to asses their potential role in surface structuring. The first instability to be discussed is similar in nature to the evaporation instability which was presented previously. The condition for instability is a negative temperature gradient in the melt close to the solid-liquid interface[18] in accordance with the coordinate system in Figure 1.3. Under these conditions, any small perturbation in the interface which protrudes slightly further into the melt than the rest of the interface will be at a lower temperature than the rest of the interface. There is therefore a greater driving force for solidification the further this region of the interface advances, and its local front velocity will continue to increase. The large variation in front velocity along the interface produces a characteristic dendritic structure. The minimum dendrite spacing is determined by the diffusion rate of the latent heat of fusion. Latent heat is released normal to the moving front and from the sides of dendrites. Dendrites are spaced so that the heat released during solidification from the side walls of the dendrites do not interfere with one another. Dendrite width is determined by the effect that curvature of the interface has on the solidification

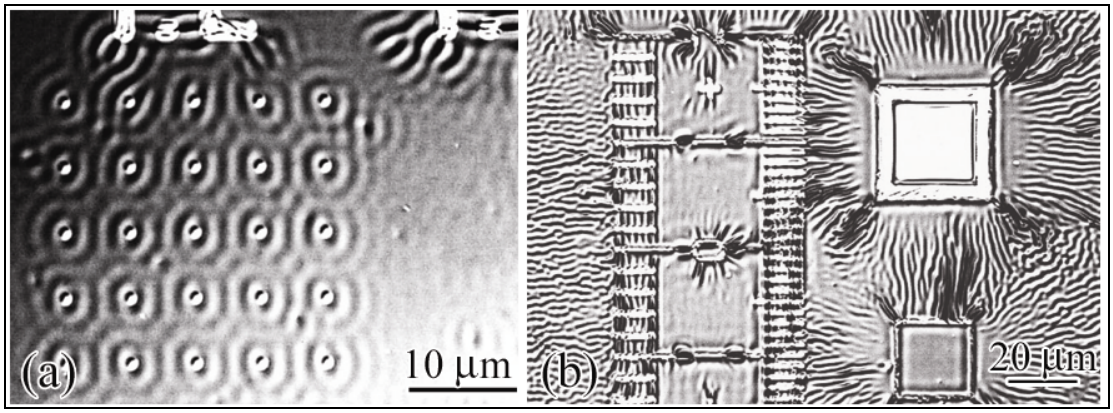

Figure 1.8. Optical micrographs of organized patterns formed by laser irradiation.

Lithographically patterned gold on selected regions of the Si/SiO_2 substrate prevented melting beneath these regions and modified the relaxation of residual stress in the silica and the formation of surface structure.

temperature. The greater the curvature, the greater the melt undercooling needs to be for solidification to occur. The results of several computer models of laser melting and solidification agree that by the time the solid-liquid interface has reached its maximum depth, the temperature gradient normal to the interface is positive, so it is not likely that this instability plays much of a role in laser surface structuring.

Experimental results show that crystallographic orientation has an influence on determining the surface structure wavelength between (100) and (111) oriented surfaces as well as completely preventing the growth of surface waves as in the case of (110) silicon. Since crystallographic orientation plays an important role in solidification processes, it is reasonable to speculate that crystallography expressed in the final surface structure may originate from faceting at the solid-liquid interface. Faceting occurs because the surface energy of different crystal faces can be different. A higher surface energy translates into a slower front velocity for the same undercooling in the melt. An initially spherical solid nucleus surrounded by undercooled melt will usually not remain spherical for long since growth rate is anisotropic. The eventual shape of the nucleus will be determined by the highest energy (lowest growth rate) faces. However, the situation is different for an initially flat surface. A slow moving facet will not dominate the shape of the front. In fact, any roughness which may exist on the interface that corresponds to crystal orientation will eventually be erased as the front proceeds.

It appears that actions at the solid-liquid interface work to reduce the amplitude of perturbations. At first it may appear that this implies that consideration of this interface can be rejected in modeling perturbation growth. In fact, this reduction in amplitude and especially the rate of the reduction in amplitude will become very important factors in the model to be presented.

1.3 Literature Review of Electronic Transport in SWNT's

The fields of nanoscience seek to explore, engineer, and utilize the unique properties that some materials acquire when any or all of their spatial dimensions are reduced to the nanometer scale. In the fields of electronics and photonics, size reduction to this scale can have particularly important results. This is mainly due to the fact that charge carriers, photons, and other particles become quantum confined. The quantum nature of these particles, usually disguised in bulk, can then be expressed. Also, on this scale some properties, for instance band structure, which is for the most part fixed on the large scale, can be tuned if the fundamental size is reduced to within this confinement regime. A third advantage of working on this scale is simply that if one is working with nano-sized components, one can assemble these into nano-sized devices. This is important in the semiconductor industry where the progress of Moore's law appears frustrated by the limitations of lithography. It may be possible to overcome this barrier by building from the bottom up with nano-components. Carbon nanotubes have been the focus of a great deal of research since they can exhibit characteristics described above and possess valuable properties that make them ideal candidates for fulfilling needs for high-performance, multifunctional materials.

The foreseen potential for carbon nanotubes in future applications is great. Mechanically, they are estimated to have the largest tensile strength of any material (1TPa[19]). Electrically, they canbe either metallic or semiconducting depending on their atomic structure. Photonically, they have been shown to have interesting properties in emission and absorption of infrared light[20]. Their small diameter and extreme aspect ratio is of interest in the theoretical exploration of the physics of 1-D systems. They can be produced in relatively large quantities, or a single tube can be deterministically grown at a precise location[21]. Barriers to realizing the full potential applications of SWNT lie mainly in processing. That is to say, organization and manipulation of nanotubes on a large scale is at present difficult. One challenge lies in the fact that single wall nanotubes are not energetically prone to exist individually. They instead, as a result of strong Van der Waals interactions between tube walls, tend to form into bundles (or ropes) of nanotubes. In addition, even if individual single-walled nanotubes can be found, they are small, unwieldy, and fragile. Another challenge lies in the fact that no successful method has been developed to sort as grown nanotubes into like-structured groups, although breakthroughs in determining the atomic structure of specific nanotubes are being made[20].

This review of the literature on carbon nanotubes will include examinations of electronic transport properties through single carbon nanotubes, between nanotube junctions, through nanotube bundles, and through nanotube/polymer composites.

1.3.1 Electronic Properties of Individual SWNT's

Band Structure

The atomic structure of a single wall carbon nanotube (SWNT or CNT) can be thought of as a rolled graphene sheet whose long edges are joined seamlessly. The angle of the rolling direction (chiral angle) relative to the 2D graphite lattice and the diameter of the nanotube completely define the structure of the nanotube. These two parameters also define the basic electronic properties of the nanotube. Other factors such as doping and structural defects can influence the electronic properties as well. The SWNT structure is often described in terms of the integer multiples (n,m) of the primitive vectors of the graphite which define the roll-up vector (see (d)). By this scheme the roll-up vector is written as $\mathbf{c} = n\mathbf{a_1} + m\mathbf{a_2}$. Two high symmetry types of nanotubes bound the many possibilities for nanotube structure. These are the *zigzag* (n,0) and *armchair* (n,n) structures. So named since the atoms form armchair and zigzag shapes if a cut is made perpendicular to the tube axis. The remaining intervening tubes are termed '*chiral*' (see Figure 1.9). The length of the roll up vector becomes the diameter of the nanotube, and the angle the roll-up vector makes with $\mathbf{a_1}$ is the chiral angle.

The basic band structure of nanotubes can be approximated using the known graphene energy structure[22,23]. A projected view of the surface of the valence band is shown in Figure 1.10(a). The peaks of the surface (lighter shade), called Fermi points, are in line with corresponding valleys in the conduction band. The slight overlap between these surfaces gives flat sheets of graphite their semi-metallic property.

The periodic boundary conditions imposed by rolling the sheets into tight cylinders has the result

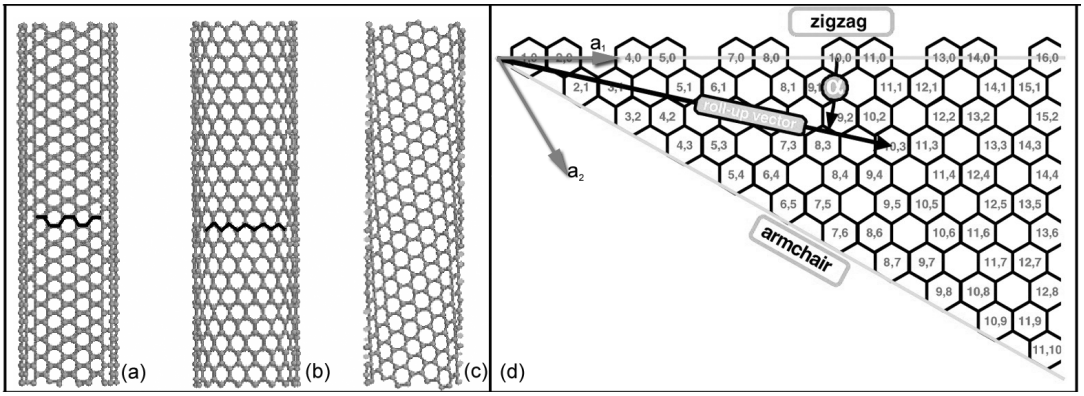

Figure 1.9. Types of nanotubes

(a) armchair, (b) zigzag, (c)chiral[21]. (d) lattice of a graphene sheet showing primitive vectors an example of the roll-up vector for a (10,3) nanotube and (n,m) designations for semiconducting tubes.

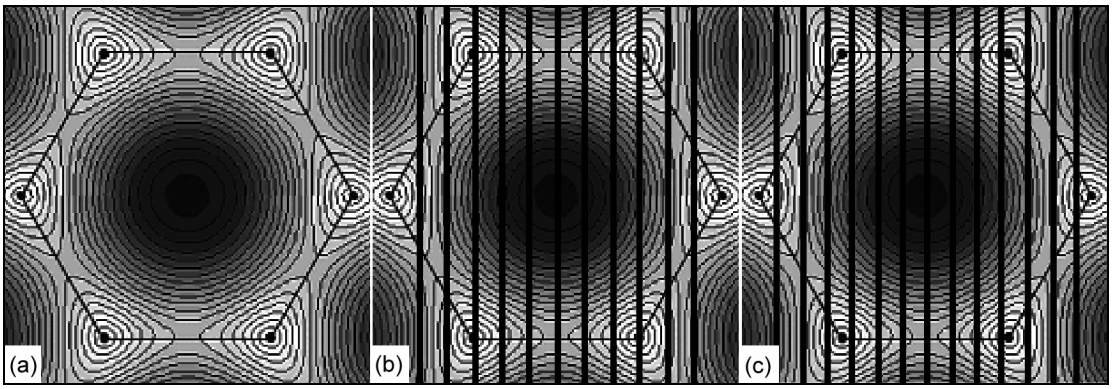

Figure 1.10. Diagram of nanotube Brillouin zones and k-vector alignment.

(a) first Brillouin of a graphene sheet. The lightly shaded regions correspond to energy peaks in the valence band.(b) dark lines indicate permitted quantized k-vectors of a (9,0) tube in the first Brillouin zone. Since the permitted wave vectors cross energy peaks, the tube is metallic. (c) dark lines indicate permitted quantized k-vectors of a (10,0) nanotube tube. These vectors do not coincide with energy band peaks therefore rendering this nanotube semiconducting.[22,24]

of quantizing the wave vector in the circumferential direction, thereby permitting the existence of only certain wave vectors. If these wave vectors are superimposed onto the first Brillouin zone, predictions on the nature of conductivity of the tube can be made; if the wave vectors pass through the peaks of the valence band, the nanotube will be metallic, otherwise the nanotube will be semiconducting. This observation can be summarized in the condition that if $|n - m|/3$ is an integer, the nanotube will be metallic, otherwise it will be semiconducting. Figure 1.10(b) and (c) illustrate this for two cases. For $(n,m) = (9,0)$ in Figure 1.10(b), the spacing of the *k*-vector results in its passing directly through the peaks of the valence band, thus making it metallic. Figure 1.9c shows the quantized *k*-vectors for a (10,0) semiconducting nanotube which do not intersect the graphene Fermi points.

In actual nanotubes, this approximation is not quite satisfactory since the curvature of the graphene sheet influences band structure. Tight binding calculations have shown that curvature tends to push the Fermi points of zigzag nanotubes in the circumferential direction and out of line of the k-vectors, while curvature induces the Fermi points of armchair nanotubes to be shifted along the length of the nanotube and in line with k-vectors. Zigzag nanotubes therefore lose their metallic nature as curvature forces a small energy gap to form[22]. The size of this gap is inversely proportional to the square of the radius of curvature[25]. Armchair nanotubes retain metallic properties despite curvature. However, it has been predicted that a small energy gap can form when armchair nanotubes coalesce into bundles.

Ballistic Transport in Nanotubes

Some of the high conductance properties of nanotubes are due to confinement of electrons in the carbon nanotubes. These spatial restrictions only permit motion of electrons in two directions, forwards and backwards along the length of the nanotube. This along with energy and momentum conservation requirements greatly reduce the likelihood for scattering of electrons of certain energies[23] and results in ballistic transport of electrons along the nanotube. Theoretical calculations[26] predict that even in the presence of impurities, given that the impurity size is larger than the lattice spacing, backscattering of carriers can be zero.

1.3.2 Nanotube Heterojunctions

A nanotube hetero-junction is valuable since it can possibly be used as a building block for electronic devices. One needs connections from metallic to semiconducting tubes in order to connect semiconductor devices to the outside world, and one needs to connected nanotubes of varying band gap widths in order to build rectifying and amplifying logic devices. The line between defect and device becomes blurred when considering nanotube junctions. A junction can be defined as the joining together of two nanotubes with different (n,m) designations. This will cause a mismatch that is accounted for by replacing some of the hexagonal rings of graphite with pentagon or heptagon rings. The pentagon and heptagon rings are treated as crystal defects, and so the junction itself can be considered a defect. Two different ways of approaching the problem of joining nanotubes are considered. One is to couple two nanotubes of any size or chirality together through a junction region[24,26]. A contrasting picture is that a junction can be formed by adding defects to an otherwise perfect nanotube[27].

Figure 1.11 shows a scanning transmission microscope (STM) image of heterojunctions between single wall carbon nanotubes. Figure 1.12(a) shows a TEM image of a junction between multi-wall carbon nanotubes. Figure 1.12(b-c) show a theoretical model of a junction that could be made between any two tubes and the generalized scheme for constructing this junction. Two studies[24,26] examine a specific class of a nanotube junctions like the ones shown in Figure 1.12. The two tubes do not have collinear axes as will be examined later[28], but instead share a wall in common. This construction is useful since it can be generalized to connecting any two tubes of any chirality by way of a junction region and a pentagon and heptagon pair. Such a construction will always result in a junction area with an asymmetric ensemble of pentagons and heptagons. From these structures, a theoretical model of conductivity is constructed by describing the probabilities for reflectance and transmission through the junction region. It is based on matching wave functions at the large tube-junction interface and the small tube-junction interface. These equations are expressed in terms of the circumference of the two tubes.

One study[24] treats transport through heterojunctions as a tunneling phenomenon. Only zigzag tubes are used with the main purpose to compare conduction through metal-metal and metal-semiconductor

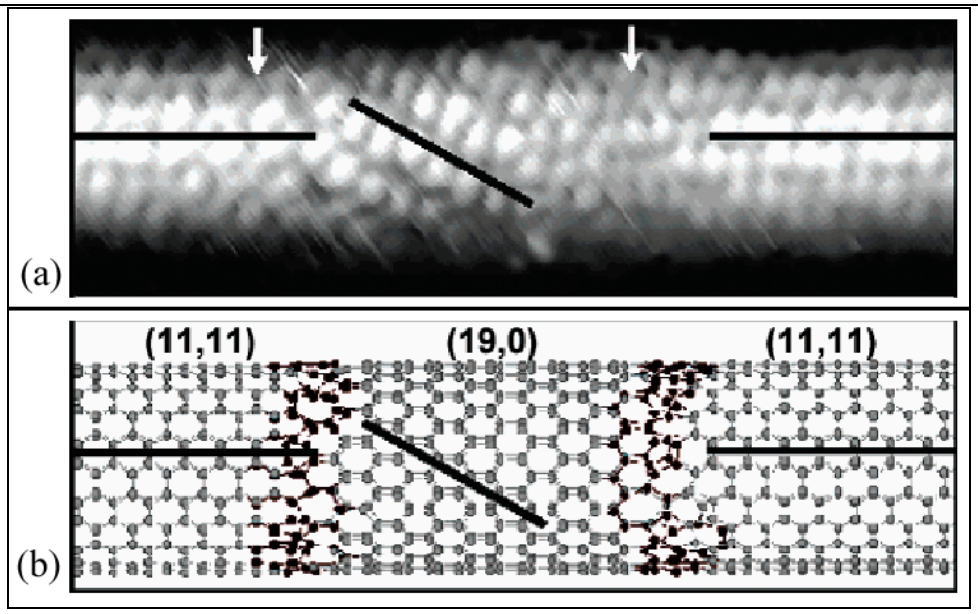

Figure 1.11. STM image of nanotube hetero-junction

(a) STM image of a junction between two nanotubes, (b) schematic representation of the junction showing chirality and topology.

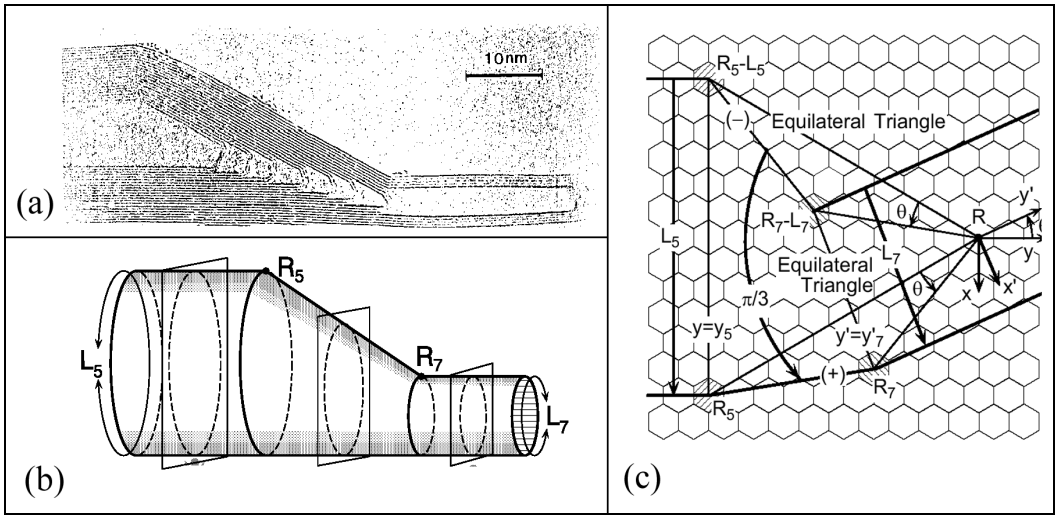

Figure 1.12. TEM image of multi-wall nanotube hetero-junction.

(a) TEM image of multi-wall nanotube junction. (b) Theoretical model of junction. (c) General scheme to construct a junction between any two nanotubes.

junctions. The conclusions of this study are: 1) that conductance through the metal-metal junction increases with increasing voltage, and there are oscillations in conductance as a function of voltage. Both of these trends are indicative of tunneling transport. The oscillation are due to resonance of tunneling probability between the two tubes. 2) In the case of the metal-semiconductor junctions, there appear to be only de-localized wave functions in the metallic side that do not transmit to the semiconductor side.

A similar theoretical analysis was performed except that a different junction topology was used[27]. The previous models placed pentagon and heptagon rings at opposing sides of the tube. This study keeps them paired and sharing two atoms (see Figure 1.13(a)). Analysis of both a metal-semiconductor [(8,0),(7,1)] and a semiconductor-semiconductor [(8,0),(5,3)] junction was performed. Results show that each side of the junction maintained the general electronic characteristics it possessed before being fused. The semiconductor-semiconductor junction did bring about the formation of electronic states within the energy gap that did not exist in the constituent tubes prior to joining. These additional interface states are ascribed to the presence of pentagon and hexagon rings near the junction.

Another approach to the problem of junctions comes from a slightly different perspective and some very interesting results were found related to defect symmetry at the junction[28]. In this study, only the junctions between metallic tubes are considered. It should be noted that hybridization due to curvature was not considered. Therefore, zigzag nanotubes are still considered to be metallic. The central axes of the two tubes lie on the same line. Three cases are considered: 1) the joining of (12,0) zigzag and (6,6) armchair nanotubes, and 2) the joining of (9,0) and (6,3) nanotubes symmetrically and 3) the joining of (9,0) and (6,3) nanotubes asymmetrically. In the first case, there is a unique arrangement of defects which will satisfy the junction. This is done by 6 alternating pentagon and heptagon rings. Figure 1.13 shows these tubes cut and rolled out to illustrate their topology. The defects, warped somewhat by the 2D projection, are shown to alternate, and it is apparent that the 3D reconstruction of these two nanotubes will yield a system of defects with radial symmetry. There is no unique arrangements of defects for the second case [(9,0),(6,3)]. The defects can take on the radially symmetric arrangement [657657657] to seamlessly join the two tubes, or the asymmetric arrangement [675667575]. As one might expect, the introduction of defects in a ring at a junction would result in a loss of conductivity. This is observed in case 3), the asymmetric case. A remarkable result is noted in that an energy gap is formed at the junction in both symmetric cases (1 and 2). Or to put in the author's terms, the probability for reflection is 1 for electrons within a certain range of energies. The fusing of two metallic tubes will result in a semiconducting junction, if the defects are arranged symmetrically. If defects are arranged asymmetrically, the junction will be metallic.

An explanation for this interesting behavior is given in terms nanotube band structure. However in this case it is necessary to consider the interaction of different Brillouin zones and the imparting of angular momentum **L** at the junction. Figure 1.14(a-b) show the first Brillouin zone and the allowable circumferential *k*-vectors for (12,0) and (6,6) nanotubes. The **k**=0 point is located at the center of the

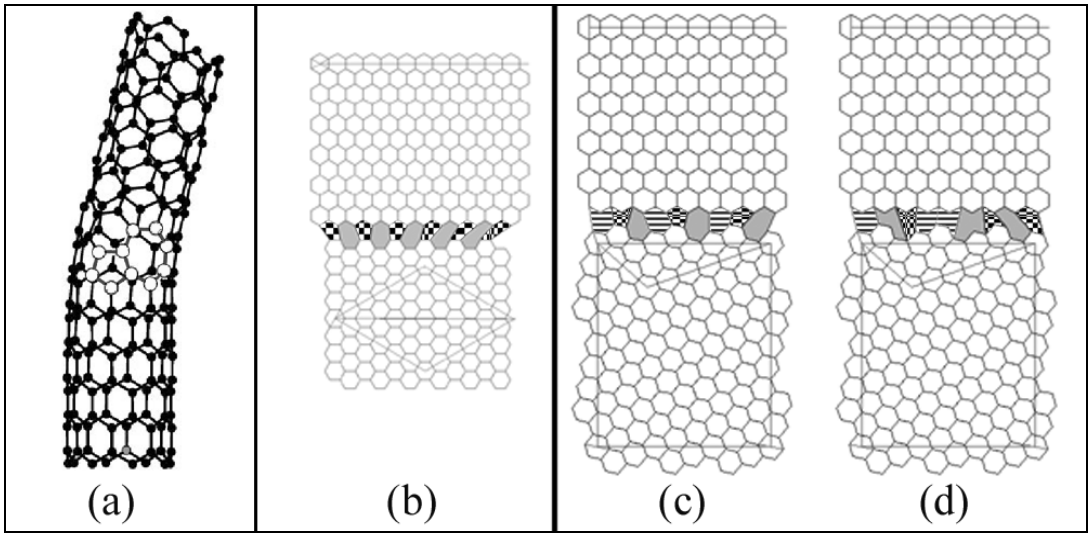

Figure 1.13. Nanotube junctions using tangent heptagon and hexagon rings

(a) Junction between (8,0) and (7,1) nanotubes[27]. (b-d) Nanotubes unrolled in 2D sheet showing the degree of symmetry for junction between (b) [(12,0),(6,)], (c) [(9,0),(6,3)] symmetric, (d) [(9,0),(6,3)] asymmetric. checkered = pentagon, striped=hexagon, gray = heptagon.

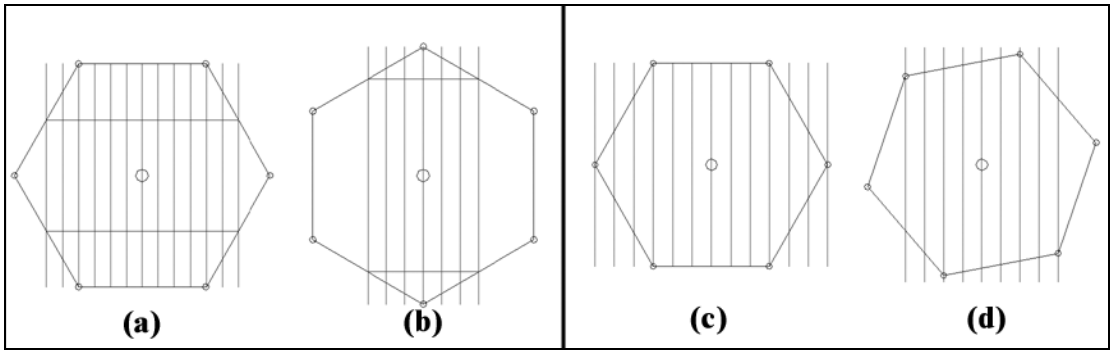

Figure 1.14. First Brillouin zone with allowable k-vectors for various nanotubes

(a) (12,0), (b) (6,6), (c) (9,0), and (d)(6,3).

Brillouin zone, the distance away from the center represents increases in angular momentum. Conduction from one tube to another can only occur at the Fermi points (corners of the hexagon), and conduction will only occur if angular momentum is conserved when crossing the junction. One can see from the figures that the angular momentum at the Fermi points are different for the two nanotubes: **L** = 0 for (12,0), and **L** = 2 for (6,6). The interface is radially symmetric and therefore can in no way to provide angular momentum to a traversing electron. Angular momentum therefore can not be conserved, an electron can not transition from the Fermi point of one nanotube to a Fermi point of the opposing tube, and current can not flow. This same explanation is valid for the symmetric case of the [(9,0),(6,3)] junction where: **L**=0 for (9,0) and **L** = 1 for (6,3). The unbalanced circumferential forces existing at the interface of an asymmetric junction can impart angular momentum to an electron. There is therefore a non-zero probability for angular momentum conservation across the junction and current flow can occur. The conductivity is smaller than that for either tube since the junction still acts as a reflecting defect. Circular asymmetry can be imposed on a symmetric junction by external means. This can be by way of mechanical deformation at the junction, or a circularly polarized external electro-magnetic field with its polarization axis parallel to the nanotube axis. With the results of this analysis in hand, novel devices can be envisioned based on this idea of symmetry breaking. This might include nano-mechanical switches, thermal switches, and polarization selective photoconductive switches.

1.3.3 Nanotube Y-Junctions

The next step up in complexity in this review of nanotube transport properties is the Y-junction. Both experimental and theoretical work has been performed on the Y-junctions that are formed by joining three nanotubes together. There are several of exciting possibilities envisioned for these structures. The most important of which being that they could be used as coveted nano-scale switches forming the basic building blocks for carbon based computers.

A study was conducted that relates the topology of the nanotube Y-junction to the electrical properties with some recognizable trends emerging. Table 1.1 gives a summary of theoretical work on transport properties through nanotube Y-junctions[29]. In this study, various configurations of zigzag and armchair nanotubes were joined together and the electrical characteristics were determined. The first column shows an image of the junction. The stem is the lower half of each picture, the branches the upper. The darker shaded rings are heptagonal defects. In every case but (d), 6 heptagons were used to join the various nanotubes of differing (n,m) designations together. In case (d), 4 heptagons and an octagon were used. The second column lists the type of tubes used (the stem is listed first), whether the tube is zigzag(zz) or armchair(ac), and whether the tube is metallic (M) or semiconducting (SC). The third column states whether the overall junction in symmetric or not. The last two columns list the results of the quantum conductance calculations. ‘Perfect’ rectifying behavior designates an asymmetric I-V curve in which there

Table 1.1: Tabulated results from [29]. First column shows image of Y-junction. Second column lists (n,m) of constituent tubes, column 3 states structural symmetry. Columns 5 and 5 give results of theoretical electrical characterization.

	Structure, electronic	Structural	Rectifying	Switching
 a	(14,0)(7,0)(7,0) zz zz zz SC SC SC	Sym.	Perfect	Perfect
 b	(8,0)(8,0)(8,0) zz zz zz SC SC SC	Sym.	Perfect	Perfect
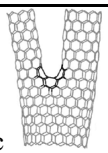 c	(17,0)(10,0)(7,0) zz zz zz SC SC SC	Asym.	none	none
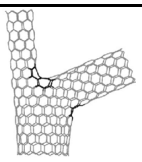 d	(17,0)(10,0)(7,0) zz zz zz SC SC SC	Asym.	none	none
 e	(10,10)(5,5)(5,5) ac ac ac M M M	Sym.	Asym. but leakage	imperfect
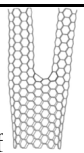 f	(10,10)(5,5)(4,4) ac ac ac M M M	Asym.	Asym. but leakage	Imperfect, worse than case d
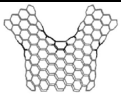 g	(10,10)(8,0)(8,0) ac zz zz M SC SC	Sym.	Asym. but leakage	imperfect
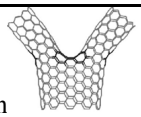 h	(10,10)(9,0)(9,0) ac zz zz M M M	Sym.	Asym. but leakage	imperfect
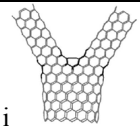 i	(14,0)(4,4)(4,4) zz ac ac SC M M	Sym.	Perfect	Perfect

is no leakage. The IV 'measurement' was made by electrically joining the two branches and measuring current as a function of voltage between the stem and branch. Switching was tested by biasing one branch opposite the other, and measuring current in the stem as a function of the bias voltage. A switch is considered 'perfect' if a plot of stem current vs. bias is symmetric and everywhere positive. This means that either branch can act as a gate to stem current. There are three main trends noted in this work:

1. Perfect rectification is obtained for symmetric carbon nanotube Y-junctions of zigzag stems. These also show perfect switching.
2. Asymmetric Y-junctions show no rectification or switching properties.
3. Junctions with armchair stems, show some rectifying characteristics with some leakage independent of chirality or symmetry. As in previous theoretical studies, chirality and symmetry play a clear role in electronic structure and performance.

Controlled growth[30] and electrical measurements[31] of multi-walled nanotube Y-junctions were performed. These were prepared by CVD growth in alumina templates of arrayed nano-channels. The alumina templates were chemically removed leaving an inverted forest of nanotube Y-junctions. The branches were of smaller diameter than the stem. Electrical contacts were made by sputtering a continuous gold layer on the exposed stems of the junctions, and branches remained connected to the original aluminum substrate. Measurements were made on approximately 100 nanotubes in parallel simultaneously. It was not feasible in these experiments to have separate contacts for the two branches. It was only possible to measure IV characteristics across the junction with branches connected. The most significant result is that the Y-junctions do display rectifying behavior. Since these are multi-walled tubes, the interesting topics considering chirality matching and symmetry discussed above can not be applied here. Instead, a more standard, straight forward approach is taken to interpret the data. It is based on the fact that the band gap in semiconducting nanotubes, multi-walled included, is inversely proportional to diameter. In the Y-junctions examined here, the stem had a larger diameter (~60nm) than the branches (~40nm). The junction then is treated simply as a hetero-junction of two p-doped materials that have different band gaps. The overarching conclusion is that a nanotube Y-junction has been shown to act as a very small rectifying component. However, if this diameter based model is correct, it would seem that the rectifying behavior would also be expected from a two nanotube junction as well. An alternative explanation not given by the authors may be that two different materials , Al and Au, were used as contacts.

1.3.4 Nanotube Crossing Junctions

One more type of transport property to be examined is that between two individual nanotubes. This is termed a '*crossing junction*'. The important parameters in crossing junctions to be consider are contact pressure, angle of contact, atomic registry matching, and tube type, metallic (M) or semiconducting (S).

One experiment that clearly demonstrates the role of atomic registry matching involved measuring the contact resistance between a multi-wall carbon nanotube and highly oriented pyrolytic graphite (HOPG) at varying relative angles[32]. The fact that multi-walled nanotubes were used instead of single wall nanotubes did not appear to effect the results since contact resistance was significantly larger than tube resistance within either multi-wall or single wall tubes. Nanotubes were dispersed onto sheet of HOPG. An atomic force microscope was used to locate nanotubes, reorient them, and perform the electrical measurements. Chirality of the tube could not be determined directly from AFM, so the angle of perfect registry was found by measuring the lateral force required to rotate the nanotube as a function of angle. A large upturn in force signified an in-registry position. Moving the nanotube out of perfect registry required a 10 fold increase in force compared to any other arbitrary angle. Current vs. voltage measurements were made between the AFM tip placed at the top of the nanotube and the HOPG substrate beneath the nanotube. (Figure 1.15). The nanotube angle was varied over 180 degrees and the contact resistance was shown oscillate with a period of 60 degrees. This result matches the angle for which the nanotube comes in and out of registry with the substrate. The contact resistance was found to change by a factor of 40 for tubes in registry with the graphite sheet as compared to tubes 30 degrees from perfect registry. Even though this is an experiment involving nanotube-graphite interactions, it does give insight into what may occur at nanotube-nanotube crossing junctions.

Another set of experiments were performed examining crossing junctions between single wall nanotubes[33]. Nanotubes of either metallic or semiconducting behavior were repositioned to cross

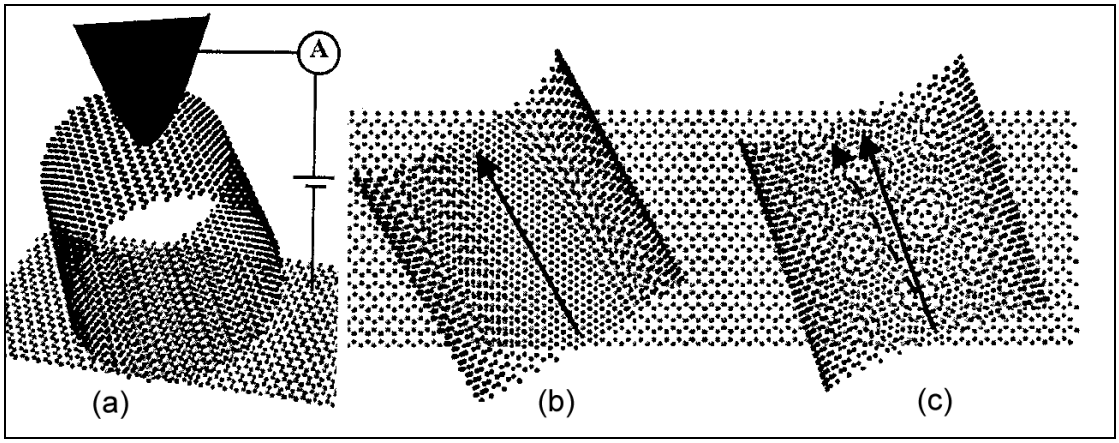

Figure 1.15. Diagram of carbon nanotube on a HOPG substrate

(a) schematic for contact resistance measurements, (b) top view of nanotube in registry with graphite substrate, (c) top view of nanotube out of registry with substrate[32].

approximately perpendicular to one another, the relative angle between tubes could not be varied in these experiments. Contacts were lithographically patterned at the ends of the nanotubes and the junctions were characterized by four terminal conductance measurements (see Figure 1.16). Three types of junctions were tested, those between: two metallic nanotubes (MM), between two semiconducting nanotubes (SS), and between a semiconducting and metallic nanotube (MS). The nanotubes were approximately 3 nm in diameter giving a contact area of about 1 nm^2. Despite this small area, the crossing junctions were surprisingly conductive in the case of the MM junction where the measured resistance was between 100 kΩ and 300 kΩ and the I-V response was found to be linear.

These measured resistances correspond to a tunneling transmission probability of between 0.02 and 0.04. Initial comparisons with theoretical estimates showed poor agreement. The measured conductance was much higher than expected. The theoretical model was then altered to Van der Waals interactions between the SiO_2 substrate and the nanotubes. This interaction has the effect of pulling the top tube into closer contact with the bottom tube causing both to deform at the junction region. With these effects taken into account, theoretical and experimental data was found to be in excellent agreement. The SS crossing junction also showed a linear I-V response, but the contact resistance was much higher, between 400kΩ and 2.3MΩ. The MS junction was qualitatively different demonstrating a rectifying

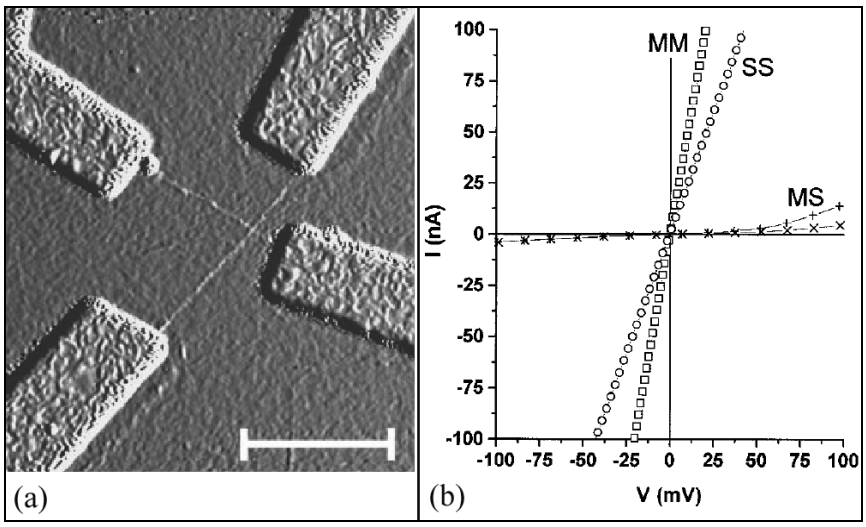

Figure 1.16. Measurement of conduction between crossed nanotubes.

(a) AFM image of crossed nanotubes with electrical contacts (b) electrical measurements of metal-metal(MM), semiconductor-semiconductor (SS), and metal-semiconductor (MS) crossing junctions[33]

response consistent with a Schottky barrier. This is reasonable if one considers that both of the nanotubes are graphene and should have the same work function. Upon contact, the Fermi level of the semiconductor is pulled down to the level of the work function of the metallic tube thereby generating an internal electrice field depleting the semiconductor of carriers at the junction. This results in a larger barrier to tunneling. A positive bias will act to reduce this barrier, a negative bias acts to increase it thereby yielding an asymmetric electronic behavior.

A fully theoretical investigation[34] into nanotube crossing junctions examined three different cases, tubes connected in parallel, tubes connected perpendicular to one another, and two tubes brought together end to end. The simplest junction arises by bringing two closed tubes together (see Figure 1.17). As before, atomic registry was critically important in determining junction resistance.

When in perfect registry, the crossing junction displayed quantum interference. This is an effect caused by the interaction of transmitted and reflected waves at the junction and is evident in the I-V curve as negative differential resistance. A closer look at the effect of atomic registry matching was made by varying the contact length (l). As is shown in Figure 1.17(c-d), conductance varied with the same period as the atomic spacing for two different nanotube junctions, [(10,10),(10,10)] and [(18,0),(18,0)], as contact length increased. The conductance between tubes connected in registry is almost as high as within a single perfect nanotubes. It is also useful to note the large variations in conductance as a function of registry matching. This could have useful applications as nano-mechanical linear position sensors or as switches. Again, registry and contact area are important factors in junction resistance and the angle between tubes, Θ, affects both of these. Figure 1.17(f) and (g) shows how junction resistance varies as a function of angle. Dips in the plot indicate when the nanotubes are in registry. Figure 1.17(f) shows the results for an [(18,0),(10,10)] junction for which the in-registry angles are Θ =30,90,150 degrees. Figure 1.17(g) shows the results for contact between two (10,10) tubes which are in registry at Θ =0,60,120,180 degrees. Contact pressure and tube deformation at the junction are shown to increase conductivity in agreement with other work[35].

1.3.5 Transport through Nanotube Composites

Geometric Considerations in Percolation

The addition of a conductive filler to an otherwise insulating or low conductivity material can improve the over all conductivity of the material. This tactic is often employed as a simple means to add conductivity to polymers. Achieving bulk conductivity requires that at least one unbroken path of conductive filler exists across the composite. Conductivity improves as the number of unbroken parallel paths increases. Even if there are a large number of parallel conducting paths, bulk transport can still be hampered if there is a large barrier between individual filler elements. From a practical standpoint, it is

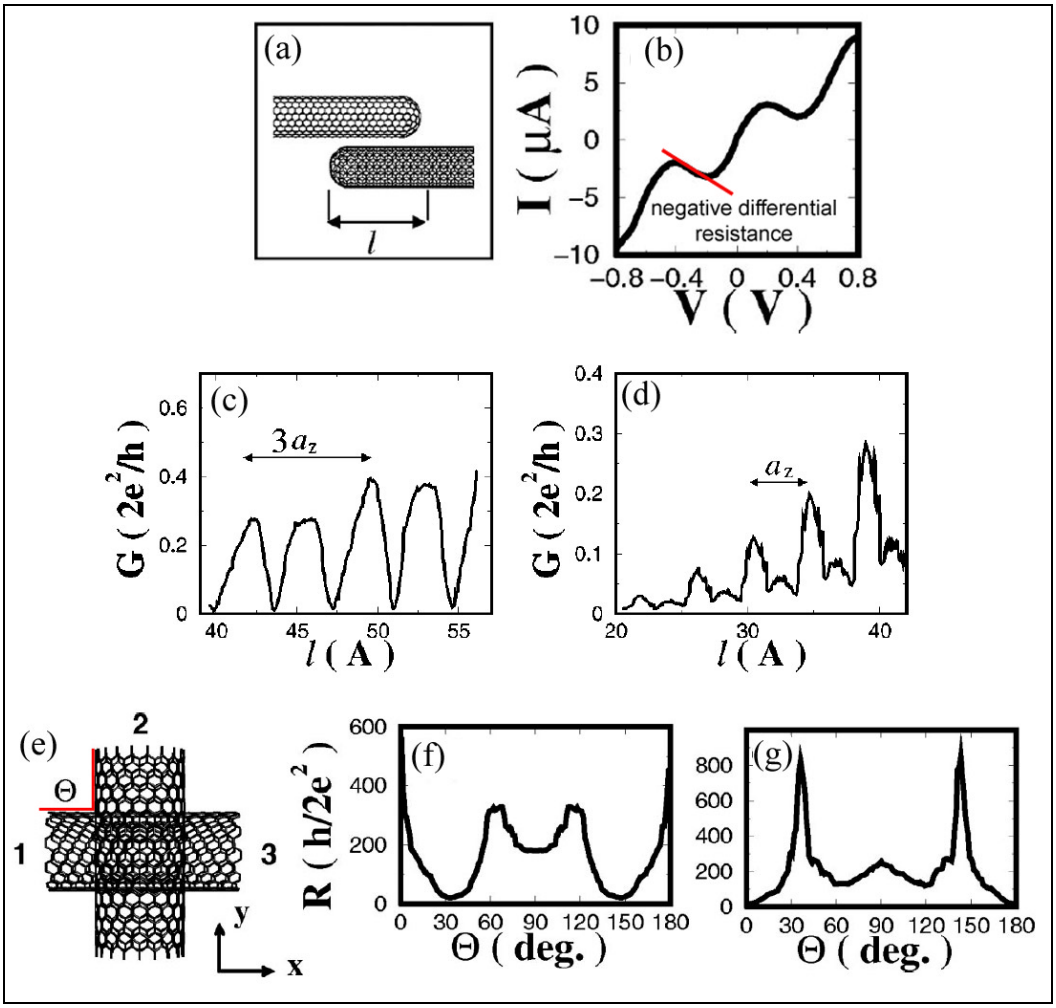

Figure 1.17. Results of theoretical study of nanotube-nanotube junctions

(a) diagram of end-to-end junction, (b) I-V curve of end-to-end junction in perfect registry (c) conductance across end-to-end junction for two (10,10) and (d) two [(18,0),(18,0)] nanotubes.(e) diagram of crossed junction (f) crossing junction contact resistance as a function of contact angle for an (18,0)-(10,10) junction and (g) a junction between two (10,10) tubes.

often advantageous if the mass ratio of filler to matrix is minimized in order to retain matrix properties. The '*percolation threshold*' is the minimum filler to matrix volume ratio at which conductivity is established and is one of the primary figures of merit for evaluating composite systems. A second important measure of a filler-matrix system is the actual conductivity that is achieved at and above the percolation threshold. Characteristic percolation response as a function of weight loading is denoted by a sharp onset of conductivity and a power law dependence of conductivity as loading increases. The following discussion will explore two theoretical analyses aimed at understanding the onset and overall conductivity of composite systems.

Models for determining percolation thresholds for composites based primarily on geometric considerations of the filler elements have been proposed by Balberg and Binenbaum[36,37]. These attempt to predict the probability that an ensemble of filler elements with a specified shape and spatial distribution will contact one another. The onset of percolation of spherical filler elements is well understood[38] however is not applicable to fiber-like filler elements such as carbon nanotubes. Analysis of rod shaped elements is needed but is complicated since much of the simplifying symmetry of a spherical filler is lost. In the Balberg model, the filler element is represented as a cylinder with hemispherical caps on either end. The sphere is the zero length limiting case of these rods and this model can be checked at this limiting case against previous research. In addition, computer simulations of large numbers of rods have been run validate their theory. The shape of the individual filler elements is not the only aspect of geometry which influences the threshold for percolation. The collective arrangement of the filler elements is important as well. An evenly dispersed filler will behave differently on a per mass basis than one with disparate regions of high and low filler concentration. Also, the standard deviation of filler orientation is important in estimating percolation and transport anisotropy.

A major finding of the work by Balberg is that the percolation threshold for rods is not a function of the volume of the filler element, but rather a function of the 'excluded volume' of the element. The excluded volume is defined as 'the volume around an object in which the center of an identical object should not be present if interpenetration is to be avoided'. Figure 1.18 illustrates this concept. Figure 1.18(a) shows the excluded volume for rods with a 5 to 1 length to diameter ratio which have a random distribution. Figure 1.18(b) shows the excluded volume for the same size rods if they are restricted to be parallel to one another. Figure 1.18 (c) shows the excluded volume for two spherical filler elements. It can be seen that the excluded volume for spheres is still a sphere, so in studying this high symmetry case, no distinction can be drawn between volume and excluded volume. The critical concentration of filler elements is achieved when the number of elements in a system times their excluded volume is equal to the total volume of the system. Or to put this another way, percolation can not begin until excluded volumes of different elements overlap. This can lend some insight into the effect of orientational anisotropy on transport. Comparison of Figure 1.18(a) and (b) shows that the excluded volume for random orientation is

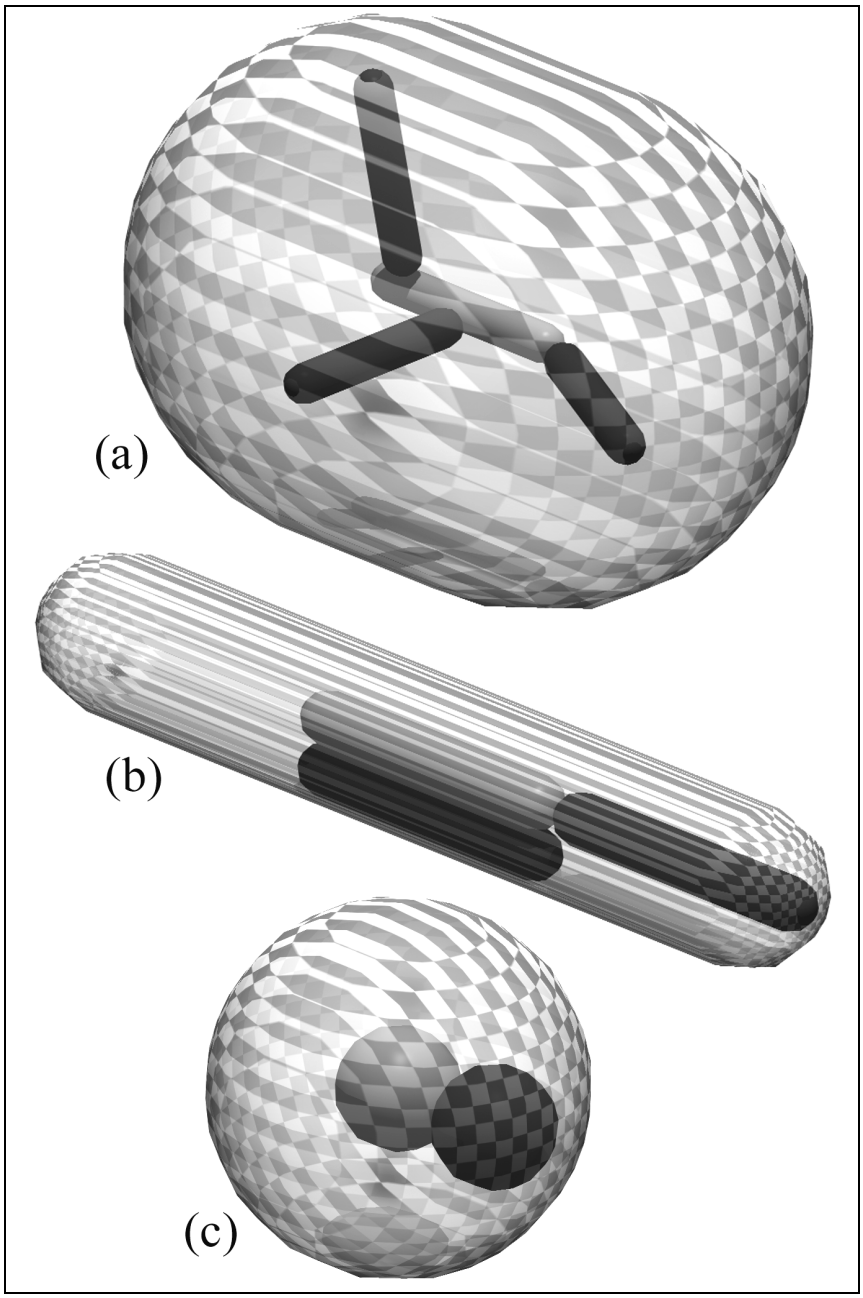

Figure 1.18. Examples of excluded volumes fillers of dimension and degrees of freedom.

The excluded volume is represented as a transparent, checkered surface. The central filler element is lightly shaded. The darker elements represent possible locations for a second element given constraints on the relative angles between elements.

larger than for parallel orientation for elements of the same size. Therefore, the onset of percolation should occur at lower weight loadings for randomly oriented filler. A related finding shows that if the elements are highly oriented in one direction, percolation will occur at lower weight loadings for transport parallel to the orientation direction compared to perpendicular to it. Also, it can be seen that the aspect ratio of filler elements can strongly affect the percolation threshold. Long, slender rods will have a large excluded volume compared to their actual volume. Therefore, the minimum weight loading for percolation drops rapidly as the aspect ratio of rods increases.

Interconnections in Percolation

Practical application of percolation theory requires that one also consider mechanisms for transport between conductive elements. The research presented above assumes that contact between rods is either complete or completely non-existent and that no middle ground exists. In practice however, this is rarely the case, especially when considering polymer composites. Instead, filler elements come into close proximity of one another but there is still some polymer between them. This thin layer of polymer acts as an insulating barrier to transport through which electrons must tunnel. The Fowler-Nordheim equation[39] given below can be used to model tunneling transport.

$$J(V_a) = q \cdot n \cdot v_R \cdot exp\left[\frac{-E_c(V_a)}{E(V_a)}\right]$$

Equation 1.4

J is the tunneling current density, V_a is the applied voltage across the barrier, q is electron charge, n is the density of charge carriers, v_R is the Richardson velocity, E_c is the critical field for tunneling and E is the field across the barrier. Further details are presented in Appendix 3. Experimental results show that bulk conductivity is higher than what would be predicted by the Fowler-Nordheim equation alone. Sheng et. al.[40,41] have suggested that random thermal fluctuations across a large number of interconnects throughout a composite material could be responsible for raising the tunneling current density. This is plausible because a thermal gradient in the direction of current flow across a barrier will do more to augment transport than a thermal gradient directed against current flow will do to diminish transport. Since the regions of closest approach between to conducting elements are highly localized, random thermal fluctuations throughout a material can easily span one junction. Even though the average temperature throughout the material is constant, small thermal fluctuations on the nanometer scale of junction widths can on average encourage tunneling. A modified tunneling current equation was derived that accounts for thermal fluctuations and is shown below.

$$J(V_a, T) = q \cdot n \cdot v_R \cdot exp\left[\frac{T_1}{T + T_o} \cdot \frac{-E_c(V_a)}{E(V_a)} \right]$$

Equation 1.5

Equation 1.5 differs only slightly from Equation 1.4 in that there is an additional factor in the exponent. Experiments performed as part of this study measured conductivity of composites as a function of the bulk mean temperature T. Despite the effort given to deriving T_1 and T_o in this study, in the end, these are used only as fitting parameters for experimental data and vary considerably between different composite systems. T_o is interpreted as the temperature at which thermal fluctuations begin to be important to tunneling and, for the systems investigated, tended to be below 20 K. T_1 is a measure of the temperature dependence of conductivity and was usually between 20 K and 40 K. With the correct fitting parameters, Equation 1.5 is in excellent agreement with experimental data and effectively estimates electrical conductivity through composites.

CHAPTER 2 EXPERIMENTAL METHODS FOR LASER-INDUCED SURFACE STRUCTURING STUDIES

The experimental techniques used in the two main projects described in this thesis are quite different and will be described separately. Description of the experimental techniques used to produce the laser-induced surface structure and measurement techniques to characterize these structures will be given as well as the experimental setup for in-situ imaging of the substrate and plume during irradiation processing.

2.1 Surface Laser Irradiation Experimental Setup

Substrates were irradiated using a Lambda Physik LPX–305i KrF excimer laser. The 248 nm wavelength laser pulse has a FWHM pulse duration of between 25 ns and 50 ns. Light exits the laser cavity through a 1 cm by 2.5 cm aperture. However, the laser beam emerging from the laser cavity is inhomogeneous in energy density so an additional variable diameter circular aperture was used to remove the low energy regions of the rectangular beam. The beam and beam path were modified by one MgF_2-coated mirror, one fused silica lens, and one fused silica vacuum chamber window. Each of these components absorbed, reflected, or scattered about 12% to 15% of the incident light. One of three lenses were used: a 25-mm-diameter 30 mm-focal-length spherical lens, 12.5-mm-diameter 45 mm-focal-length-lens, or a 25 mm by 25 mm 40 mm-focal-length cylindrical lens. The beam was focused by about a factor of 10 to an average energy density of between 2 J/cm^2 and 3 J/cm^2 at the substrate surface. The laser fluence was varied by either adjusting the position of the lens array with respect to the substrate or by adjusting the excitation voltage. The substrate was always positioned beyond the focal point of the lens but not necessarily at the image plane of the aperture. The laser was usually operated at an excitation voltage between 17 kV and 18 kV as this was found to be the range where the laser operated most reliably and the energy density was most homogeneous. Beam energy was measured using a digital calorimeter (Scientech, Astral AD30) and the energy was determined by averaging calorimeter measurements of 10 pulses separated by at least 20 seconds. Laser spot size was determined from SEM images of the laser spot.

Diagrams of the experimental setup including the imaging equipment are shown in Figure 2.1 and Figure 2.2. Figure 2.1(a-c) shows a large overhead view, side view, and oblique view respectively and indicate the position of the components described above. Figure 2.2 shows a closer, more detailed view of the vacuum chamber construction and mounting equipment for the imaging and diagnostic devices. The beam is directed into the front of a 15 cm stainless steel cubical vacuum chamber through a 25 mm diameter 6–way cross used for handling gas pressure and flow inside the vacuum chamber. The sample is held in place by a motorized substrate holder, which enters through the top of the chamber. This sample holder can be used to adjust the vertical position of the sample. The ability to easily change the vertical

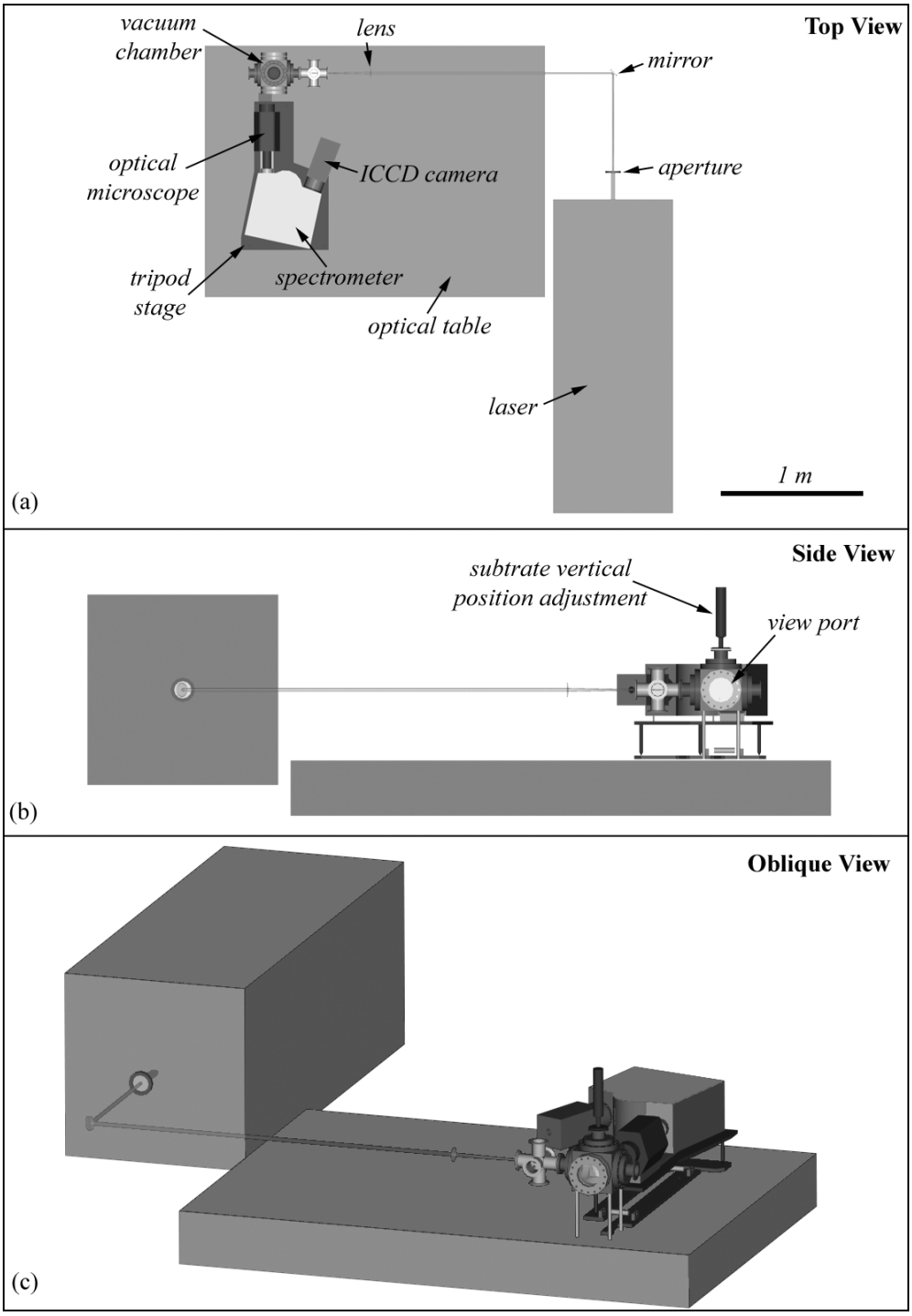

Figure 2.1. View of surface treatment and diagnostic experimental setup.

(a) top view, (b) front view, (c) oblique view.

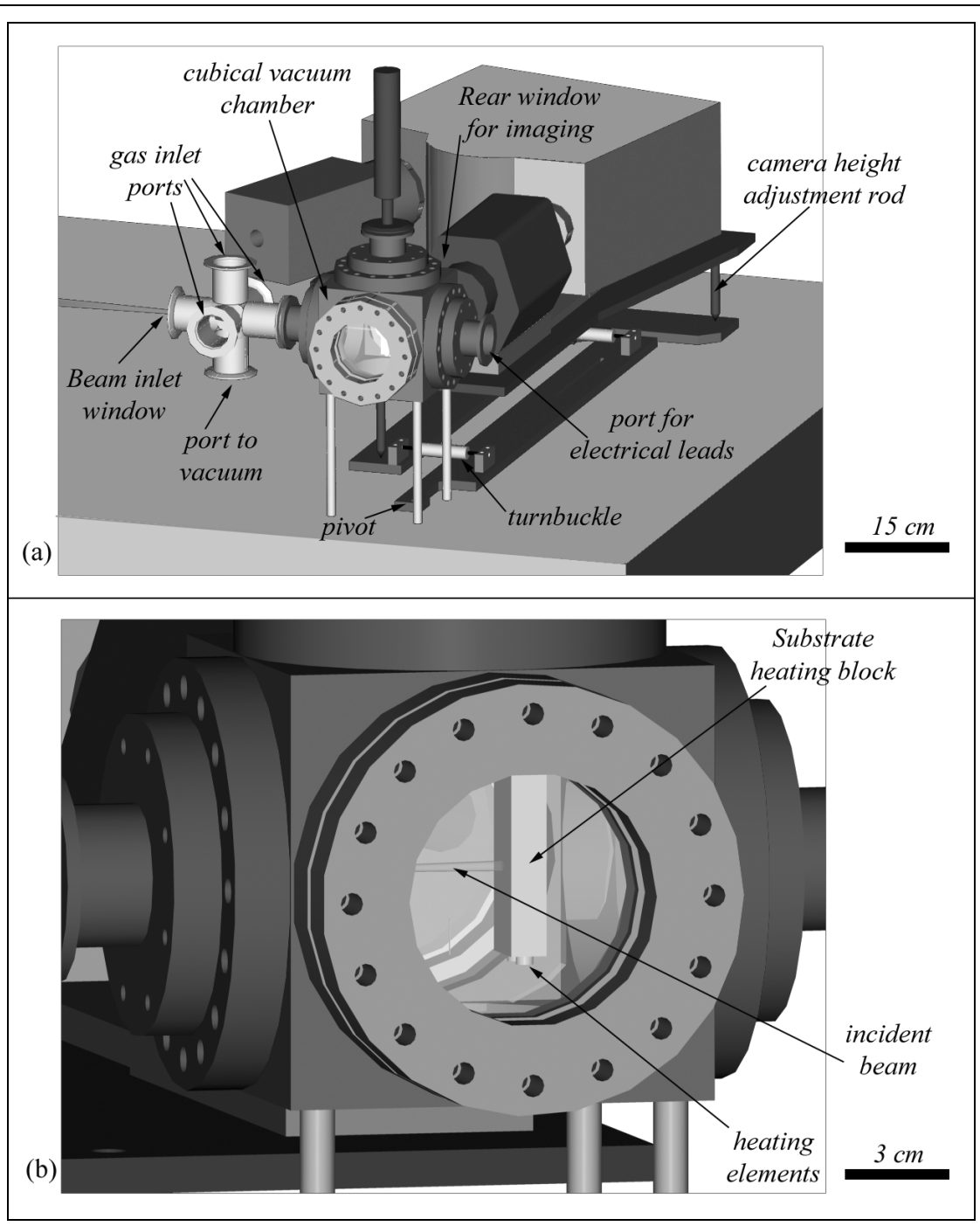

Figure 2.2. Close-up views of surface treatment and diagnostic experimental setup.

(a) components of the vacuum chamber, (b) view of the inside of the vacuum chamber.

position of the sample greatly expedited experimentation since several experiments could be run on a single substrate without removing it from the vacuum chamber. The end of the chamber opposite the laser inlet is reserved for electrical leads. There is a 12 cm glass view port on one side of the cube. A 10 cm fused silica window is mounted at the opposite side from the view port and it is through this window that all the in-situ imaging and other diagnostic measurements are performed. The bottom of the cube holds a smaller, 25 mm fused silica window which is available for a second excitation beam.

An intensified charge coupled device (ICCD) camera is used to capture images and spectrographic information. In the diagrams, it is shown to be coupled to a spectrometer and a long focal length microscope. It is possible to capture images through the spectrograph, but it is usually omitted from the optical path when only imaging information is collected. The camera, spectrometer, and microscope are all attached to the top of an imaging equipment platform. This platform offers many degrees of freedom for the accurate positioning critical for imaging. The angle within the horizontal plane can be varied from 0º to 30º from normal to the imaging window about the pivot point directly below the sample as shown in Figure 2.2(a). Further fine tuning of the horizontal position can be accomplished using two turn-buckles attached to the bottom of the platform. The vertical position and angle relative to the horizontal plane is determined by three threaded rods at the corners of the imaging equipment platform. The imaging equipment is attached to platform through tracks which permits easy adjustment of the distance between the substrate and the front of the microscope.

Figure 2.2(b) shows a close-up view of the vacuum chamber and the sample holder within. The sample holder is a 2.5 cm by 1 cm by 8 cm inconel block. The temperature of the block is heated by two 6-mm-diameter, 6-cm-long, 250 W cylindrical heaters inside the block. The surface temperature of the block can be varied from room temperature to 550˚C. One thermocouple imbedded in the heating block provides feedback to the heater controller but is not an accurate measure of the substrate surface temperature. Separate measurements of the substrate surface temperature were performed at various locations on the substrate prior to irradiation to determine the temperature profile across the surface of the substrate as a function of the thermocouple reading.

Most laser surface treatments were carried out in a mixture of two gases: Ar and SF_6 – both 99.95% pure. The irradiation chamber was pumped to a base pressure of 10^{-6} Torr and then filled with the appropriate gas mixture and pressure.

Various types of substrates were used as targets including research grade, polished, 0.5-mm-thick Si wafers with (100), (110), and (111) surface orientations of either n-type or p-type doping, polished 0.5-mm-thick (111) Ge, and nominally 0.3-mm-thick edge-defined grown (EFG) polycrystalline silicon for which the predominant orientations of the surface were either (112) or (110). Any native oxide present on the silicon substrates was removed prior to irradiation by 5 minutes immersion in 10% aqueous HF solution, followed by rinsing in deionized water, spraying with a stream of methanol, and finally being

blown dry by a jet of 99.95% pure He. Within 1 minute of this treatment, the wafer was then placed in the vacuum chamber that was immediately filled with Ar and then evacuated.

2.2 In-situ Imaging of the Surface and Ablation Plume

In-situ imaging of the ablation process was performed using a Questar QM100 long focal distance microscope coupled to a Princeton Instruments PI-MAX ICCD camera. The focal distance of the microscope was set to approximately 24 cm. All lenses within the microscope are fused silica and transparent to 248 nm laser radiation. The charge-coupled device is comprised of a 512 x 512 pixel imaging array. The amount of time that the ICCD gate is open is termed the *'pulse width'* and determines the length of time over which one image is captured. The pulse width can be thought of as being equivalent to the shutter speed of a film camera. The minimum pulse width for this imaging system is 2 ns. The maximum image resolution of the substrate achieved using this combined camera/microscope setup was approximately 1 μm/pixel.

Figure 2.3(a) illustrates the relative orientation of the substrate, microscope image plane, and incident beam. All the images of the ablation process were taken nearly edge-on to the substrate. That is, the irradiated surface was at an angle of ~5˚ to the normal of the image plane of the microscope. By doing this, the line of cones at the edge of the substrate could be clearly observed with little interference from the surface structure and plume formed beyond the image plane. The center of the laser spot was positioned at the edge of the substrate insuring surface was fully irradiated up to the edge. The side of the sample was undercut to eliminate reflection of the incident beam into the camera. The undercutting of the substrate also made possible the detection of micro-holes formed near the edge during the ablation process. In the schematic drawing they are represented by small dots on the undercut surface. Figure 2.3(b) shows an example of images taken using this experimental setup and methodology. The cones can be observed extending above the original surface, holes are visible as they penetrate through the undercut edge of the substrate, and the front edge of the ablation plume is visible just beyond the tips of the cones. An SEM image of a cross-section substrate is shown in (c).

2.2.1 Description of Continuous Mode Imaging

It is possible with this setup to combine together a series of images captured during successive laser pulses. Several different camera timing techniques were used in this study. The time elapsed between the initial arrival of the laser beam to the target and the acquisition of the image is defined as the *'delay time'*. One method of image acquisition was to maintain a constant delay time for each image. This acquisition mode is referred to as *'continuous mode'* ,and it is used primarily to characterize surface structure changes associated with increasing numbers of laser pulses.

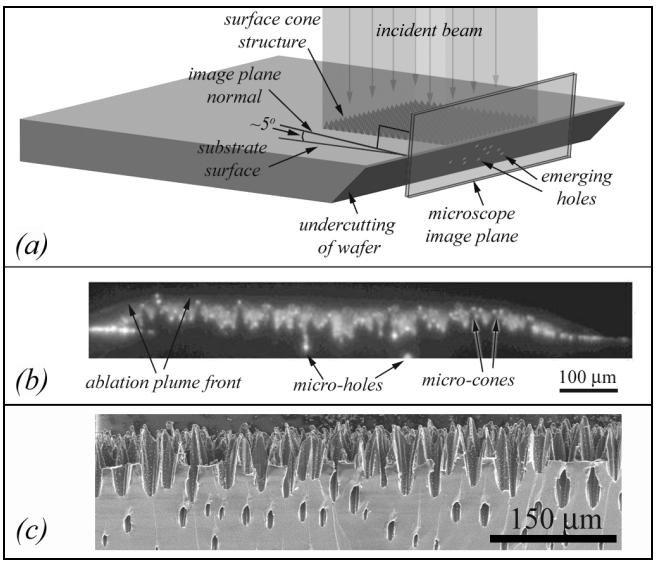

Figure 2.3. Diagram of setup used for in-situ surface irradiation imaging.

(a) diagram illustrating the orientation of the substrate relative to the microscope image plane. (b) example of an image captured during laser irradiation.(c) SEM image of cross-section.

2.2.2 Description of Sequential Mode Imaging

Images of the substrate can also be acquired by progressively increasing the delay time from one exposure to the next. This mode is referred to as *'sequential mode',* and it is used to approximate the sequence of events occurring during and after a *single laser pulse*. In reality, the target is being modified with every pulse so this method is only useful if the changes in surface structure and plume behavior is small from laser pulse to laser pulse. This appears to be the case in this study since modification of the substrate surface is appreciable over spans of hundreds of pulses and sequential plume images were captured over a span of tens of pulses. The plume evolution was studied by recording images in sequential mode usually between the 800th and 900th laser pulse after the micro-cone surface structure was well developed.

2.3 Surface Characterization Techniques

Profilometry was used to collected information on the height and roughness of evolving surface structures. The profilometer (Sloan, DekTack IIA) traces a line across the sample surface with a stylus having a tip radius of 2.5 μm and tip angle of 20º and measures the height of the tip as a function of distance along the surface. Usually two different scan lengths were used per sample. The first scan length was around 3 mm and traced a line from an untreated region of the sample, through the middle of the laser

spot, to an untreated region at the other side of the laser spot. Information from such a scan was used to measure variations of wave or micro-cone height relative to the untreated surface. A second smaller scan length of around 300 μm through the center of the laser spot was used to measure peak to valley heights and average root-mean-square (RMS) roughness of the of the undulating surface.

Atomic force microscopy (Digital Instruments, Dimension 310) was employed to study the 2-D topographic evolution of the irradiated surface with increasing number of laser pulses. Two aspects were recorded in the evaluation of the progressive surface changes: the crest height to depression depth distance, which is termed '*amplitude'*, and the angle of the depression wall with respect to the original horizontal surface, the '*grade'*.

SEM imaging (Leo 1525, and Hitachi FESEM-4700) of the laser treated surface was the primary means used to determine feature spacing. Low magnification images of around 25X were taken of the entire laser spot in order to determine its size and the incident energy density. Images taken at 50X and 100X were analyzed by 2-D fast Fourier transform (FFT) to determine average feature spacing. This included averaging together the FFT's of 9 partially overlapping 512 by 512 pixel subsets of a single SEM image and finding the distance, in k-space, from the origin to the distance at which the FFT was most intense.

CHAPTER 3 EXPERIMENTAL RESULTS OF LASER INDUCED SURFACE MICROSTRUCTURING

3.1 Results of Profilometry

In nearly all cases of surface micro-cone/micro-hole formation, surface wave development is a precursor to the development of micro-cone structure. Plots of profilometric measurements of laser induced surface roughness produced with a laser fluence of 3.0 J/cm^2 under three different atmospheres - Ar at 0.5 (Ar), Argon at $1 \cdot 10^{-8}$ bar (vac), and 0.5 bar of SF_6 (SF_6) - are shown in Figure 3.1. The roughness measurements were taken over a 400 μm length in the center of the laser spot. Figure 3.1(a) shows results up to 10,000 laser pulses. Figure 3.1(b) is a magnified view the of shaded region in Figure 3.1(a), presenting more clearly the surface roughness evolution at the early stages of its development.

Two different growth regimes are evident. Within the first 600 laser pulses, there appears to be little difference in the rate of increase of surface roughness for irradiation under the different atmospheres. The average rate of increase within the first 600 laser pulses is 24.7 Angstroms/pulse. After this point, the rate of surface roughness growth in the SF_6 atmosphere quickly increases. This rapid increase in roughness indicates the onset of micro-cone/micro-hole formation. Profilometric measurements of surface roughness of the micro-cone structure are considered somewhat inaccurate since the profilometer stylus is not sharp and slender enough to accurately follow the extremely rough surface. In contrast to SF_6, the rate of surface roughness increase for the Ar and vacuum atmospheres drops off to 3.5 Angstroms/pulse as measured up to 10,000 laser pulses.

Other surface profile measurements sought to find the rate at which material is removed from the substrate surface by comparing the average height of the laser spot compared to the height of the original, non-irradiated surface. Again a laser fluence of 3.0 J/cm^2 was used. Figure 3.2(a) shows the rate at which mass is removed from the substrate for irradiation occurring in a 0.5 bar SF_6 atmosphere. The average rate of material loss for both crystal substrates is approximately 1.0 nm per laser pulse. The Si(111) surface appeared to be ablated with a slightly faster rate, 1.15 nm/pulse, than the Si(100) surface, 0.85 nm/pulse. A similar study of substrates irradiated under Ar or vacuum atmospheres showed no measurable loss of material.

Highly accurate measurements of material loss is difficult using profilometry for very rough surfaces due to convolution between the finite sized tip and the surface. In the case of micro-holes and micro-cones, the sidewalls of the surface features are too tall and close together for the profilometer to capture all of the detail. Examples of surface profiles are shown in Figure 3.2(b-c) for substrates irradiated under different atmospheres.

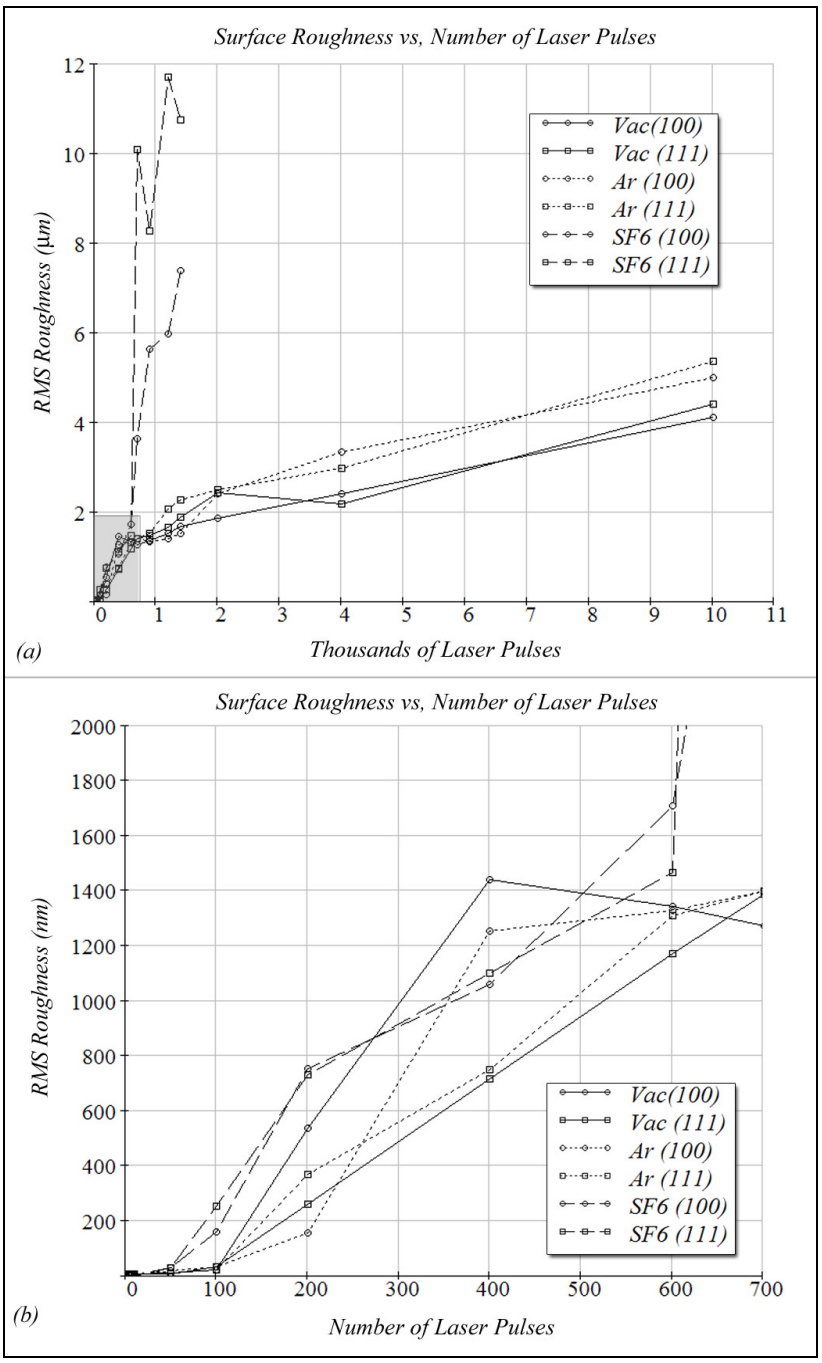

Figure 3.1. Plots of results from profilometric measurements of laser induced surface roughness

Experiments were carried out in three different atmospheres. These are: Ar at 0.5 bar (Ar), Argon at $1 \cdot 10^{-8}$ bar (Vac), and 0.5 bar of SF_6 (SF_6). Laser fluence was 3.0 J/cm^2. (a) large scale view of results. (b) closer view of results in the shaded region of (a).

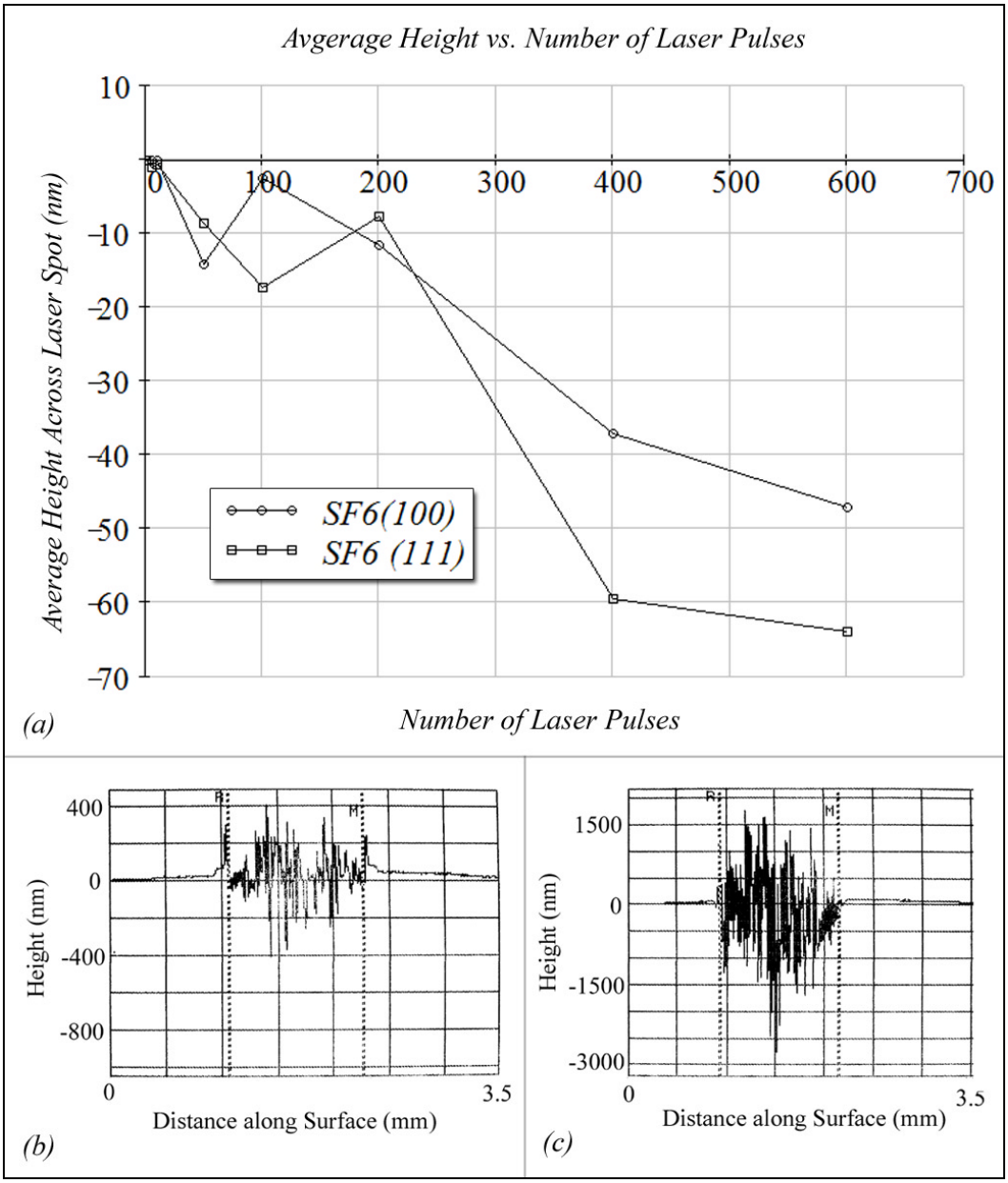

Figure 3.2. Profilometry measurements material loss due to laser irradiation

(a) Plot of results from profilometric measurements of average height within a laser spot with respect to the untreated surface.(b) Surface profile of a (100) Si substrate irradiated by 200 laser pulses in 0.5 bar Ar at 3.0 J/cm^2. (c) Surface profile of a (100) Si substrate irradiated by 200 laser pulses in 0.5 bar SF_6 at 3.0 J/cm^2.

The increased ablation rate measured in substrates irradiated under an SF_6 atmosphere is likely due to the thermal decomposition of SF_6 near the substrate surface during laser irradiation. The fluorine produced by decomposition is adsorbed at the surface where it reacts with Si producing a volatile compound. This laser induced etching does not appear to play a significant role in surface modification in early stages, that is within the first 600 laser pulses, of surface modification.

Another set of profilometry measurements, the results of which are shown in Figure 3.3, focused primarily on the latter stages of micro-cone development. These measurements were performed on substrates irradiated with 2.5 J/cm^2 under a *total background pressure of 0.5 bar of SF_6*. No micro-cone growth above the initial surface was detected within the first 500 pulses, but after 750 pulses, the average micro-cone in the central region of the laser spot had grown to a height of 10 μm. The average height of the micro-cones increased steadily with the number of pulses, reaching a maximum of approximately 40 μm above the non-irradiated surface after 1000 pulses. After this point, there was a steady decrease in height of the tips of the micro-cones above the non-irradiated surface as the number of laser pulses was further increased (Figure 3.3(d-h)). After 2250 pulses the average height decreased to 10 μm (Figure 3.3(h)). There is a significant difference in the height of the profile shown in Figure 3.3(b) and the shorter profile shown in Figure 3.3(h). In Figure 3.3(b), the maximum height is seen in the central region of the laser spot while the profile of Figure 3.3(h) is fairly uniform. In Figure 3.3(b), the profile of the micro-cones roughly follows the laser energy profile across the laser spot. However, after the irradiated area was entirely covered with micro-cones, this is no longer the case. As seen in Figure 3.3(e-h), the non-uniform distribution of energy across the beam becomes a less important factor in the uniformity of micro-cone height across the irradiated region after a large number of laser pulses.

Another series of results were obtained by fixing the number of laser pulses but varying the *total pressure of SF_6 between 0.125 and 1 bar*. The maximum height of the micro-cones was reached between 1000 to 1500 pulses and a significant decrease in micro-cone height was observed after 2250 pulses independent of background pressure. As the background pressure of SF_6 was increased from 0.125 bar to 0.5 bar, an increase in the micro-cones' height was observed for the same number of pulses. However, when the pressure was increased further to between 0.5 and 1 bar, the micro-cones' height decreased. Figure 3.4 shows height profiles as a function of pressure after 2000 pulses at a laser fluence of 2.5 J/cm^2.

In order to gain further understanding of the effect of the ambient atmosphere on micro-cone growth, irradiations were performed under atmospheres with *different proportions* of SF_6 and Ar while the total background gas pressure was held at a constant value of 1 bar. Profilometry measurements were made after 2000 laser pulses. The micro-cones' height increased and then decreased with an increase in the partial pressure of SF_6 as shown in Figure 3.5. The maximum height was attained at a partial pressure of 0.5 bar of SF_6 (Figure 3.5(c)). These results show a similar dependence on the *partial* pressure of SF_6 as was measured when the total pressure of pure SF_6 was varied. However, the maximum height of the micro-cones was taller when the substrate was irradiated under a pure SF_6 atmosphere.

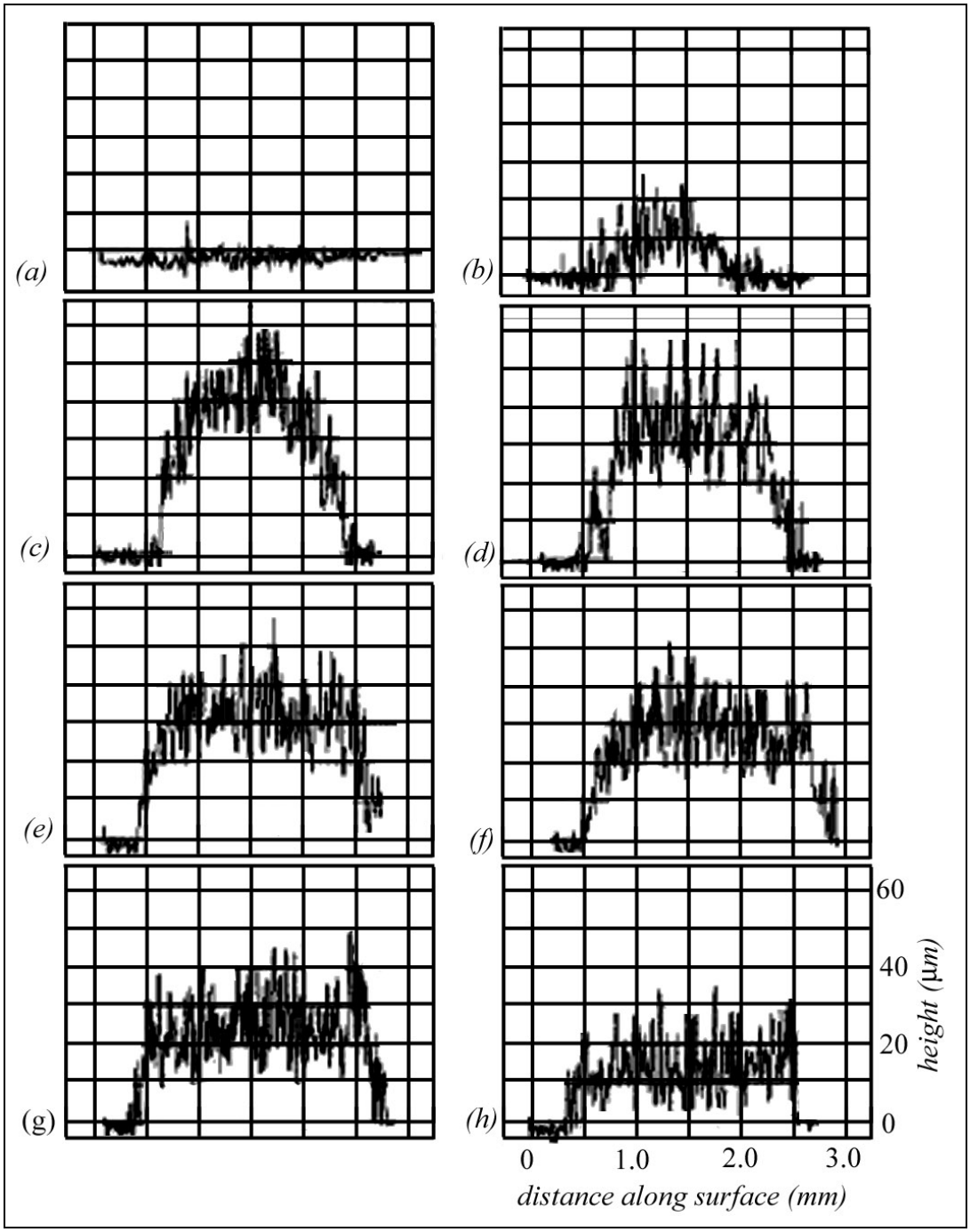

Figure 3.3. Profilometry measurements of Si substrates irradiated with varying number of pulses

Irradiation of Si at a laser fluence of 2.5 J/cm^2 under 0.5 bar of SF_6 with (a) 500, (b) 750, (c) 1000, (d) 1250, (e) 1500, (f) 1750, (g) 2000, and (h) 2250 pulses.

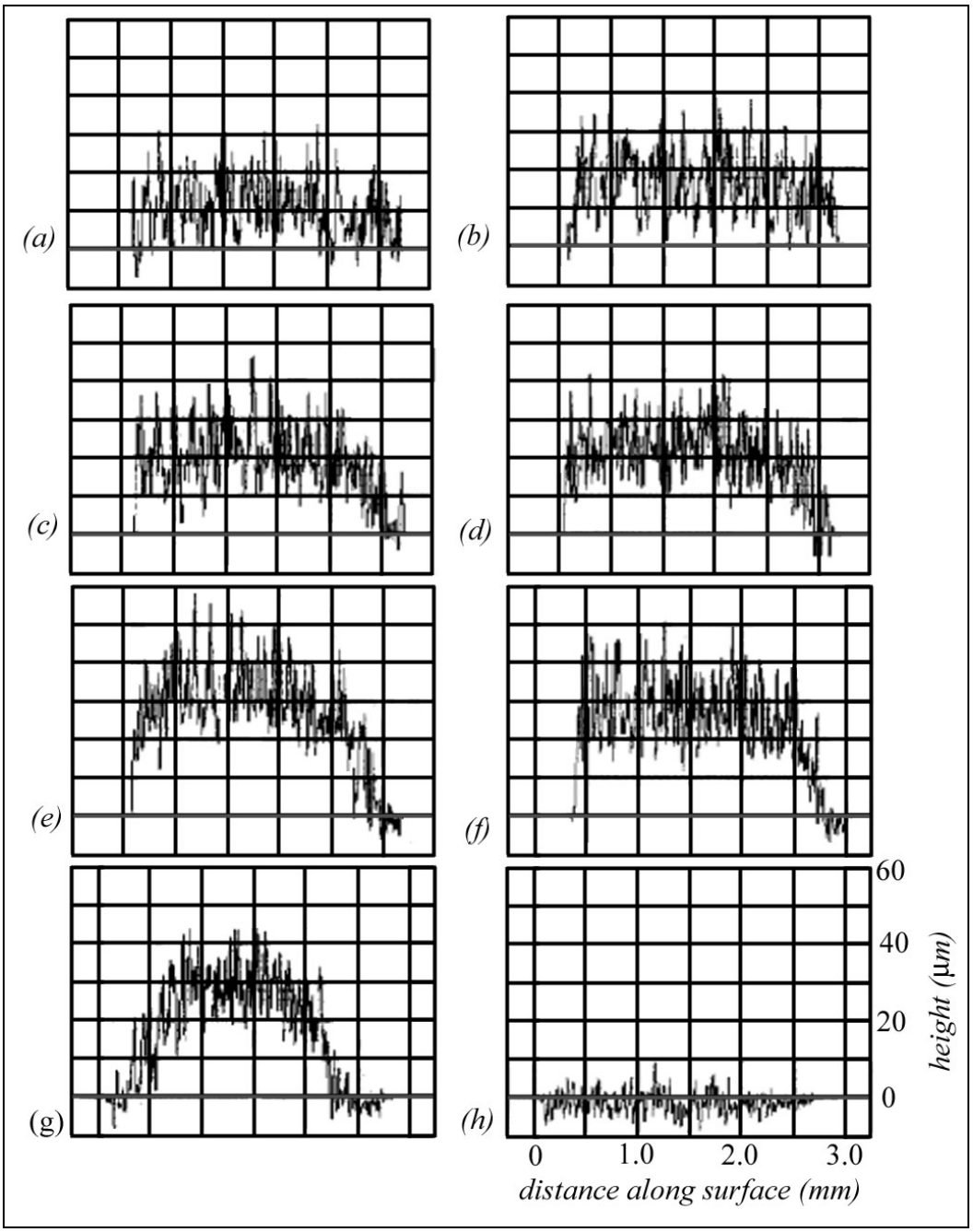

Figure 3.4. Profilometry measurements of Si substrates irradiated with varying background pressures

Substrate irradiated with 2000 laser pulses at a laser fluence of 2.5 J/cm^2 under SF_6 atmospheres with total pressures of :(a) 1, (b) 0.875, (c) 0.75, (d) 0.625, (e) 0.5, (f) 0.375, (g) 0.25, (h) 0.125 atm.

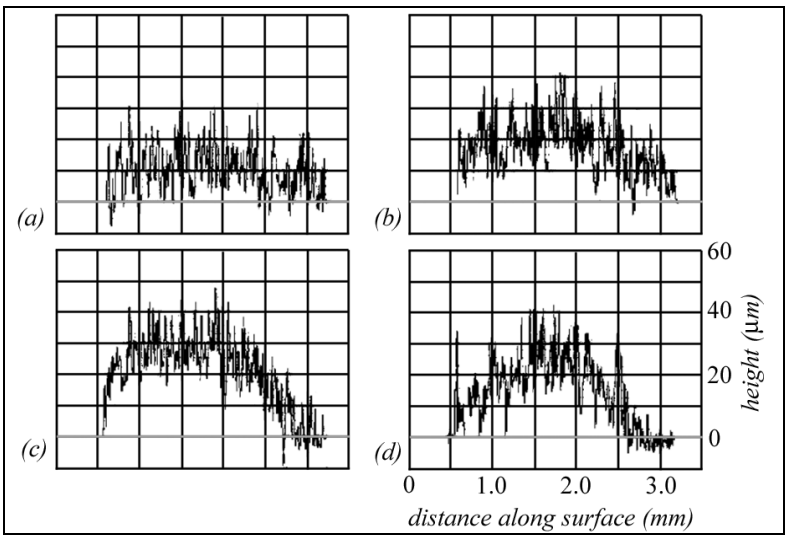

Figure 3.5. Profilometry of Si substrates irradiated with varying partial pressures of SF_6

Substrate irradiated with 2000 laser pulses at a fluence of 2.5 J/cm^2 under an atmosphere that is a mixture of Ar and SF_6 with a total pressure of 1 atm. The partial pressure of SF_6 in each case was: (a)1.0, (b) 0.75, (c)0.5, and (d) 0.25 atm.

3.2 Results of Atomic Force Microscopy

Atomic force microscopy was used to study the very early stages of evolution of the irradiated surface. The advantage of AFM over profilometry is that a 2-D map of the surface topography can generated. One disadvantage of AFM measurements is that it is not possible to measure changes in the height compared to the non-irradiated surface - it is only possible to make measurements relative to other features in the irradiated region and so is a compliment to profilometry measurements. Two aspects of the topographic features were evaluated. One was the crest height to depression depth distance, which is termed *'amplitude'*, and the other was the angle of the depression wall with respect to the initial surface, termed *'grade'*.

Very shallow perturbations are observed after just a few laser pulses for fluences of 1.5 J/cm^2 and 3.0 J/cm^2. These perturbations appear as isolated surface depressions that are a few tens of nanometers deep but have diameters of 10 μm to 30 μm. Smaller diameter structures are observed when the laser fluence was 1.5 J/cm^2. Irradiation at 3 J/cm^2 generated depressions with diameters between 20 μm and 30 μm. The initial depressions have a grade of less than 1°. As the number of pulses increases, new depressions soon develop filling the spaces between the first ones.

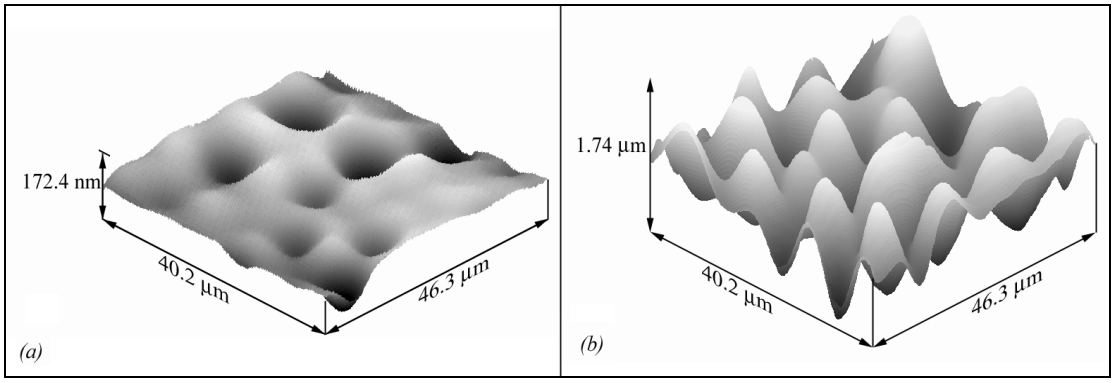

Figure 3.6. AFM images of early stages of laser induced surface structuring

AFM images of a (111) silicon surface irradiated in 0.5 bar pressure of SF_6 at a laser fluence of 1.5 J/cm^2 , after (a) 60, and (b) 600 pulses.

Figure 3.6(a-b) shows two images of a (111) surface irradiated at 1.5 J/cm^2 in 0.5 bar of SF_6 after 60 and 600 laser pulses respectively. In Figure 3.6(a), the sparsely distributed depressions have an average diameter of 14.5 µm. Also, some of the depressions are significantly deeper than others in these very early stages of development. After 600 pulses (Figure 3.6(b)) the surface is completely covered with much deeper depressions, and the distance between depressions is about 15 µm.

Figure 3.7 shows plots of increasing amplitude and grade as a function of the number of pulses under various atmospheres and for two different crystallographic surface orientations. In all cases, the substrates were irradiated with a laser fluence of 2.0 J/cm^2. The data in these plots represent values averaged over AFM measurements performed at six different locations on each substrate. It is apparent from the plots that the increase of the amplitude of the perturbation with the number of pulses depends on the crystallographic orientation of the surface. The influence of the ambient atmosphere appears to be less significant. After 600 pulses in SF_6, the perturbation amplitude on a (111) surface grew to 1400 nm, while the amplitude for a (100) surface was less at only 200 nm. After a larger number of laser pulses, the growth rate of the amplitude of (100) surfaces increases to a steady value similar for the (111) surface. In Figure 3.7(a), the growth rate of the amplitude is in the range of 1.0 nm/pulse to 1.7 nm/pulse. Measurements of depression diameter for substrates having differently oriented surfaces and under three different atmospheres are summarized in Table 3.1. The depression diameter is smaller when irradiation took place in SF_6 and for (111) orientation relative to the (100) orientation. After 50 laser pulses at a fluence of 3.0 J/cm^2 these perturbations have become 30 nm-deep, both in vacuum and in an SF_6 atmosphere. As the number of pulses increases the depressions deepen maintaining a fairly constant diameter.

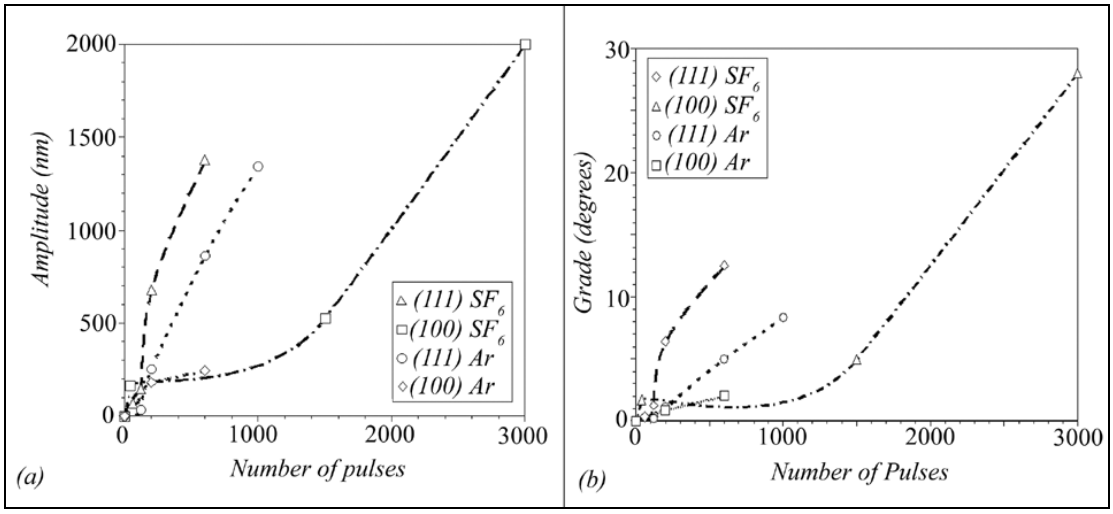

Figure 3.7. Plots of AFM measurements of surface structure amplitude and grade

(a) amplitude and (b) grade of surface depressions as a function of the number of laser pulses for (100) and (111) silicon irradiated with 2.0 J/cm2 under SF6, Ar, and vacuum atmospheres.

Table 3.1. AFM Measurements for average depression diameter produced by laser irradiation of 50 pulses at a fluence of 3.0 J/cm^2 under three different atmospheres.

	Depression Diameter (μm)	
Atmosphere	Si(111)	Si(100)
Vacuum	24	27.7
Ar	22.9	30.4
SF_6	20.4	24.3

3.3 The Effect of Temperature and Energy on Feature Spacing

It was found that crystallography, laser energy, and most importantly substrate temperature have a measurable effect on feature spacing. Figure 3.8 shows results of a series of experiments in which a (100) silicon substrate was irradiated with 400 pulses at 2.2 J/cm^2 under a 0.5 bar Ar atmosphere. The initial substrate temperature was varied over a range of about 400 ˚C resulting in a change of the periodicity of the surface structure.

Figure 3.8(a-e) were captured at the same magnification and it is apparent that the surface structure spacing increases with increasing substrate temperature. However, except for the difference and scale, the general appearance and organization of the surface structure remains unchanged. The spacing of the quasi-periodic surface structure was measured by taking the fast Fourier transform (FFT) of the SEM images. Figure 3.8(f) is a plot showing the change in feature spacing as a function of initial substrate temperature as measured from the images in (a-e).

Additional experiments were performed for different incident energies and on both (111) and (100) surfaces. The results of these experiments are shown in Figure 3.9. The data are plotted along with their least squares 3rd order best fit surfaces. The equations for the data fitting of the (111) and (100) cases are given below.

$$\Lambda_{exp.111}(E,T) = -87.87 + 132\cdot E - 52.4\cdot E^2 + 7.03\cdot E^3 - 5.5\cdot 10^{-2}\cdot T \ldots + 4.\cdot 10^{-3}\cdot E^2\cdot T + 1.50\cdot 10^{-5}\cdot T^2 - 5.86\cdot 10^{-6}\cdot E\cdot T^2 - 8.67\cdot 10^{-8}\cdot T^3$$

Equation 3.1

$$\Lambda_{exp.100}(E,T) = 40.43 - 20.09\,E + 4.18\,E^2 + 0.00365\,T \ldots + 0.0168\,E\cdot T + 3.17\cdot 10^{-5}\cdot T^2 + 4.42\cdot 10^{-8}\cdot T^3$$

Equation 3.2

In these equations, E is the incident flux in J/cm^2, T is the substrate temperature in degrees K, and Λ_{exp} is the measured average feature spacing for the corresponding substrates.

3.4 In-situ Optical Microscopy of Surface Evolution

The evolution of the surface was studied in-situ and in real time as it was being irradiated by using the ICCD camera/microscope system described in section 2.2 (p.2.41). Two different configurations can be used while imaging the substrate. In one, the surface of the substrate can be imaged by rotating the substrate 45º to the incident beam and positioning ICCD camera so that it is normal to the substrate surface. The second configuration is shown in Figure 2.3 and is used for viewing the evolving surface profile during irradiation.

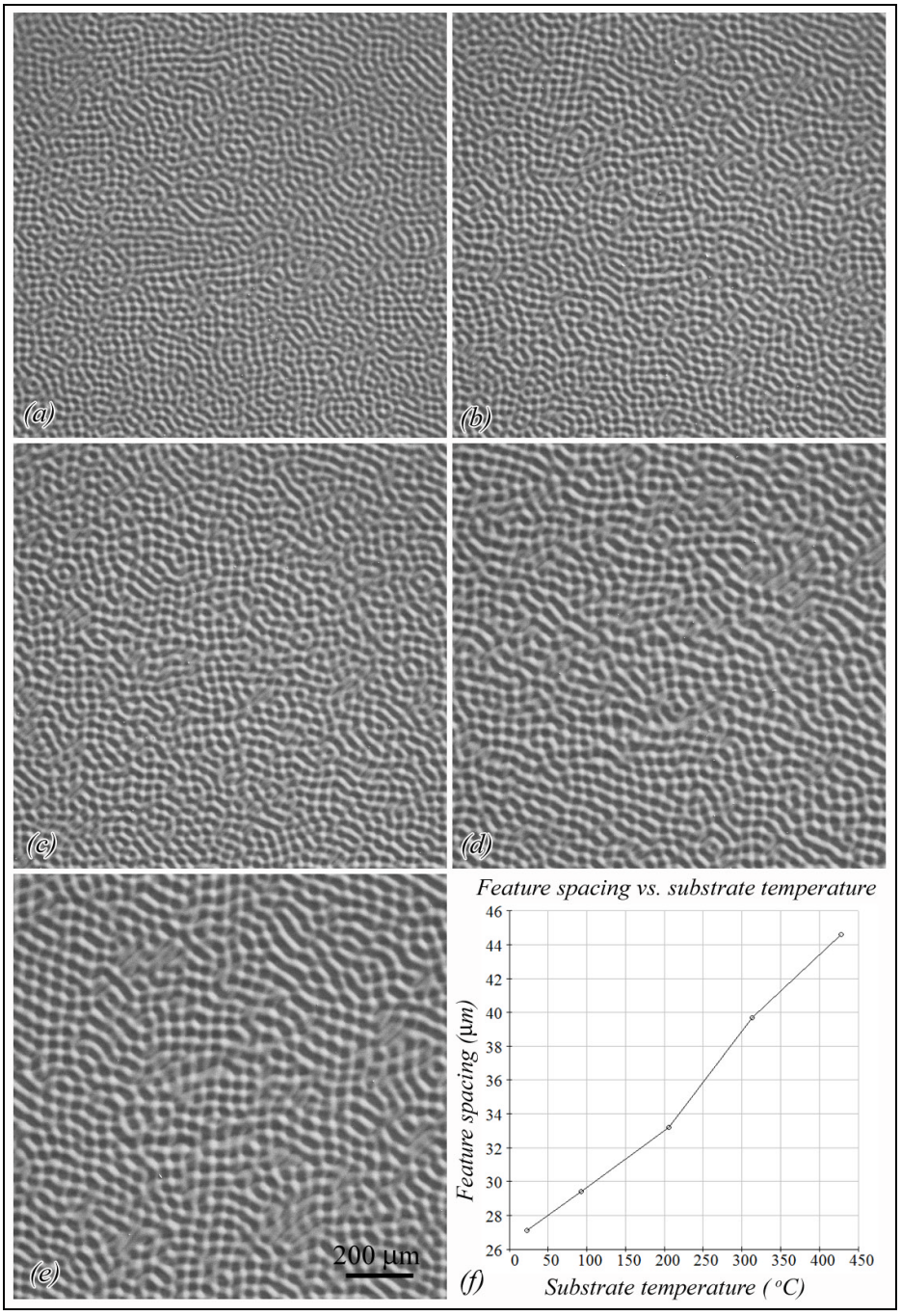

Figure 3.8. Results of the effect of substrate temperature on feature spacing

(a-e) SEM images of laser irradiated substrates performed with the initial substrate temperature at 22˚C, 92˚C, 205˚C, 312˚C, and 427˚C respectively. (f) a plot of the average feature spacing as a function of substrate temperature as measured from images (a-e).

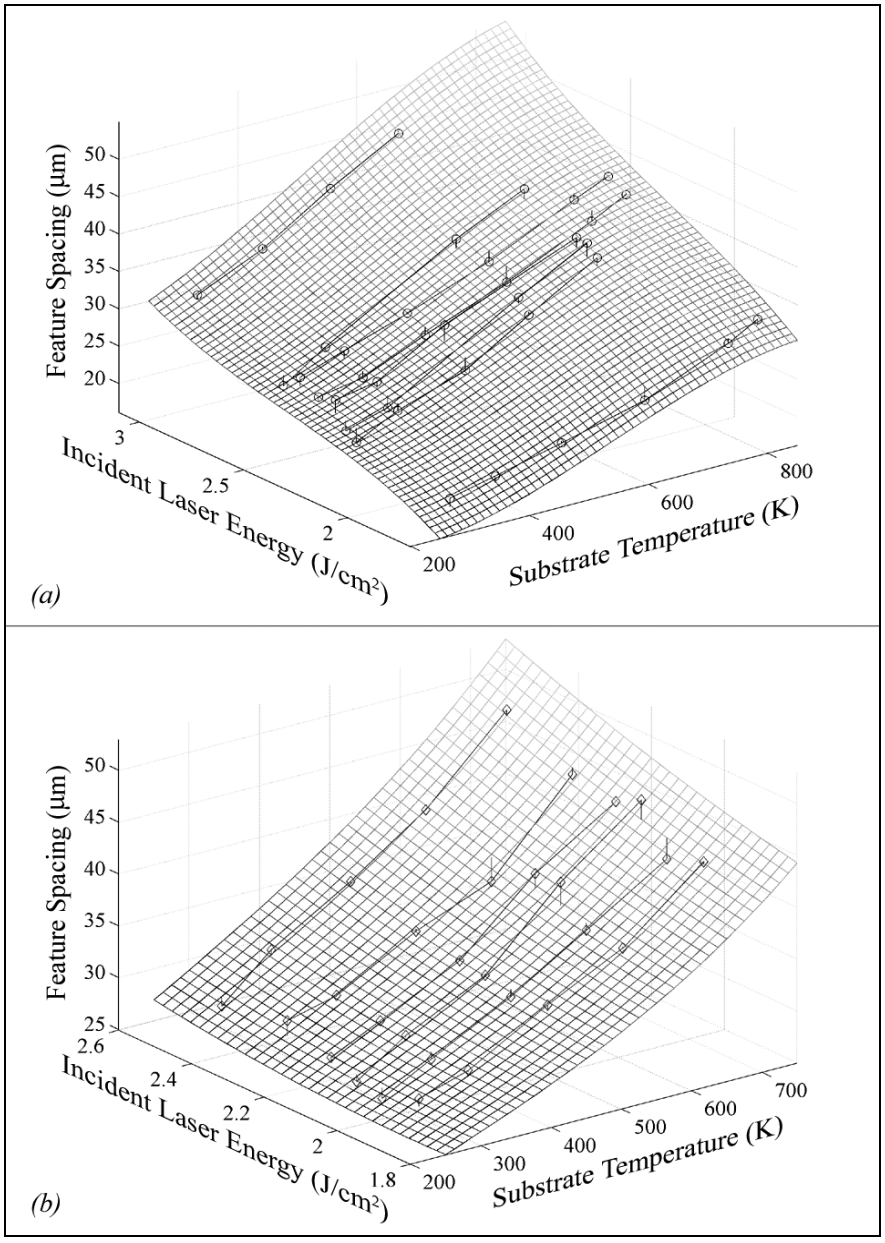

Figure 3.9. Plots of the effect of incident energy and substrate temperature on feature spacing

Plots of results of a series of experiments in which laser generated surface feature spacing is measured for substrates irradiated at different temperatures and with different incident energies on, (a) (111) silicon substrates, and (b) (100) silicon substrates. The mesh plots are the 3rd order best fit surfaces to the data and the vertical lines indicate the error between the best fit surface and the data points.

3.4.1 Plan view of the substrate

Results using the first configuration are shown in Figure 1.1(a-d) (1.2) in which the evolution of the relief on a Si(100) surface is shown for an increasing number of pulses under a 0.5 bar Ar atmosphere. A prominent feature at the upper left edge quickly develops ahead of other perturbations. This type of perturbation is often seen in these types of experiments and is perhaps due to some small particle or other kind of surface inhomogenaity which may obstruct or intensify the light. The relief on most of the surface is subtle at the 50th pulse, but becomes more pronounced after 200 pulses. Similar developments and similar microstructures are observed on (100) surfaces irradiated in SF_6 or in vacuum. Because the surface relief features keep their shape and location from pulse to pulse, the microstructure shown in Figure 1.1(b) can not result from the production of capillary waves.

3.4.2 Cross-Sectional view of the substrate

For a substrate irradiated with 3.0 J/cm^2 under an SF_6 atmosphere, the ICCD camera first detects micro-cones and micro-holes and the formation of a plume at about the 550th laser pulse. Prior to this, only the flash of the laser is evident. The development of micro-cones and the evolution of the plume were followed using continuous mode (p. 2.41). The delay time, as measured from the time when the laser pulse first strikes the substrate, was held constant at 55 ns. After 55 ns of delay time, the laser light has essentially ceased, but the substrate continues to be immersed in a fluorescent plume. The pulse width of the ICCD intensifier was set to 4.5 ns and the surface structure was monitored over 22,000 pulses. Figure 3.10(a-i) shows selected images taken after 520, 550, 600, 700, 800, 900, 1300, 1500, 1700 and 22,000 pulses. The imaged plume extends across the entire width of the exposed area and the leading edge of the plume is clearly delineated in these images. This light in the image is due only to components within the plume which decay from excited electronic states emitting visible and UV photons. Therefore, non-emitting atoms, ions, molecules, or clusters can not be detected. The tip of the emerging micro-cones in Figure 3.10(b-d) can be seen as small bright spots elevated above the surface of the substrate. In these first images, the edge of the fluorescent plume extends up to 40 μm to 60 μm beyond the tips of the micro-cones, and the plume edge is higher in the region where micro-cones underwent the fastest growth.

In the early stages of growth, it was observed that the plume height is not the same throughout the irradiated area. Micro-cones are first detected in regions where the plume height is greatest. When the micro-cones reach a certain height in these areas, the plume tends to become higher in some other area in the field of view, and micro-cones begin to develop in this new area. After the 900th pulse, shown in Figure 3.10, the micro-cone profiles are well resolved by the long focal distance microscope. Together with the growing micro-cones, deepening micro-holes are observed in Figure 3.10(e-i) as bright spots below the initial substrate surface. When micro-holes perforate the undercut surface, refer to Figure 2.3 (p.2.42), the

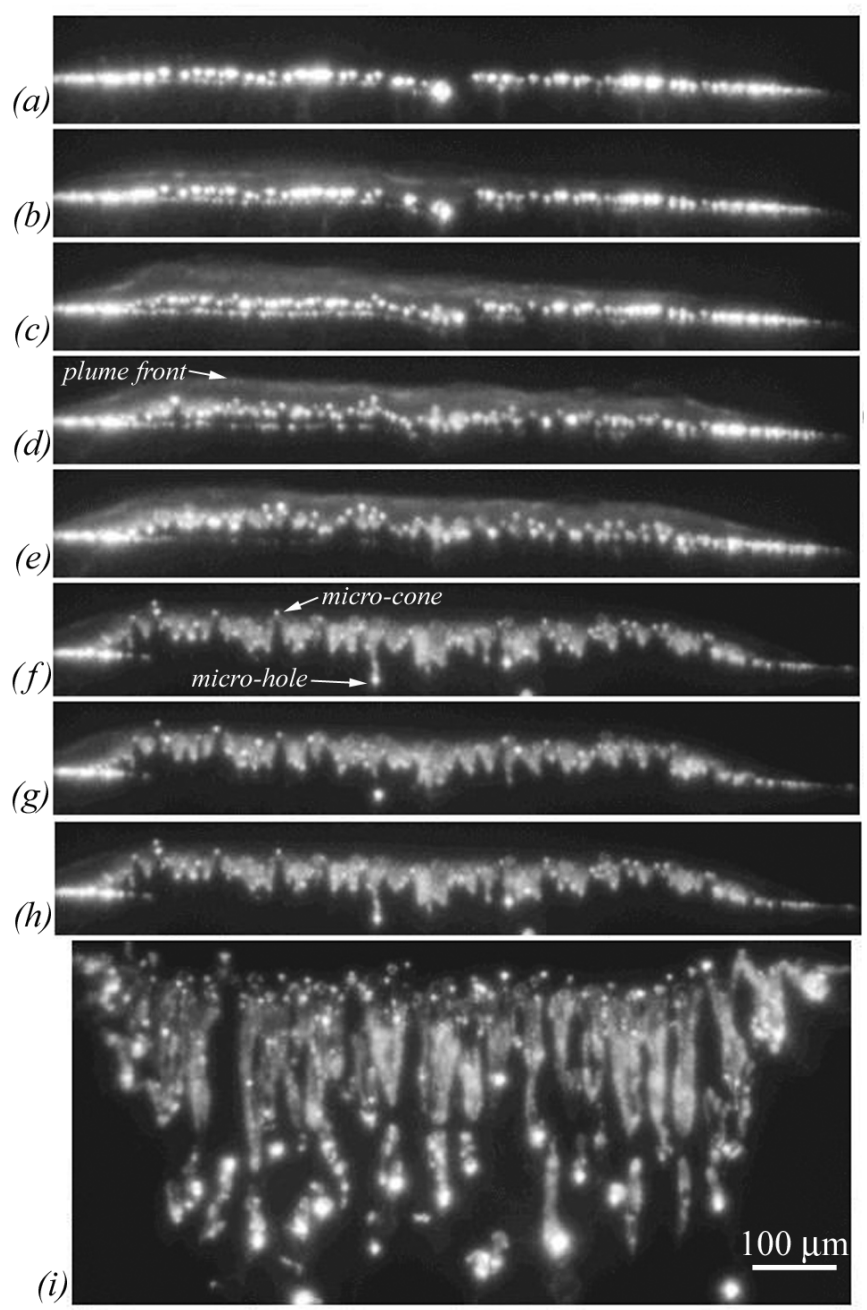

Figure 3.10. In-situ images of the profile of the evolving surface captured in continuous mode

Surface irradiated with 3.1 J/cm^2 under a 0.5 bar, SF_6 atmosphere. ICCD images were taken in continuous mode with a delay time of 55 ns. Images of the cross-section were captured at (a) 520, (b) 550, (c) 600, (d) 700, (e) 800, (f) 900, (g) 1300, (h)1700, and (i) 22,000 laser pulses.

bright spots at the bottom of the micro-holes reveal a strong increase in fluorescence. The maximum ablation rate in the micro-holes measured by the ICCD images is 1.4 μm/pulse - a value three orders of magnitude larger than the 1.2 nm/pulse measured on flat surfaces. This measurement was made by following the progression of the cross section of a micro-hole through the substrate. It is important to note that the ablation rate is not constant throughout the growth of a micro-hole. In the beginning stages of the formation of the micro-hole, the ablation rate is comparatively small. As the depth of a micro-hole is increased to between 20 μm and 70 μm, the ablation rate is highest. As the micro-hole deepens further, the ablation rate decreases.

3.5 In-Situ Imaging of Plume Motion

Images of the target during irradiation can also be acquired with the camera operating in sequential mode in which the delay time is increased from one exposure to the next (2.42). A series of images is presented in Figure 3.11 in which the delay time was increased from 45 ns to 95 ns and shows the expansion of the plume under 0.5 bar of SF_6 and with a laser fluence of 3.1 J/cm^2. The distance from the micro-cone tip to the plume edge was measured over a series of 30 images and plotted as a function of the camera delay time in Figure 3.12(a). The error bars represent uncertainties in measuring the plume front position since defining its exact edge can be difficult. In addition, the resolution of the camera/microscope setup was 1 μm/pixel, and these images were captured at the upper limit of the experimental setup's capabilities. The drag model for describing the propagation of a laser-generated plasma fits the data well and predicts that the plume front position, x, should advance with time, t, according to Equation 3.3, where x_f, the final plume position, and β, a constant related to viscosity, are adjustable parameters determined by fitting to the data.

$$x(t) = x_f\left(1 - e^{-\beta \cdot t}\right)$$

Equation 3.3

Results of measurements of the effects of background pressure on the plume are shown in Figure 3.12(b-c). In Figure 3.12(b), the plume front propagation distance is plotted as a function of background pressure for three different delay times. For any of the plotted delay times, the plume reaches a local maximum when the background pressure is 0.5 bar. The initial velocity, v_o, of the plume has been estimated by taking the derivative of Equation 3.3 for $t = 0$, so that $v_o = x_f \cdot \beta$. The initial velocity is plotted as a function of ambient pressure in Figure 3.12(c). The maximum initial velocity was reached at 0.5 bar, but it should be noted, that initial plume velocity increased again as the pressure was decreased below 0.2 bar. The results of in-situ imaging of the plume stand in good agreement with profilometry measurements that show the maximum micro-cone height is achieved when either the partial or total pressure SF_6 is 0.5 bar.

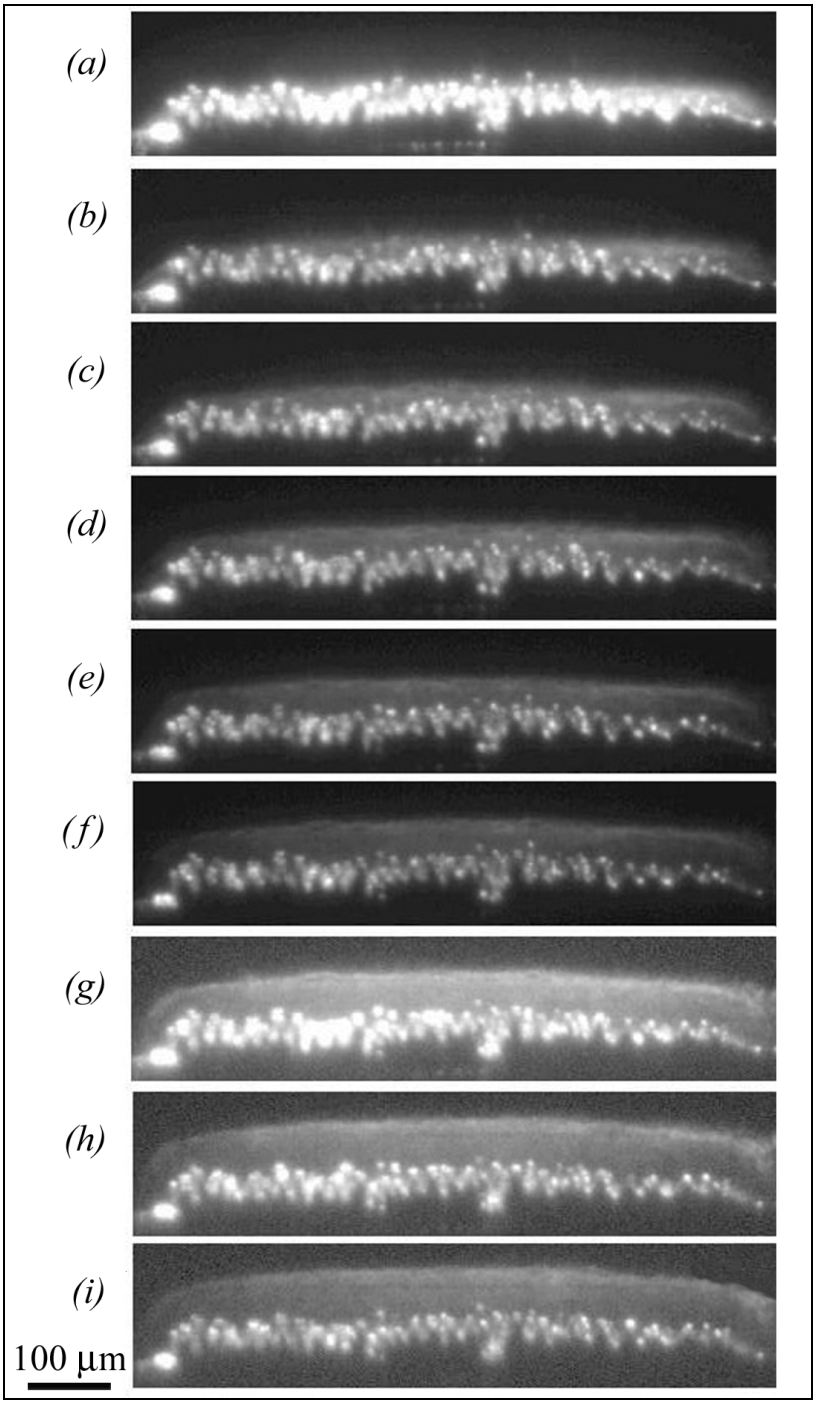

Figure 3.11. In-situ images of the profile of the evolving plume captured in sequential mode Substrate irradiated with 3.1 J/cm^2 under a 0.5 bar, SF_6 atmosphere. Delay times for images are (a) 40, (b) 50, (c) 55, (d) 60, (e) 65,(f) 70, (g) 75, (h)80, and (i) 95 ns.

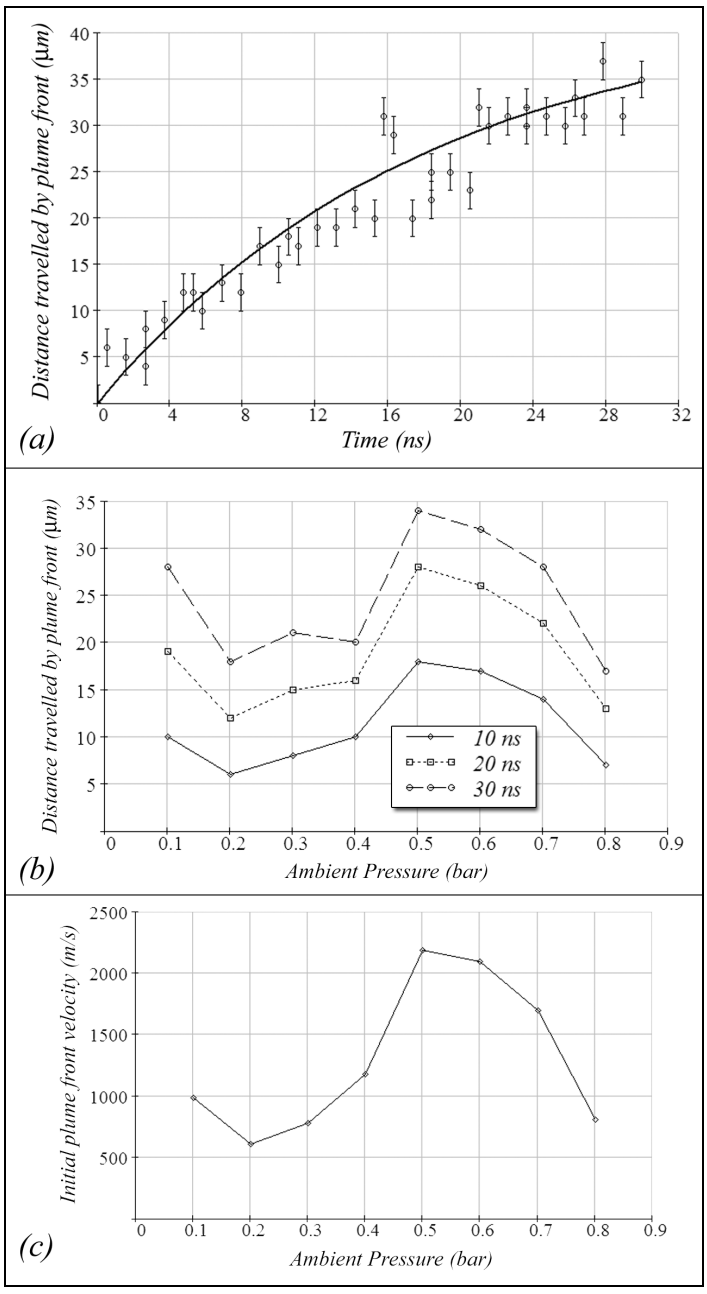

Figure 3.12. Plots of plume propagation as a function of time and ambient pressure

(a) propagation distance of the plume front vs. propagation time. solid line is the best fit to Equation 3.3.(b) plot of the position of the plume front edge relative to the target surface as a function of the ambient pressure of SF_6 at three different delay times.(c) a plot of the initial velocity of the plume front vs. ambient pressure of SF_6 as estimated by curve fitting Equation 3.3 to experimental data.

The maximum height achieved by the surface structure occurs under atmospheric conditions where initial plume velocity, or final plume position, are greatest.

3.6 Crystallography and the Morphology Surface Structure

It has been shown already that the crystal orientation of the substrate surface has an effect on the average spacing between surface features, but other, more subtle effects can be observed in the shape of the individual surface features that are also related to crystal texture. Figure 3.13 shows the relief that is produced by laser irradiation on three different crystallographic surfaces. Comparison of these images reveals that some aspects of the surface relief morphology depend on the surface orientation. Figure 3.13(a) shows laser induced patterns on (100) silicon. Although not immediately apparent, the four-fold symmetry of the (100) surface does appear in localized regions where peaks are interconnected to one another by ridges. In these regions, one peak is connected to four other peaks by four ridges. One such region is highlighted.

Figure 3.13(b-c) shows the typical results laser induced surface structuring of the (111) surface. The optical micrograph in Figure 3.13(c) was acquired with a Nomarski contrast attachment and reveals with remarkable clarity the crystallographic surface symmetry. The three-fold characteristic of cubic (111) surfaces is expressed in the surface structure formed by laser treatment. It may appear as though the surface is covered in cubes, but this is an optical illusion. It should be noted that the height of these features is about 10 times smaller than their breadth. So, these are not corners of cubes, but rather squat, triangle-based pyramids. To aid the eye, some of the peaks are indicated in the picture with arrows. The edges of the pyramids tend to, on average, form at 120º to one another and point in (211)-type surface directions. Similar morphologies can occur in (111) silicon surfaces due to chemical etching, but since the peaks of the laser induced features extend above the original surface, etching cannot be the only reason for crystallographic expression. The relief on (211) surfaces after irradiation at 3.0 J/cm^2 is composed of undulating parallel lines as shown in Figure 3.13(d).

3.7 Micro-cone Evolution on (110) Crystal Faces

One remarkable finding is that surface waves does not evolve on the (110) crystal surface of silicon. However, this fact does not entirely preclude the formation of micro-cones and micro-holes. But, the conditions which promote surface structuring are quite different from those found on the other crystal faces that were studied.

No surface relief appears to form on (110) surfaces even after 3000 laser pulses at a fluence of 3.0 J/cm^2, regardless of ambient atmosphere. However, if the laser energy density is increased beyond 4 J/cm^2 and irradiation occurs within an SF_6 atmosphere, nucleation sites of micro-cones appear, expand, and eventually cover the entire irradiated region. Figure 3.14 shows a series of SEM micrographs illustrating

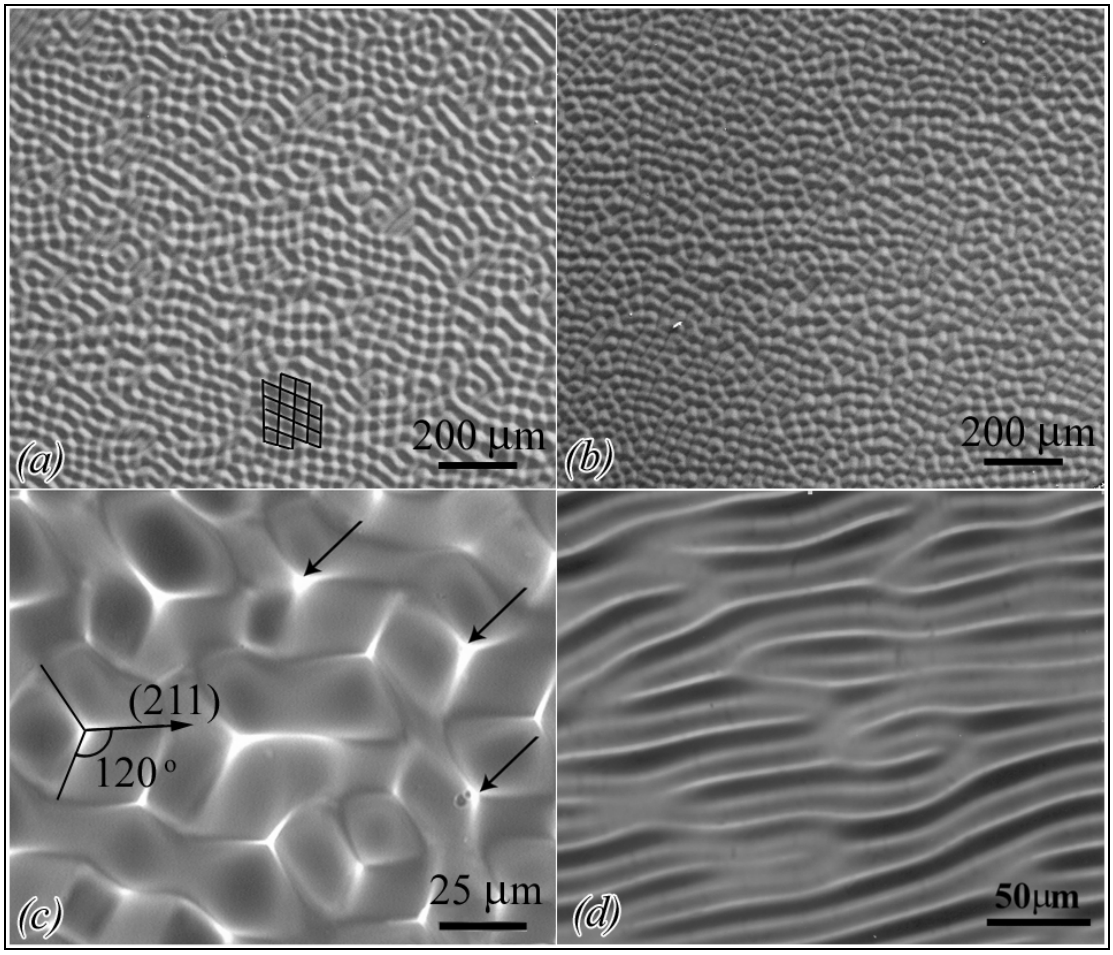

Figure 3.13. Micrographs showing the role of crystallographic orientation on structure morphology.

(a) SEM micrograph of (100) surface (b) SEM micrograph of (100) surface.(c) Nomarski contrast optical micrograph of (111) surface. Arrows indicate peaks on surface.(d) SEM micrograph of laser treated (211) silicon. All irradiation performed in 0.5 bar Ar atmosphere at 2.8 J/cm^2.

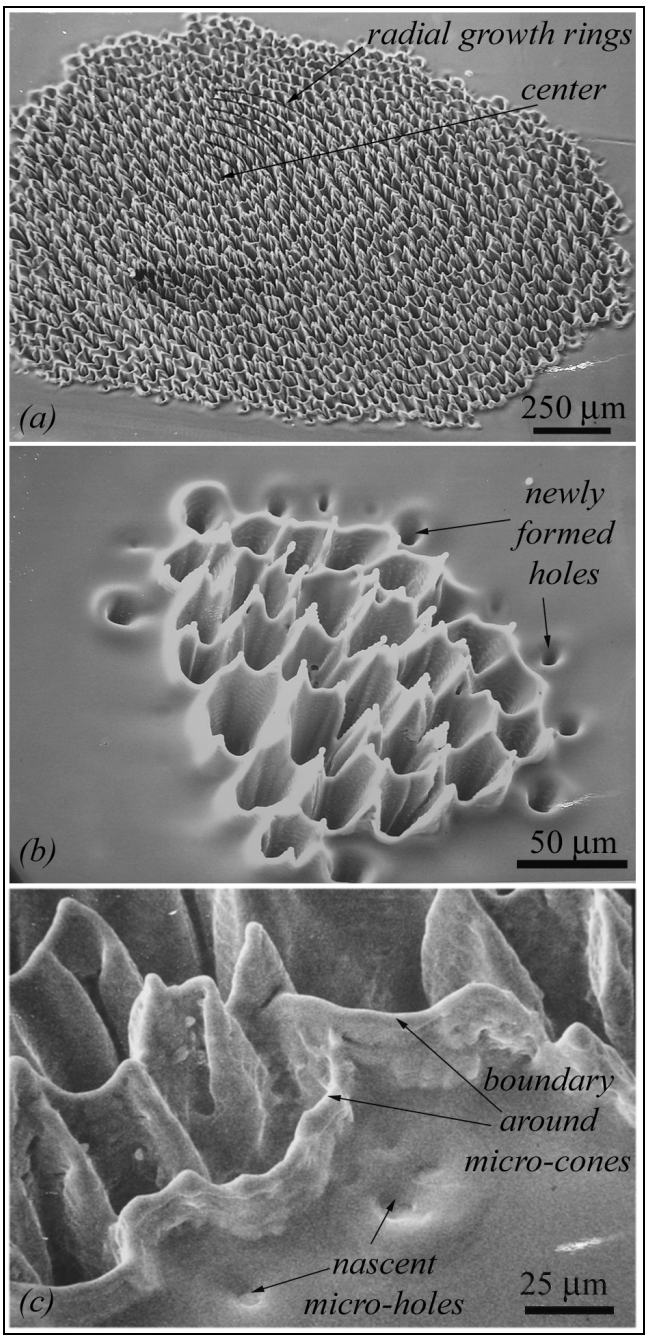

Figure 3.14. SEM images of micro-cone growth on (110) silicon surface

Substrate was irradiated under a 0.6 bar SF_6 atmosphere at a fluence of 4.0 J/cm^2.(a) Large region of micro-cones. The center nucleus is indicated along with rings showing stages of radial expansion. (b) Nucleus of cone growth at a very early stage of development.(c) Closer view of the boundary between micro-cones and flat substrate. Small pits at the boundary are likely precursors to micro-holes.

properties of micro-cone formation on the (110) surface. A first notable characteristic, most clearly shown in Figure 3.14(a,b), is that there is a clear boundary between the region where highly developed cone-structures exists and the apparently unaffected region surrounding it. Note that this boundary does not correspond to the shape of the laser spot that is several mm's in diameter. Contrast this with Figure 1.1(f) in which surface waves first cover the entire irradiated region followed by micro-holes between wave crests. Figure 3.14(a-b) were imaged at two different locations on the same substrate and presumably capture surface structure formation at different stages of development. In Figure 3.14(b), the nucleus for cone formation is still small, but the micro-holes surrounding this nucleus indicate that growth will progress outward. Figure 3.14(a) shows the surface after radial growth has progressed further. However, evidence of the radial nature of growth remains as the site of nucleation and layers of outward expansion are apparent. Figure 3.14(c) shows a closer view of the boundary between micro-cones and flat silicon where the first indications of new micro-hole formation pock mark the adjacent and otherwise smooth surface.

3.8 The Induced Organization of Surface Structure

It was recognized early on in this project, that imperfections or inhomogeneities in either the energy profile of the beam or the original surface had an effect on the large scale organization of surface waves. For instance, waves tend to align along the edge of laser spots, and circular ripple patterns tend to form around small foreign particles on the surface. This observation lead to the conjecture that if the beam or surface is purposefully altered in an organized fashion, then some overall order could be imposed on surface patterning.

Results of the successful application of this conjecture are shown in Figure 3.15. These patterns were formed by placing a wire mesh in the beam path several meters from the substrate surface. The mesh was not placed on the image plane, so its exact pattern was not projected onto the surface without significant blurring, and it appears as though the location of the mesh along the beam path is an irrelevant factor in the formation of surface organization. What is important however, is that the presence of the mesh produces very slight but organized variations in energy density across the laser spot. The surface waves tend to align themselves along these small gradients in flux.

Two different meshes were used: on is an array of squares composed by wires crossed 90˚ to one another, and the other is an array of equilateral triangles formed by wires crossed 60˚ to one another. In both cases the pitch of the mesh was approximately 3 mm and the thickness of the wires was 30 μm. Figure 3.15(a) shows the results of using the square mesh on a (100) surface, and Figure 3.15(b) shows the results of using the triangle mesh on a (111) surface. It is apparent from these micrographs that the geometry of the mesh has been mapped to the ordering of the surface structure. Choice of the surface crystal surface orientation was not critical to surface structure organization. But, by visual inspection, it appears that the combination of a crystalline surface, with a mask with the same order of symmetry, yielded improved

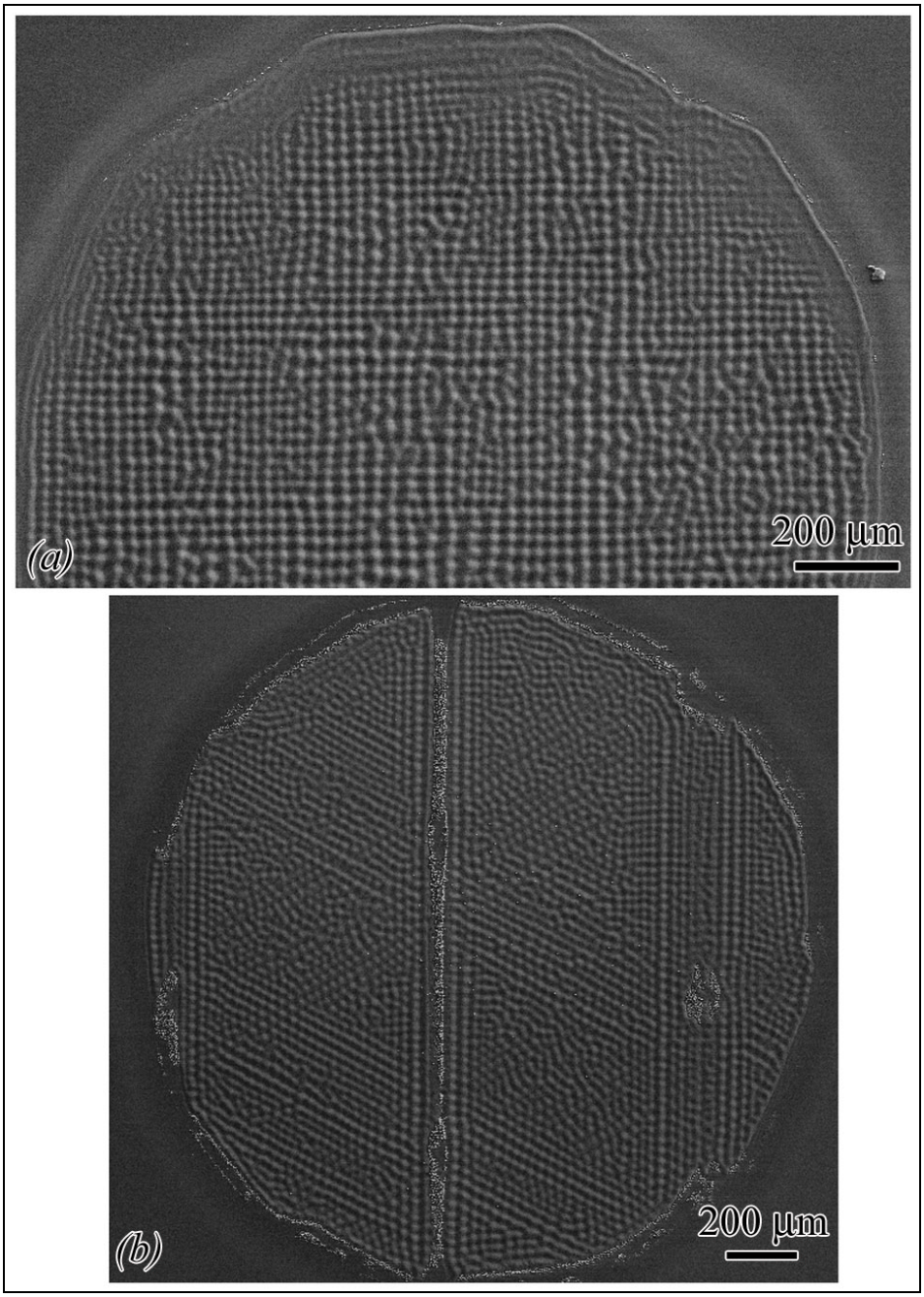

Figure 3.15. SEM micrographs of patterns imposed placing a coarse wire mesh in the beam path

The periodicity of the wire mesh was approximately 3mm. (a) result of using a square grid patterned mesh on a (100) substrate. (b) result of using an equilateral triangular patterned mesh and a (111) substrate.

organization. Also, since the position of micro-cones is determined by that of the surface waves, this method can be used to compel ordering in the micro-cone structure.

One very notable result of these experiments is that the periodicity of the surface structure is largely unaffected by the presence of a wire mesh. The distance between adjacent surface structures does not change, but the mesh does affect the positional relationship between them. This shows that a rather crudely constructed mask can be used to compel long range order onto micron scale features. Combining knowledge gained about the effects of substrate temperature with this ordering technique provides one with the ability to control feature spacing and feature organization *independently*.

3.9 Liquid Chemical Etching of Micro-cone Structures

Micro-cones represent a unique surface structure in themselves, but they can also be used as a starting point for generating more refined surface structures. One set of experiments investigated a possible post-processing technique for reshaping the surface and takes advantage of crystallographic anisotropy in order to do this. Figure 3.16 shows a series of SEM images of a (100) silicon substrate on which micro-cone structures were produced and then submerged for 20 minutes in a 20% KOH aqueous bath at 90˚C. The rate at which silicon is etched by KOH is highly surface orientation dependent; the (111) plane etches at a rate about 10 times slower than other low order planes[42]. Etching is therefore effectively terminated at the (111) plane.

The micro-cone structure offers many surface orientations to the etchant bath, but etching helps to expose the underlying crystal structure by attacking some exposed planes faster than others. Figure 3.16(a-c) are overhead views of the etched substrate at different magnifications. The originally round micro-holes have been etched out to form rectangles. Figure 3.16(d-f) were taken at an angle and show how the micro-cones have been shaped into tall, pyramidal structures with sharp tips. Figure 3.16(f) is a highly magnified view of a tip showing its approximately 50 nm tip radius.

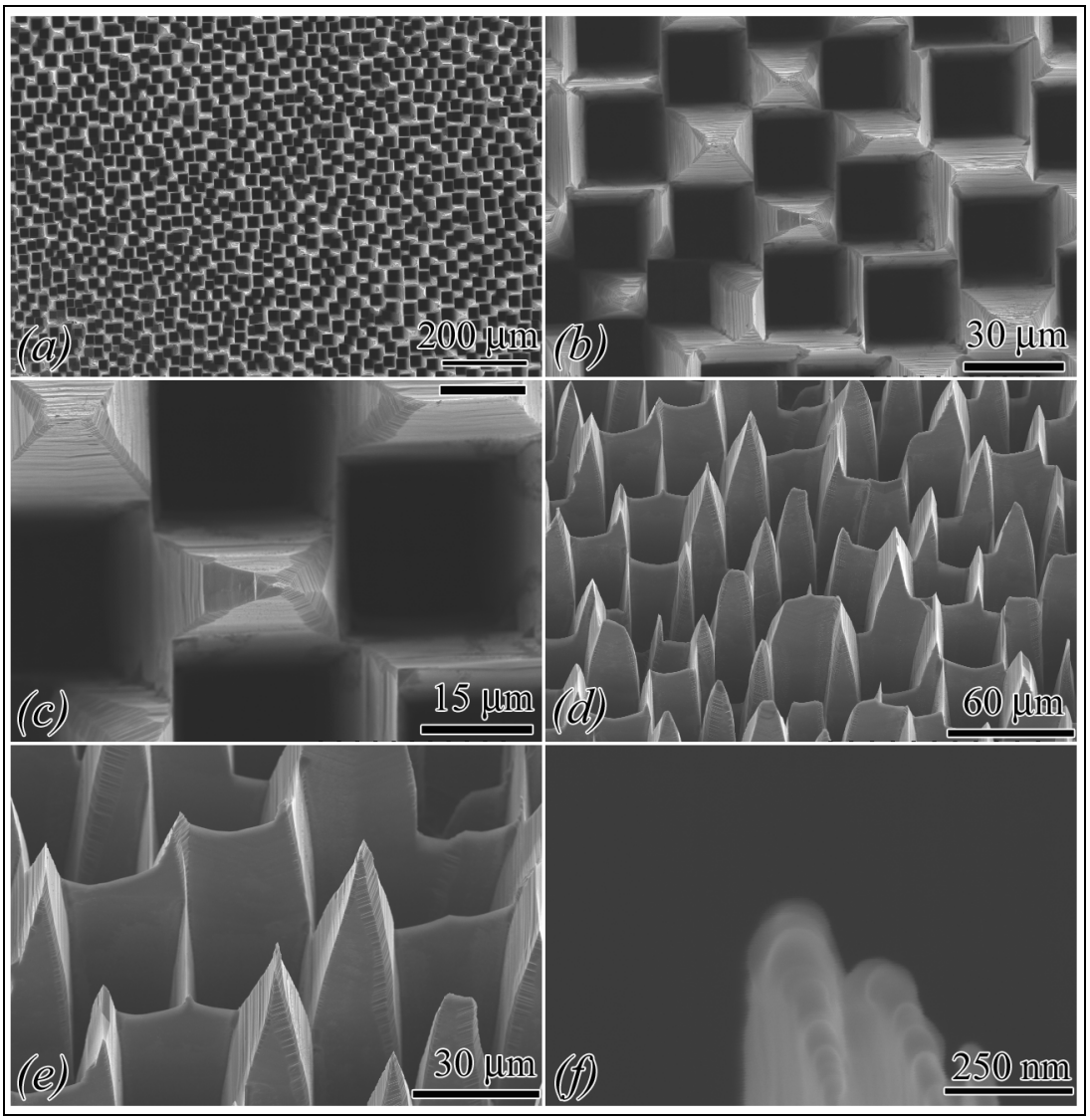

Figure 3.16. SEM micrographs of micro-cones on a (100) surface after etching in KOH.

CHAPTER 4 DISCUSSION OF RESULTS AND MODELING OF LASER-INDUCED SURFACE MICROSTRUCTURING

The following chapter will discuss in detail a series of models that explain the evolution of laser induced surface restructuring from its very initial stages as barely perceptible waves of the substrate surface to micro-cones and micro-holes constituting the surface of black silicon. These models elucidate the mechanisms that play the primary roles in establishing the spacing between surface features and explain the role that substrate crystallographic orientation has on morphology. Discussions on the conditions necessary for micro-cone and micro-hole growth will be presented along with analysis of data that indicate the best conditions for growth.

4.1 A Model of Laser Induced Melting

Many of the concepts involved in understanding the formation of surface structures deals with actions at the solid-liquid and liquid-vapor interfaces that exist during the melt time. It is, therefore, of critical importance to this model that reliable information on the melt time and melt depth of the substrate be determined. Previous work on both the measurement and modeling of melting by pulsed lasers is vast [43-46], and usually provides information on the melt time and melt depth as a function of laser fluence and sometimes pulse width. But, detailed information is not available about the effects of initial substrate temperature on laser induced melting. Computer simulations were used as part of this thesis work in order to ascertain this information.

A computer model was developed using the 2-D finite element based software FlexPDE. The script for this code and a detailed description of thermo-physical parameters used are provided in Appendix 6 and 7. This code has the capability of solving two and three dimensional non-linear partial differential equations, but for the purposes of laser melt calculations, the geometry was reduced to essentially a 1-D solution space. The total depth of the substrate was set to approximately 5 times the thermal diffusion length. This model does not treat phase change directly. Instead, all of the thermo-physical properties are treated as continuous functions across the solid-liquid interface. Physical properties, such as density, which in reality change abruptly at the interface, are modeled as *arctan* functions centered at the melt temperature. By doing this, the abrupt change is smoothed over a range of about 5 degrees thus avoiding discontinuities and singularities in the finite element solution process. The laser pulse is modeled as having a Gaussian profile in time with a FWHM equal to that of the laser pulse. Changing the pulse width in the model over the 25 ns to 50 ns pulse width range specified by the laser manufacturer had a negligible effect on the

results of melt time calculations. This model did not take into account any effects of substrate evaporation. This omission is not likely to affect results in the lower energy regime, but above ~3.0 J/cm^2, this may result in overestimation of the melt time as energy, which in reality would have gone into evaporation, remains in the substrate only to be dissipated by conduction.

A 3-D plot summarizing the results of melt time calculation over a range of laser energy densities and initial substrate temperatures is shown in Figure 4.1. The meshed surface in the plot represents a 3rd order least squares best fit surface to the results of the calculations which are represented as circles. The vertical lines from the circles to the surface indicated the error between the calculation and the best fit surface. The description of the fit is given in equation 4.1, in which t_{melt} is the melt time in ns, E is the incident energy in J/cm^2, and T is the initial substrate temperature in K.

$$t_{melt}(E,T) = -708 + 675 \cdot E - 198 \cdot E^2 + 25.9 \cdot E^3 + 2.13 \cdot E - 1.06 E \cdot T \ldots$$
$$+ 0.199 E^2 \cdot T - 3.36 \cdot 10^{-3} \cdot T^2 + 9.95 \cdot 10^{-4} \cdot E \cdot T^2 + 1.56 \cdot 10^{-6} \cdot T^3$$

equation 4.1

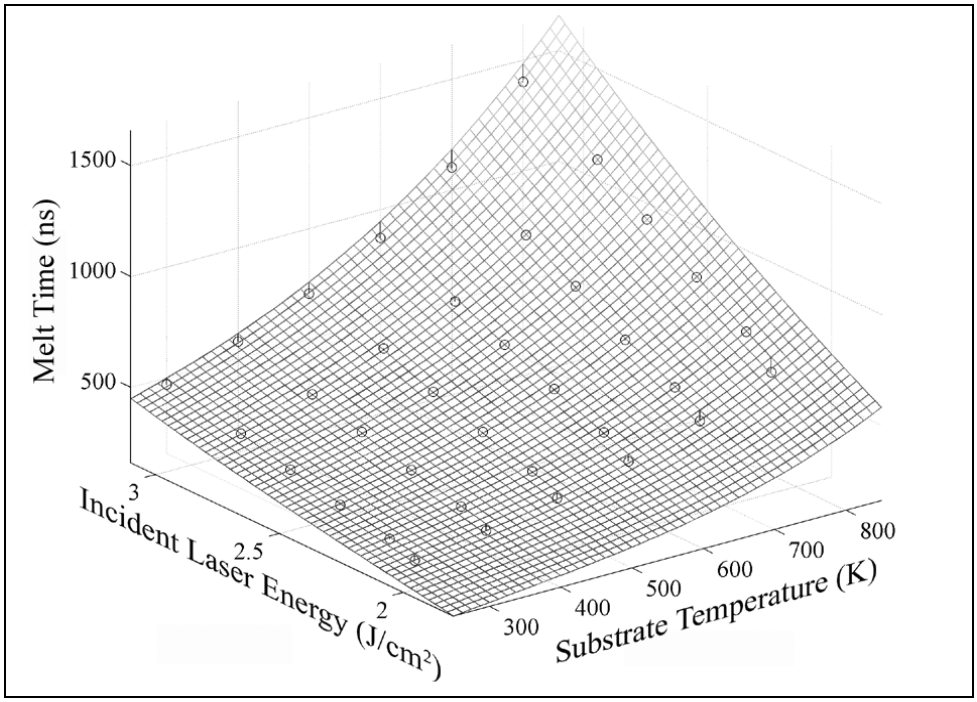

Figure 4.1. 3-D plot of results of melt time calculations vs. incident energy and substrate temperature. The circles represent the various conditions under which the model was run and the mesh represents a 3rd order best fit surface described by equation 4.1.

4.2 The Role of Thermal Diffusion and Capillary Wave Motion in Establishing Surface Structure Spacing

Many of the results regarding the spacing of surface features can be explained through careful consideration of the changing shape of both the solid-liquid (SL) and liquid-vapor (LV) interfaces during the melt time of the substrate. All of the previous work in this area, as described in chapter 1, relied entirely on actions occurring at either the SL or the LV interface but fail to predict feature spacing.

The approach taken in this model is concerned with the stability, or more precisely, the rate of decay of perturbation amplitude of the two interfaces as a means to determine feature spacing. Morphology of the SL interface is mediated by the evolving thermal field in the substrate, and morphology of the LV interface is governed by the action of capillary wave motion of the free molten surface. It will be shown that the differences in the way that the shape of these two interfaces change during the melt time determines in large part what the feature spacing will be. At this point in the discussion, the anisotropy in substrate crystallography is ignored.

4.2.1 The Role of Lateral Heat Diffusion in the Evolution of the SL Interface

The computer modeling of melting, which was described above, considers only the diffusion of heat perpendicular to a flat substrate surface. Indeed, nearly all of the published work in this area ignores the possibility of thermal transport parallel to the mean height of the surface, termed here *'lateral heat diffusion'*. Since the shape of the SL interface is determined almost entirely by the thermal field within the substrate, it is necessary to consider this lateral heat diffusion when analyzing the changing morphology of the SL interface during the melt time.

For a perfectly flat substrate irradiated by a perfectly uniform laser pulse, there will be no temperature gradient developed parallel to the surface and thus no cause for lateral thermal diffusion. The temperature gradient would be directed perpendicular to the surface everywhere. This is often the assumption made for 1-D laser melting simulations. If however there is a slight modulation of surface height, laser irradiation will induce a temperature field in which there is a non-zero gradient parallel to the mean height of the substrate. A simple argument demonstrating this can be made if one assumes that incident irradiation results in a uniform temperature across the surface and that isotherms within the substrate in close proximity to the surface will follow the shape of the surface. In the case of a corrugated surface, a point within the substrate directly below a peak will be at a lower temperature than a point, at the same depth relative to the mean height of the substrate, directly below a valley. A negative thermal gradient is therefore established from regions within the substrate below valleys to regions below peaks. This concept is illustrated in Figure 4.2.

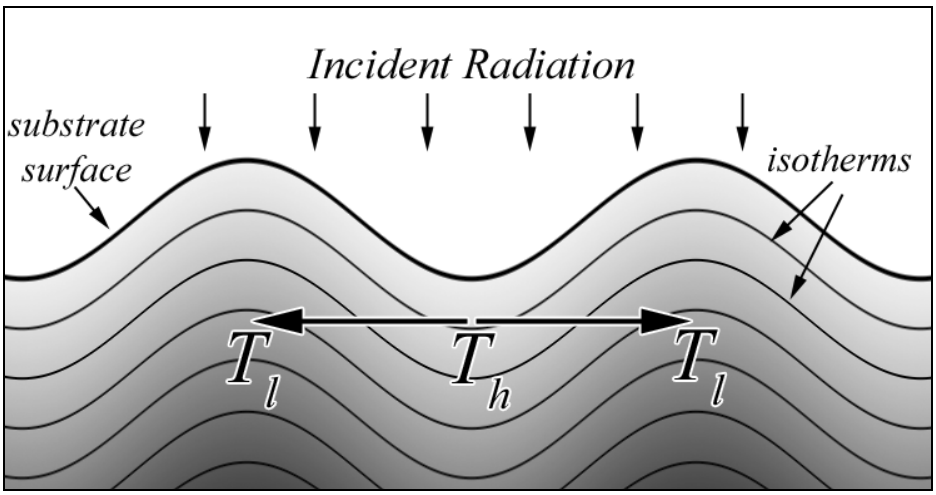

Figure 4.2. Diagram showing lateral thermal diffusion within an irradiated corrugated substrate

Initially, isotherms within the substrate closely follow the shape of the top surface. A negative thermal gradient will be established from higher temperature regions (T_h) below the valleys to lower temperature regions (T_l) below the peaks.

The morphology of isotherms will change in time as the system proceeds toward equilibrium according to the thermal diffusion equation. Since the solid-liquid interface can be regarded as a special case of an isotherm near the melting temperature, its shape can be predicted by the thermal diffusion equation as well. The purpose of the following derivation is to develop a description of how the amplitude of undulations of the SL interface will reduce in time. The 1-D thermal diffusion equation given below is sufficient to meet this end. The 1-D diffusion equation is:

$$\frac{\partial T}{\partial t} = D \cdot \frac{\partial^2 T}{\partial x^2} \quad , \qquad D = \frac{k}{\rho \cdot c_p}$$

equation 4.2

where T is temperature, t is time, x is lateral position, D is diffusivity of the substrate, k is thermal conductivity, ρ is density, and c_p is heat capacity. The general solution to equation 4.2 is given below in which A_n, B_n, and L_n are to be solved for in terms of initial and boundary conditions.

$$T(x,t) = \sum_{n=0}^{\infty} \left(A_n \cdot cos\left(L_n \cdot x\right) + B_n \cdot sin\left(L_n \cdot x\right)\right) \cdot exp\left(-L_n \cdot D \cdot t\right)$$

equation 4.3

For simplicity sake, the initial shape of the surface is assumed to be a sinusoid with amplitude A_o and wavelength Λ, and so the initial condition for the temperature field will be a sinusoid as well and is described as,

$$T(x,0) = A_o \cdot cos\left(\frac{2 \cdot \pi \cdot x}{\Lambda}\right).$$

equation 4.4

A solution describing the temperature field, and thus the shape of the solid-liquid interface, in time is then easily found to be,

$$T(x,t) = A_o \cdot cos\left(\frac{2 \cdot \pi \cdot x}{\Lambda}\right) \cdot exp\left[-\left(\frac{2 \cdot \pi}{\Lambda}\right)^2 \cdot D \cdot t\right].$$

equation 4.5

Note that the wavelength of the perturbation does not change with time, only the amplitude changes. The amplitude of a sinusoidal perturbation on the solid-liquid interface, A_{sl}, as a function of time and wavelength is given by the expression below,

$$A_{sl}(\Lambda,t) = A_o \cdot exp\left[-\left(\frac{2 \cdot \pi}{\Lambda}\right)^2 \cdot D \cdot t\right].$$

equation 4.6

4.2.2 The Role of Surface Tension in the Evolution of the LV Interface

As before, the assumption is made that a sinusoidal roughness exists on the surface of the substrate prior to irradiation. Whatever perturbations exist on the substrate surface prior to melting become the initial shape of the liquid-vapor interface at the onset of melting. Surface tension at the liquid-vapor interface combined with inertial effects of the melt, will results in cyclic oscillation of this interface. The frequency of this surface oscillation can be described by the capillary dispersion relation, equation 4.7 [9], and is determined by the wavelength of the perturbation, Λ, the surface tension of the interface, σ, the density of the liquid ρ_l, and the depth of the liquid layer, h.

$$\omega(\Lambda) = \sqrt{\frac{\sigma}{\rho_L}\cdot\left(\frac{2\cdot\pi}{\Lambda}\right)^3\cdot\tanh\left(\frac{2\cdot\pi\cdot h}{\Lambda}\right)}$$

equation 4.7

Since the initial shape of the liquid-vapor interface is assumed to be sinusoidal, the relation above can be used directly to determine the amplitude of the liquid-vapor interface (A_{lv}) as a function of time and wavelength shown in equation 4.8.

$$A_{lv}(\Lambda,t) = A_o\cdot\cos(\omega(\Lambda)\cdot t) = A_o\cdot\cos\left[\sqrt{\frac{\sigma}{\rho_L}\cdot\left(\frac{2\cdot\pi}{\Lambda}\right)^3\cdot\tanh\left(\frac{2\cdot\pi\cdot h}{\Lambda}\right)}\cdot t\right]$$

equation 4.8

Both equation 4.6 and equation 4.8 have been written in terms of sinusoids and are therefore applicable to any initial surface shape that can be described by a Fourier series. In this light, the solutions above represent the behavior of a single mode in a Fourier series. In the interest of simplifying the following discussion, this single mode approach will be maintained.

4.2.3 Convergence of the Solid-liquid and Liquid-Vapor Interfaces

Now that expressions are available to describe how the shape of the SL and LV interfaces changes in time, it is possible to predict their morphology during a single melt/solidification cycle. The process begins with the rapid melting of the surface and the advance of the solid-liquid interface into the substrate. As thermal energy is dissipated, energy balance dictates that the solid-liquid interface will reach a maximum depth and begin retreating back to the liquid-vapor interface. During this process, perturbations in both the liquid-vapor and the solid-liquid interfaces are changing shape according to equation 4.6 and equation 4.8. Resolidification approaches its conclusion with the convergence of the solid-liquid and the liquid-vapor interfaces. Upon the initiation of melting, these interfaces were of the same shape, but the mechanisms acting upon them during the melt cycle are different and so an incongruity in shape is apparent upon their convergence. *The purpose of this section is to illustrate the reasons for incongruity, and explore the implications that this mismatch has on perturbations of different wavelengths.* The mechanisms driving perturbation growth from one pulse to the next will not be examined just yet, but this discussion will lay the ground-work for an investigation of growth mechanisms.

Figure 4.3 illustrates the development and consequences of SL/LV interfacial incongruity related to determining which wavelengths are most likely promote perturbation growth from one pulse to the next. The wavelength that results in the largest growth rate from laser pulse to laser pulse is designated Λ^*. Two additional bounding cases are considered: one in which the wavelength of the surface structure is less than Λ^*, and the other for perturbations wavelengths greater than Λ^*. Illustrations of the cross-sections of the

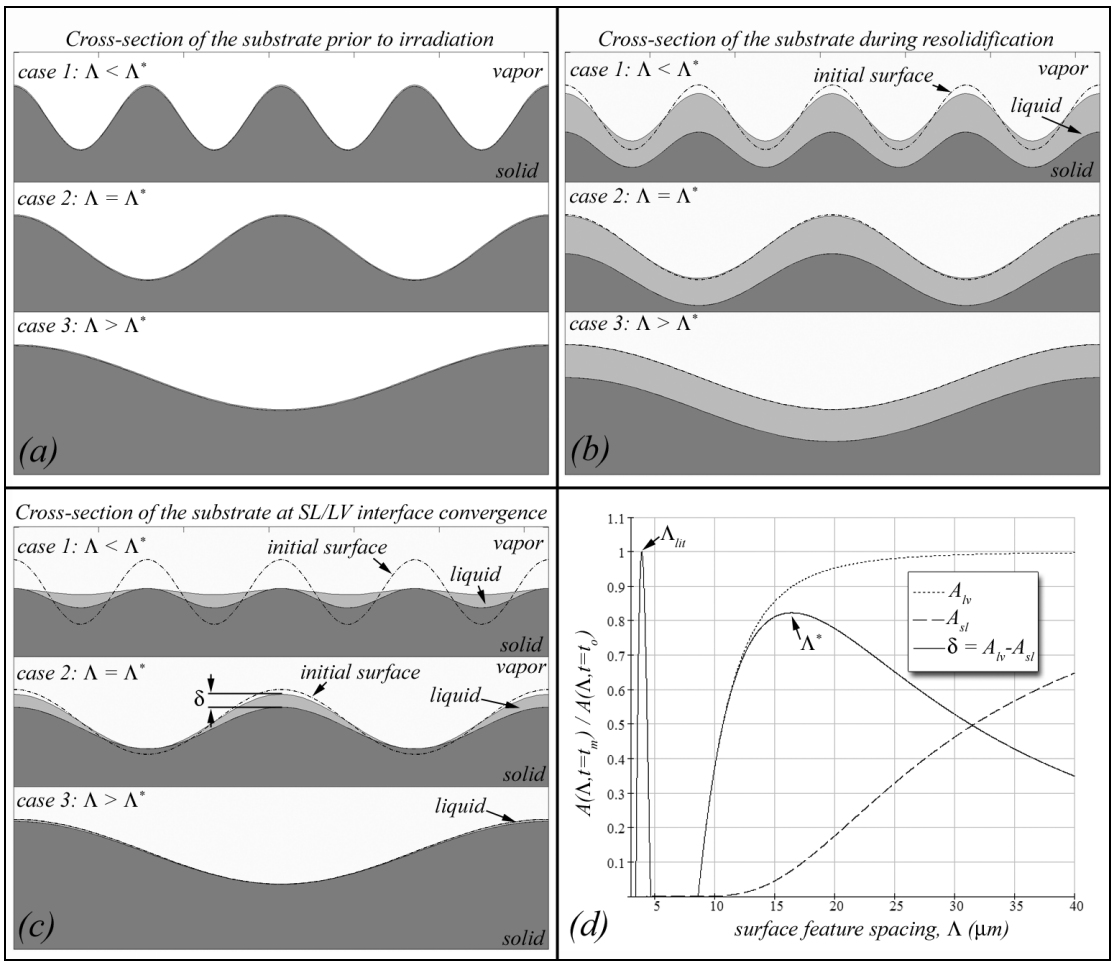

Figure 4.3. Diagrams illustrating the cause for SL and LV interface mismatch

Cross-sections of substrates are shown for three different times in the melt/solidification cycle: in (a) just prior to irradiation,(b) at some point near the middle of the resolidification cycle, and (c) at a point very near the end of resolidification when the SL and LV interfaces first intersect. The depth of the remaining liquid pool, δ, is indicated in case 2. The initial shape of the solid-vapor interface is represented as a dashed line. Solid regions of the substrate are darker, and molten regions are lighter gray. (d) shows a plot of how equation 4.6, A_{sl}, and equation 4.8, A_{lv}, vary as a function of Λ for a fixed melt time. The difference between these two curves, δ, is plotted as well . Λ^* indicates the wavelength that will yield the largest δ at the time when the SL and LV interfaces first intersect.

substrates are shown for three different times in the melt/solidification cycle: in Figure 4.3(a) just prior to irradiation, in Figure 4.3(b) at some point within the resolidification cycle, and in Figure 4.3(c) at a point very near the end of resolidification when the solid-liquid and liquid-vapor interfaces first intersect. In these images the initial shape of the solid-vapor interface is represented as a dashed line, solid regions of the substrate are darker gray, and molten regions are lighter gray.

The only difference between cases 1, 2, and 3 is the perturbation wavelength. One effect of wavelength is first visible in case 1 of Figure 4.3(b). In this, it is apparent that the LV interface has deviated from its original shape and the perturbation amplitude has been reduced. The effects of surface tension become appreciably stronger at smaller wavelengths. In case 2 and case 3 of Figure 4.3(b), motion of the LV interface has occurred as well, but it is too small at this point to be visible.

In case 1 of Figure 4.3(c), the LV interface is at a point in its oscillation cycle where its amplitude is nearly 0. The amplitude of the SL interface has been reduced as well, but by a smaller factor. Isolated pools of molten material are subsequently left in the valleys of the solid substrate. This liquid will solidify, but it is hard to imagine a mechanism that would cause the surface at this point to attain a roughness with an amplitude greater than what was present before irradiation. In order for the amplitude of the surface roughness to become larger, liquid from the valleys would have to be displaced to the tops of the solid peaks. For this to occur within the relevant time and length scales, liquid would need to be transported over distances of μm's in the time span of ns's requiring an average transport velocity on the order of 1000 m/s. There is no apparent driving force which could accomplish this extremely fast material transport. Therefore, while under the action of surface tension and thermal diffusion, perturbations with a wavelength smaller than a specific wavelength will be diminished with successive laser pulses.

In case 2 of Figure 4.3(c), where it is argued that perturbation growth from pulse to pulse will be a maximum, the effect of surface tension on the LV interface amplitude has been smaller than that of thermal diffusion on the SL interface. The result is isolated pools of molten material on the *peaks* of the solid. At this point, the overall amplitude of the surface roughness is still less than that prior to irradiation, but the potential for further growth after solidification has completed exists and does not require significant material transport. Details regarding further growth will be discussed later in section 4.3. But if for no other reason, further amplitude growth can occur because solid silicon is less dense than liquid silicon and the peaks will increase in height after complete solidification compared to the valleys.

The result of having surface roughness with a wavelength longer than Λ^* is shown in case 3 of Figure 4.3(c). As in case 2, the intersection of the SL and LV interfaces first occurs in the valleys of the surface waves and last vestiges of molten material are located on the peaks of the solid. However, at this longer wavelength, neither surface tension nor thermal diffusion played much of a role in modifying the shapes of either interface during the melt time. Therefore, a mismatch of the SL and LV interfaces is practically nonexistent, the surface roughness will remain the same from pulse to pulse, but perturbation growth is not likely to occur.

To summarize so far, it appears that a mismatch in shape of the SL and LV interfaces at the time they converge can give some indication of the potential for growth. As the next step in the development of this model, it is necessary to *quantify* the mismatch of the interfaces in order to establish a means of determining Λ^*. Perhaps the most obvious and straight-forward approach is to use the maximum height of the liquid as a gauge of mismatch. Another option is to use cross-sectional area of the liquid region as a measure. At this point in the development of this model, the choice is arbitrary, but a plot illustrating the first option is shown in Figure 4.3(d). In this plot, equation 4.6 and equation 4.8 are plotted as a function feature spacing for a constant time $t = t_{melt}$ = 600 ns. The difference in value between equation 4.8 and equation 4.6, $\delta_{int}(\Lambda,t_{melt})$, is plotted as well. Λ^* is denoted at the point where $\delta_{int}(\Lambda,t_{melt})$ is a maximum.

Previously published work in this area, which was discussed in chapter 1, proposed that the criterion for surface feature spacing be the wavelength for which the capillary wave passes through exactly one full cycle during the melt time. The resulting wavelength for this supposition, indicated on the plot by Λ_{lit}, is first of all not a very good predictor of wavelength giving a solution 3 to 4 times smaller than experimental results. And secondly, if the liquid surface is allowed to go through one full cycle, then there is little guarantee that the peaks and valleys of the surface structure would remain in the same place from one laser pulse to the next. Experimental findings show that the position of the surface structure remains fixed throughout its evolution. Therefore, another requirement of this model is that the capillary wave must move through less than ½ of an oscillation.

A trend which is not immediately apparent in Figure 4.3(d) is that, as melt time increases, the value of Λ^* increases as well in agreement with experimental results. Calculations to find the wavelength that will yield the largest mismatch between the SL and LV interfaces as a function of melt time have been carried out. The results of using both the maximum distance of the mismatch (δ_{int}) and the maximum cross-sectional area of the mismatch (CA_{int}) as criteria for predicting wavelength are shown in Figure 4.4 along with experimental results. The experimental data is the same as was presented in Figure 3.9 (p. 3.53) except that *energy density* and *substrate temperature* axes have been collapsed onto one *melt time* axis by use of equation 4.1. Using cross-sectional area as a gauge for determining wavelength (CA – *model*) appears to be in better agreement with experimental results than using the difference in amplitudes (δ – *model*). Both criteria underestimate the measured wavelength, but the agreement between the general trend in the data and the model is promising. The curve for the experimental data and the model are:

$$(a)\ \Lambda_{exp.100} = 1.4906\, t_{melt2}^{0.5288} \qquad (b)\ \Lambda_{exp.111} = 1.4121\, t_{melt}^{0.5028}$$

$$(c)\ \Lambda_{CA} = 1.283\, t_{melt}^{0.507} \qquad (d)\ \Lambda_{\delta} = 0.96\, t_{melt}^{0.5109}$$

equation 4.9

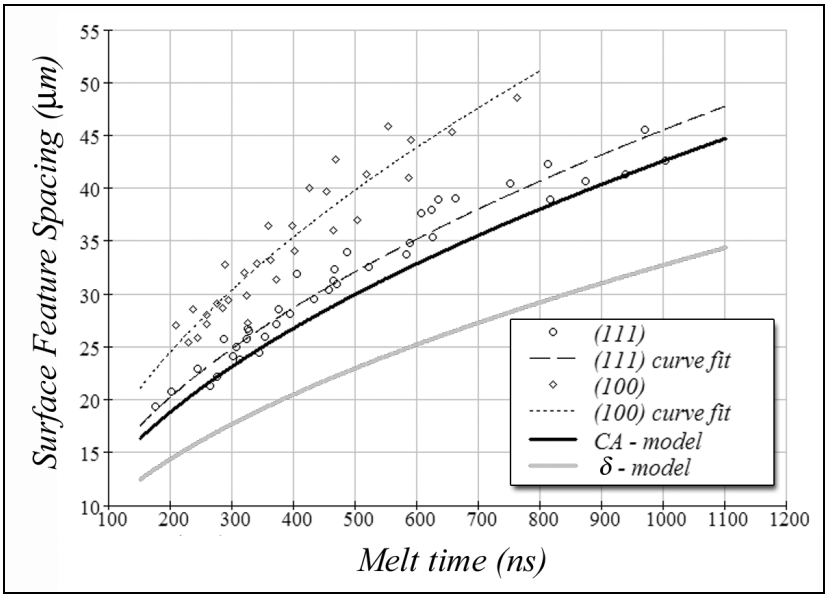

Figure 4.4 Plot of surface feature spacing as a function of melt time

Plotted are measured data for two different crystal surfaces and results of the model when using two different means of quantifying incongruity between the SL and LV interfaces (δ-model : difference in amplitude, CA-model: cross-sectional area of mismatch region).

4.3 The Last Stage of Solidification and the Role of Crystallography

Mechanisms have been presented which give some indications as to why certain feature spacings may be chosen over others as a result of the melt and resolidification processes. However, the conditions necessary for the growth of these perturbations from pulse to pulse has yet to be explained. Note that the model so far predicts that the amplitude will be smaller after the melt time than it had been before regardless of wavelength. The melt and resolidification cycle has been examined up to the time that the SL and LV interfaces first converge. At this point, thin pools of isolated liquid still remain on the surface yielding a geometry like the one depicted in Figure 4.5. Further solidification will occur, but now under very different conditions than it had up to this point. This last stage or '*end-stage'* of solidification is differentiated by the fact that now there is a line of intersection between *three* phases. The existence of a solid-liquid-vapor (SLV) line will play a role in this last stage of solidification. The problem now is to determine the final shape that the solid surface will assume as the molten pools solidify, and the effect that the crystallization process will have in this process.

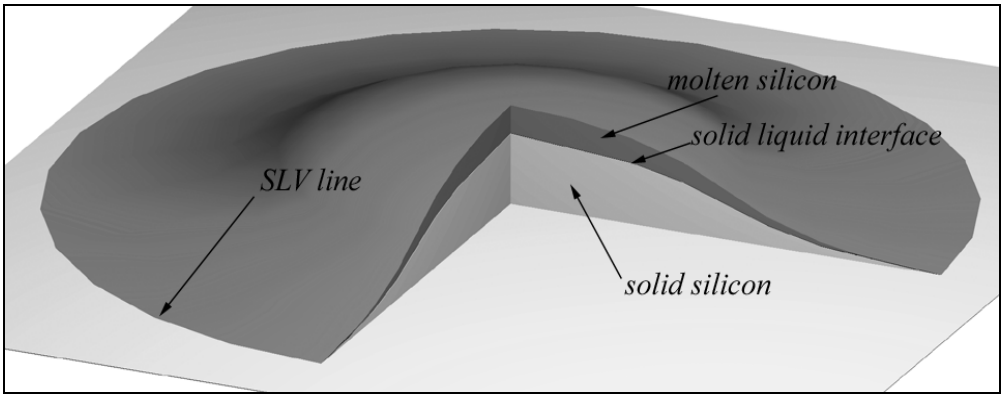

Figure 4.5. Illustration of the geometry of liquid and solid regions at the last stage of solidification

The cut-away reveals the shape of the solid-liquid interface.

The conditions under which solidification of these liquid pools occurs are unusual in that the process occurs so rapidly. The resolidification rate is about 6 m/s [47,48]. Since the depth of the molten pool region can be no larger than the amplitude of the surface waves, the last stage of solidification can be estimated to occur in the range of 2 ns to 20 ns during the early stages of the surface structure evolution. Surface tension is not strong enough to have an appreciable effect on the shape of the liquid in over its ~20 μm expanse. Under these circumstances, phase change is the only process left that can play a role and provide a means for growth. Through solidification, crystallography will play a role as the atoms move from a state of random order to one of crystalline order and there will be movement and a re-arrangement of atoms on both the atomic and macroscopic scales. Analysis of the solidification process will focus on details of the solid-liquid interface, most critical of which is the density of atoms on the surface of the interface.

4.3.1 Discussion of Atomic Densities

Much of the following discussion utilizes concepts of atomic density as way of describing crystallographic anisotropy. Three varieties of atomic density are considered: volumetric atomic density (η), which has units of m^{-3}, surface atomic density (κ) measured in atoms m^{-2} , and edge atomic density (χ) measured in m^{-1}.

Volumetric atomic density is the number of atoms per unit volume and, with the exception of small changes due to thermal expansion, is constant within a single phase. Silicon represents one of the less common materials in which the solid phase is less dense than the liquid phase. This is in part due to the fact that the diamond crystal structure is a relatively open one as a solid, having a coordination number of 4, but is slightly more compact as a liquid with a coordination number of ~5.6 [49].

Surface atomic density is a measure of the number of atoms at the surface of a crystal face. For the purposes of this analysis, this is defined as the number of atoms needed to form an epitaxial layer over a given area. The value of κ can vary significantly within a material depending on the surface orientation and can differ by as much as 40% between different surface directions in diamond crystal structures. Note that surface atomic density is a measure of the number of atoms on a surface, not the number of chemical bonds. This is not necessarily an important distinction which needs to be made for ionic or metallic crystals, but can be important in covalently bonded materials. This way of counting surface atoms implies that the values for surface density will be twice that normally found in the literature. Usually surface density is calculated by assuming that the atoms are shared between two sides of a plane thus halving the total number of atoms in a layer.

Edge atomic density is a measure of the average number of *atomic layers* encountered per unit length when moving along a vector normal to a particular crystal face. It is perhaps better to think of edge density as the inverse of the height of one epitaxial layer ($H_{(hkl)}$). The height of an epitaxial layer will be considered here to be equal to the distance from one atom to its second nearest neighbor for a particular orientation. Surface density is inversely related to edge density by the proportionality constant of volumetric density. This interrelationship leads to and is embodied in the idea of '*atomic volume elements'*, which will be useful in the discussions of epitaxial crystal growth, as it combines the concepts of crystal anisotropy, η, κ, and χ into one.

Volume elements are the building blocks of an epitaxial layer. Several volume elements along with corresponding unit cells are shown in Figure 4.6 for three different crystal orientations. The dimensions of the volume element depend on the surface to which it is ascribed. The choice of the shape is arbitrary, but for simplicity is taken to be a parallelepiped. For a given phase, the volume of the element is fixed and is equal to the volume occupied by two atoms. For solid silicon, the volume is $a^3/8$ where a is the edge length of the diamond unit cell. η is therefore $8/a^3$. The height of the volume element is equal the average height one epitaxial layer and the area of the base equal to $1/\kappa$.

A unit cell of silicon with the top face in the (100) direction is shown in Figure 4.6(a). The unit cell is 2 atomic layers tall. Each layer contains 2 full atoms, 6·¼ atoms, and 2·½ atoms. This sums to a total of 4 atoms sharing an area of a^2 resulting in $\kappa_{100} = 4/a^2$. This approach is similarly taken with the (111) and (110) directions.

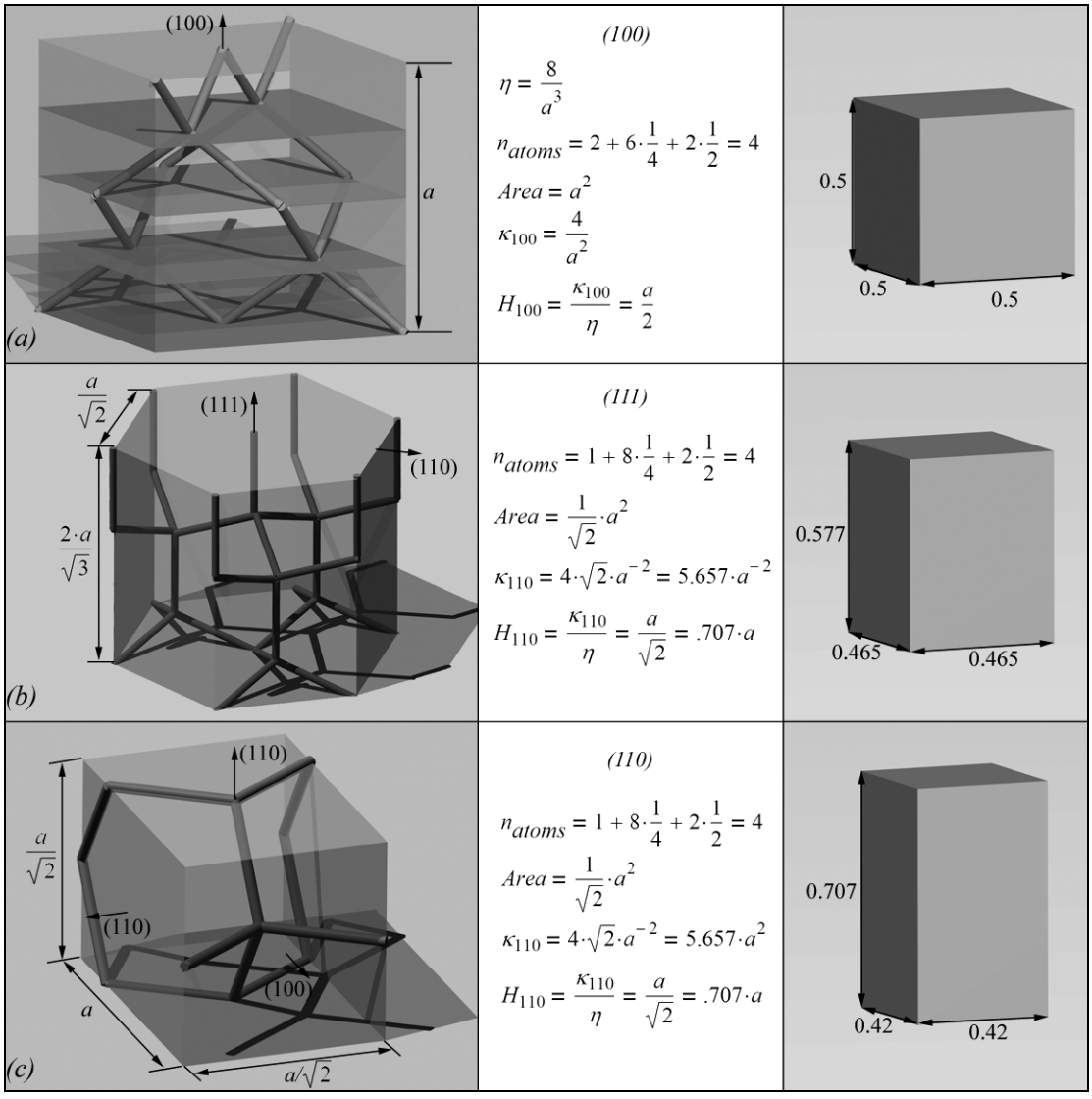

Figure 4.6 Crystal structures, surface atomic densities, and the volume elements for three crystal faces

4.3.2 *General Method for Calculating Surface Atomic Densities for all Crystal Orientations*

As part of this study, it is necessary to know more than just the surface density of three low index faces, a detailed map of surface density over all surface orientations is required. To this end, a general scheme has been devised that is based primarily on the knowledge of the bonding in silicon and less so on the locations of atoms within the unit cell.

Usually, surface density calculations involve slicing along a plane through the unit cell and counting the number of atoms intersecting that plane. For low index directions like the ones discussed above, this is simple since the planes line up with the centers of atoms. However, a slight deviation from a low index plane quickly complicates the situation since the crystal surface no longer intersects the centers of atoms exactly, except over large distances spanning many unit cells. In such cases, a question remains as to how to count atoms which are close to a plane but are not intersected by that plane.

The approach taken here sidesteps this problem by abandoning the unit cell to some degree and focusing on the coordination number and direction of atoms. In silicon, the centers of nearest neighbors to an atom locate the points of a tetrahedron around that atom. Since this study is concerned with epitaxial growth, it is only necessary to consider the orientation of this tetrahedron relative to a crystal surface to determine epitaxial step height. Because the volumetric density of a phase is constant, surface atomic density can be derived from the step height. This is to say that the distance from one epitaxial plane to the next is on average equal to the largest extent from one end of a tetrahedron to the next.

Various orientations that the silicon tetravalent structure takes relative to crystal surfaces are shown in Figure 4.7. The points of a tetrahedron are located at the centers of nearest neighbor atoms. Orientation of the tetrahedron relative to the unit cell is shown in Figure 4.7(a). Faces of the tetrahedron point in (111)-type directions, and edges point in (110)-type directions. Figure 4.7(b-d) duplicate some of what was shown in Figure 4.6 but under a different light. Where before the aim was to count directly the number of atoms on a surface, these images help to show that the same solution can be arrived at by considering the height of a rotated tetrahedron ($H_{(hkl)}$). This approach exploits the fact that surface density is equal to the height of the tetrahedron times the bulk volumetric density, $\kappa_{(hkl)} = H_{(hkl)} \cdot \eta$. By this approach, the surface density is not determined directly by counting atoms on a given surface. Rather, it is determined only through geometric considerations of the nearest neighbor atoms. This approach helps build a more intuitive sense of surface density and simplifies predictions and trends in surface density across many surface orientations. For instance, the configuration of the tetrahedron on a (100) surface is the shortest possible configuration. Therefore, the (100) surface will necessarily have the lowest surface density, see Figure 4.7(b). By contrast, there is no orientation of a tetrahedron that can be taller than that associated with the (110) surface. The (110) surface then necessarily has the highest surface atomic density(Figure 4.7(c)). The tetrahedron on a (111) surface is oriented so that one of its faces is co-planar with the surface.

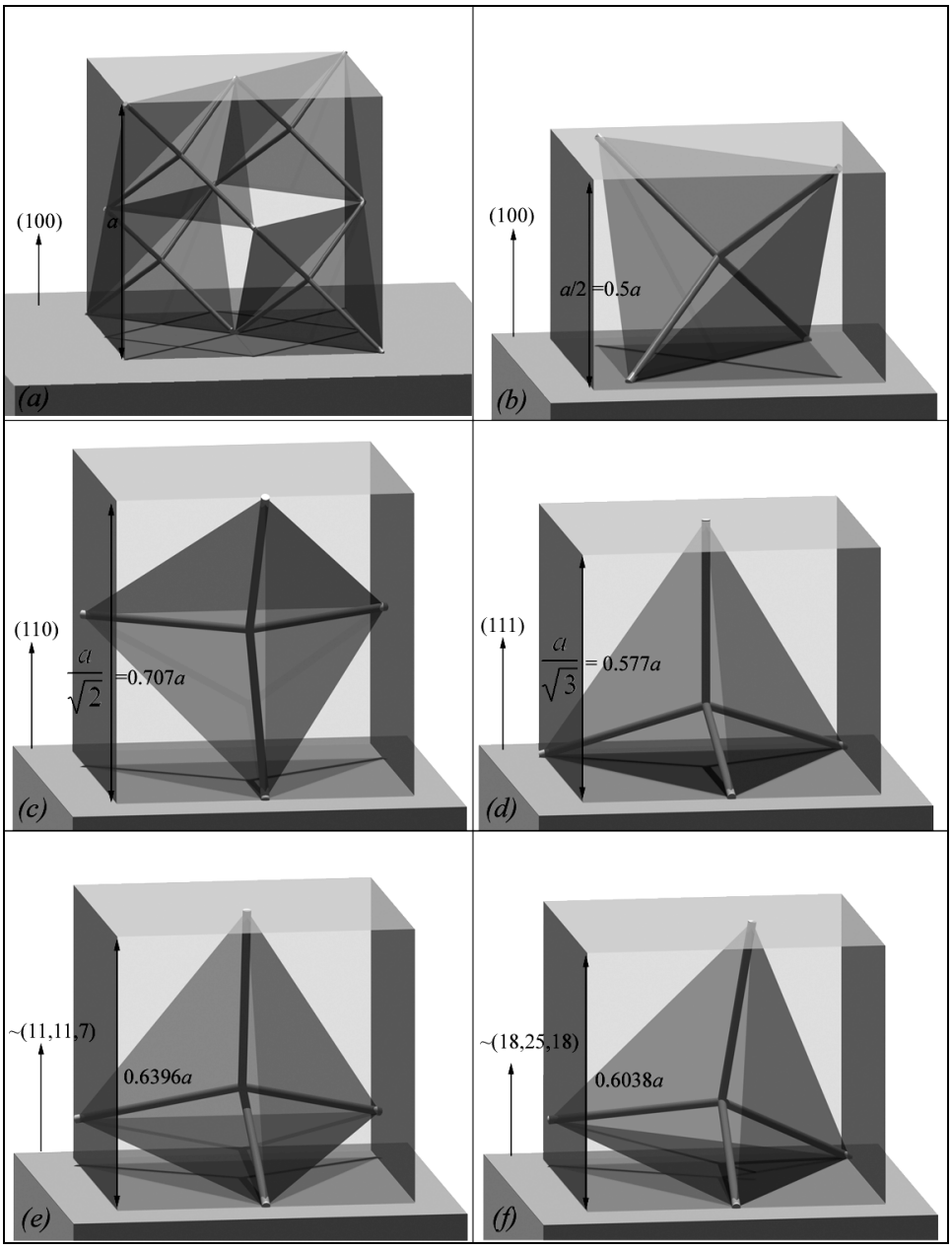

Figure 4.7. Configuration of the silicon tetravalent bonding relative to various surface orientations

The surface direction and epitaxial layer height are indicated.(a) unit cell on a (100) surface.(b-d) single tetrahedron on a (100),(110), and (111) surface respectively.(e) 10 degree deviation from the (111) surface approaching the (110) direction. (f) 10 degree deviation from the (111) surface approaching the (112) direction.

If small deviations from the (111) surface are made, the direction of these deviations can result in quite different surface densities. This is demonstrated in Figure 4.7(e-f) where the tetrahedron has been tipped relative the surface by 10 degrees, but in two different directions. If the tetrahedron is tipped towards a corner, as in Figure 4.7(e), the total height increases quickly, and so the surface density. If the tetrahedron is tipped so as to be rotated about a base edge, the total height still increases, but not as dramatically. Since there are three corners (and edges) at the base of the tetrahedron, this simple denken experiment elucidates the three fold symmetry in the proximity of the (111) surface.

A map of surface densities over all orientations based on this approach is shown in Figure 4.9 and is presented so that the axes of the map correspond to the 1st and 2nd Euler rotation angles as defined in Figure 4.8. The map is centered about a (100)-type surface and the location of several low index surfaces are indicated as well. Their relative surface densities can clearly be seen as well as the kinds of symmetry which exist in the vicinity of these directions. The (110) surface is the most dense and possesses virtually no symmetry. The (112) surface is less dense and exhibits two fold symmetry. As discussed previously, there is strong three-fold symmetry in planes close to the (111) surface. There is four-fold symmetry about the (100), but it is not as prominent as the (111) case.

The ratio of surface densities between the crystalline and molten phases is an important factor to consider when describing the solid-liquid interface. A discussion of liquid surface density will follow, but as a preview, a contour line outlining κ_l is also shown in Figure 4.9. This line divides crystal surfaces with atomic densities larger than that of the liquid from ones which have smaller surface densities.

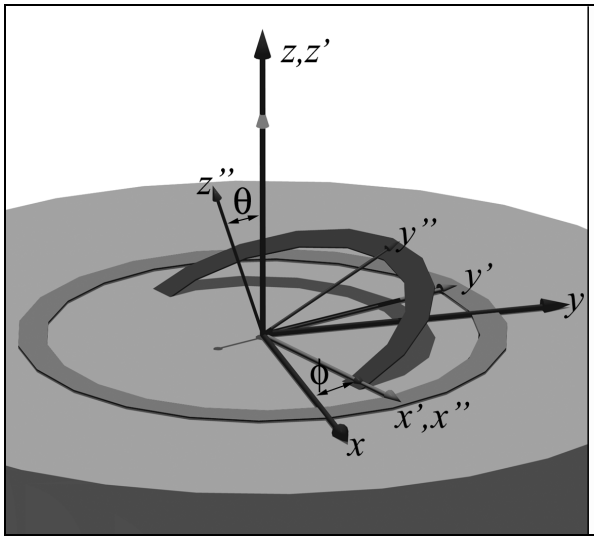

$$R_z(\phi) = \begin{pmatrix} cos(\phi) & sin(\phi) & 0 \\ -sin(\phi) & cos(\phi) & 0 \\ 0 & 0 & 1 \end{pmatrix}$$

$$R_x(\theta) = \begin{pmatrix} 1 & 0 & 0 \\ 0 & cos(\theta) & sin(\theta) \\ 0 & -sin(\theta) & cos(\theta) \end{pmatrix}$$

$$R(\phi,\theta) = R_x(\theta) \cdot R_z(\phi)$$

Figure 4.8. Diagram and equations of Euler rotation angles

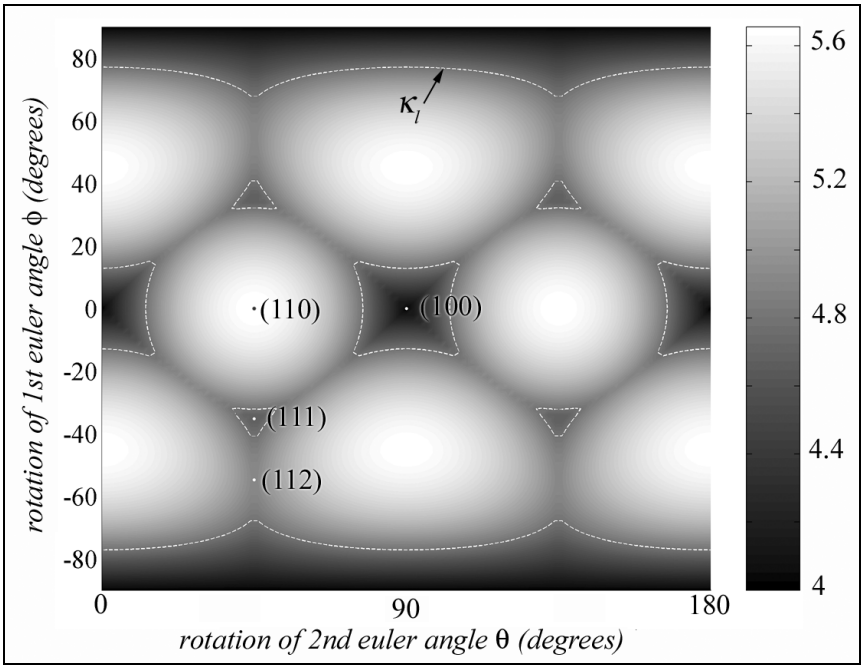

Figure 4.9. Surface atomic density map of crystalline silicon for all crystal orientations

Data is scaled in units of a^{-2} where a is the edge length of the unit cell. The surface density of several low index faces are indicated. The dotted contour line indicates the surface density of liquid silicon.

4.3.3 Surface Atomic Density of Molten Silicon

The strict geometric approach used in determining κ for solid surfaces is not applicable to the short-range order of atomic arrangements of the liquid phase. Fortunately, there has been a fair amount of both experimental and computer based molecular dynamics study to provide useful information about the atomic structure which does exist[50-54]. Liquid silicon possesses several interesting properties that do not exist in most molten metals. The liquid does not have a close-packed structure, but instead appears to retain some of the tetrahedral characteristics of the solid phase mixed with a cubic-type structure. This hybridization is evident in the nearest neighbor coordination number which ranges between 4.6 and 6.2. There are also indications that molten silicon can undergo a first-order liquid-liquid phase transition at low enough under coolings[52].

Waseda et. al.[54] have performed X-ray diffraction analysis on molten silicon and have determined the structure factors, pair-correlation functions, and the interference functions of the liquid-phase at several temperatures near the melt temperature. The pair-correlation is derived from the structure factor and provides a histogram of the average number of atoms which can be found at a given distance from a central atom. The interference function is a further refinement of the pair-correlation function and has been applied

to distinguish between closely spaced atoms into subsets of 1st, 2nd , and 3rd nearest neighbors etc.. The results of this work by Waseda show that the 1st and 2nd nearest neighbors in liquid silicon are on average a distance of 0.245 nm and 0.288 nm from a central atom respectively.

Previously, the height of an epitaxial layer in a solid was defined as the distance from an atom to its second nearest neighbor perpendicular to a specified crystal surface. In keeping with this definition, the average height of a layer of atoms in the liquid is also taken to be the distance to the second nearest neighbor so that H_l = 0.288 nm. The gives a liquid surface atomic density of $\kappa_l = \eta_l \cdot H_l$ = 16.06 nm^{-2} = 4.79$\cdot a^{-2}$.

4.3.4 Accounting of Atoms at the Solid-Liquid Interface

As a first step in the development of a model to predict the end result of solidification of the system in Figure 4.5, a highly simplified, discretized representation will be used. This cartoon is not necessarily realistic but in its simplicity it serves to present two important points: the final shape of the solid is determined by the *initial shape of the liquid*, and more importantly by the *difference in surface atomic densities between the liquid and the solid phases.* The epitaxial crystallization process will act to redistribute mass so that, for the same initial shape of the liquid, the final shape of the solid will depend on the crystal surface on which it has crystallized.

The first example will step through epitaxial growth on a (110) type surface meaning that the solid surface is relatively dense and therefore the volume element of the solid is tall and slender. The initial shape of the liquid is a square based pyramid shown in Figure 4.10(a). The SLV line fixes the area of the SL interface for a given atomic layer. When the first layer solidifies, a consequence of surface density difference between the two phases becomes clear. κ of the solid is greater and requires more atoms to fill the area of the interface than the first layer of the liquid atoms alone can provide. For this example, the comparison of the first solid and liquid layers is shown in Figure 4.10(b). The liquid base is a square of 10X10 atoms, and for that same area, the crystal requires 12X12 atoms. There is a deficit of 44 atoms and unless a void should form, the required atoms will be absorbed from a liquid layer above. The equal sign in the figures represent equivalence in the number of atoms.

The second layer of liquid consists of 8X8 atoms. This is enough to fill in the rest of the first layer of solid with 20 atoms remaining. Figure 4.10(c) shows a fully formed first solid layer and the number of atoms needed from the liquid in order to fill it. The dark blocks represent the second layer liquid atoms that have been absorbed into the first solid layer.

This line of reasoning can be followed with subsequent layers. In order to maintain the same surface area, 20 atoms of the second liquid layer will become part of the second solid layer, the remaining again will need to come from liquid atoms above. The third layer of liquid can provide 6X6 atoms, the forth will give 4X4 and the fifth can offer 2X2. There are not enough atoms in all of the liquid to complete the

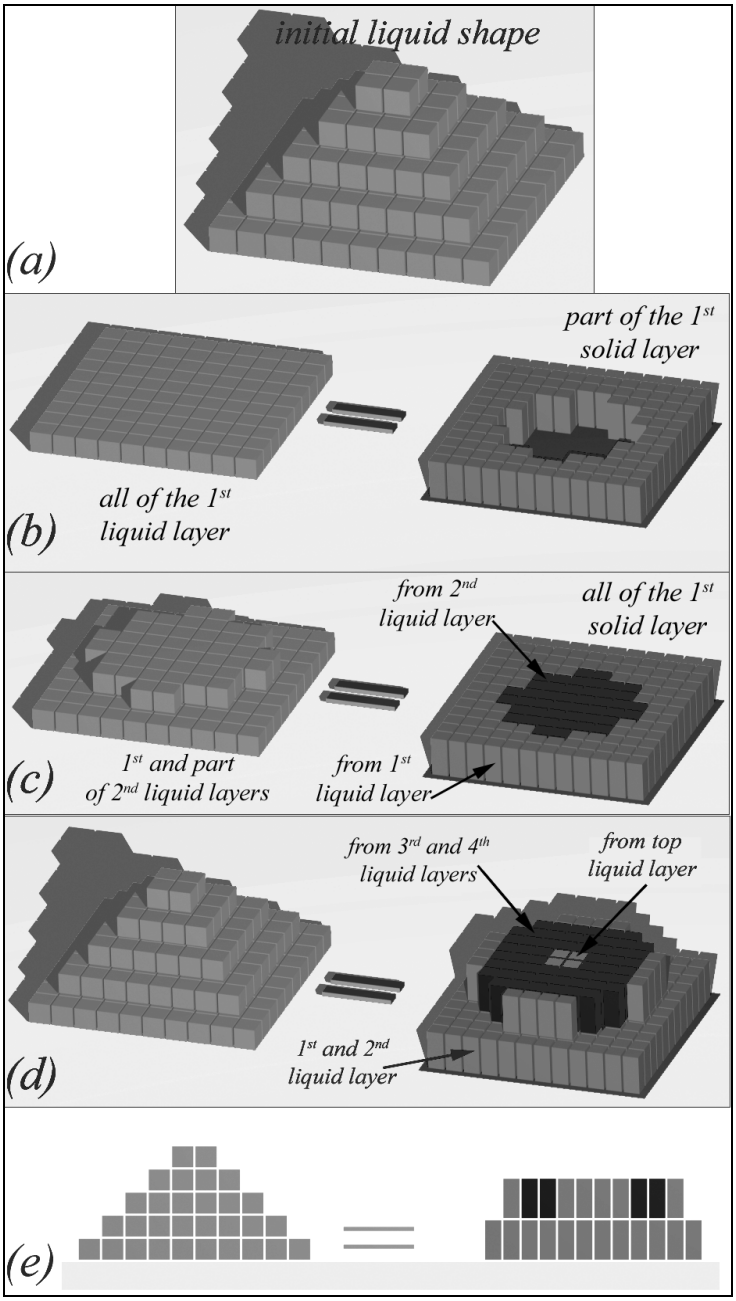

Figure 4.10. Volume element representation of epitaxial solidification on a (110) surface

Atoms in the liquid state are represented by lightly shaded cubes, atoms in the crystal state are represented by tall parallelepipeds. Equal sign implies same number of atoms. (a) initial shape of the liquid, (b-c) formation of first solid layer, (d) final shape of the solid compared to initial liquid shape, (e) profile of results in (d).

second solid layer, and solidification terminates after two atomic steps as shown in Figure 4.10(d). A side view of the initial and final shapes are shown in Figure 4.10(e). Despite the fact that there is volumetric expansion under solidification, the overall height has decreased. This decrease occurs as a result of the interplay between initial liquid geometry and surface atomic density difference.

Profiles of the final shapes due to epitaxial crystallization of two different initial liquid shapes on two differently oriented substrates are shown in Figure 4.11. In Figure 4.11(a), the initial liquid shape is a pyramid like the one in the previous example. The ultimate height of the solidified structure on (110) is smaller than the initial height of the liquid because the surface density of the solid is greater than that of the liquid. However for the same initial conditions, growth on the (100) surface results in a final height that is greater than the initial. This due in part to the fact that $\kappa_{100} > \kappa_l$. For each new layer that solidifies, there will be an *excess* of atoms in the liquid state present at the SL interface than will fit into the solid (100) layer, so the liquid is pushed higher with each solidified layer.

In Figure 4.11(b), the initial shape of the liquid has a constant cross-sectional area. Under these conditions, any difference in surface atomic density is ultimately cancelled out by the volumetric density so that at the end of solidification, the height of the solid will always be greater by the ratio of η_l/η_s. The reason why surface density can have an effect as illustrated in Figure 4.11(a) is that a change in volume of the liquid that occurs with each crystallizing layer results in a change in shape of the remaining liquid. In

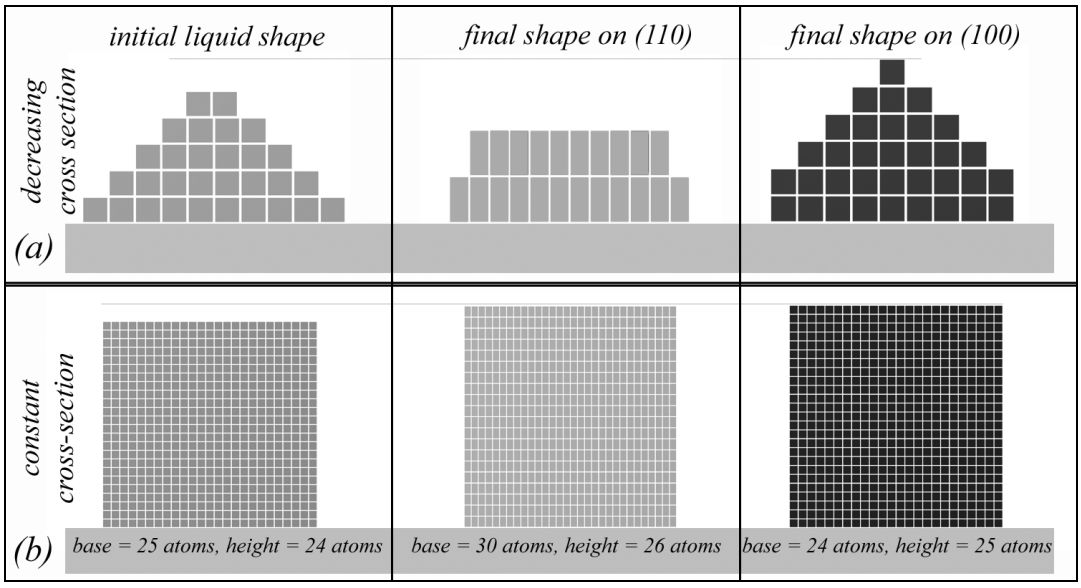

Figure 4.11.Volume element epitaxial growth for two different initial liquid shapes

Figure 4.11(b), the area of the SL interface is constant throughout the solidification process, and the slope of the sides remains the same throughout the solidification process. The size of the base and the total mass is the same before and after solidification. The number of atoms on the base changes and there is still a rearrangement of atoms as a consequence of crystallography, but this occurs absent a change in overall morphology.

4.3.5 A Continuum Model for Solidification

A continuum model based on the same principles as discussed above has been formulated. Where the discrete model was used to illustrate the relevant concepts more clearly, the continuum model simulates the solidification process more accurately. The discrete model was concerned almost exclusively with properly accounting for mass crossing the SL interface. The continuum model is just as rigorous in this regard, but also takes into account the changing shape of the liquid during the process. Again the purpose of this is to step more closely towards a method to predict the final geometry given the initial conditions represented in Figure 4.5. However, a more simple initial geometry, that of a cone of liquid on a flat surface, will be used and is shown in Figure 4.12 with a quarter removed revealing the cross-section.

The initial shape of the liquid is defined by a line with and initial slope, y'_o , and base radius , r, revolved about the y-axis. At any stage during solidification, the geometry of the liquid above the interface is permitted to change in order to accommodate the change in its volume resulting from the surface atomic density mismatch between phases. As before, it is assumed that gravity and surface tension forces have a negligible influence on morphology in this last stage of solidification. Instead, the change in volume and

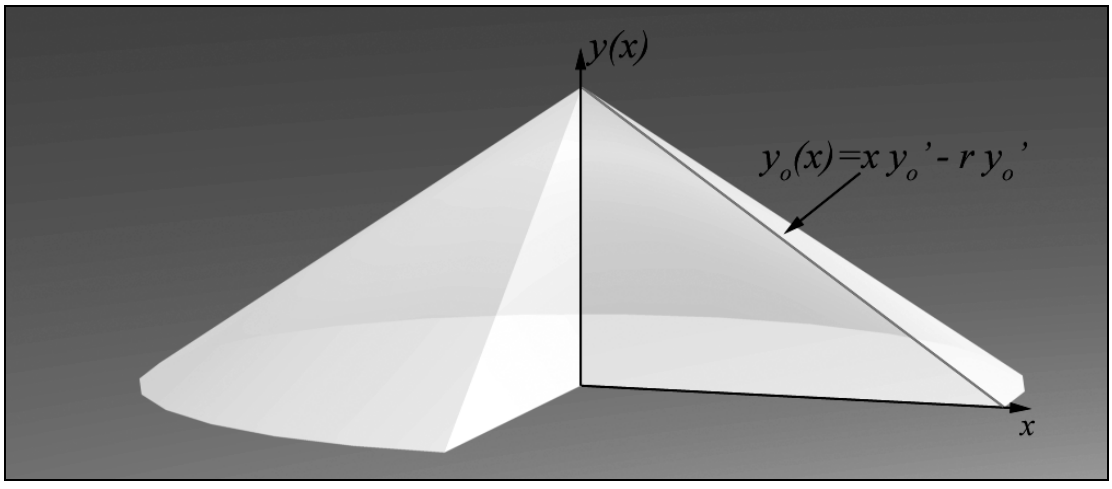

Figure 4.12. Initial shape of a liquid cone on a flat, solid surface.

shape of the liquid will be accounted for simply by changing the slope of the line that defines the LV interface. The slope will therefore be made a function of x. The goal of this derivation is seek to determine $y'(x)$, the slope of the liquid at the SLV line, and then finally $y(x)$, which is the final shape of the solid and maps the trajectory of the SLV line, as they are shown in the equation below.

$$y(x) = x \cdot y'(x) - r \cdot y'_o$$

equation 4.10

Upon solidification, the interface will advance a differential amount Δy. The differential volume element which is undergoing phase change is defined by the previous and current positions of the interface and the previous radius of the cone. For this small advance in the y-direction, there will be an advance inward, Δx, of the SLV line as it follows the liquid-vapor interface as shown in Figure 4.13. Because of density mismatches, there will be a difference in the number of atoms in the liquid state that occupied this differential volume before solidification and the number of solid state atoms that occupy it afterwards. Important distinctions between volumetric atomic density and surface atomic density must be made at this point. As discussed earlier in the simple building block model, differences in surface atomic densities at the interface between the two phases must be reconciled by transfer of liquid atoms across the interface. If the solid has a lower surface density, more atoms than are needed will be present at the interface, so they will be pushed further into the liquid. If the solid has higher surface density, atoms from deeper within the liquid will have to be used to fill in the layer. This derivation will assume the latter case, but the final solution will be general and can accommodate either case.

The differential volume is found by assuming that it is a cylinder with radius x and height Δy.

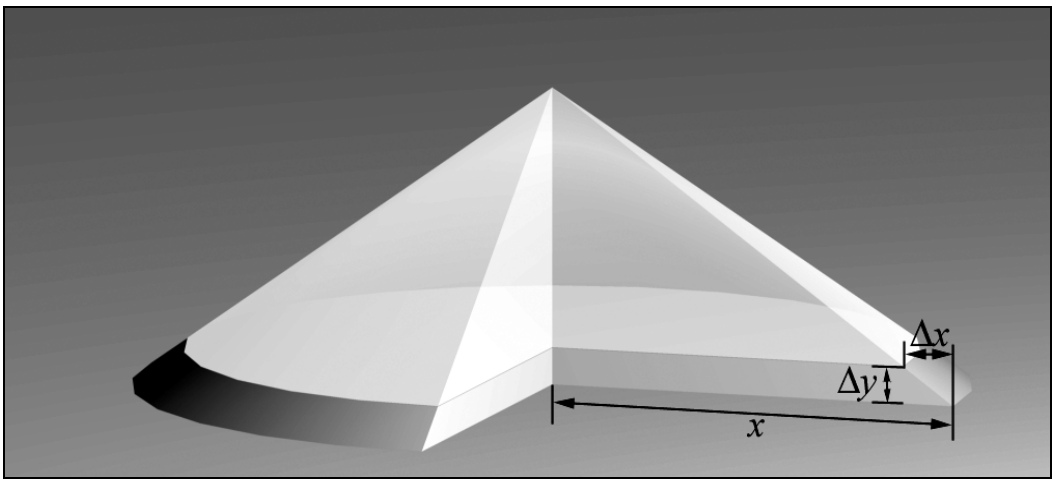

Figure 4.13. Solidification of the first infinitesimal layer

Ignoring the slope at the perimeter at this point is acceptable since the limit as Δx approaches zero will eventually be taken and including this small feature does not change the final solution. The volume, V, undergoing phase change at this point is given by equation 4.11 where it is expressed in terms of slope. The number of atoms in the liquid state, M_l, that occupy this volume is determined from volumetric density using equation 4.12.

$$V = \pi \cdot \Delta y(x) \cdot x^2 = \pi \cdot y'(x) \cdot \Delta x \cdot x^2$$

equation 4.11

$$M_l = \eta_l \cdot V$$

equation 4.12

Greater care has to be taken for the solid. Crystallographic information does not fit naturally into this continuum approach. But, the anisotropy inherent in the crystal structure can be artificially imposed by considering that Δy for the liquid means something different than Δy for the solid. For instance, a layer of atoms in the liquid is shorter than a layer of atoms in the solid for Si (110), but the surface density of atoms in the solid is larger than that for the liquid. The information on *surface density* has to be separated from information on *atomic step height, h*, in order to use this differential equation approach. One way to do this is to allow Δy to be different for the solid by the ratio of atomic step heights of the solid and liquid so that.

$$\Delta y_S = \Delta y \cdot \frac{h_s}{h_l}$$

equation 4.13

Using equation 4.13 to calculate the number of atoms needed to complete a solid layer, M_s, gives,

$$M_S = \eta_S \cdot \Delta y_S \cdot \pi \cdot x^2 = \frac{\kappa_S}{h_s} \cdot \Delta y_S \cdot \pi \cdot x^2 = \frac{\kappa_S}{h_s} \cdot \left(\Delta y \cdot \frac{h_s}{h_l} \right) \cdot \pi \cdot x^2 = \frac{\kappa_S}{h_l} \cdot y' \cdot \Delta x \cdot \pi \cdot x^2$$

equation 4.14

This approach can be thought of in the following way. In reality the heights of the atomic layers are different, it is not possible to consider this fact now, so it will be assumed that $h_s = h_l$ for the time being. This contrivance is added to give the continuum expressions their needed discrete characteristics which will be accounted for again at the end of the derivation.

The phase change within the differential volume will result in atoms being absorbed from the liquid above the new interface. The volume of the liquid due to the surface density considerations will change by an amount ΔV_κ and is determined by the equation below.

$$\Delta V_{\kappa} = \frac{-M_s}{\eta_l} = \left(\frac{-\kappa_s}{h_l} \cdot y' \cdot \Delta x \cdot \pi \cdot x^2 \right) \cdot \frac{1}{\eta_l} = \frac{-\kappa_s}{\kappa_l} \cdot y' \cdot \Delta x \cdot \pi \cdot x^2$$

equation 4.15

Changing the volume of the liquid necessarily changes its shape. It is assumed that the liquid will remain conic, it will maintain the same radius at the base, but the slope of the LV interface will be allowed to change. No attempt has been made to model how the shape of a free standing cone of liquid will change when there is mass transfer through its base, but the assumption that the liquid will remain conic in shape is equivalent to assuming that the stream lines within the liquid all emanate radially from the cone tip. The liquid shape change is depicted in Figure 4.14 where clearly an advance of the solid-liquid interface results in a change in slope of the liquid-vapor interface.

Calculating the new slope is relatively simple. The volume of the conically shaped liquid above the SL interface in terms of slope before and after solidification are V_1 and V_2 respectively, and the change in volume due to this change in geometry, ΔV_G, is the difference between the two.

$$(a)\quad V_1 = \frac{\pi}{3} \cdot y'(x) \cdot x^3 \qquad (b)\quad V_2 = \frac{\pi}{3} \cdot y'(x + \Delta x) \cdot (x + \Delta x)^3 \qquad (c)\quad \Delta V_G = V_1 - V_2$$

equation 4.16

Equating the ΔV_{κ} with ΔV_G and solving for $y'(x + \Delta x)$ gives a description for the change of slope.

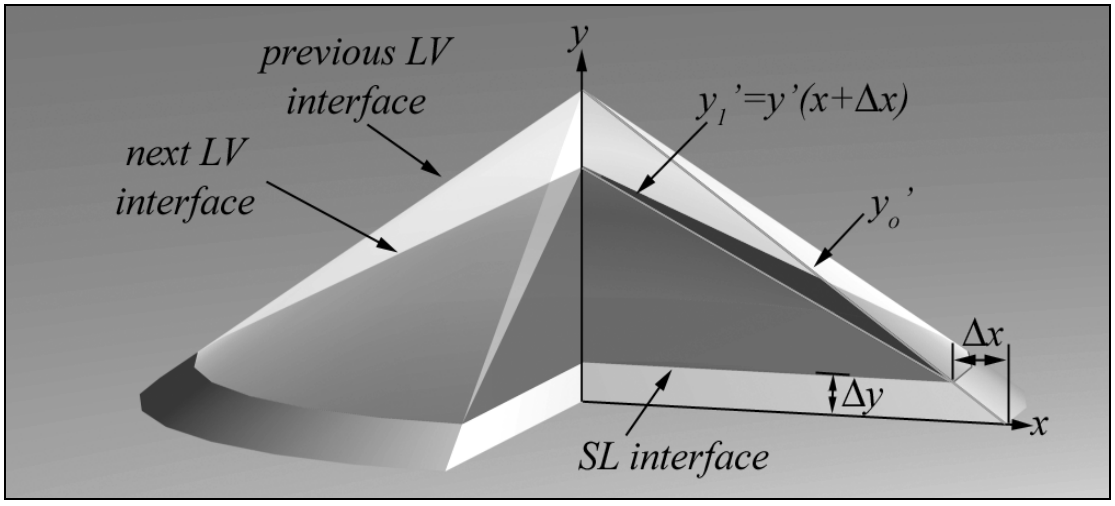

Figure 4.14. Change in the volume and shape of the liquid due to SL interfacial advance

$$y'(x + \Delta x) = -y'(x)\cdot x^2 \cdot \frac{\left(3\cdot \kappa_S \cdot \Delta x - x\cdot \kappa_L\right)}{\left[\kappa_L \cdot (x - \Delta x)^3\right]}$$

equation 4.17

A differential equation can be formed by inserting equation 4.17 into the definition of a derivative and taking the limit as Δx approaches 0. This differential equation and its closed form, exact solution are given in equation 4.18. Further details on the solution process are given in Appendix 4.

$$(a)\quad y''\cdot x = q\cdot y' \;,\quad (b)\quad q = 3\cdot\left(\frac{\kappa_S - \kappa_l}{\kappa_l}\right),\quad (c)\quad y(x) = \frac{y'_o \cdot x}{(q+1)}\cdot\left[\left(\frac{r}{x}\right)^{(-q)} - \frac{r}{x}\right]$$

equation 4.18

The derivation is not quite yet complete however. It is necessary to redress the assumption in equation 4.13. The heights of the atomic layers are in fact different; this will be accounted for by inserting a multiplicative factor into equation 4.18(c). Again, the difference in the height of the atomic layers for the two phases was ignored to facilitate the accounting of surface density differences. Doing this violated mass conservation, but this violation has been corrected for in this final step.

$$y(x) = \frac{h_s}{h_l}\cdot\frac{y'_o \cdot x}{(q+1)}\cdot\left[\left(\frac{r}{x}\right)^{(-q)} - \frac{r}{x}\right]$$

equation 4.19

This equation has been applied to the solidification of silicon with the results shown in Figure 4.15. The surface density of the crystal can clearly have a profound effect on the final shape that the solid assumes. The ultimate purpose of this derivation is to assess the potential for perturbation growth as it relates to substrate crystal orientation. These results indicate that whatever perturbation might have existed before melting on a (110) surface will tend to be reduced at the end of the solidification cycle. This implies that successive laser shots will tend to smoothen a (110) surface.

Perturbations on a (100) surface, in contrast, possess the potential for growth since the final height of the solid is greater that that of the liquid. This is not a proof of an instability yet since the ultimate criterion for growth lies in whether the perturbations are made taller after consecutive laser pulses. The capacity for perturbation growth arising from end stage solidification must be greater than the capacity for surface tension to reduce the amplitude of perturbations in the intervening melt cycle.

The results in Figure 4.15 predict that (111) surface perturbations will not increase in height from pulse to pulse. This is contrary to experimental findings, but the following section will show this to be a consequence of the chosen initial liquid shape. Figure 4.16 shows in greater detail the intermediate steps in solidification and follows the process through its conclusion.

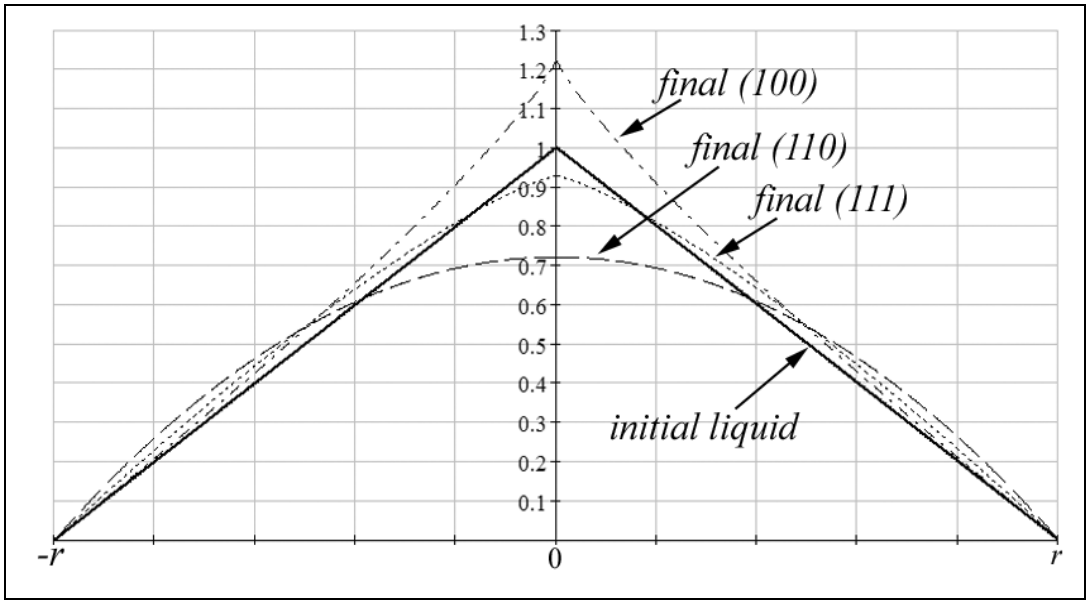

Figure 4.15. Results of applying equation 4.19 to a liquid silicon cone solidification.

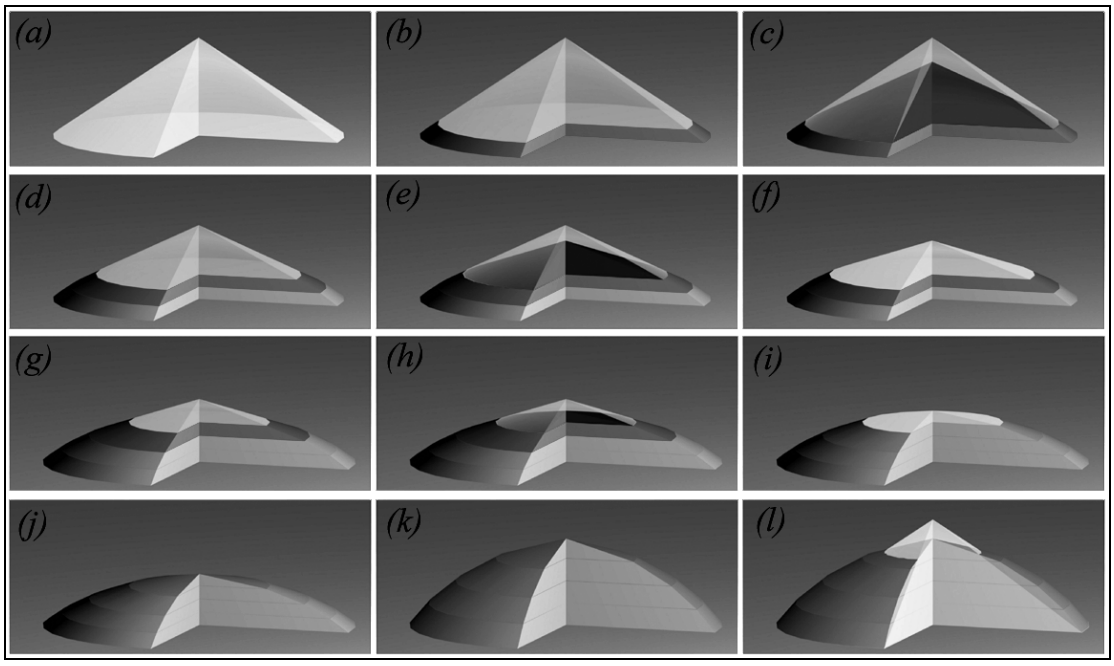

Figure 4.16. Solidification process of a liquid cone on a crystalline surface

In this example, the surface density of atoms of the solid is larger than that of the liquid. (a) The original shape of the liquid in contact with the crystalline surface below. (b) Solidification initiates with a thin layer of atoms changing phase as epitaxial solidification begins. (c) Because of the mismatch of surface atomic density between the liquid and the solid at the interface there will be a requisite volume change the liquid. The shape of the remaining liquid will change to reflect this change in volume to what has been assumed to be a cone with the same radius but a different height. The new volume is shown as a dark region within the lighter shaded previous volume. (e) The next step of solidification will follow the shape of this new liquid cone. The new liquid cone has sides which are less steep, so the slope of the solid-vapor interface will reduce as solidification proceeds. (f-k) This process continues in a similar way - as the interface advances upward, slope changes, and the to solid-vapor interface follows this change. (l) This model has, up to this point, been ignoring the difference in atomic step heights, and for this reason the difference in volumetric atomic density. Frame (i) represents the inclusion of this difference. The amplitude of the solid in (k) is increased so that mass is conserved. Frame (m) shows a comparison of the original liquid cone and the final solid..

4.3.6 The Solidification of General Shapes

A similar derivation of a general equation to describe the crystallization of sinusoidal shape, instead of a cone, on a flat surface was performed, but no exact solution could be found, see Appendix 5. The attempt to even find an equation to describe the freezing of a sinusoid on a curved surface, like the one in Figure 4.5, proved fruitless. A program was therefore written that employs the same concepts, but is general enough to handle any reasonable initial SL and LV interface morphology. This program also includes the effects of capillary forces and thermal diffusion on the SL and LV interfaces, and the equations describing these effects have been generalized so that they too can handle any reasonably shaped initial surface. This program can be set into a feed-back cycle so that the results of the solidification can be input as the initial conditions for capillary and thermal diffusion processes. This allows the evolution of surface structures to be modeled over multiple laser pulses. The code is provided in Appendix 8-12.

This computer program has been used to predict the increase in amplitude from one pulse to the next for a range of melt times and wavelengths. The wavelength that results in the largest increase in amplitude from one pulse to the next is considered to be the one which will populate the surface after laser irradiation.

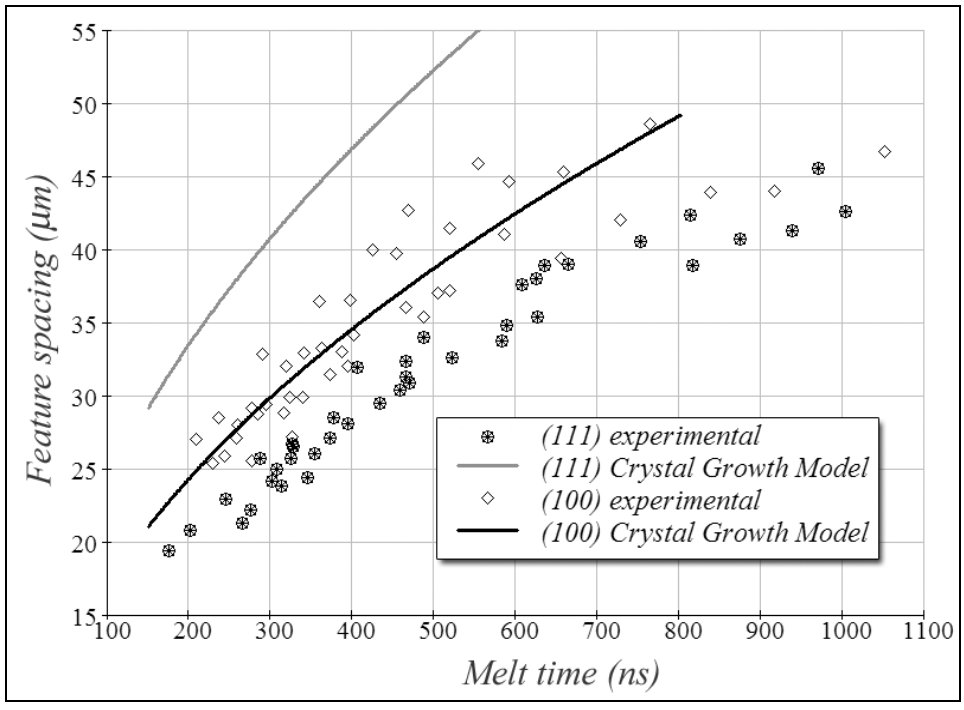

Figure 4.17. Results of modeling growth of sinusoidal surface perturbations

The results of this computer model are shown in Figure 4.17 and demonstrate that there is excellent agreement between the measured and expected wavelengths on the (100) surface. However, with all other parameters being the same, the model, as it stands, is a poor predictor experimental results on the (111) surface and grossly overestimates the feature spacing. It so happens that the (111) interface of a diamond crystal possesses some properties unique among the crystal directions. The most important of which is exhibited in the fact that (111) solid-liquid interface is the only one that facets during solidification. If this phenomenon is factored in along with a correction that accounts for the three-fold symmetry of the surface features, then a reasonable agreement can be found between the model and experiments.

4.3.7 Faceting of the (111) Interface During Solidification

The velocity at which a solid-liquid interface advances during solidification depends in large part on how the distribution of temperature evolves in time. However, variations in the atomic configuration of different solid surfaces can introduce anisotropies in solidification rates. One notable trait of the (111) surface is that the large atomic bond density. In referring to Figure 4.7(d) (p. 4.82), one can see that the atom at the center of the tetrahedron is connected to the surface through three atomic bonds. All other surfaces require no more than two. This means that during solidification, the addition of a new (111) atomic layer requires that a relatively large amount of energy be provided to form the bonds. This larger energy barrier is exhibited macroscopically in the fact that a larger undercooling of the (111) interface is needed in order to achieve the same interfacial velocity as compared to other crystal directions. The effect on the atomic scale is more striking in that the manner in which new atomic layers are formed is quite different. Interfacial advance occurs through a single nucleation event on the coldest part of the (111) interface followed by the rapid expansion of this nucleus parallel to the (111) surface. It is, energetically speaking, ten times more favorable to add an atom to the step edge of an expanding nucleus than to attach an atom to a smooth (111) surface[55].

The model so far is predicated on the assumption that the SL interface follows the shape of the melting temperature isotherm, which means that the shape of the interface can be predicted entirely by knowledge of the temperature distribution. This assumption is adequate for the (100) surface and for nearly any other direction as well. But, since the spreading or lateral velocity of nuclei on the (111) surface, $V_{x,111}$, is different than the velocity normal to the (111) surface, $V_{z,111}$, there is no longer any guarantee that the interface will follow isotherms. This can be demonstrated through closer examination of these two velocities.

Jackson et.al.[55] have performed Monte-Carlo based molecular-dynamics (MD) simulations of the solid-liquid interface of silicon over a range of interfacial undercooling temperatures in order to quantitatively determine interfacial velocities in the Czochralski growth rate regime. The authors do present data however that suggests their results are adequate to undercooling temperatures of at least 20 ºC, implying that these results are applicable to solidification rates occurring after pulsed laser melting.

Equations relating velocity to undercooling are given in equation 4.20 and plotted in Figure 4.18. $V_{z,100}$ is the velocity perpendicular to the (100) face, ΔT is undercooling (ºC), H_{111} is the atomic level step height of the (111) surface. Velocities are in m/s.

(a) $$V_{x.111}(\Delta T) = 2.16\,\Delta T$$

(b) $$V_{z.100}(\Delta T) = 0.864\,\Delta T$$

(c) $$V_{z.111}(\Delta T) = H_{111}\cdot\left[8.4\cdot 10^{26}\cdot exp\left(\frac{-140}{\Delta T}\right)\cdot\left(2\cdot V_{x.111}(\Delta T)\right)^2\right]^{\frac{1}{3}}$$

equation 4.20

Experimental measurements of the interface temperatures during resolidification after pulsed laser heating show that undercooling for flat (111) substrates is around 35 K, and 18 K for (100) substrates. However, the melt time is independent of the interfacial direction, with a melt speed of 10 m/s and solidification rate of 6 m/s regardless of crystal orientation[47,48]. This means that during solidification in a flat (111) substrate, the interface moves at the same speed but is positioned on an isotherm slightly farther from the melt temperature isotherm as compared with any other orientation. It should be noted that the

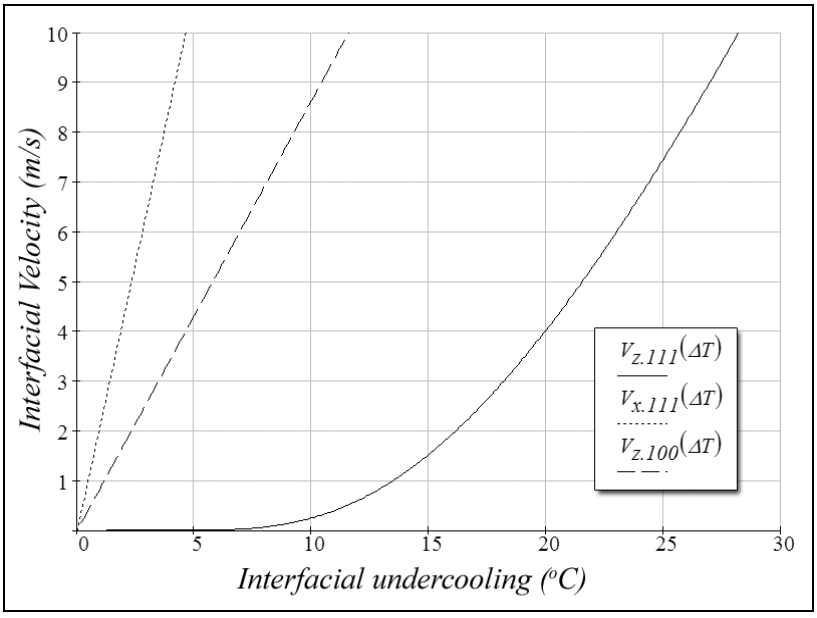

Figure 4.18. Plots of the velocity of the interface velocity as a function of undercooling

equations of Jackson overestimates the speeds of the different interfaces, but appear to be accurate in estimating the relative solidification rates between different interfaces. In order to achieve a solidification rate of 6 m/s using equation 4.20, an undercooling of 23 K is required for the (111) interface and 7 K for the (100) interface. Since the relative velocities of interfaces are important to this study, the error in absolute temperature estimates is acceptable.

It is well known that silicon will facet on the (111) interface during solidification because of its relatively slow solidification velocity. The same mechanisms that brings about faceting in more common solidification processes are at work here, but they will operate somewhat differently owing to the sinusoidal character of the thermal field. Figure 4.19(a) shows a diagram of the typical solid and liquid geometry and the thermal field within the liquid in this study. The stepped edge of the interface exaggerates the actual atomic step sizes but helps to illustrate the idea that a difference between the vertical and lateral velocities can, with time, significantly affect the shape of the solid liquid interface. $V_{z,111}$ and $V_{x,111}$ are both functions of the local temperature but their dependencies on temperature are quite different. This diagram also makes clear that the shape of the interface provides many ledges on which lateral growth can occur compared to a perfectly smooth surface.

In this analysis it is assumed that the whole interface initially follows the isotherm 23 K below the melting temperature. At this temperature the velocity in the vertical (111) direction is 6 m/s, but the lateral velocity is much larger with $V_{x,111}$ = 50 m/s. Rapid solidification laterally increases the width of the interface everywhere, but what is perhaps more important is that, since the isotherms are corrugated, this lateral motion brings the interface into a higher temperature region. In this higher temperature region, the undercooling is not large enough to support a vertical growth rate of 6 m/s, and this part of the interface will slow relative to the peak of the interface.

Figure 4.19(b) shows the results of estimating the evolving shape of an interface in time for conditions approximating those in this study. The thermal gradient in the z-direction in the liquid G_z is 25 K/μm. This value has been calculated using the same model for laser melting described in section 4.1. The amplitude of the interface is 100 nm and the wavelength is 20 μm. The vertical displacement of the peak of the interface at each time step has been subtracted away so that each of the curves are shown to share the same peak position. This simulation was run up to 400 ns and the intermediate interface shape is at 40 ns intervals. For this particular wavelength it appears that the steady-state interface shape is achieved after approximately 200 ns. The solidification time, over which these faceting mechanisms can operate, is about 2/3 of the total melt time. It is usually the case that the interface reaches its steady-state shape within the allotted solidification time. Figure 4.19(c) shows the results of growth in a steeper thermal field.

Clearly, the relatively high rate of lateral growth has acted to fill in the valleys between neighboring structures. This effectively reduces the amplitude of the solid-liquid interface roughness. Where before, the amplitude of the SL interface was assumed to only be affected by thermal diffusion,

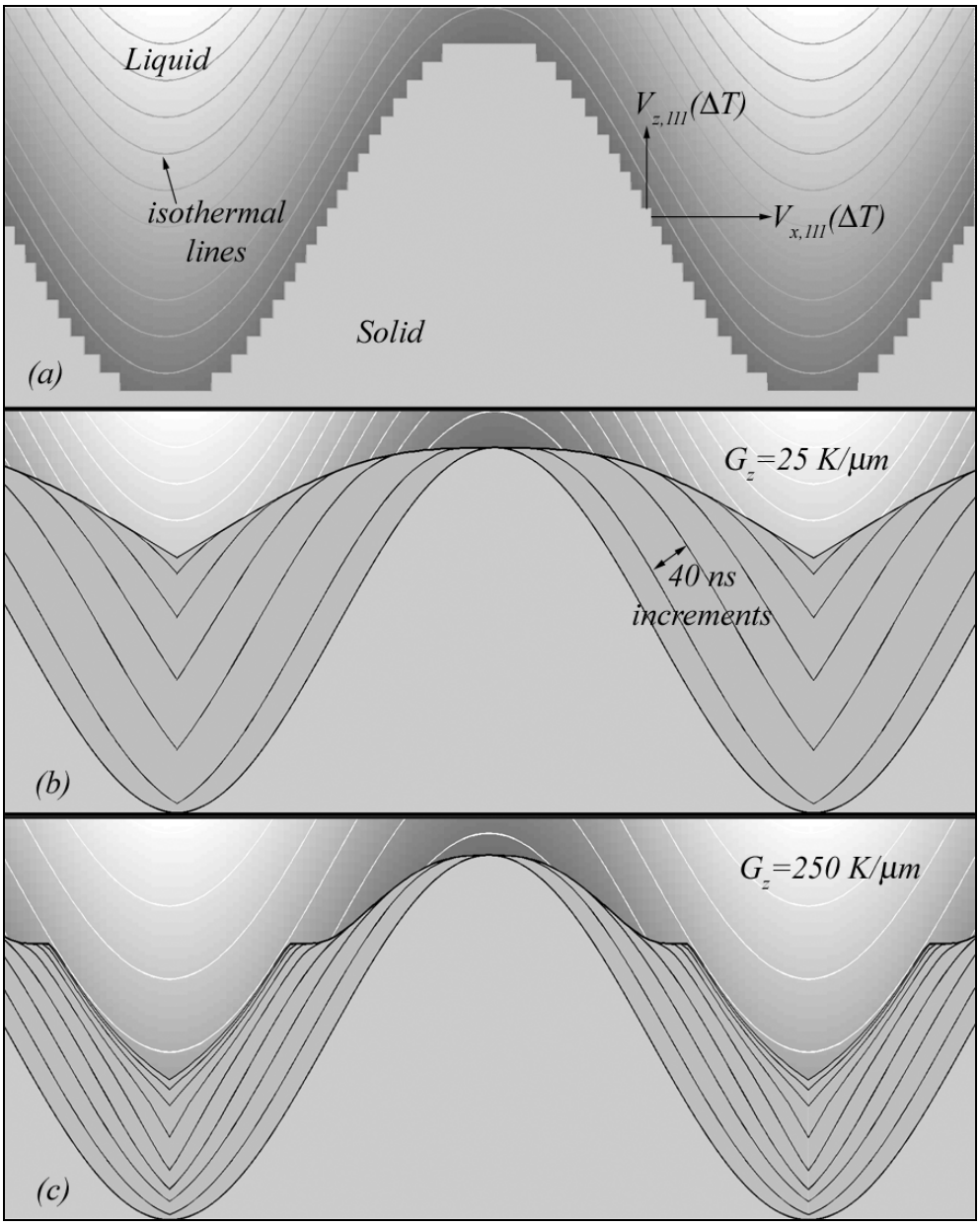

Figure 4.19. Illustrations of the effect of (111) faceting during solidification in a wavy thermal field

(a) Initial state of the interface is which it follows the shape of an isotherm. The stepped surface represents atomic steps.(b) The resulting change of shape of the interface in time as difference in vertical and lateral velocities take effect in the thermal field. (c) same as (b) except in the presence of a steeper vertical thermal gradient.

faceting effects have demonstrated a strong influence on the interface that is nearly 2.5 times that compared to thermal diffusion. With all other parameters the same, a smoother SL interface will tend to favor the growth of surface structures with shorter wavelengths. It should be noted that if the vertical velocity is equal to the lateral velocity, which is the case in nearly all crystal orientations other than the (111), this model predicts that the SL interface will not change shape and will continue to follow the shape of isotherms.

This investigation into the effects of faceting go a long way to explain the experimental results. But one more factor, which is concerned with extending the equations for thermal diffusion and capillary wave motion from 1-D to 2-D surfaces, will be explored in the following discussion.

4.3.8 Thermal Diffusion and Capillary Wave Motion Acting on 2-D Interfaces

The equations describing the evolving shape of the SL and LV interface presented in sections 4.2.1 and 4.2.2 assume that the solution depends only on one of the spatial dimensions of the surface. All experimental evidence clearly shows that there are variations across the surface. The purpose of this discussion is to investigate some implications of using 1-D solutions.

Extending the thermal and capillary equations to two dimensions is actually very easy in practice. It requires replacing the 1-D wave with a surface plane wave. This can be done by replacing the wave number, $k = 2 \cdot \pi / \Lambda$, by the wave vector $\boldsymbol{k_n} = [\, k_{x,n}\ k_{y,n}\,]$, where k_x and k_y are orthogonal components on the surface. If the original shape of the surface can be described by the sum of series of plane waves, then the capillary and thermal equations can be applied to each of the plane waves individually to describe the evolving shape of an interface in time. The magnitude of a wave vector is given by,

$$k_n = \left| \overrightarrow{k_n} \right| = \sqrt{\left(k_{x,n}\right)^2 + \left(k_{y,n}\right)^2}$$

equation 4.21

The shapes of the SL interface, z_{sl}, and the LV interface, z_{lv}, as a function of time are given by,

$$z_{sl}(x,y,t) = \sum_{n=1}^{N} A_{o,n} \cdot exp\left[i \cdot \left(k_{n,x} \cdot x + k_{n,y} \cdot y \right) \right] \cdot exp\left[-\left[\left(k_{x,n}\right)^2 + \left(k_{y,n}\right)^2 \right] \cdot D \cdot t \right]$$

equation 4.22

$$z_{lv}(x,y,t) = \sum_{n=1}^{N} A_{o,n} \cdot exp\left[i \cdot \left(k_{n,x} \cdot x + k_{n,y} \cdot y \right) \right] \cdot cos\left[\sqrt{\frac{\sigma}{\rho_L} \cdot \left(k_n\right)^3 \cdot tanh\left(k_n \cdot h\right)} \cdot t \right]$$

equation 4.23

Note that the parts of equation 4.22 and equation 4.23 which are functions of time only depend on the magnitude of the wave vector. Details about the angle of a particular wave front do not factor in.

A short series of plane waves will be used to approximate the local ordering of structures on the (100) and (111) surfaces. Plan views and oblique views of the resulting surfaces are shown in Figure 4.20. The shape of the (100) surface structure can be approximated very well with two perpendicular wave vectors with equal amplitudes such as $\boldsymbol{k}_1$ = [1 0], and $\boldsymbol{k}_2$ = [0 1]. In this case, the change in amplitude as a function of time for the 1-D interface will be identical to the response of the 2-D interface for both thermal and capillary effects. No correction is needed when extrapolating the results of a 1-D interface to two dimensions.

The three-fold symmetry evident in (111) surface structures can be captured by summing three plane waves angled 120º to one another. The surfaces shown in Figure 4.20(a,b) were generated with wave vectors: $\boldsymbol{k}_1$ = [2/√3 0], $\boldsymbol{k}_2$ = [1/√3 1], and $\boldsymbol{k}_2$ = [1/√3 -1]. The spacing between the surface features is the same as in Figure 4.20(c,d), but the magnitude of each of the vectors is 2/√3. So, in order to create a surface with three-fold symmetry that has structures with a spacing of for instance 1 μm, the wavelength of the surface waves constituting this surface must be √3/2 μm. Therefore, if the results of a 1-D model are to be extrapolated to a 2-D surface with 3-fold symmetry, they should be multiplied by a factor of √3/2.

4.3.9 Results of Including Faceting Effects and Surface Symmetry

The effects of faceting during solidification in the (111) direction as well as corrections to account for the observed surface symmetry have been included in the model predicting the surface spacing of structures on the (111) surface. The result of this are shown in Figure 4.21. Neither of these additional effects influence (100) results, but these additions to the model do bring predictions for the (111) surface into closer accord with experimental results. Deviations between the model and the experimental results are larger for larger melt times. This could be due to inaccuracies in account for faceting effects over long melt times. If the SL interface were to become smoother at long melt times than what was predicted to be the steady state surface shape, this would have the effect of reducing the predicted feature spacing.

4.3.10 The Expression of Crystallography in the Surface Structure

The proposed model for the evolution of laser induced surface features coupled with a map of surface atomic densities (Figure 4.9) can be used to gain further insight into the reasons that the *shape* of the laser induce surface structures is influenced by the crystal orientation of the surface on which they form. Figure 3.13 (p.3.61) shows micrographs of the typical shapes that surface features acquire on different crystal faces.

An illustration of the geometry of the liquid and solid regions at the last stage of solidification is shown again in Figure 4.22, this time with the varying angle of the solid-liquid interface highlighted. As revealed in the cross-section of this nearly solidified perturbation, the portion of the interface at the center and at the perimeter of the SL interface has the same orientation of the original substrate, but the orientation

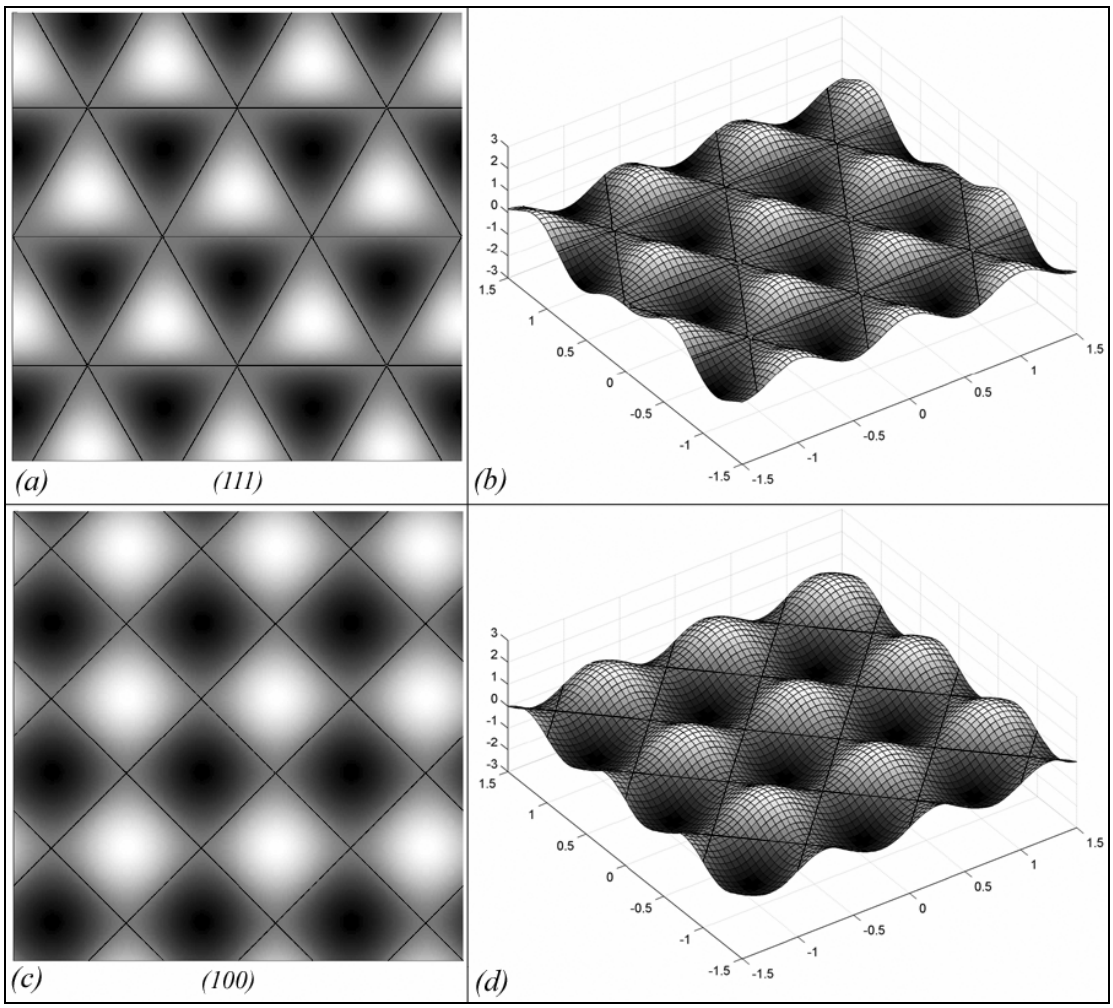

Figure 4.20. Illustrations of surfaces approximating the shape of (111) and (100) surface structures

(a) plan view of (111)-type surface structures with 3-fold symmetry composed of wave vectors: $\mathbf{k}_1$ = [$2/\sqrt{3}$ 0], $\mathbf{k}_2$ = [$1/\sqrt{3}$ 1], *and* $\mathbf{k}_2$ = [$1/\sqrt{3}$ -1]. *(b) oblique view of (a). (c) plan view of (100)-type surface structures with 4-fold symmetry composed of wave vectors* $\mathbf{k}_1$ = [1 0], *and* $\mathbf{k}_2$ = [0 1]. *Oblique view of (c).*

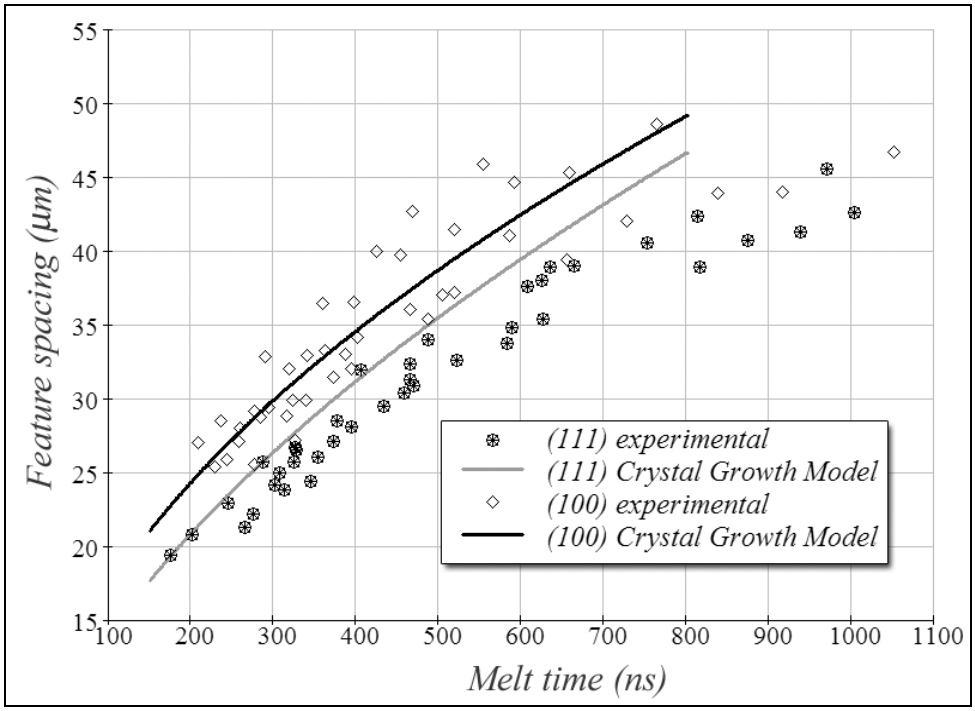

Figure 4.21. Results of modeling the evolution of surface structures includes faceting effects

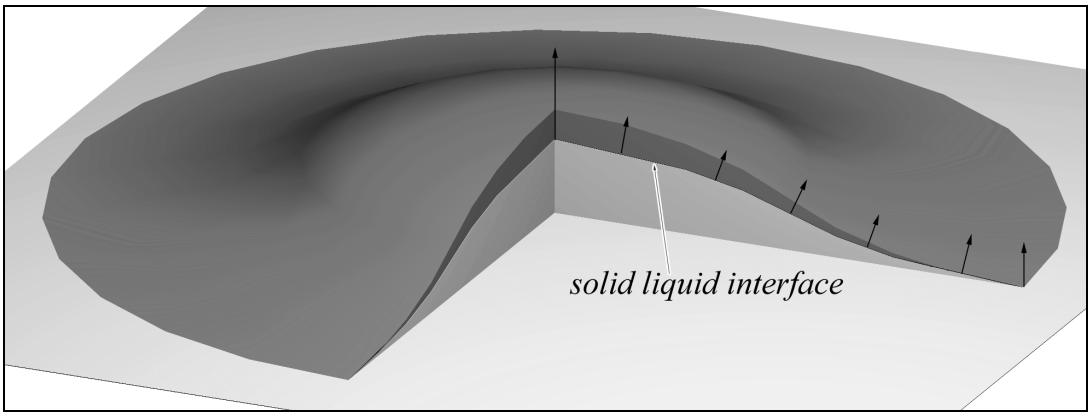

Figure 4.22. Illustration highlighting varying surface orientations at the last stage of solidification

of the remainder of the interface does not. The angle of a region of the interface depends on its distance from the center. This implies that the different regions of this curved interface will have slightly different surface atomic densities. and growth rate will vary across the interface. The anisotropy in growth rate is related to crystallographic anisotropy, and it is this relation that provides an avenue for the underlying atomic structure to be expressed in the surface features.

Quantitative modeling of this concept has not been performed. However, a qualitative argument is presented in Figure 4.23 and Figure 4.24, revealing remarkable correlations. The surface density (κ_s), calculated using the tetrahedral method described above, and has been mapped to the surface of a radially symmetric sinusoid. Over head views of the structures show the distribution of surface density as both shaded and contour plots. Dark regions of the shaded plots indicate relatively high surface density where growth will be largest during the end stage of solidification. The contour plots show more clearly the magnitude of surface density of the solid. Comparison of solid surface density with the surface density of liquid, $\kappa_l = 4.79$, gives some measure of the amount of growth that will occur.

Figure 4.23(a,b) shows the solid surface density mapped to a sinusoidal perturbation, with a wavelength of 20 μm, and an amplitude of 0.5 μm, onto a (100) surface. (c) is an SEM image of structures that form on this face. Note that everywhere $\kappa_s > \kappa_l$, which means that substantial growth will occur everywhere during solidification. But, there are four lines emanating from the center above which, it is reasonable to assume that growth will be slightly greater. Therefore, a perturbation which originally exhibited no circumferential height variation, will after a single melt/solidification cycle take on a four fold symmetry because of the underlying symmetry in κ_s. This four fold symmetry is apparent in the image of the surface in that the surface structures have assumed the shape of square based pyramids.

A similar argument can be made for the (111) surface as demonstrated in Figure 4.23(d-f). However, the crystallographic texturing is more prominent than in the (100) case. This is likely due to the fact that the variation in the value of κ_s across the curved interface straddles κ_l. The white contour lines in (d) indicate the value of κ_l. Therefore, there are regions that will increase in height and others that will decrease during crystallization. The three dark lines emanating from the center, along which the increase in height is expected to be the largest, point in the same direction as ridges evident in the micrograph in (f).

A final example is shown in Figure 4.23(a-c) for the (211) surface. As in the (111) case, there are regions of positive growth and negative growth across the surface of a single perturbation. The symmetry in this case however is 2-fold. Thus, one would anticipate positive growth only over two opposing regions on the interface. Therefore, after successive laser pulses, an originally smooth perturbation will degenerate into the parallel ridges evident in (c). The same mapping was applied to the (110) surface in Figure 4.23(d,e). Across the surface, κ_s is quite a bit larger than κ_l, so no growth would be expected anywhere in agreement with experimental results.

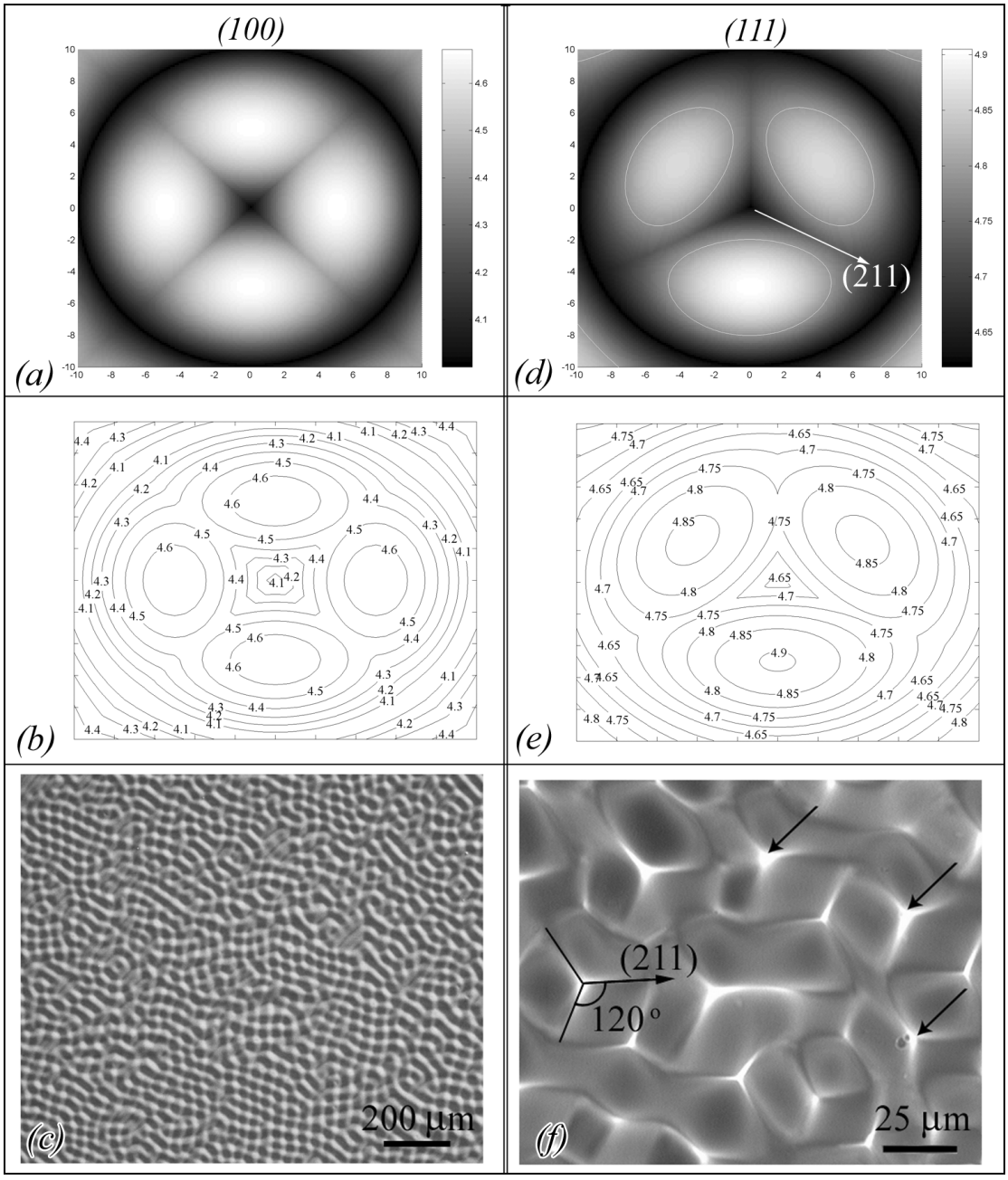

Figure 4.23. Surface density mapped onto sinusoidal perturbations on (100) and (111) surfaces (a,b) shaded and contour maps of κ_s near the (100) face. (c) micrograph of surface structure on the (100). (d,e) shaded and contour maps of κ_s near the (111) face. (f) micrograph of (111) structures.

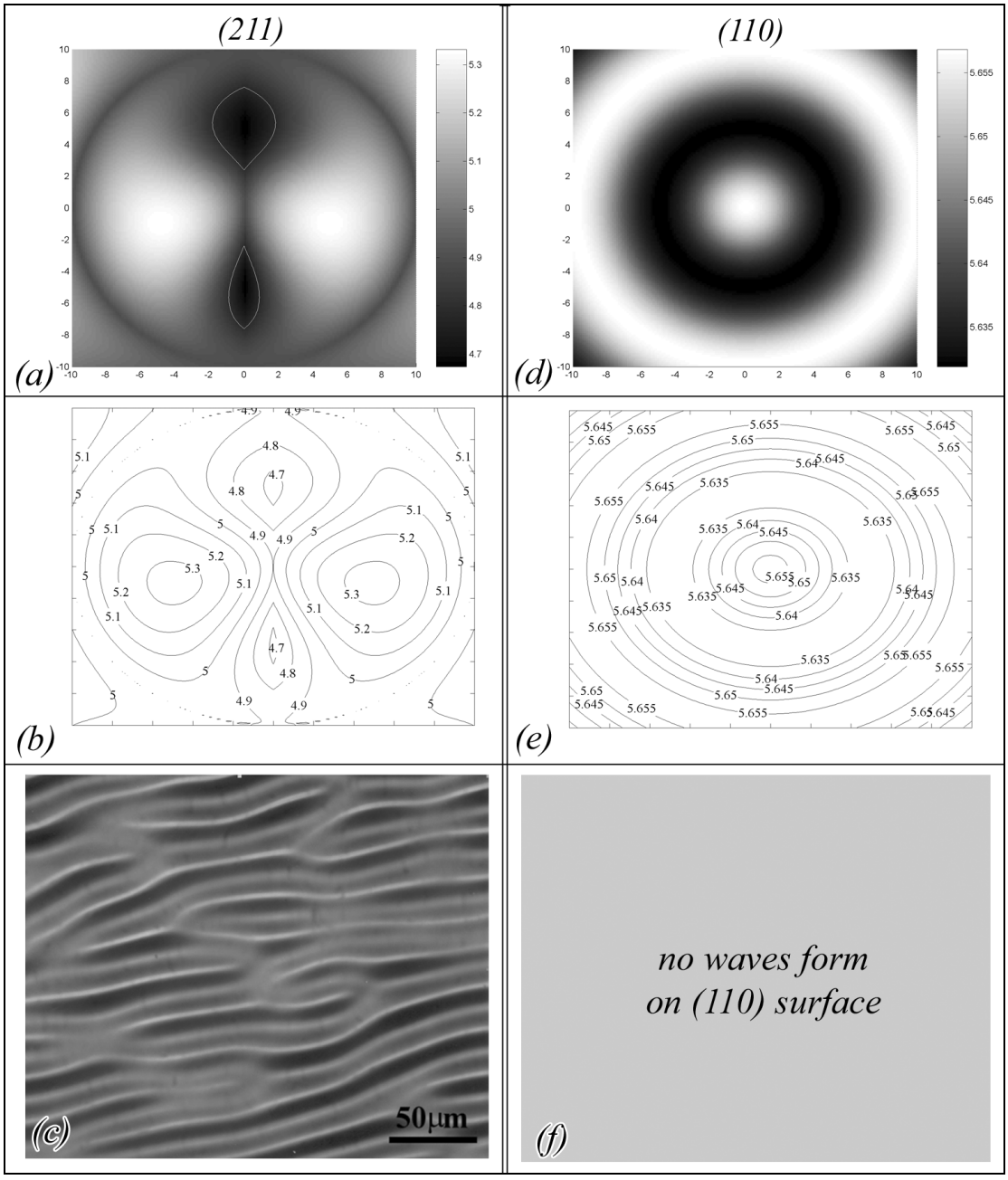

Figure 4.24 Surface density mapped onto sinusoidal perturbations on (211) and (110) surfaces

(a,b) shaded and contour maps of κ_s near the (211) face. (c) micrograph of surface structure on the (211). (d,e) shaded and contour maps of κ_s near the (110) face.

4.4 The Evolution of the Micro-Cone Surface Structure

A model has been developed for the purpose of understanding the processes responsible for determining the spacing of surface features and the rates of growth of these features. Experimental results have indicated that, in most cases, the wavelike surface features are the precursors to micro-cone structure and define the location of micro-holes and micro-cones. The following discussion will explain possible mechanisms of how the gently sloping surface waves, which have taken several hundred pulses to form, abruptly transition to the very rough and fast growing surface structure of black silicon. Further investigations into the continued growth micro-cones will also be addressed.

4.4.1 The Transition from Waves to Cones and the Interaction of Surface and Light

The experiments performed as part of this project show that black silicon only forms in the presence of SF_6. Other published experimental results[56] have shown that an ambient atmosphere containing Cl_2 can also generate a micro-cone populated surface as well. SF_6 is an inert gas at room temperature but can dissociate into reactive products and at elevated temperatures, by photonic excitation[57], or when bombarded by electrons or ions[58]. It is assumed that the formation of micro-holes is due to etching by reactive products of SF_6 dissociation. Considerations of the lifetime of these reactive products suggest that they must be generated close to the surface in order to have any effect on the surface.

A clear determination of the threshold for dissociation is elusive, but whatever this threshold might be, it does not appear to be crossed under the experimental conditions used in this study if the surface of the silicon substrate is flat. If the surface of silicon is relatively smooth, the rate of material removal by laser ablation is not much larger in an SF_6 atmosphere as compared to an atmosphere of Argon (p. 3.44). The production of fluorine in close proximity to the surface seems to require some kind of surface roughness. Possible explanations for this dependency can be found in an examination of the light reflected from the surface. First however, it is useful to re-examine experimental results to determine the point at which surface roughness becomes sufficient to induce surface etching.

Experimental Evidence of Critical Roughness

Profilometry measurements of roughness at various stages is surface evolution have been presented in Figure 3.1 and show that micro-cone formation occurs between the 600th and 700th pulse when irradiated with 3.0 J/cm^2 laser light. This indicates that there is a critical roughness, or amplitude, at which laser induced etching can occur. Since the evolution of surface waves is atmosphere independent up to the 600th pulse, the data from all 6 experiments conditions can be averaged together to improve estimates on amplitude growth rates. This is plotted in Figure 4.25. The vertical axis has been rescaled from RMS roughness to amplitude by assuming that the surface is sinusoidal in shape. Extrapolation of the best fit line

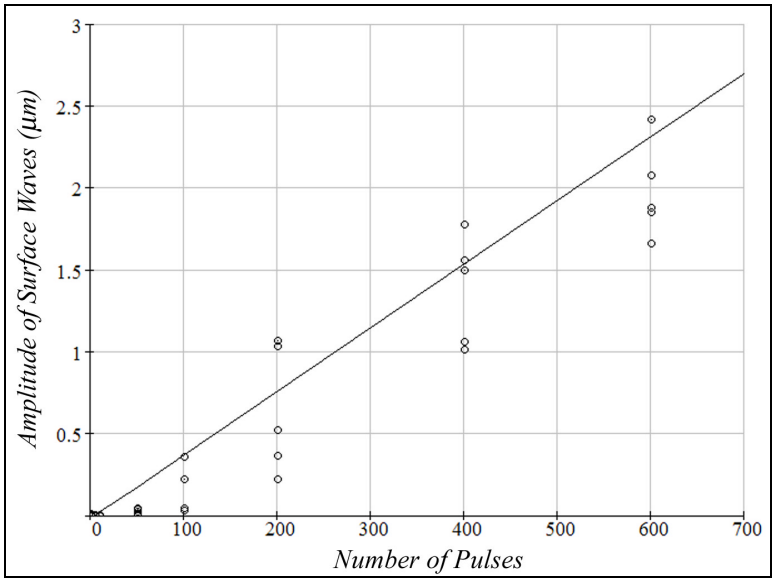

Figure 4.25. Measured amplitude of surface waves as a function of the number of pulses.

The data from the first 600 pulses has been averaged into one best fit curve and extrapolated to the 700th pulse. The irradiation intensity is 3.0 J/cm^2.

of the averaged data beyond the 600th pulse shows that the onset of the formation of micro-holes and cones occurs when the amplitude of surface waves is between 2.3 μm and 2.7 μm.

Ray-Tracing of Reflected Light

The interaction between incident light and the surface was analyzed by looking at the manner in which reflected light is dispersed from the surface. A program was written to examine the paths taken by an ensemble of parallel rays as they strike and are reflected from a surface. In this ray tracing approach, the wave nature of light is ignored so that no considerations of interference patterns are made. This is a valid simplification since the feature spacing on the surface is about 100 times the wavelength of the incident light.

Figure 4.26(a) presents the result of this ray tracing technique applied to a sinusoidal surface having a wavelength of 20 μm and an amplitude of 0.4 μm. The incident rays are not shown, but are all parallel to each other and perpendicular to the mean height of the surface. The reflected rays are shown and, as might be expected, many appear to converge on a region at some height above the surface minima. These results were processed further to estimate the distribution of light intensity above the surface by counting the number of rays, both incident and reflected, passing through a cross section of space. The data

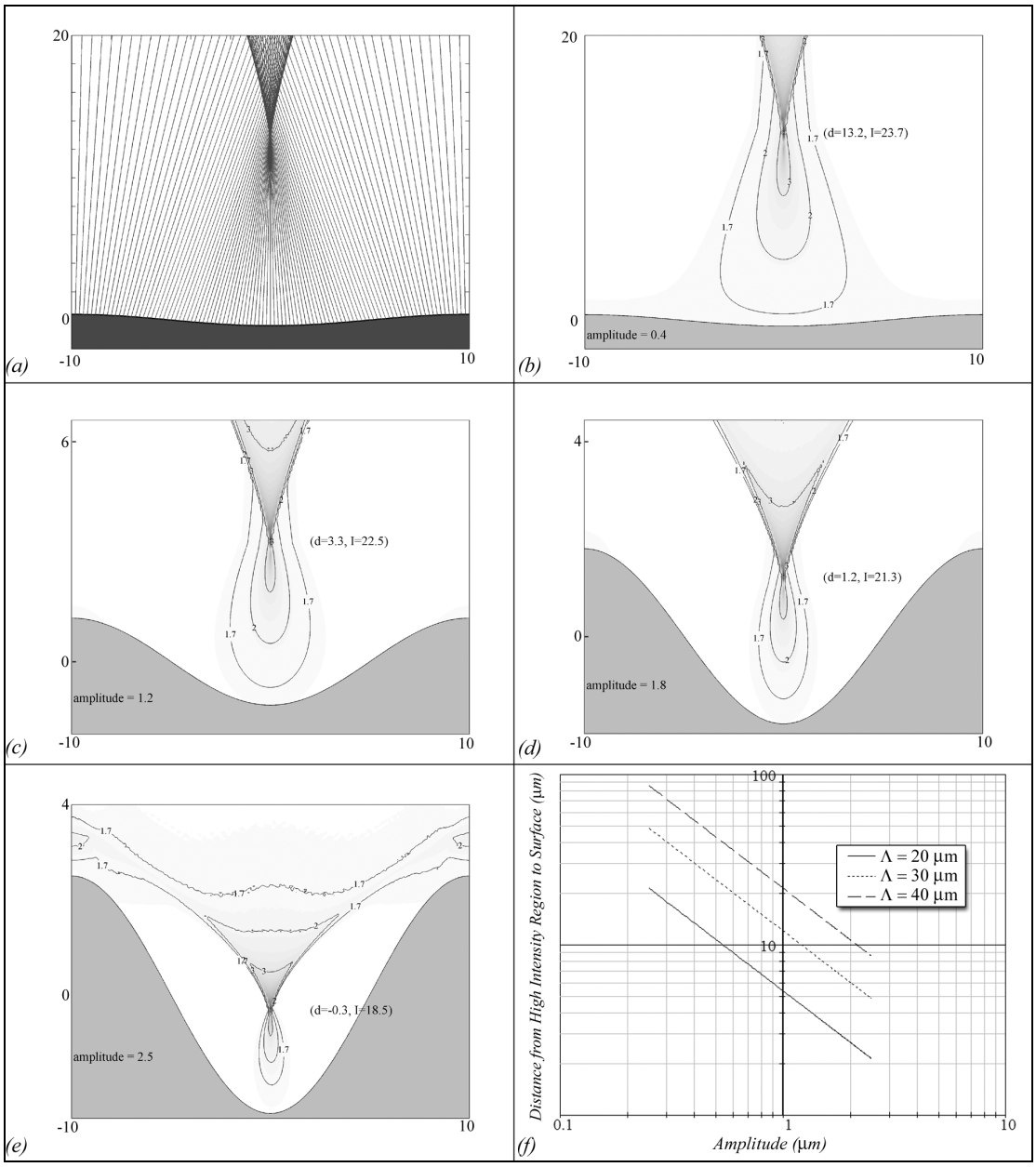

Figure 4.26. Results of modeling the distribution of reflected light above a sinusoidal surface

(a) Trace of reflected rays from a surface with 20 μm wavelength and amplitude = 0.4 μm. (b) re-plot of data in (a) showing contours of constant intensity. (c) amplitude = 1.2, (d) amplitude = 1.8 μm, (e) amplitude = 2.5 μm. (f) log-log plot showing distance from region of highest intensity to surface vs. surface amplitude for three different wavelengths.

has been smoothed by taking a moving average with a window of 0.5 μm. A contour map of the reconfigured results are shown in Figure 4.26(b). The data has been normalized to the incident intensity, and represented in terms of an intensity factor, which should be multiplied times the incident flux to find the actual intensity at a point. Silicon reflects about 65% of 248 nm light. So the intensity factor just above the surface would be 1.65. Contour lines are shown which trace intensity factor lines with values of 1.7, 2.0, and 3.0.

The point where the light is most intense is indicated and the numbers in parenthesis give the distance from this point to the mean height of the surface, d (μm), and the intensity factor at that point, I. Except for the fact that a moving average of the data was performed, this program assumes a perfectly smooth surface that is perfectly sinusoidal in shape. Scattering due to surface roughness, variations in the index of refraction of the atmosphere due to heating, and other mechanisms that would reduce the peak intensity have been ignored so it is difficult to determine how accurate the estimate of highest intensity is. But it is reasonable to conclude that a region with an intensity at least three times that of the incident flux is generated close to the surface.

Figure 4.26(b-e) show how the distribution of intensity changes with increasing surface wave amplitude. Note the change in scale of the vertical axis. As amplitude increases, the region of high intensity moves closer to the surface, and the triangularly shaped area above the point of highest intensity widens. The high intensity region approaches the surface asymptotically as a function of surface wave amplitude, and so never comes into direct contact. Profilometry measurements indicate that, for feature spacings of 20 μm, the critical amplitude for micro-hole formation is between 2.3 μm and 2.7 μm. There is no conclusive evidence in these figures to indicate exactly what initiates substrate etching. The high intensity region is not much closer to the surface when the amplitude is 2.5 μm as compared to 1.8 μm, but the high intensity region is somewhat more confined in the 2.5 μm case. Also, the contour line for the 1.7 intensity factor stretches from one surface peak to another creating a kind of high flux cap over the valley. So, if reactive products are generated in the high flux region, it may be possible that they are held close to the surface long enough or expand in such a way in the 2.5 μm case to permit etching to occur.

The log-log plot in Figure 4.26(f) charts the relationship between surface amplitude and the distance between the high flux region and the surface for three different surface feature wavelengths. The plot shows that as wavelength increases, the amplitude must increase in order to render the same effect. This is expected since these results are based on the morphology of the surface and an isomorphic sinusoid with a larger wavelength necessarily has a larger amplitude. But, it should be noted that this trend is apparent in experimental results since it takes many more shots to form black silicon on a heated substrate because it has larger feature spacings. This means that the critical amplitude for the onset of micro-cone formation is greater for longer wavelengths. The code used to generate this data is supplied in Appendix 13-14.

Multiple Surface Reflections

As the amplitude of surface waves is increased beyond what is shown in Figure 4.26, a new mode of light-surface interaction emerges, that of multiple reflections. An increasing amplitude to wavelength ratio results in steeper surface sidewalls, and if the sidewall angle is sufficiently high, incident light can be redirected to another part of the substrate. Under these conditions, the flux at the surface can increase dramatically.

Plots of ray paths and intensity resulting from light reflecting from a sinusoid with a amplitude of 2.8 μm are shown in Figure 4.27. The secondary reflections in (a) are shown darker than the primary ones. From the contour plots in (b), it can be observed that the summed intensity on some regions of the surface has increased to 3 times that of the incident intensity. The threshold amplitude at which double reflections occur can be roughly estimated by finding the amplitude to wavelength ratio for which some part of the surface has an angle of 45˚ to the incident beam. For a sinusoid, this critical amplitude (A^*) is reached at $A^* = \Lambda/(2\pi)$. For a 20 μm wavelength, A^* would be 3.18 μm. The intensity map at this amplitude shows that the flux at specific regions on the surface reaches 10 times the incident intensity. Again, scattering by surface roughness has been ignored, which means that the actual intensity at the surface is probably not really this large. This is evident by the fact that micro-holes are not produced in an Ar atmosphere, regardless of amplitude. If the intensity factor at the surface was really 10, micro-hole formation would likely occur in any atmosphere. But, the intensity is likely to be large enough to induce coupling between the SF_6 atmosphere and the Si substrate, the production of volatile Si_xF_y species, and the rapid removal of material. Once rapid etching is initiated, the shape of the surface changes quickly making the sidewalls steeper. Steeper sidewalls direct light towards the valleys and drilling of micro-holes begins.

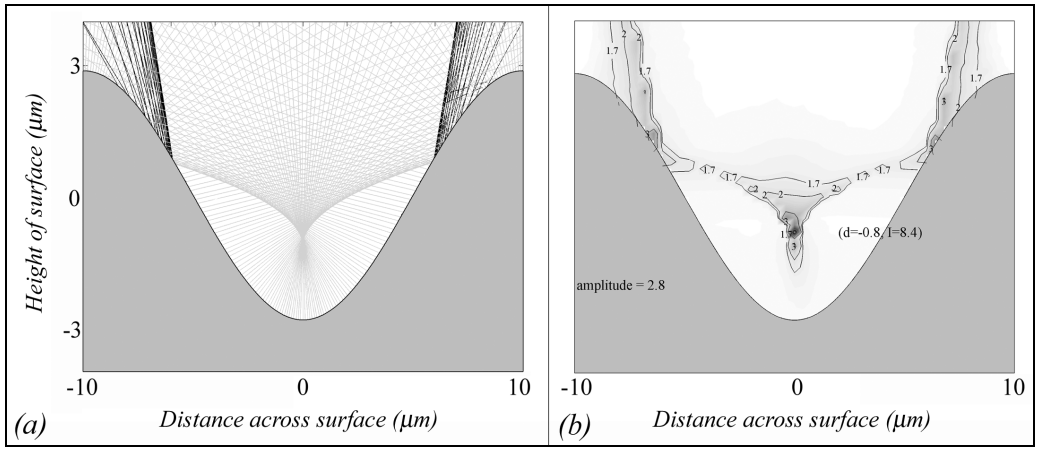

Figure 4.27. Multiple surface reflections on a sinusoidal surface

The estimated amplitude threshold for micro-hole formation, $A^* = \Lambda/(2\pi)$, is larger than what the profilometry data suggests. A likely explanation for the disagreement is that the profile roughness measurements give the *average* roughness over 10's of surface waves. Some surface waves will have greater amplitude than the average. In addition, profilometry measures changes in surface height along a single line, and there is no guarantee that this line passes directly over surface maxima and minima. More likely than not, this line will pass to either side of the surface height extrema. Therefore, profilometry measurements of a surface which exhibits waviness in two dimensions will always underestimate average roughness. Also, the $\Lambda/(2\pi)$ condition is based on some part of the surface achieving an angle of 45˚, multiple reflections occur at slightly smaller amplitude. Therefore this condition slightly over-estimates when multiple reflections first occur.

Though it is not possible to exclude the possibility that high intensity regions formed close to but not in contact with the surface, as illustrated in Figure 4.26(e), are responsible for micro-hole formation, the preceding analysis shows that it is more reasonable to conclude that laser induced micro-hole growth under an SF_6 atmosphere is initiated by multiple reflections of the incident beam on a textured surface. Multiple reflections result in the intensification of energy in specific regions directly at the surface. This high intensity induces the dissociation of SF_6 and the rapid removal of material. Removal of material can increase the intensity of multiple reflection creating a positive feed-back in the formation of micro-holes. The following section will discuss the role of multiple reflections as valley deepens by etching.

4.4.2 The Continued Evolution of the Black Silicon Surface Structure

SEM images of cross-sectioned black silicon substrates, as shown in Figure 2.3(c), were used to determine the evolving shape of micro-holes and micro-cones as the number of laser pulses increased. These images were used as templates so that the same ray-tracing approach that was employed in the study of surface wave reflections could be used to interpret observed trends in the evolution of black silicon.

Figure 4.28(a-e) are images of rays traced as they are reflected inside micro-holes of increasing depth. Incident rays are not shown, but up to eight orders of reflected rays were determined and are plotted. The order of a ray increases by one each time it strikes the surface. The first order reflected rays are drawn the darkest, and the eighth, if occurring at all, are shaded the lightest. Flux was measured at the surface as a function of distance along the sidewalls by counting the number of rays striking the surface along a given length. A histogram showing the result of such a measurement is presented in Figure 4.28(g). The peak in intensity in this plot occurs at the base of the micro-hole while the sidewalls of the micro-hole receive a negligible amount of energy meaning that most of the laser energy is channeled to the base of the micro-hole.

A plot of peak intensity factors at the base of the micro-hole as a function of depth is shown in Figure 4.28(f). The highest curve is the total intensity factor, the smaller curves beneath it represent the

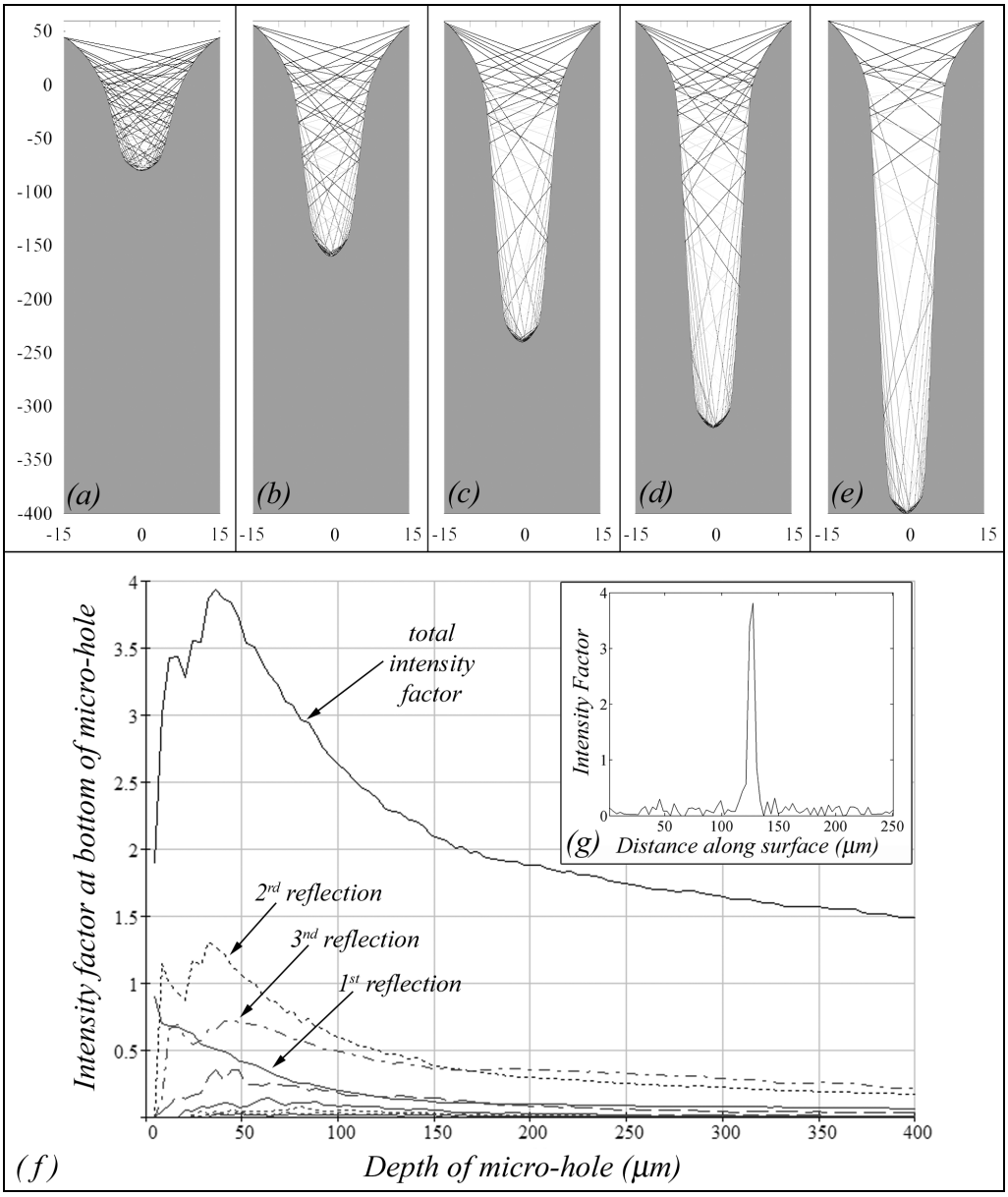

Figure 4.28. Analysis of multiple reflections in micro-holes

Cross-sectional views of ray-tracing in micro-holes with depths of (a) 80 , (b) 160, (c) 240, (d) 320, and (e) 400 μm. (f) A plot of intensity at the bottom of a micro-hole as a function of depth. (g) plot of intensity factor as a function of position along the surface of an 80 μm deep micro-hole. The peak corresponds to the bottom of the micro-hole.

individual contributions to the total intensity by differently ordered reflections. The total intensity rises quickly in the early stages of the deepening of the micro-hole, and reaches a maximum when the hole depth is just below 50 μm. The intensity factor is almost 4 implying that the energy density at the base of the hole is nearly 12 J/cm^2. After this point, the drop-off in intensity is gradual and eventually reaches a value of 2 for 400 μm deep holes. This curve asymptotically approaches unity for increasingly deeper holes.

This trend in estimated intensity follows very closely the trend in the rates of micro-hole deepening observed by way of in-situ imaging using the ICCD camera set-up. In early stages of micro-hole growth, when the hole depth is between 25 μm and 75 μm as in Figure 3.10(f-h) (p. 3.56), the measured ablation rate is a remarkable 1.5 μm/pulse; a rate 3 orders of magnitude larger than that for flat Si in the same SF_6 atmosphere and for the same beam energy density. As the micro-hole deepens further, the rate of material removal drops off considerably. From approximately the 4000th to the 22,000th pulse, when micro-holes are between 200 μm and 400 μm deep, deepening occurs at a rate of about 0.02 μm/pulse.

Some further insight into the build-up of energy at the base of the micro-hole can be gained by observing the order of the multiple reflections reaching the base of the micro-hole. When the micro-hole is very shallow, 1st order reflections are the largest contributors to flux build-up. After only a little more deepening, 2nd order reflections dominate, and 3rd order reflections become significant contributors as well, and the total intensity reaches its maximum. It should be noted that each reflection reduces the flux of the ray by a factor of 0.65, the coefficient of reflectivity for silicon. But despite this reduction, it appears that most of the energy accumulated at the base of the micro-hole under conditions when the deepening rate is the fastest has arrived after being reflected twice from the surface. After the micro-hole has become more than about 200 μm deep, except for the direct 0th order laser beam, 3rd order reflections provide most the energy, but this is a relatively small amount. Reflections above the 4th order have little influence on incident energy. According to the ray-tracing results, approximately the same number of rays strike the base of the micro-hole regardless of its depth, but the energy that is delivered per ray is much smaller for deeper holes since more reflections are required for them to reach the bottom.

The rate of evaporation of silicon can be approximately calculated assuming that ablation takes place as the irradiated surface is rapidly heated resulting in a solid-gas interface progressing into the target material[3]. Melting is ignored as a part of the physical process that leads to ablation. This assumption is suitable since the heat of vaporization is several times larger than the heat of melting and therefore dominates the energy balance. For silicon, the heat of melting is 50 kJ/mol while the heat of vaporization is 359 kJ/mol. Also, no atmosphere or plume-surface interactions are considered. In this model, the velocity and temperature of the solid-gas front is governed by the energy absorption and heat transfer characteristics of the target. The Drude-Zener theory of optical absorption is used which is based on a linear relation between absorptivity, A, and temperature, T_S. The following two relations can be obtained[3]

$$A \cdot I = V_s \cdot \rho \cdot \left(L_v + c_p \cdot T_s \right)$$

equation 4.24

$$V_s = V_o \cdot exp\left(\frac{-M \cdot L_v}{k_b \cdot T_s} \right)$$

equation 4.25

where I is the laser fluence, ρ is the density of silicon, L_v is the latent heat of vaporization, c_p is the heat capacity, V_o is the speed of sound in the material, M is the molar mass, and k_b is Boltzman's constant. The equations are then solved simultaneously to find V_s and T_s, the evaporation front velocity and temperature. At a laser fluence of 12 J/cm^2, the estimated maximum intensity at the bottom of the micro-holes, V_s is found to be 38.2 m/s. A rough estimate of the time required to establish steady state evaporation, t_c, is given by

$$t_c = \frac{D}{V_s^2}$$

equation 4.26

where D is the thermal diffusivity. For the same high laser fluence, this equation yields t_c = 5.8 ns. If it is assumed that most of the evaporation takes place after the establishment of a steady state front and until the end of the 25 ns pulse, this model yield an ablation rate of 0.6 μm/pulse for a laser fluence of 12 J/cm^2. This rate is 500 times higher than the ablation rate of a flat surface in the presence of SF_6.

4.4.3 Ablation Plume Analysis as Related to the Evolution of Micro-cones

The formation of micro-holes discussed in the previous section results in the production of silicon-fluorine volatiles at the base of the micro-hole. The generation of these volatiles increases the atmospheric pressure inside these deep channels significantly and the expanding gas has no other escape path but up through the top surface. This high temperature gas, ejected from a multitude of micro-holes across the surface, converges together to form the plume visible in the in-situ ICCD images. Some of the silicon that is bound to fluorine in the plume will re-condense on the surface to form micro-cones. Analysis of the plume under different experimental conditions will serve to explain the connection between plume characteristics and micro-cone growth as well as show what factors create the optimal conditions for micro-cone growth.

The Role of the Plume over Multiple Laser Pulses

A clear correlation is seen between the rates of growth and dissolution of micro-cones as a function of the number of laser pulses. To state this simply, micro-cones grow in the presence of an

ablation plume and grow to a height approximately equal to final height of the plume suggesting that material within the plume provides feedstock to the cones.

Continuous mode in-situ imaging of the surface, like that shown in Figure 3.10, show that micro-cones grow quickly and continually from about the 500th to 1200th pulse. After this point, the peak height of the micro-cones slowly decreases eventually receding below the initial substrate. Two mechanisms are competing during the life cycle the micro-cones: that of re-deposition of material from within the micro-holes and that of laser ablation of the micro-cone tips. Up to the 1200th pulse, the material ablated from within the micro-holes and re-deposited at the tips of the cones is larger than the amount of silicon that is ablated from the micro-cone tips. Like any other laser-exposed area on the substrate surface, the micro-cones are continually etched and ablated, but the plasma that surrounds them, supplies the tip and sides with enough silicon to yield a net cone growth. The laser-melted silicon at the micro-cone tip can efficiently collect both the silicon-rich vapor as well as small clusters that form at these relatively high ambient pressures. According to deposition theory, a negligible supersaturation is required to initiate the deposition on the substrate. The accommodation coefficient for molecules and atoms in a liquid is very close to one[59]. For this reason the deposition takes place preferentially at the cone tips which remain melted for a longer time than any other part of the micro-cones.

As the micro-holes deepen, the maximum plume height decreases as well. After ~1700 pulses, the fluorescent plume no longer reaches beyond the tips of the cones. If the fluorescent plume is an indication of the amount of ablated material present, less silicon-rich molecules or clusters are reaching the tips of the cones after 1700 shots. The balance between material ablated and material re-deposited at the cone's tip tilts toward the former and the micro-cones begin to recede. At a sufficient number of pulses, micro-holes are deeper and not only is the laser intensity at the bottom of the micro-hole diminished, but the distance to the surface is farther. The silicon-rich plume becomes completely trapped within the 300 μm deep holes, and the cones recede below the initial surface. The cones that once protruded 30 μm above the original surface after the first 1700 pulses are fully ablated after 22,000 pulses, as in Figure 3.10(i).

Plume Motion During a Single Pulse

Profilometry results show that both the pressure and the type of the gases present affect the microstructure produced during multiple pulsed-laser irradiation. Micro-cones attain a maximum height when irradiation is conducted at a background pressure of 0.5 bar of SF_6. In agreement with this finding, both the initial plume velocity and the final plume edge position were found to be a maximum at this pressure.

Although the maximum initial plume velocity was reached when the pressure was 0.5 bar, there is an upturn initial plume velocity when the ambient background pressure drops below 0.2 bar as shown in Figure 3.12(c). These results suggest that SF_6 fulfills two roles: first, it acts as an etchant of silicon, and second, it exerts a background pressure that tends to restrict the expansion of the plume. An increase in the

ambient background pressure produces an increase in etching rate thus increasing the pressure produced by the laser-generated plume. This increase in pressure is reflected in an increase in the velocity of the laser-generated plasma. However, as the background pressure is increased, the role of SF_6 as an etchant is increasingly counteracted by its role as a background gas that tends to slow the plume front. When the ablation chamber is filled with a mixture of SF_6 and Ar gasses at a constant total pressure of 1 bar, the maximum height of the cones is reached when the partial pressure of SF_6 is also 0.5 bar. However, the maximum height reached in this case is significantly lower than for the case where only 0.5 bar of pure SF_6 is present. This behavior is to be expected because the addition of Ar further contributes to contain the plasma without altering the etching power of the background gas.

The advance of the plume front as a function of time can only be measured with the ICCD camera within approximately the first 100 ns because the ambient gas quickly quenches the laser-induced fluorescent light. The pressure at which these measurements were performed was thousand times higher than in other reported measurements of plume expansion[60,61]. At a pressure of 0.5 bar the plume front reaches 60 μm before the background gas quenches the excitations producing the fluorescent light. We have found that at these very early stages of plume expansion, the drag-force model fits better than the shock model originally described by Zel'dovich and Raizer[62]. In the drag-force model it is assumed that the ablation products are moving as a whole and that the background gas produces a viscous deceleration of the plume proportional to the expansion velocity,

$$\frac{d}{dt}v = -\beta \cdot v$$

equation 4.27

This model leads to equation 4.28 and fitted values of maximum front distance x_f = 46 μm and drag coefficient β = 47.5 μs^{-1}.

Geohegan[61] observed a similar behavior for the ablation of $YBa_2Cu_3O_{7-x}$ in a 100 mtorr of oxygen with a value of x_f = 3.0 cm and β=0.36 μs^{-1} . The initial velocity of the plume

$$v_o = \beta \cdot x_f$$

equation 4.28

was in his case 1 cm/μs. The initial velocity of the plume due to ablation/etching of silicon in our case is 2.4 cm/μs indicating that the pressure of the gases produced during etching is very high. However our drag coefficient, β, is 150 times larger than in the case of ablation of $YBa_2Cu_3O_{7-x}$. This difference is due to the fact that the background gas pressure is almost 4000 times larger than in the $YBa_2Cu_3O_{7-x}$ experiments.

CHAPTER 5 EXPERIMENTAL METHODS FOR SWNT TRANSPORT STUDIES

5.1 Sample Preparation

Nanotube-polymer composite films were prepared by spin casting purified (< 0.01 wt. % metal), laser vaporization-grown SWNTs [63,64] which were co-solubilized with poly-methyl methacrylate (PMMA) in ortho-dichlorobenzene (ODCB). The nanotube/polymer/solvent solutions were prepared in a two step process. First, a dispersed suspension of SWNTs in ODCB was prepared by gentle sonication (Branson 1210 sonicator) for approximately 20 minutes. Of the solvents tested in this study, ODCB provided the best dispersion of the highly-purified, strongly-bundled SWNTs. ODCB's relatively high boiling point was also compatible with the spin casting process. The SWNT/ODCB suspensions remained stable for several days after sonication. PMMA (MW 540,000) does not readily dissolve in ODCB, so separate PMMA/ODCB solutions were prepared by sonication, stored for several days to give time for the PMMA to dissolve, and filtered through a 0.2-μm mesh polyvinylidene fluoride filter to remove any undissolved polymer. The final solution was prepared by mixing the separate solutions of SWNT/ODCB (weight loadings between 10–100 μg/g) and PMMA/ODCB (1.0–2.0 wt%) together.

These solutions were spun cast onto test structures comprised of lithographically patterned gold electrodes on a 500nm-thick SiO_2 layer deposited on silicon. After drying, the resulting samples were 40–100 nm-thick SWNT/PMMA composite films with weight loadings between 0.1–1.0 wt%. The small film thickness was advantageous since the possible conductive pathways were reduced to essentially two dimensions. Hence, the complete topology of the conductive network could easily be determined from SEM micrographs.

5.2 Current-Voltage Measurements

Analysis of DC transport across the patterned electrodes was carried out using a parameter analyzer (Hewlett-Packard 4156 precision semiconductor parameter analyzer). Current flow across the electrode gap is measured as a function of voltage drop across the electrode gap. These two terminal current measurements were accurate in the pA range and above.

5.3 Transmission Electron Microscopy of Composites

In order to determine the range of SWNT bundle diameters in the dried films, high-resolution transmission electron microscope (HRTEM) imaging was performed on composite films using an Hitachi

HF-2000 microscope. These films were prepared spin casting SWNT/PMMA/ODCB solutions onto holey carbon grids. The solutions used for spin casting onto the TEM grids was 2 to 4 times more dilute than the solutions described above to ensure that the polymer films would be thin enough.

5.4 Scanning Electron Microscopy of Composite Networks

SEM imaging of composite networks was performed to image nanotube bundles within the polymer film and also to conduct transport studies. Scanning electron microscopy was performed at various excitation voltages and with various surface potentials applied. The specimen current (SC) imaging technique was used as well to study electronic transport.

5.4.1 SEM Sample Stage

A custom built SEM stage was designed to provide a convenient way to bring electrical connections from outside the SEM vacuum chamber to electrodes on the sample surface. Photographs of the sample stage are shown in Figure 5.1. This stage fits through the same sample exchange chamber and into the sample stage holder in the same manner as standard sample stages. This design also permits ±30º rotation of the top of the stage while the electrical interconnects remain in tact. An eight pin electrical connector at one end of the sample stage mates with a second connector fixed permanently inside the

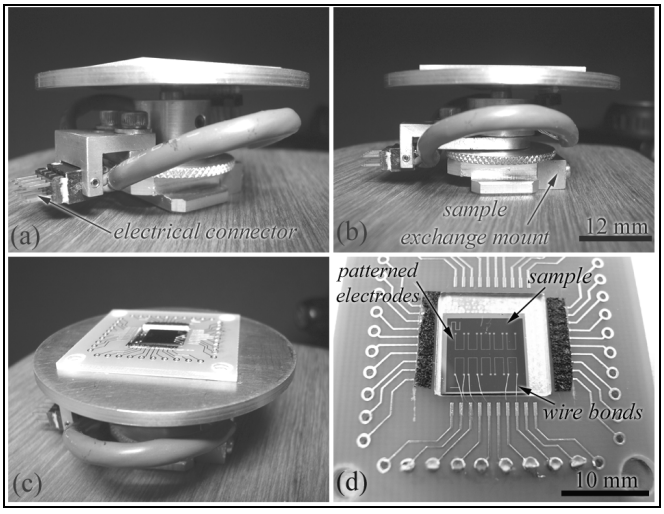

Figure 5.1. Photographs of the SEM stage

(a) view of the 8-pin electrical connector at the front of the stage.(b) side view. (c) view of sample mounted on the top of the stage. (d) closer view of electrodes on the sample surface and wire bonds

vacuum chamber. This permanent connector is attached to wires the lead to the outside of the SEM. Gold electrodes on the sample surface can be wire bonded to leads on the SEM stage.

5.4.2 Imaging while Applying Bias to the Sample Surface

Bias, on the order of several volts supplied by a voltage source (Keithley 6430) outside the SEM, was applied to electrodes on the sample surface. Nanotubes in electrical contact with these electrodes acquired some of this potential resulting in measurable changes in brightness of these nanotubes. Applying bias reveals embedded nanotube networks, their connectivity paths, and the distribution of potential throughout the network.

5.4.3 Specimen Current Imaging

In its normal mode of operation, the SEM generates images by measuring secondary electrons emitted from a sample surface while an electron beam raster scans the surface. The principle behind specimen current imaging is different. In SC imaging, electron are collected and measured directly from the substrate. The primary electrons in the rastering electron beam can induce current flow to or from the electrodes in the sample. A diagram of the SC setup is shown in Figure 5.2. One or both of the embedded electrodes are connected to ground via a current amplifier (GW Type 31). The signal from the current

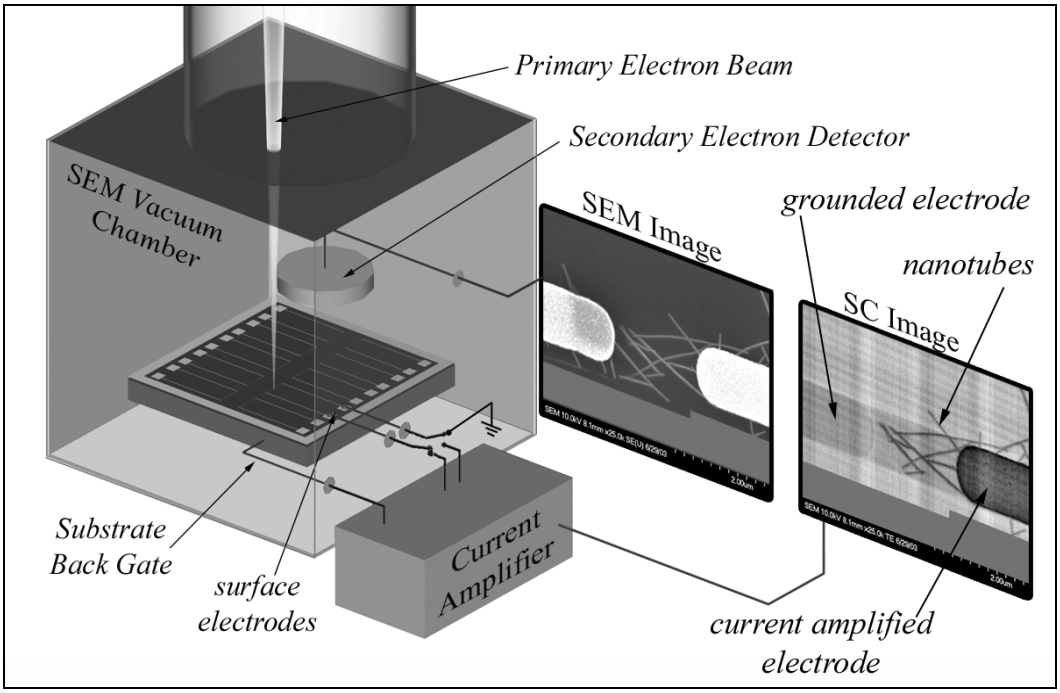

Figure 5.2. Diagram of setup for specimen current imaging

amplifier is displayed concurrently with information from the secondary electron detector. If the beam is incident on a region of the substrate connected to the current amplifier, current will flow resulting in a change of contrast in the SC image. The flow of electrons out of the sample through the amplifier, defined as a negative current, appears dark in the SC image, while positive current appears bright. Portions of the sample not connected to the amplifier appear as a mid-toned gray. Figure 5.2 illustrates an SC configuration in which one of the patterned electrodes on the substrate is connected to the current amplifier while the other is connected directly to ground. The incident primary electron beam induces electrons to flow out from the substrate and through the current amplifier. The resulting SC image shows which electrode is connected to the amplifier and, more importantly, which nanotubes are connected to that electrode.

Nanotube networks embedded in thin polymer films are particularly well suited to analysis by SC imaging for two reasons: first, because the generation volume of the secondary electrons is restricted by the sample thickness, and second, since the nanotube bundles form the only electrical path through the composite, the generation volume is further restricted to the dimensions of the nanotube bundles. For these reasons, thin film nanotube networks provide the conditions to form remarkably high resolution SC images containing spatial information nearly as fine as in standard SEM imaging but containing additional information about transport properties.

5.5 Measurements Using the Scanning Probe Microscope

SEM and SC imaging provides a means of measuring potential distribution when the applied bias is constant. Scanning Impedance Microscopy (SIM) can be used to measure the behavior of the network driven by an AC bias. Frequency-dependent electrical transport of conducting networks in carbon nanotubes composites was studied by SIM. This technique allows current flow through the nanotubes inside a polymer matrix to be imaged directly and provides a non-invasive approach to study transport in these materials. Both voltage oscillation *amplitude* and *phase lag* distribution throughout the network can be measured and imaged.

A standard AFM (Digital Instruments MultiMode NS-IIIA) was used to perform topographic imaging of sample surface. A function generator (Stanford Research Systems, DS340) and lock-in amplifier (Stanford Research Systems, SRS 830) where used to provide the additional functionality needed for scanning impedance microscopy. Gold coated AFM tips (Micromasch, NCSC 12 Cr-Au, spring constant = 1-5 N/m) were used for measurements. The gold coating is needed in order to maintain the AFM tip at a prescribed voltage.

An illustration of the experimental setup and the steps involved in SIM measurements are shown in Figure 5.3. SIM uses to interleaved passes when scanning. Surface topography is determined in a first

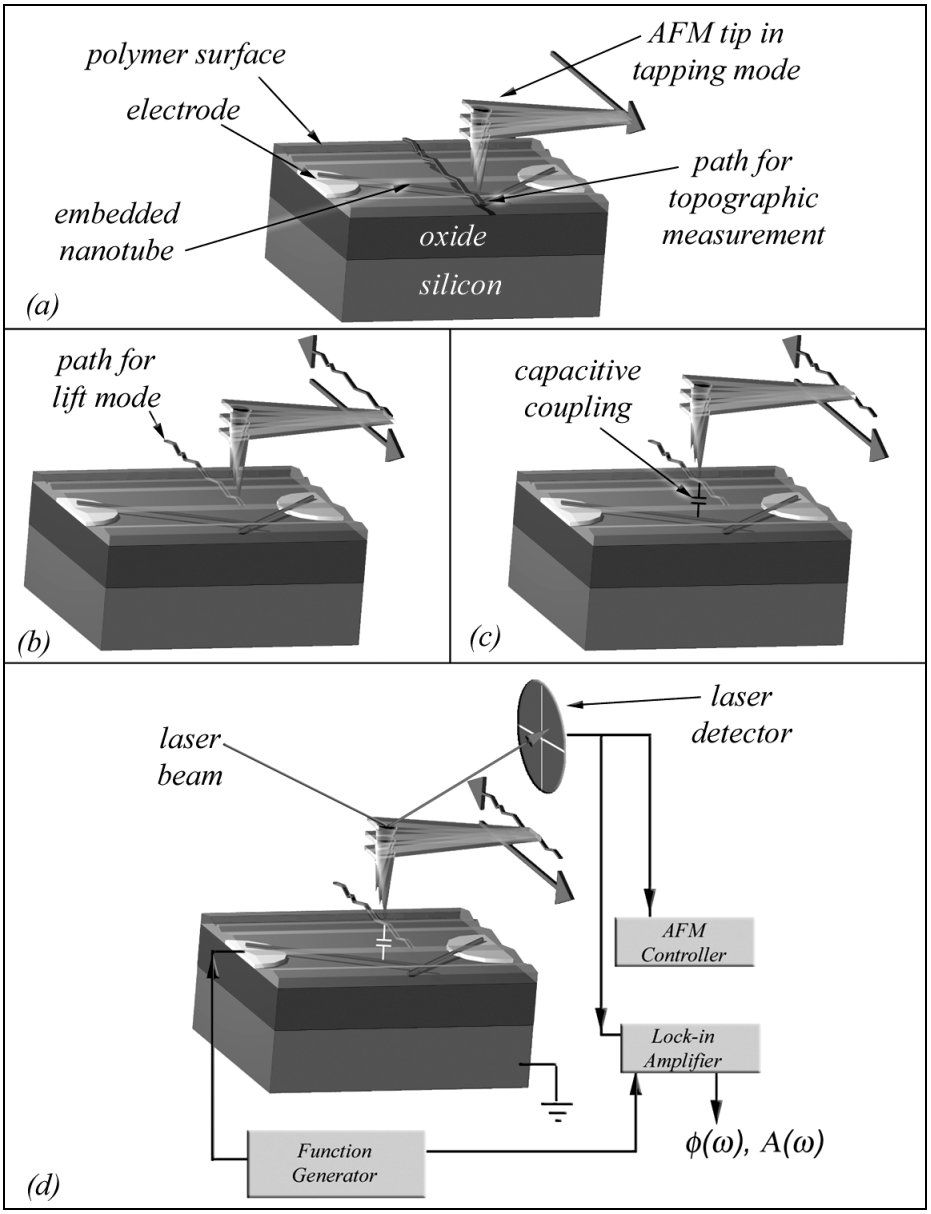

Figure 5.3. Diagram of SIM technique

The SIM scanning probe technique requires two passes of the AFM tip to collect information. (a) The first pass records topographic data. (b) Then, the tip is lifted ~100 nm above the surface, and traces the same line as the previous scan, except in the opposite direction and at a constant distance from the surface. (c) Capacitive coupling can occur between the tip and a conductive region within the substrate. (d) Setup used for generating and amplifying the impedance signal.

trace, (a), while in standard intermittent contact (tapping) mode. The tip is retracted slightly and then retraced along the same line as in the topographic measurement. The height of the tip above the surface is held constant while following the surface topography, as shown in (b) and (c). The lift height for the retrace scan is usually ~100 nm. The scan rate varied from 0.5 Hz for large scans (~80 μm) to 1 Hz for smaller scans (~10 μm). Phase and amplitude data are collected during the retrace. If the tip is in close proximity to a conductive region near the surface of the substrate, the applied oscillating voltage of the surface capacitively couples with the AFM tip and results in a periodic force on the cantilever and an oscillating mechanical deflection.

Figure 5.3(d) shows how the impedance signal is generated and collected during the retrace. A function generator is connected to one or both of the patterned electrodes and provides the driving voltage, V_{ac}, to the nanotube network. A timing signal from the function generator is also fed to the lock-in amplifier. Except for the fact that the tip has been raised during retrace, the AFM operates normally. That is, a laser beam is reflected from the top of the AFM tip and the degree of deflection is detected by a position detector. The amount of deflection is directly proportional to the force applied to the AFM tip. Therefore, deflection of the tip due to tip-surface capacitive forces can be measured. However, this signal due to surface potential oscillation is relatively weak and, if it is to be of any use, must be distinguished from other influences. The purpose of the lock-in amplifier is to do just that. It amplifies only those components of the signal oscillating at the specific frequency of the output of the function generator. The output from the lock-in amplifier is a filtered signal composed exclusively of information on the force induced on the AFM tip when it encounters a region electrically connected to the function generator. The lock-in amplifier provides both the amplitude and phase lag of the impedance induced signal, and this information is combined with information on lateral tip position to build amplitude and phase maps of the surface.

CHAPTER 6 EXPERIMENTAL RESULTS 0F SWNT TRANSPORT STUDIES

6.1 Results of TEM Studies

In order to determine the range of SWNT bundle diameters in the composite films, high-resolution transmission electron microscope (HRTEM) imaging was performed on composite films which were formed by spin casting SWNT/PMMA/ODCB solutions onto holey carbon grids. Figure 6.1 shows TEM micrographs of SWNT bundles in PMMA. While individual SWNT's or small SWNT bundles are present, typical nanotube bundles range between 10 nm to 20 nm in diameter. Figure 6.1(a) shows a bundle which is approximately 20 nm in diameter. Figure 6.1(b-c) show a region of the polymer which has torn to expose nanotubes within the polymer. In these later cases, single walled nanotubes can clearly be seen.

6.2 Results of SEM Studies

6.2.1 Variations of the Incident Beam Excitation Energy

The experimental setup provides the ability to control directly the voltage of the electrodes and conductive elements connected to the electrodes. However, some insight into the electronic properties of the composites can be gained by leaving the electrodes unconnected and varying the beam excitation voltage. Variation in excitation voltage changes the average kinetic energy of incident primary electrons, and this in turn affects the secondary electron (SE) yield from a material. Experimental results show there to be a reversal in contrast within conducting components of the composite when the excitation voltage is varied between 1 kV and 20 kV.

The images in Figure 6.2 illustrate the resulting change of contrast between the polymer and nanotubes. At a 1 kV excitation voltage, shown in Figure 6.2(a), nanotubes connected to the electrodes appear dark. Also, the dark region around the nanotubes extends about 75 nm to either side of the nanotube. The thin white core which is visible at the center of the dark halo in some of the bundles is likely due to nanotubes that have breached the top surface of the polymer and are exposed to the beam directly.

In Figure 6.2(b), a 10 kV excitation voltage was used, and the sample appears quite differently. The bundles are lighter and appear thinner with an apparent diameter closer to their actual diameter. The surrounding polymer is darker. Nanotubes not connected to the electrodes are barely visible and are brighter than the surrounding polymer.

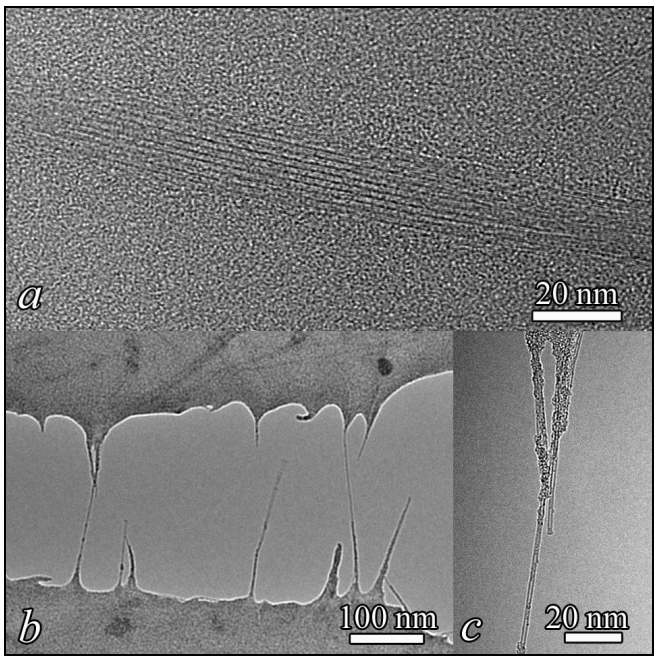

Figure 6.1. TEM images of SWNT's in PMMA

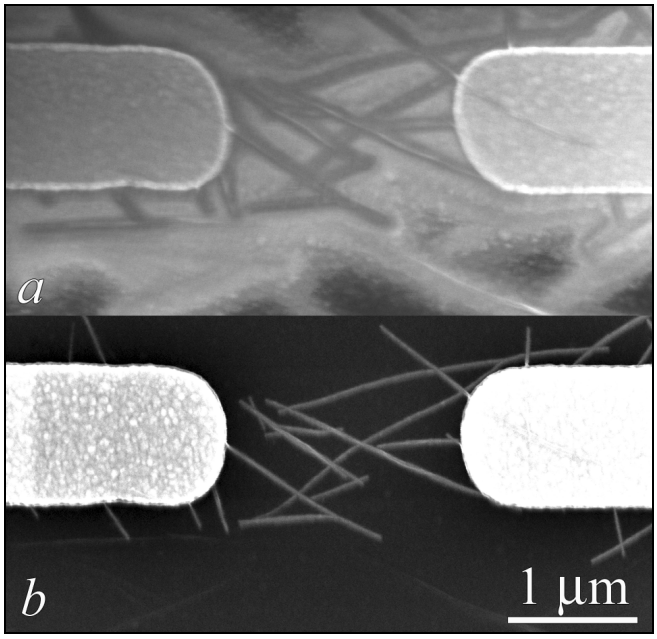

Figure 6.2. SEM image of SWNT bundles at two different primary beam excitation voltages (a) 1 kV and (b) 10 kV.

6.2.2 Variation of the Applied Surface Bias

Figure 6.3(a-f) shows a series of SEM images taken over a range of applied biases. In each of these images, both electrodes were held at the same bias relative to one another therefore insuring that all connected nanotubes are at the same bias. The applied voltage is measured relative to the silicon back gate held at the same potential as microscope ground. When bias is applied to the electrodes, a resulting change in brightness is observed in both nanotubes and the gold electrodes. In this series of images, the settings for brightness and contrast control were constant. Figure 6.3(a) is the only image in this series for which a positive bias was applied. The electrodes are hardly visible, and the nanotubes are indiscernible from the background. The nanotubes become faintly visible in Figure 6.3(b) when grounded to the back gate. Brightness of conductive regions steadily increases in Figure 6.3(c-d) and reaches a maximum brightness at -15 V in Figure 6.3(e). A further increase in negative bias to –20V results in a decrease in brightness as seen in Figure 6.3(f).

These voltage induced contrast results have been quantified by defining brightness as the difference in the value, as measured on an 8-bit scale, of a pixel and the average value of the background pixels. A computer program was written so that user defined boundaries indicate the pixels within the image corresponding to the nanotubes and those belonging to the background . The *average brightness* over all of the nanotubes has been determined over a range of bias conditions and are plotted in Figure 6.3(g). The units of brightness are arbitrary and the curve has been normalized relative to the point of greatest brightness. The points on this curve corresponding to the images (a) – (f) are indicated. A model will be presented later to explain the origin and nature of the surprisingly sensitive response to the small applied biases. However, the curve in Figure 6.3(g) is very useful in itself in that it provides a means to relate pixel brightness to surface potential directly. With this information, one can generate a map of surface potential over a range of bias conditions from just an SEM image.

Transport measurements can be performed if the bias between the two electrodes is different. Results of this are shown in Figure 6.4. In Figure 6.4(a), both electrodes are held at the same potential. In Figure 6.4(b), the left electrode is grounded and the right electrode is biased to –20 V. Figure 6.4(c) shows opposite bias condition with the right electrode grounded and the left electrode at –20 V. In both of these images, there is a gradient in brightness of the nanotube bundles between the two electrodes. This results directly from the fact there is a gradient in potential across the nanotube network. Image processing utilizing the information in Figure 6.4(a-c) can lend further insight into electronic transport. This is shown in Figure 6.4(d) which was formed by subtracting Figure 6.4(b) and Figure 6.4(c) from Figure 6.4(a). This simple image processing procedure distinguishes the nanotubes participating in current flow through the network from those merely attached to one or the other electrode and also provides information as to their relative degree of participation.

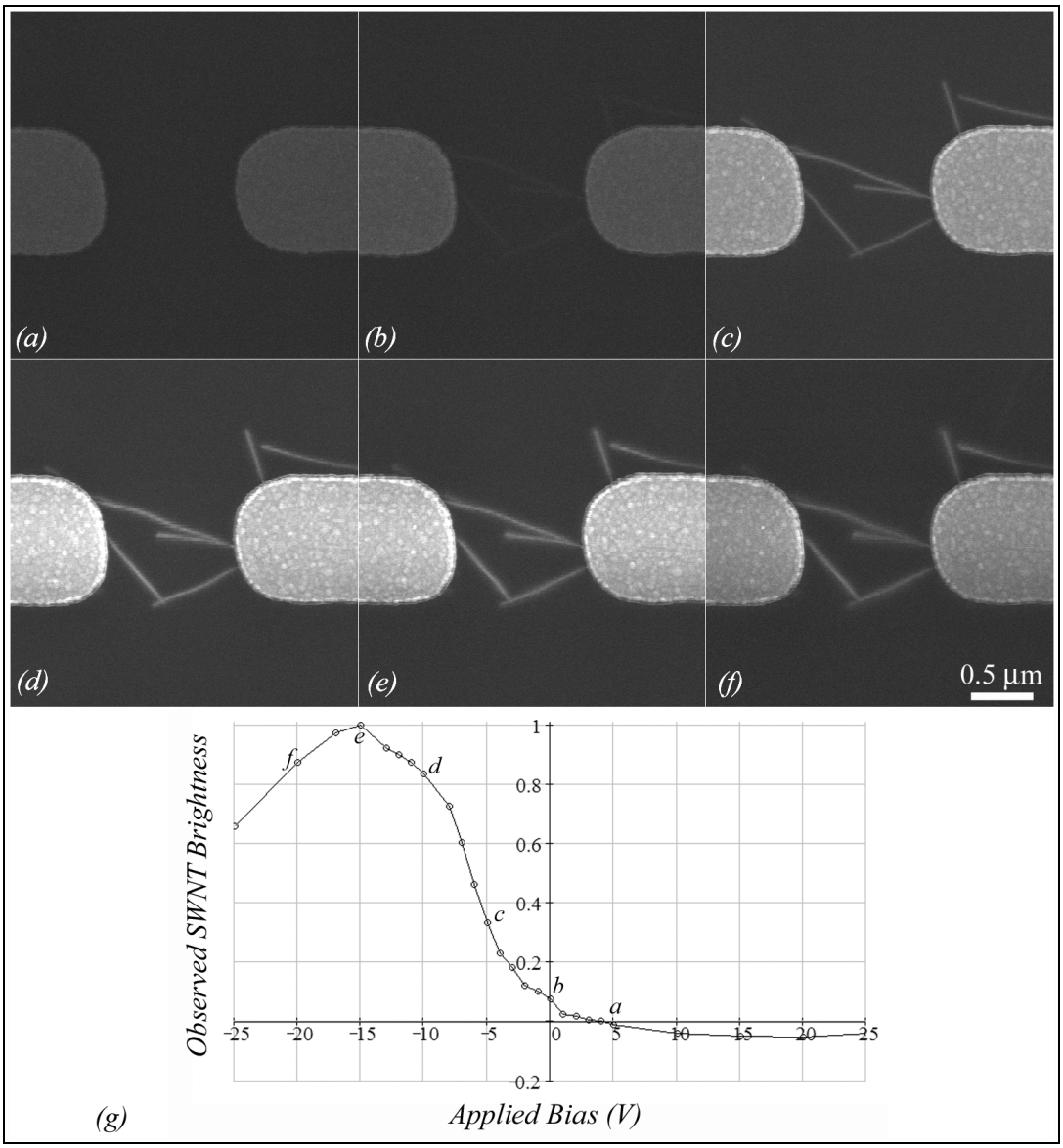

Figure 6.3. Results of measuring the effects of applied bias in the SEM

Equal bias was applied to both electrodes. (a-f) SEM images of SWNT bundles in PMMA with applied biases of (a)+5 V, (b) 0 V, (c) 5 V,(d) 10 V,(e)15 V, (f) 20 V relative to the back gate. (g) plot of the normalized measured brightness of nanotube bundles as a function of applied bias.

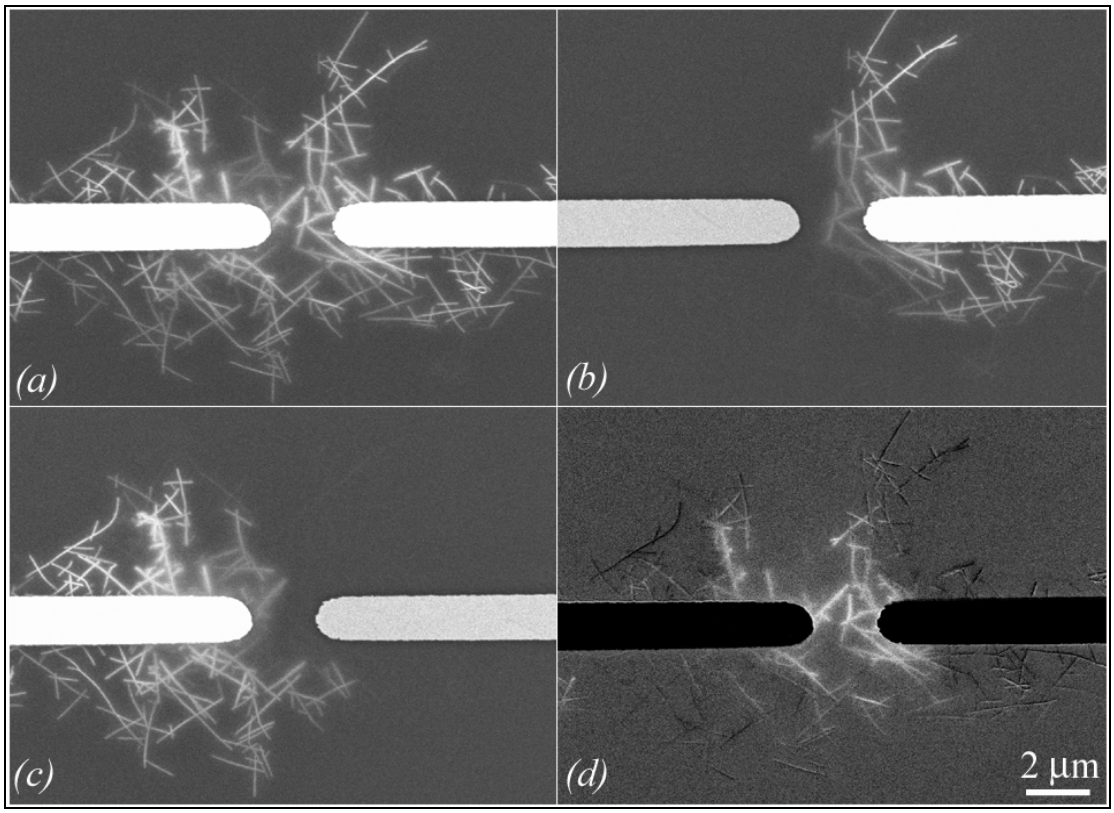

Figure 6.4. SEM images of nanotube/polymer composites under various bias conditions.

(a) both electrodes at –20 V. (b) left electrode grounded, right electrode at –20 V. (c) right electrode grounded, left electrode at –20 V. (d) Image formed by subtracting (b) and (c) from (a) revealing viable current pathways.

6.2.3 Specimen Current Imaging

Figure 6.5 shows a series of specimen current (SC) images for the same nanotube network shown in Figure 6.2 and illustrates the effect of beam excitation energy on current flow. Two primary electron energies, 1 kV in Figure 6.5(a-b) and 10 kV in Figure 6.5(c-d), were used to generate SC images for two different electrical connection configurations. In Figure 6.5(a and c), the left electrode is connected to ground, and the right electrode is connected to a current amplifier. Figure 6.5(b and d) shows results when the right electrode is connected to the amplifier. Since the magnitude and direction of current flow is represented as brightness in SC imaging, information about beam/composite interactions can be ascertained. When a 1 kV excitation is used, the nanotubes in Figure 6.5(a-b) appear lighter than the background indicating that electrons are flowing from ground, through the amplifier, to the nanotubes. In Figure 6.5(c-d), the fact that the nanotubes appear darker than the background implies that electrons are flowing out of the nanotubes towards ground. This particular sample has very low conductivity and this fact is apparent in the SC images. Current flow, from the beam, through the nanotube network, is localized to either one electrode or the other, and there is a clear boundary within the network showing with which electrode a nanotube bundle is associated.

A case in which a sound connection exists through a network between two electrodes is shown in Figure 6.6. The only difference between Figure 6.6(a) and Figure 6.6(b) is the electrode connected to the amplifier. What is important to note in this image is that there is a gradient in brightness, and thus a gradient in the amount of current flowing to the amplifier through the nanotube. At first glance, this might appear to violate Kirchhoff's current conservation law if the nature of the information that SC images provide is forgotten. SC imaging does not give information about current flow from one electrode to the other, but rather current flow from the incident electron beam to the amplifier. One must not forget that the electron beam acts as a third branch in the circuit. SC imaging reveals how many electrons, generated by the beam/surface interaction, travel to the amplifier from a given location on the surface. The network in Figure 6.6 acts as a voltage divider, splitting the beam induced current to flow either straight to ground through the grounded electrode, or to ground via the amplifier thus showing up as a contrast change in the SC image.

6.3 Results of Scanning Probe Microscopy Studies

Surface topography and SIM amplitude images of the polymer-embedded nanotube network captured at a driving frequency of 1 kHz are shown in Figure 6.7 along with an SEM image of the same sample. The surface topography images in Figure 6.7(a-b) exhibit height variations at the locations of some of the nanotube bundles. However, the topology of the full network can not be determined from

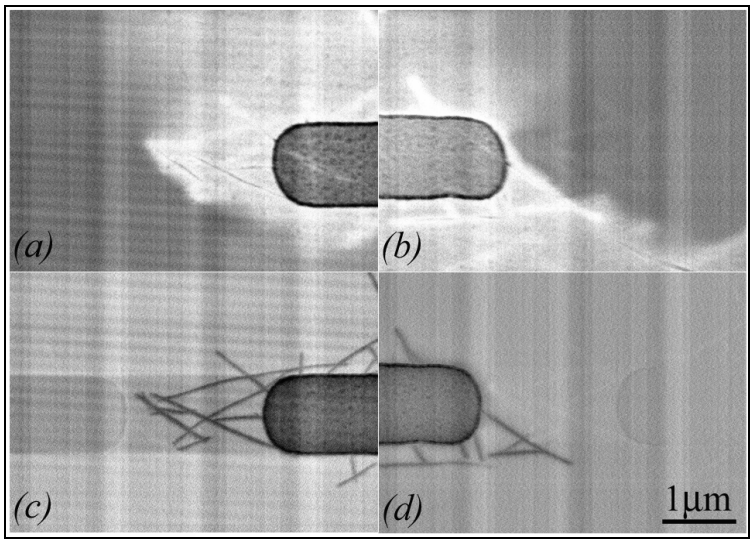

Figure 6.5. A series of SC images taken at different incident beam voltages

(a) 1 kV excitation, current through right electrode amplified, (b) 1 kV excitation, left electrode amplified, (c) 10 kV excitation, right electrode amplified, (d) 10 kV excitation, left electrode amplified.

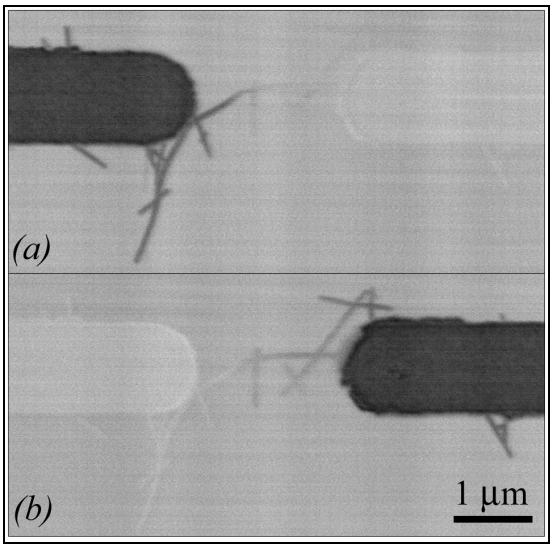

Figure 6.6. SC images taken illustrating a gradient in current flow across the network

(a) right electrode grounded, left electrode amplified, (b) left electrode grounded, right amplified

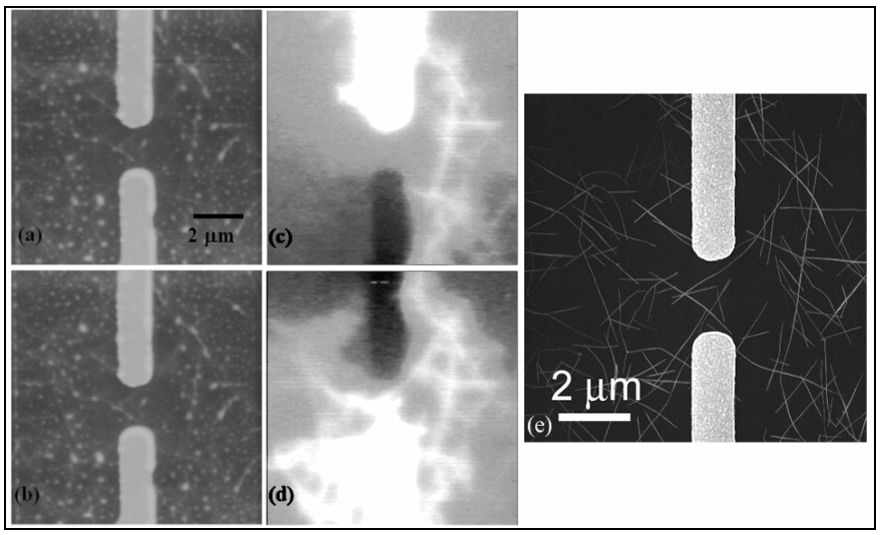

Figure 6.7. AFM, SIM, and SEM images of nanotube polymer composites

(a,b) AFM topographic maps of the composite top surface under difference bias conditions.(c) SIM image in which the top electrode is biased. (d) SIM image in which the bottom electrode is biased. (e) SEM image of the same sample showing all nanotube bundles which are present.

topographic data alone due to the roughness of the polymer. Compare the number and position of nanotubes in Figure 6.7(a-b) to the true count indicate in the SEM image in Figure 6.7(e). The SIM amplitude images in Figure 6.7(c-d) indicate voltage potential distribution throughout the network for the differently biased conditions. In Figure 6.7(c), the top electrode has been biased, and in Figure 6.7(d), the bottom electrode has been biased. The SIM method allows access to measure electronic transport inside the 100 nm thick polymer layer.

Further information on frequency-dependent transport behavior through nanotube networks can be obtained from combined SIM phase and amplitude data. Illustrated in Figure 6.8 are larger scale SIM amplitude and phase images in dual, bottom, and top biased electrode configurations. The amplitude decays as the distance from the biased electrodes increases. This is the case even in the dual-electrode configuration Figure 6.8(a). This is unexpected, since there is an apparent lack of current sinks in the nanotube network. SIM phase lag images shown in Figure 6.8(b,d,f) clearly exhibit significant phase variations along the network. The phase shift is chosen to be zero at the electrodes by setting the lock-in amplifier accordingly, but there is a significant phase shift between the nanotubes and the electrode which can be as much as 20˚. The phase distribution along the network is non-uniform and generally increases as the separation from the contact increases.

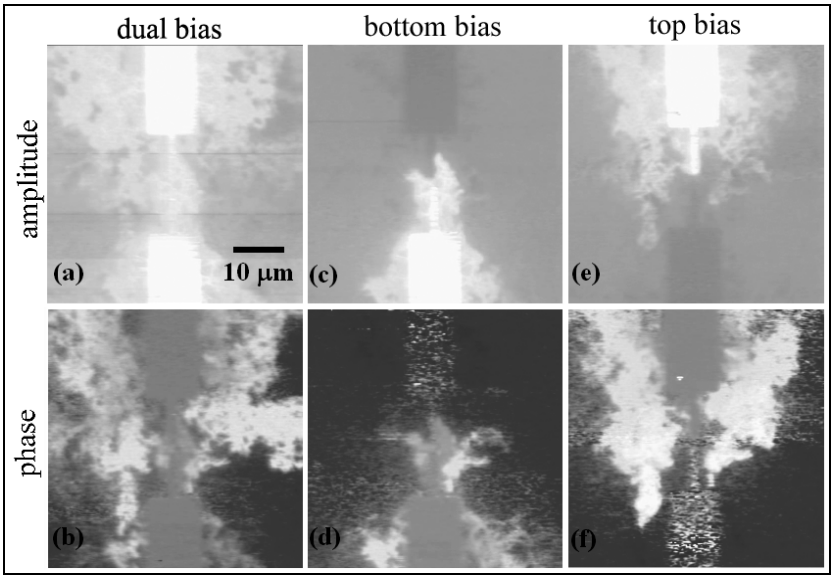

Figure 6.8. SIM images of phase and amplitude data for three different bias conditions

(a,b) amplitude and phase data for dual bias condition. (c-d) bottom biased condition. (e-f) top biased condition.

In order to quantify the phase lag behavior, the frequency dependence of the average phase lag at 20 μm separation from the contact was measured and plotted in Figure 6.9. At low frequencies below 50 kHz, this phase lag is shown to be proportional to square root of the driving frequency as indicated by the slope of the linear best fit curve.

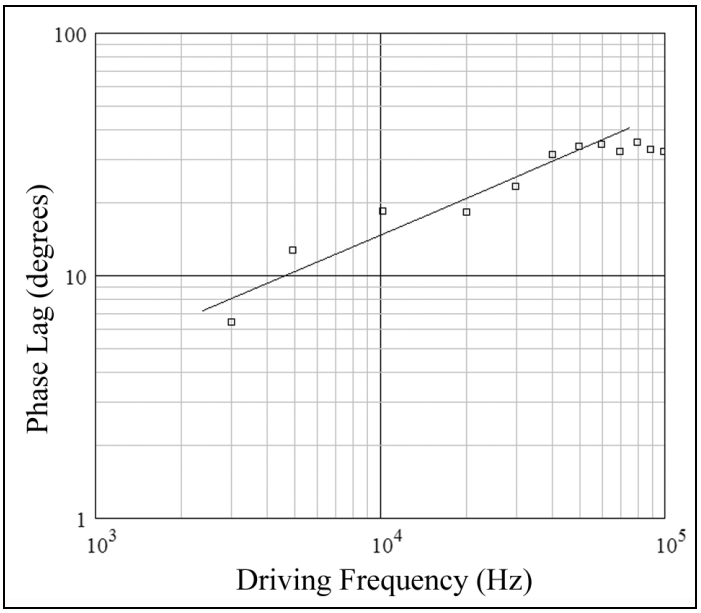

Figure 6.9. Plot of phase lag as a function of driving frequency

Measurements taken at a distance of 20 μm from an electrode over a range of driving frequencies. The linear fit indicates that the phase lag is proportional to the square root of the driving frequency.

CHAPTER 7 DISCUSSION OF RESULTS AND MODELING FOR NANOTUBE-COMPOSITE TRANSPORT STUDIES

7.1 Discussion of Non-linearity and Rectifying Behavior in Current-Voltage Measurements

Micron scale transport measurements through single walled carbon nanotube composites show that this system can exhibit both non-linear and asymmetric current-voltage (I-V) relationships. A model based on quantum tunneling current and network geometry has been developed which explains the reasons for the unusual electrical response of this system. It will be shown that the rectifying behavior is not due to semi-conducting properties of any of the components, but rather is a result of the interaction of conductors and insulators whose critical dimensions are on the nanometer scale. The electrical characteristics can be described very well by considering the combined effects of quantum tunneling through very thin insulating barriers, the Fermi-levels of the components, and most importantly, the geometry of the insulator/conductor composite.

Percolation through composite networks, like the ones considered here, are characterized by extensive regions of highly conductive additives, joined together at junctions, but separated from one another by much smaller insulating barriers of polymer. An illustration of such a network is shown in Figure 7.1. Transport through the barriers is mediated by electron tunneling and is therefore highly sensitive to the width of the polymer gap. Tunneling is the source for the non-linear I-V response of the network.

Network topology can play a role in the overall response of the system. If one considers a network in which all of the junctions have the same gap width, network topology can act to either magnify or mitigate the effects of tunneling. A highly serialized network will magnify the effects of tunneling since the junctions resistances will be additive, but a highly parallel network will act to mitigate the effects of tunneling since the total area over which tunneling can occur will be additive, thus increasing the probability for tunneling.

The simplified Fowler-Nordheim equation, equation 7.1, has been used to estimate tunneling current across the polymer barrier. This equation takes into consideration the Schottky effect in which high electric fields, like the ones developed across the polymer gaps between nanotubes, can act to effectively reduce the work function of conducting species thus further facilitating current flow. In addition, the shape of the emission surface is considered as well since the high curvature of the nanotube bundle acts to increase field strength.

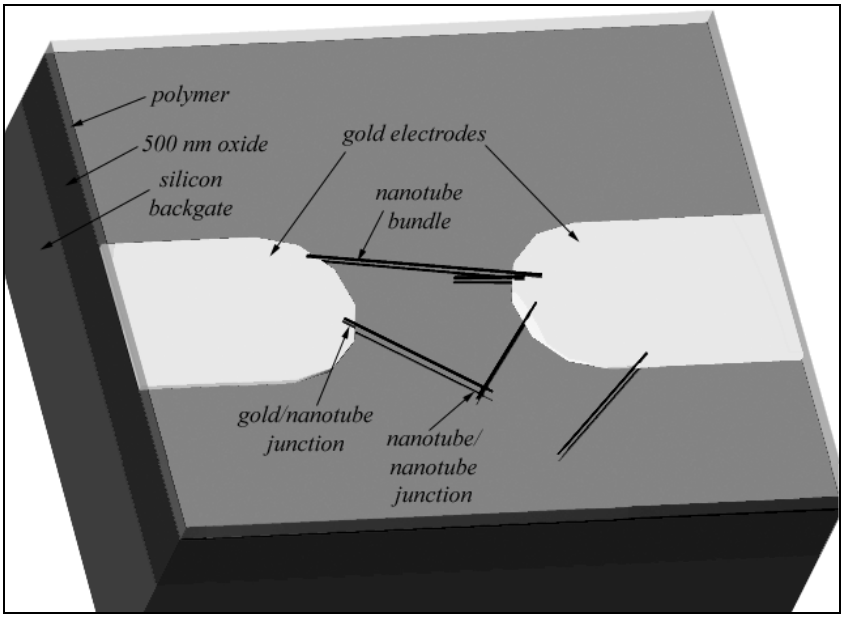

Figure 7.1. Illustration of a sample substrate

$$I(V_a) = q \cdot n \cdot A_c \cdot v_R \cdot exp\left[\frac{-E_c(V_a)}{E(V_a)}\right]$$

equation 7.1

In this equation, q is electron charge, n is mobile charge density, A_c is the area of the contact, and v_R is the Richardson velocity which estimates average electron speed within the emitter perpendicular to the emission surface. E is the applied field at the junction as a function of V_a, the voltage drop applied across the junction. E_c is the critical field for tunneling and is given in equation 7.2,

$$E_c = \frac{4 \cdot \pi \sqrt{2 \cdot m_e \cdot \Phi_{eff}(E)} \cdot \Phi}{q \cdot h}$$

equation 7.2

where h is Boltzmann's constant, m_e is electron mass, Φ is the height of the potential barrier. Φ_{eff} is the effective potential barrier and in given in equation 7.3 where ε_o is permittivity of free space.

$$\Phi_{eff} = \Phi - \sqrt{\frac{q^3 \cdot E(V_a)}{4 \cdot \pi \cdot \varepsilon_o}}$$

equation 7.3

In order to facilitate current analysis of the network, the tunneling barriers will be described in terms of their resistance as a function of applied voltage by using Ohm's law, so that

$$R(V_a,) = V_a / I(V_a,)$$

equation 7.4

It is important to consider the effects that tunneling between two dissimilar metals will have on the system response. At a nanotube/polymer/gold junction, dissimilar metals sandwich the polymer and the difference in work function of the two metals must be taken into account. It should be noted that the bundles are considered to be metallic since the ~1.4 nm diameter nanotubes tend aggregate into bundles of between 10-20 nm. Within the approximately 50 – 200 nanotubes composing a single bundle, there are enough metallic nanotubes, around 33%, to render the entire bundle metallic. The difference in work function across the junction generates a built-in field across the insulator that can act either with or against the applied field. Since it is treated as an additive factor to the applied field, work function mismatch has the effect of shifting the I-V curve along the *Voltage*-axis.

The shift in the I-V response is one critical component in explaining the rectifying behavior evident in these experiments. Its role will be demonstrated using the simplest possible composite network – a single nanotube bundle bridging two gold electrodes. A diagram of this network is shown in Figure 7.2(a). As illustrated, the width of the polymer, w, between the nanotube and each of the gold electrodes is different. This difference in width is the other critical component of rectification. An energy band diagram and the circuit diagram corresponding to the network is presented in Figure 7.2(b). Steps in the energy band diagram represent changes in the work function when moving from one material to another. The work function of gold is 5.3 eV, the work function of the nanotube bundle is taken to be the same as that for carbon, 5.0 eV, and the work function height for the polymer is and 4.68 eV, which is the energy difference between the vacuum level and the half-way position between the HOMO and LUMO energy bands for PMMA. w1 and w2 are the tunneling distances through the insulating polymer at either end of the network. The circuit diagram then is composed three resistors in series. R_{NT} is the resistance of the nanotube, which is treated here as a simple ohmic resistor. The magnitude of R_{NT} is considerably smaller than the other components and does not play much of a role in this analysis. R_1 and R_2 are non-linear components that simulate tunneling transport and are determined by combining equation 7.1 and equation 7.4. The equivalent resistance, R_{eq}, for this simple circuit is $R_1 + R_{NT} + R_2$, and the I-V response of the whole network is $I = V_a / R_{eq}$.

Figure 7.2(c-e) shows the I-V curve of this circuit for three different cases. In Figure 7.2(c), results are plotted if it is assumed that the tunneling barrier widths were the same, $w_1 = w_2 = 10$ nm. The individual I-V responses of R_1 and R_2 are plotted, and one can see the horizontal shift in the I-V curve due to work function mismatch. The response of the entire network, labeled R_{eq}, is plotted with a solid gray line. The response of this serial system is dominated by whichever component has the largest resistance.

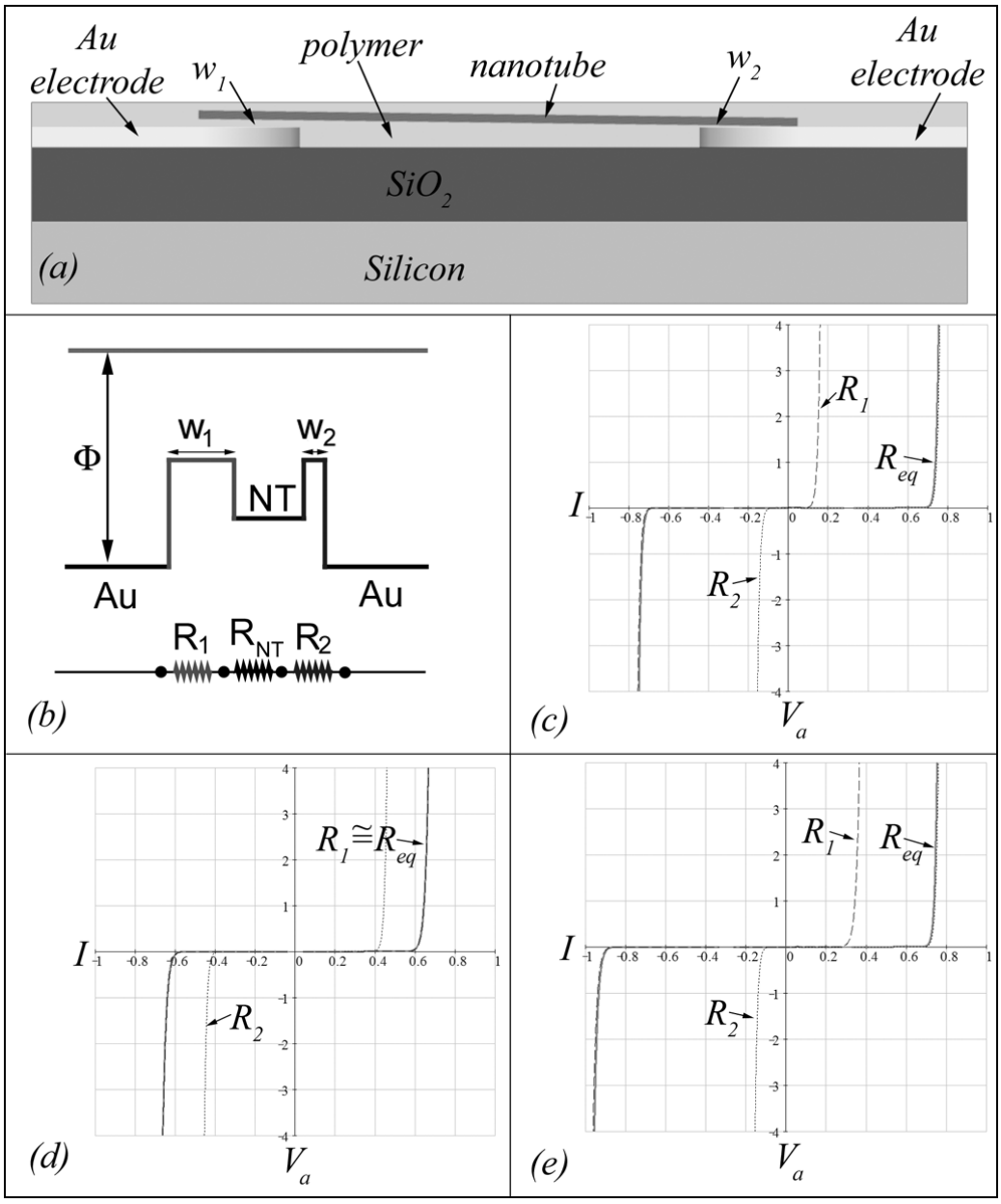

Figure 7.2. Rectifying behavior in nanotube composite experiments.

(a) diagram showing side-view of an nanotube embedded polymer bridging two gold electrodes. (b) Plot of work function vs. position within the network along with the corresponding circuit diagram. (c) Resulting I-V response if $w_1 = w_2$. (d) I-V response if work functions of the metals were the same. (e) Asymmetric I-V response resulting from the combined effects of different tunneling widths and work functions.

Combine this with the fact that small differences in either work function or tunneling widths can result in large swings in resistance of a junction and one can understand that the response of the network will nearly trace the outer bounds of the curves of the three components. The response of the network follows R_2 when V_a is positive, and R_1 when V_a is negative. The important point to be made here is that the response of this particular system is symmetric. The resistance encountered by current tunneling from gold to carbon while flowing from left to right is equal to the resistance when moving in the opposite direction.

Figure 7.2(d) shows the I-V response if it is assumed that the *work functions of the metallic components are the same*. However, the *tunneling widths are different* with w_1 = 15 nm and w_2 = 10 nm. In such a case, resistance across the network is dominated by the wider tunneling barrier, and again as in (c), the I-V response is symmetric.

Figure 7.2(e) illustrates the results of this analysis *if $w_1 > w_2$, and the work functions correspond to those is (b)*. In this case, the combined effects of difference in tunneling widths and potential energy steps results in current encountering less resistance when flowing in one direction compared to the opposite direction. A larger voltage is needed to achieve the same likelihood for tunneling from gold to carbon across w_1 than that when tunneling across w_2 in the opposite direction. The end result is that I-V response of system will be asymmetric, and if voltages, in the region between –0.8 V and 0.8 V, were applied, the system would exhibit rectifying behavior.

In summary, a possible explanation for the non-linear and rectifying electronic transport properties exhibited in the experimental results has been presented in which both geometric and material electronic factors are taken into account. In this model, the unusual transport behavior is not ascribed to any sort of semi-conducting properties of the constituent materials. Rather, it results from electronic tunneling across nano-scale insulating barriers between well conducting, metallic components. The main conclusion of this analysis is that a nano-scale geometric asymmetry, manifested as different tunneling widths, will result in an electronic transport asymmetry if there is a difference in work function between the electrodes and the nanotube.

7.2 Discussion of SEM Based Transport Studies

The electron microscope provides not only a means of imaging nanotubes embedded within a thin polymer layer but also the capability to image the distribution of voltage throughout a biased nanotube network with surprisingly high sensitivity. A model, termed here '*electric field induced contrast*' (EFIC), is proposed to explain the reasons behind the high sensitivity. Then, the mechanisms operating while imaging *unbiased* electrodes will be discussed. It will be shown that even though the electrodes in these 'unbiased' experiments are not connected to any outside voltage source, the characteristics of the incident beam can induce a bias in the sample so that some of results can be explained by the EFIC model.

7.2.1 Electric Field Induced Contrast

Scanning electron imaging involves raster scanning a finely focused electron beam, with an average kinetic energy on the order of 10's of keV, across the surface of a sample. Incident electrons from this primary beam enter the sample and can impart their kinetic to electrons within the sample. Some of these electrons will remain within the sample and dissipate their energy through multiple collisions. Others however, may exit the sample through the top surface and be emitted as secondary electrons (SE). An SE detector measures the number, not the energy, of secondary electrons and correlates this value to the position of the rastering beam to construct an image.

Types of Voltage Induced Contrast

Bias applied to regions of the substrate can influence the interaction of the beam and the substrate and affect the relative brightness of these regions. This contrast change is commonly called voltage contrast (VC). The literature suggests several possible causes for voltage contrast[65].

One type of VC deals with applied voltages that are on the order of kilovolts and arises because a material has a specific response curve that relates the yield of secondary electrons, δ_{SE}, to primary electron kinetic energy (E_p). An example of such a curve is presented in Figure 7.3. Secondary yield is the ratio of the number of emitted SE per incident primary electron. Two values of primary electron energy are of special note since they result in a SE yield equal to one. This implies that at these energies, the number of incident electrons equals the number of emitted electrons. In this plot these are labeled E_{p1} and E_{p2}. E_{p1}

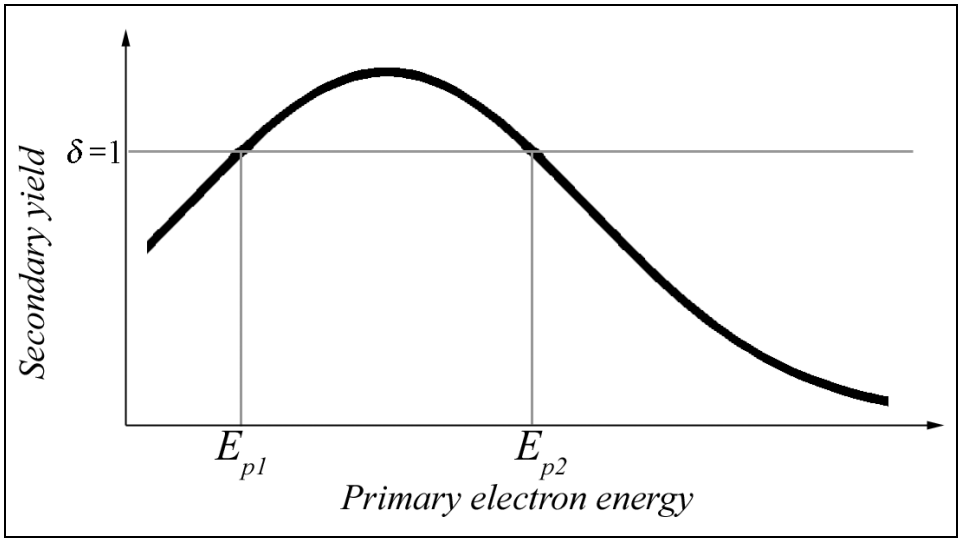

Figure 7.3. Plot of secondary yield as a function of primary electron energy

usually occurs the sub keV range, and E_{p2} is normally within the 1 keV to 5 keV range. One type of voltage contrast can occur if the bias of the substrate is large enough to retard or accelerate incident electrons so as to significantly change their kinetic energy. A large enough change in primary energy would change the SE yield according to the curve in Figure 7.3, and this change in yield is observed as a change in brightness in the SEM image. However, the applied biases used in transport measurements here rarely exceeds 20 V, so this VC mechanism is not applicable.

A second type of voltage contrast can occur if the applied voltage introduces a shift in the secondary electron energy distribution as depicted in Figure 7.4. The shape of the spectrum is described very well by the Chung-Everhart equation[66],

$$\frac{d}{dE_S}n = \alpha \cdot \frac{(E_{SE} - E_F - \Phi)}{(E_{SE} - E_F)^4}$$

equation 7.5

in which α is a material constant, E_{SE} is the secondary electron energy, E_F and Φ are the Fermi energy and work function of the material, respectively. n is the number of electrons emitted. Applying a voltage has the effect of changing the Fermi energy directly, and will, according to equation 7.5, result in a horizontal shift of the energy spectrum. Figure 7.4 shows three spectra for three different bias conditions, unbiased, +5 V,

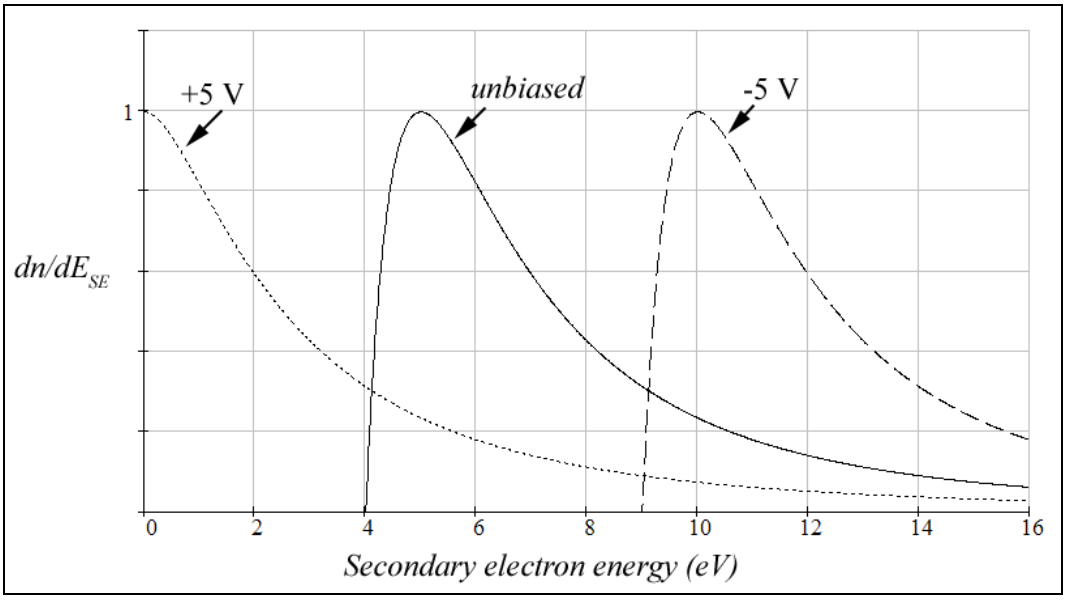

Figure 7.4. Voltage induced shift in the energy spectrum of secondary electrons

and – 5 V. Under these conditions, the only way that voltage can affect contrast is if enough positive bias is applied so that the part of the spectrum, with energy less than 0 eV, is removed. If a negative bias is applied, the shape of the spectrum, and therefore the number of electrons, remains unchanged and no change in contrast takes place. Experimental results, see Figure 6.3, show a very noticeable change in brightness when negative bias is applied, which means that some other factor is at play influencing the shape of the spectrum. It should be noted that if one uses an SE detector in combination with an energy analyzer and measure both the number and energy of electrons, it is possible to measure minute shifts in the peak of the energy spectrum and from this, ascertain surface potential.

One other type of voltage contrast can occur if the shape of the biased region is such so as to deflect slow moving, low energy secondary electrons away from the detector. This is not likely to be an important factor in the experiments in this study since the measured change in brightness is independent of the position of the sample inside the SEM. Neither the angle of the sample nor its distance from the detector appear to have an effect on contrast.

Electric Field Induced Contrast

The previous discussion on explanations for voltage induce contrast found in the literature revealed that they are not sufficient to properly predict the experimental results of this project. A slightly different approach has been taken here in which the fact that, for the samples used in experiments, the applied bias does not only result in a change in surface potential, but as shown in Figure 7.5, is also

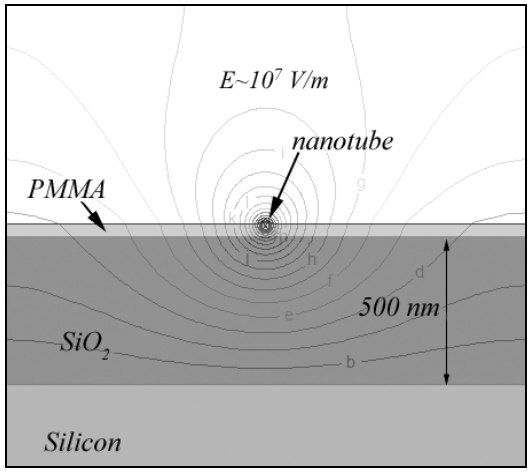

Figure 7.5. Illustration of a cross-sectional view of a biased test sample

A strong electric field is generated a the surface of a 20 nm diameter nanotube bundle, biased at 1 V, and the silicon backgate. Equipotential field lines are shown maximum field strength ~10^7 V/m.

responsible for generating an electric field.

Illustrations of a typical sample, in Figure 7.1 and also Figure 7.5, shows that the nanotube bundles and the gold electrodes are separated from the silicon backgate by an approximately 500 nm thick layer of silicon oxide. The potential of the back gate can be adjusted but is normally grounded. With only a relatively small bias, on the order of volts, applied to the conductive elements on the top surface, a significant electric field is produced across the oxide layer. For a nanotube with a diameter of ~20 nm, field strengths on the order of 10^7 V/m are generated at the surface of the bundle. Under such conditions, the Schottky effect, given in equation 7.3, becomes appreciable resulting in an effective shift in the work function of the material. According to the Chung-Everhart equation, equation 7.5, a change in Φ will influence the energy distribution of secondary electrons.

Figure 7.6 shows the results of including the Schottky effect into the Chung-Everhart equation. With the electric field effect included, an applied voltage has the effect of not only moving the emission spectrum along the energy-axis, but also changing its shape (compare with Figure 7.4). The more negative the applied voltage, the larger the drop in the effective work function will be, which results in an enhanced emission of secondary electrons. This effect is evident in the fact that the SE spectrum for an applied bias of –5 V is larger than in the unbiased case. Since the SE detector counts only the number of electrons, not their energy, regions with a negative surface potential appear brighter, consistent with experimental results.

An estimation of the change in brightness as a function of applied voltage can be made by

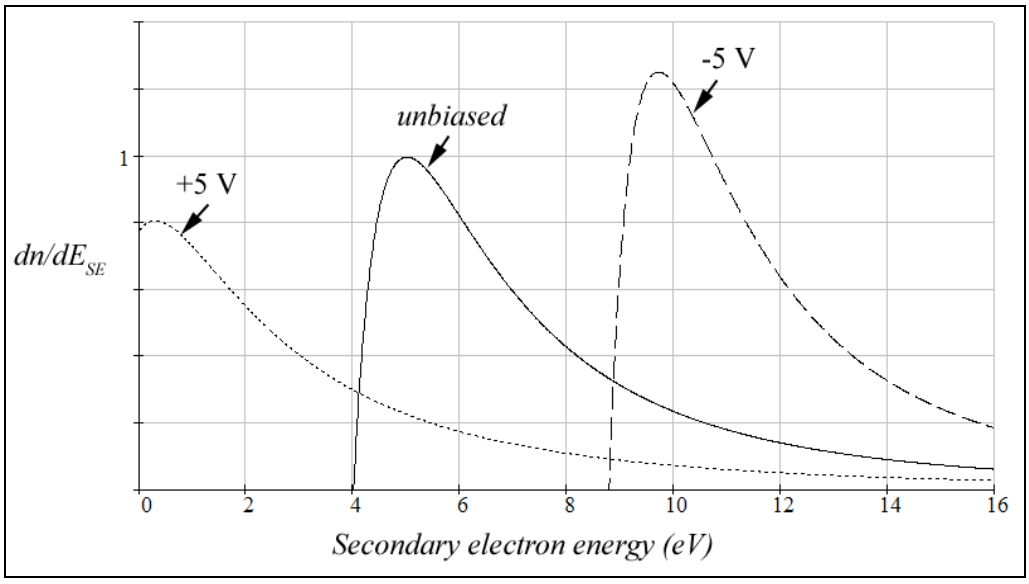

Figure 7.6. Plots of the SE emission spectra with the Schottky effect considered

integrating the emission spectra to find the total intensity over a range of bias conditions. In this calculation it is also necessary to take into account the response characteristics of the SE detector. A plot of this relation along with experimental results are shown in Figure 7.7. There is reasonable agreement between experimental results and the EFIC model. The detector response is included in order to account for the drop in brightness at large negative voltages. With the detector response included, the EFIC model alone would predict a continuously increasing brightness with larger negative surface potential.

Now that a relationship between bias and brightness has been established, it is possible to calibrate SEM images and render maps of surface potential. This is shown in Figure 7.8. The background, and most of the electrodes have been removed for clarity. Two bias conditions are shown. In (a), the left electrode is -10 V and the right electrode is grounded, and in (b), the opposite bias condition is shown. This particular sample is an example of a network in which the electrical interconnections between gold contacts and the nanotube and between nanotube bundles are quite good. But, a slight asymmetry in conduction is evident. The connections between the network and the right electrode show an approximately 1.5 V drop across either junction, but there is a ~3 V drop across the bundles connected to the left electrode. This asymmetry is also evident in the I-V response of this network.

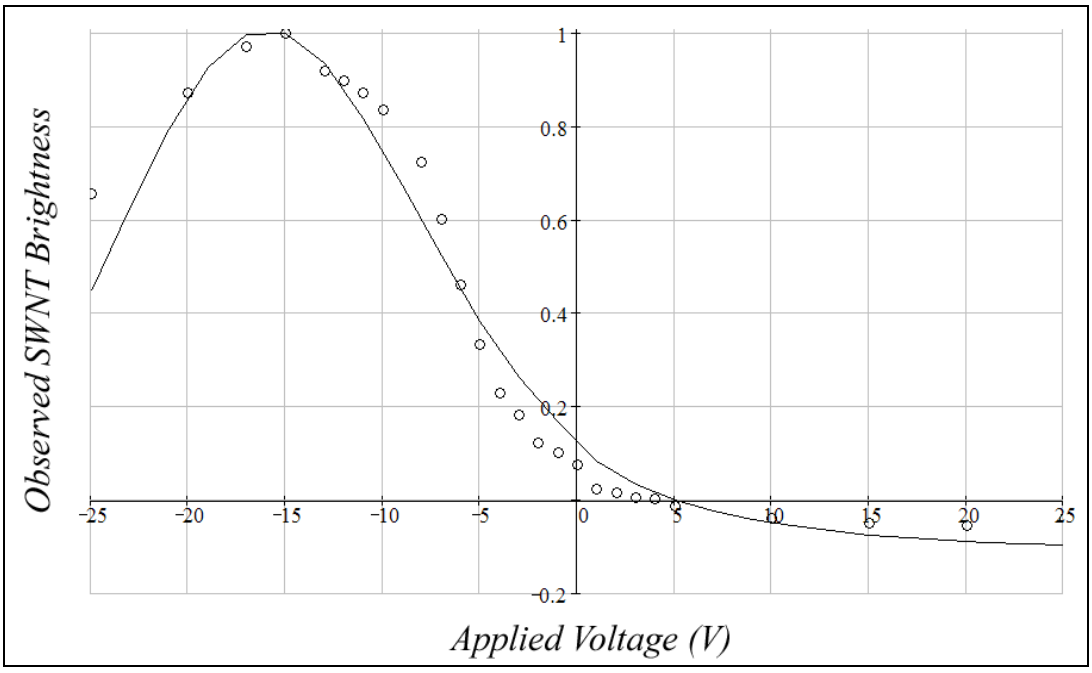

Figure 7.7. Comparison of EFIC model and experimental measurements of brightness

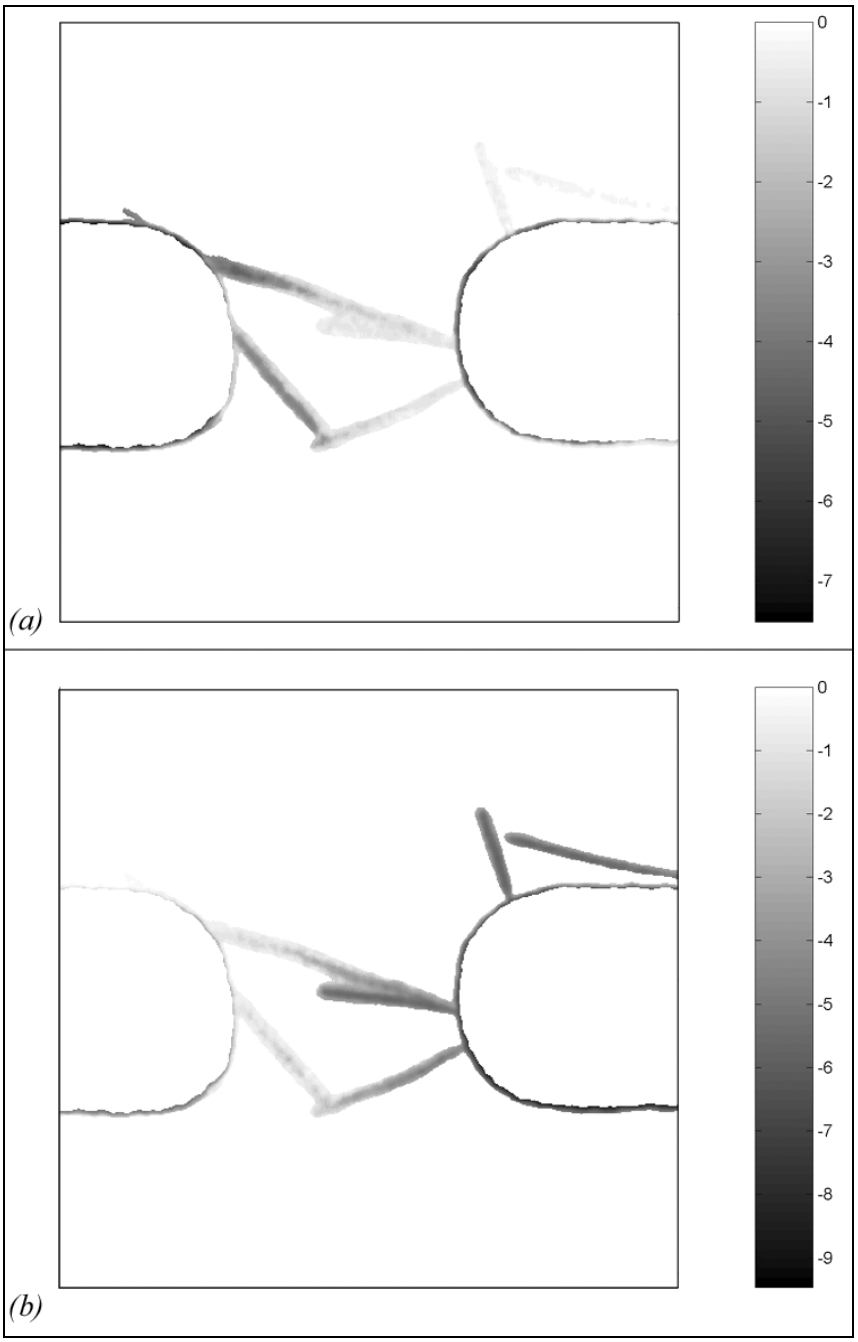

Figure 7.8. Surface potential maps of nanotube composites

The background and all but the outline of the contacts have been removed. Scale in volts (a) left electrode at –10 V, right electrode grounded (b) right electrode at –10 V, left electrode grounded.

7.2.2 Relationship Between Image Contrast and Electron Beam Excitation Voltage

Discussion of SEM Imaging

Experimental results, see Figure 6.2, show that the relative brightness of the nanotubes can be changed by adjusting the primary beam excitation voltage even while the electrodes are left unconnected. It is proposed here that this occurs because a bias is inadvertently applied to the nanotubes by beam/substrate interactions. An understanding of the relationship between observed contrast and excitation voltage is rooted in the properties of the SE yield curve, shown in Figure 7.3, and results discussed above regarding applied surface potential.

As discussed above, E_{p1} and E_{p2}, denote two important transition points on an SE yield curve where the number of primary electrons entering a material is equal to the number of secondary electrons exciting the material. E_{p1} is in the sub-kV range and was not investigated, but E_{p2} was experimentally found to be about 4 keV for the nanotube bundles inside PMMA. At excitation voltages below 4kV, the ratio of secondary to primary electrons is greater than 1. Above this excitation voltage, less than 1 secondary electron is emitted for every incident primary electron.

The micrograph in Figure 6.2(a) was taken when the excitation voltage was 1 kV, a point at which the secondary yield is close to its maximum. This implies that the beam/substrate interaction results in a net outflow of electrons from the nanotube surface. Exiting electrons results in the nanotubes acquiring a net positive charge. According to the EFIC effect, a net positive charge will cause the nanotubes to appear dark compared to the surrounding unbiased material.

When the excitation voltage is increased to 10 kV, secondary yield from carbon becomes less than one. Under these conditions, less than one SE leaves the nanotube for ever primary electron that enters. This means that the nanotubes will acquire a negative net charge relative to the backgate, and as seen in Figure 6.2(b), appear brighter.

This contrast reversal phenomenon depends to some degree on the construction of the substrate being imaged. The small effect of charging due to secondary yield does not generally induce such wide swings in contrast. But, for the particular test substrates used here, the small amount of charging induces a significant electric field between the nanotubes and the nearby grounded backgate. In the 1 kV case, a field is generated which suppressed SE emission. In the 10 kV case, the field between the nanotubes and the backgate is such so as to promote secondary electron emission above what the SE yield curve predicts.

Discussion of Specimen Current Imaging

Specimen current (SC) imaging provides a visual map of the direction of current flow on the sample surface, and SC images taken at various excitation voltages exhibit contrast changes consistent with SEM imaging. Figure 6.5 shows a series of SC images for the same nanotube network shown in Figure 6.2 and at the same two primary electron energies, 1 kV and 10 kV.

Low-energy primary electrons produce more secondary electrons resulting in net positive flow of current from ground through the current amplifier to the nanotubes resulting in white nanotube bundles. Dark images of the nanotubes at high primary beam energies occur when fewer secondary electrons are emitted than primary electrons are absorbed thereby causing a negative current flow through the amplifier to ground. Note that the contrast of the gold electrodes does not change. Surface contamination of samples occurs and is due to exposure to air. High-energy primary electrons hardly interact with the surface contaminants, but the larger interaction volume closer to the surface resulting from a low-energy beam does interact with the thin layer of contamination on the surface. Current flow through surface contamination, likely excited by the larger interaction volume of the low-energy primary electrons, are evident on the 1 kV images in the vicinity of the nanotube networks. Thus, the bright contrast in these images is a joint result of charge generation from the contaminant and the efficient collection by the nanotube network.

7.3 Discussion of SIM Based Transport Studies

Scanning impedance microscopy has been used to measure transport throughout the same type of samples studied using the SEM. However, the SIM technique is based on using an ac signal to drive current flow through a network and so can be used to determine frequency dependent transport. The effect of frequency is negligible when samples are driven with signals below 10^4 Hz. So, these low frequency measurements can be used to approximate dc transport. Higher driving frequencies provide an opportunity to derive information about the interconnections between nanotubes and the effect of the backgate as well.

7.3.1 Imaging at Low Frequency and Determination of Potential Distribution

It is possible to use the SIM amplitude imaging technique to determine the true potential distribution within the nanotube composite. However, this information cannot be extracted from a single image directly. This is because the amplitude signal (A_{SIM}) is a product of the potential (V_{ac}), which is information of interest, and the tip/surface gradient of capacitance (∇C_{t-s}), which is an artifact dependent on the geometry of the tip and conductive elements imbedded within the polymer.

$$A_{SIM} = \nabla C_{t-s} \cdot V_{ac}$$

equation 7.6

Computing the capacitance gradient would be a difficult task. Fortunately though, this is not necessary to do this since capacitance can be accounted for by simply combing information from two SIM images. This is possible because ∇C_{t-s} is independent of the bias condition, and if an SIM amplitude map acquired with one electrode ($A_{SIM,1}$) biased is divided by a map acquired while both electrodes are biased ($A_{SIM,2}$), the tip-surface capacitance effect is cancel out so that $A_{SIM,1} / A_{SIM,2} = V_{ac,1} / V_{ac,2}$. Solving for the voltage distribution for the case when a single electrode is biased yields,

$$V_{ac,1} = \frac{A_{SIM,1}}{A_{SIM,2}} \cdot V_{ac,2}$$

equation 7.7

At low frequencies, $V_{ac,2}$ is constant throughout the network and equal to the amplitude of the applied bias so it acts only as a scaling factor in equation 7.7. This technique is demonstrated in Figure 7.9 in which images captured with one electrode biased and one grounded are divided by images captured with both electrodes biased to yield the true potential distributions.

In the normalized image in Figure 7.9(c), the potential is constant between the contact and the tube network and throughout the network. Interestingly, the potential drop occurs almost exclusively at the interface between the nanotubes and the top contact. For this particular sample is appears that the resistance between bundles is much smaller than the resistance between the network and one of the contacts. Shown in Figure 7.9(f) is the normalized potential distribution with the top contact biased. In this case, most of the nanotube network is grounded, indicating again that there is a high resistance between the top contact and the network.

7.3.2 High Frequency Transport and the Line Transmission Model

Results of measuring transport through the nanotube network for high driving frequencies, presented in Figure 6.8, show that the potential drops and phase shifts with increasing distance from an electrode. This behavior has been explained by considering the capacitive coupling between the *network and the backgate*. Capacitive coupling across the 500 nm oxide layer between nanotubes and the silicon substrate provides a channel for alternating current at high enough frequencies. The line transmission model[67] has been applied to quantitatively analyze this behavior. The line transmission model was originally developed to determine the power loss from high power electrical transmission lines to the ground beneath them due to capacitive coupling over many miles. This model treats the system as a circuit with distributed resistors in series connected to ground through evenly distributed capacitors as shown in Figure 7.10. The equation describing the voltage distribution is,

$$\frac{d^2 V_{ac}(x)}{dx^2} = i\omega RC V_{ac}(x)$$

equation 7.8

where $V_{ac}(x)$ is the position dependent ac amplitude, R is the resistivity of the nanotube, C is the specific nanotube-substrate capacitance, and ω is the signal frequency. This equations has been solved assuming three different boundary conditions: (a) an infinitely long nanotube biased at one end, (b) a finite length

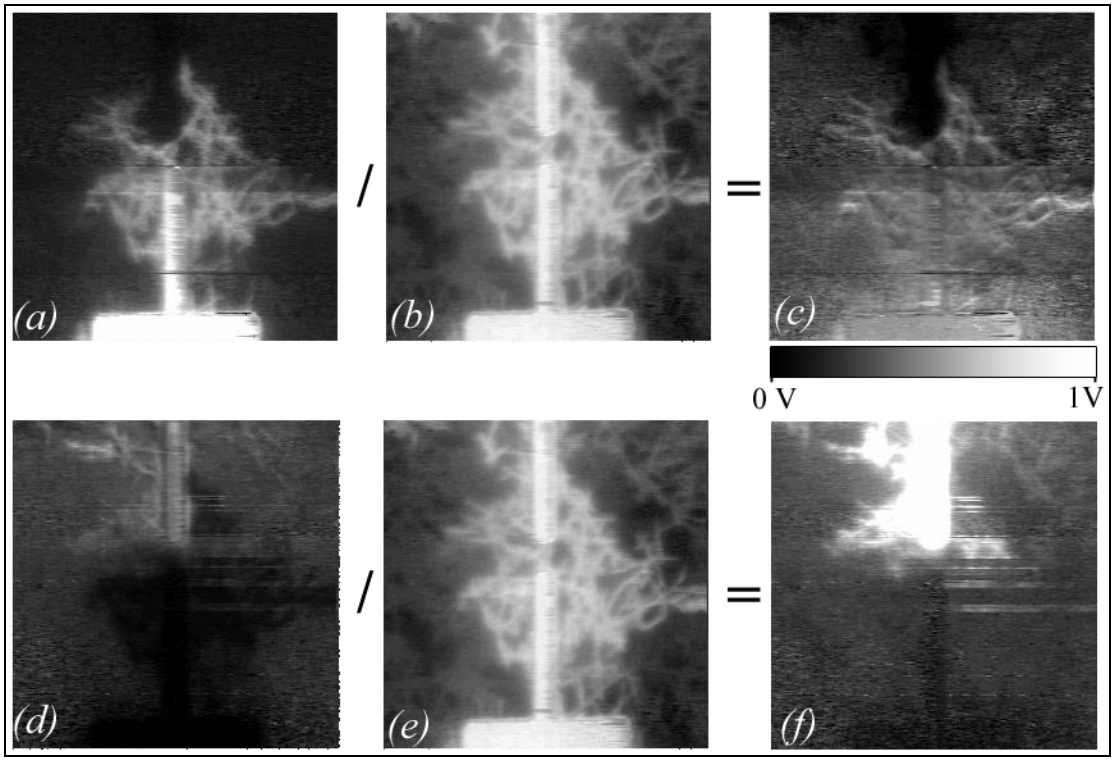

Figure 7.9. SIM amplitude images and maps of potential distribution throughout a composite network

(a) SIM amplitude image with bottom electrode biased, (b) SIM amplitude image with both electrodes biased. (c) potential distribution derived by dividing (a) by (b). (d) SIM amplitude for top electrode biased. (e) same as (b). (f) potential distribution derived by dividing (d) by (e).

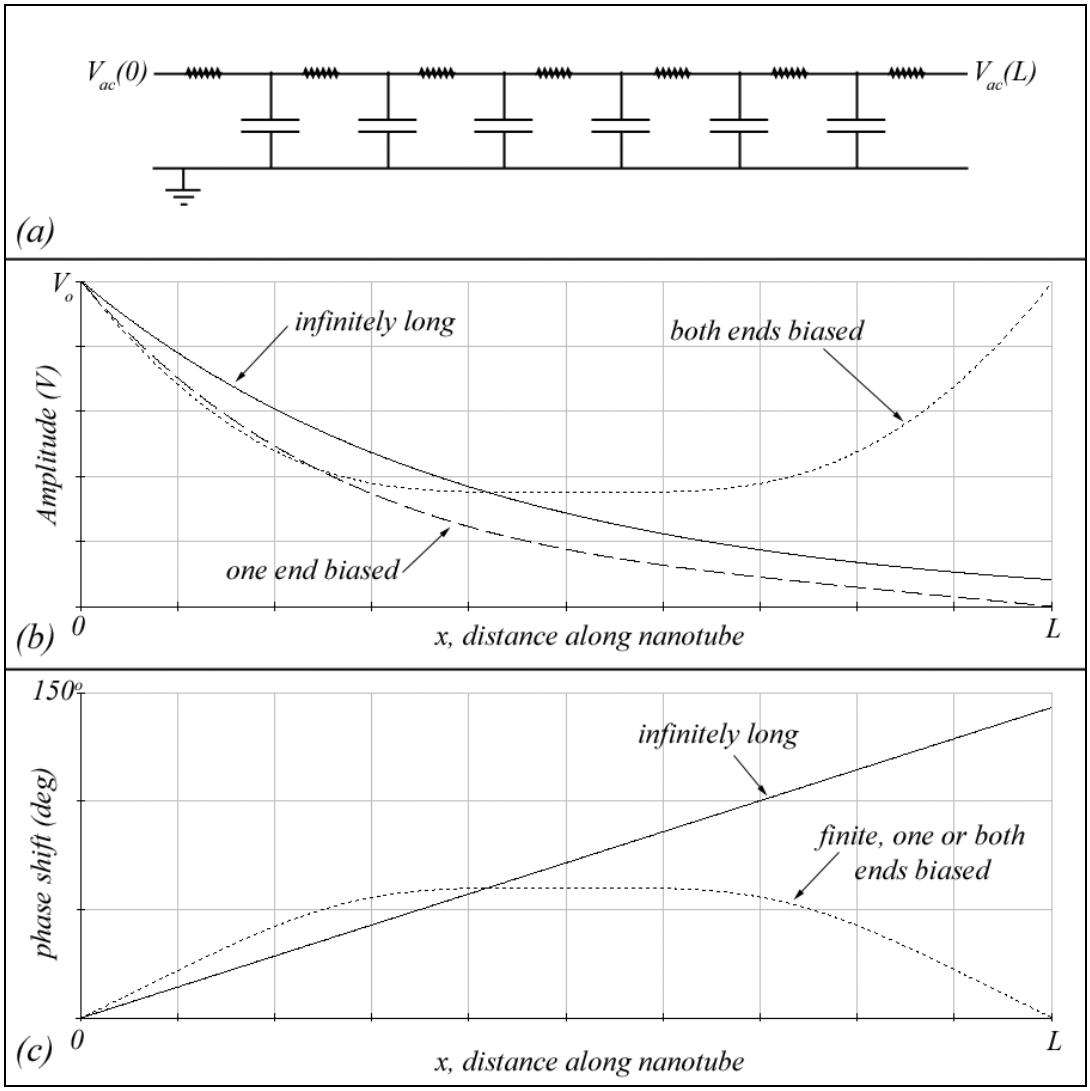

Figure 7.10. Predicted voltage and phase lag distribution at high frequencies

(a) circuit diagram of the transmission line model. (b) Plots of voltage amplitude as a function of position for three different boundary conditions. (c) phase lag distribution as a function of length.

nanotube biased at both ends, and (c) a finite length tube biased at one end and grounded at the other. The solutions for the voltage amplitude across the nanotube for the respective boundary conditions are given below.

$$\textit{(a)} \qquad V_{ac}(x) = V_0 \exp(-\alpha x)$$

$$\textit{(b)} \qquad V_{ac}(x) = V_0 \frac{\exp\left((L-x)\sqrt{i\omega CR}\right) + \exp\left(x\sqrt{i\omega CR}\right)}{1+\exp\left(L\sqrt{i\omega CR}\right)}$$

$$\text{(c)} \qquad V_{ac}(x) = V_0 \frac{\exp\left((2L-x)\sqrt{i\omega CR}\right) - \exp\left(x\sqrt{i\omega CR}\right)}{-1+\exp\left(2L\sqrt{i\omega CR}\right)}$$

equation 7.9

where $\alpha = \sqrt{R\omega C/2}$. The phase lag for the case of the infinitely long nanotube is linearly related to position so that $\varphi(x) = \alpha x$. Plots of voltage and phase lag distribution are shown in Figure 7.10.

To establish the parameters of the polymer-embedded nanotube network, the macroscopic transport properties were studied by two probe transport measurements between the electrodes. The resistances measured for various 1 μm sections of the nanotube networks were determined to be in the range of 10 M Ω–10 G Ω, from which effective resistivity can be estimated to be between R/L ~ 10^{13}–10^{16} Ω/m. The nanotube-substrate capacitance is modeled by the cylindrical capacitor model, $C = L2\pi\varepsilon\varepsilon_0 / \ln(d/R)$, where R is bundle radius, d is the oxide thickness, L is the nanotube length, and ε is the dielectric constant of the oxide. For R = 10 nm and d = 500 nm, the effective capacitance can be estimated as C/L = 4.61 10^{-11} F/m. From these estimates, the decay constant along the network is $\alpha = (0.48-15.2)10^3\sqrt{\omega}$ m^{-1}, where ω is in kHz. Typical frequencies on the order of ~100 kHz yield characteristic decay lengths, $l = 1/\alpha$, from l ~ 200 to ~ 6 μm depending on nanotube resistance. Hence, for a poorly conductive nanotube network, the ac potential is expected to be confined to within a few microns of the electrode. Conversely, applying bias to a well conducting network effectively biases the network over hundreds of microns[68].

This predicted transport behavior is in qualitative agreement with experimental observations in Figure 6.8. To quantify this behavior, the frequency dependence of the average phase lag at 20 μm separation from the contact was measured and plotted in Figure 6.9. For low frequencies (ω < 50 kHz), this behavior clearly follows $\varphi \sim \sqrt{\omega}$ dependence in agreement with Eq. (5). From the linear part of the plot, the average RC product of the nanotube network can be estimated as 3.23 10^4 s/m^2. The decay length at 100 kHz is then α^{-1} = 25 μm which is in a good agreement with observed potential decay length in Figure 6.8. The phase shift saturates at high frequencies. This can be ascribed to the effect of the back-gate at large distances from the contact.

CHAPTER 8 CONCLUSION

This investigation into the characteristics of materials and materials processing on the scale of nanoseconds, in the case of laser-induced surface structuring, and nanometers, in the case of nanotube composites, has necessitated the development of several new experimental techniques and theoretical models to explain the experimental results. This thesis has shown that laser irradiation of single-crystal silicon substrates can result in the formation of quasi-periodic surface micro-structures. The spacing between features and the shape of individual features is shown to be dependent upon the crystal orientation of the irradiated surface, the incident flux, and the initial substrate temperature. A series of models have been proposed to explain the formation and evolution of the surface structures.

The spacing between surface features is determined in large part by the melt time. This has been explained through consideration of the changing morphology of both the liquid-vapor and solid-liquid interfaces during a single melt cycle. It has been demonstrated that an incongruity can develop between these two interfaces near the very end of the solidification process leaving isolated pools of molten material on the surface. A detailed investigation into the solidification of these isolated pools has shown that differences between the surface atomic densities of the two phases at the SL interface will greatly effect the shape that the surface will assume after solidification. A model has been developed which takes into account the shape of the SL-LV interface incongruity as a function of melt time, the effect of surface atomic density on amplitude growth, and faceting to accurately predict experimental results.

The initiation and growth of micro-cones and micro-holes from surface waves has been ascribed to multiple reflections that redistribute incident light and generate regions of high intensity on the surface. The SF_6 atmosphere can dissociate near the surface at these high intensity regions and cause rapid removal of material. This highly localized laser induced etching is responsible for the formation of micro-holes. The deposition of material from of micro-holes to the surface results in the formation of micro-cones.

Two types of microscopy techniques have been employed to non-invasively probe electronic transport in carbon-nanotube polymer composites. The scanning electron microscope has been used to image nanotube bundles within the polymer matrix. Additionally, the SEM was found to be particularly sensitive to applied surface potentials thus enabling its use in constructing two dimensional voltage maps of the embedded nanotube networks. The specimen current imaging technique has been demonstrated to be another viable method to image current paths in the polymer composites using the SEM. Scanning impedance microscopy has been employed to measure transport through composite networks which are driven by ac bias. At low driving frequencies, the networks behave as though there were a DC potential applied thus providing a means to validate SEM measurements. At higher driving frequencies however, coupling between the network and the back gate degrades transmission. The rectifying behavior that is apparent in current-voltage measurements of these networks has been ascribed to differences in the tunneling widths between each of the gold-contacts and the networks.

BIBLIOGRAPHY

(1) Mazur, E. *mazur-www.harvard.edu/research/detailspage.php?rowid=1* **2004**.

(2) Younkin, R.; Carey, J. E.; Mazur, E.; Levinson, J. A.; Friend, C. M. *Journal of Applied Physics* **2003**, *93*, 2626-2629.

(3) Anisimov, S. I.; Khokhlov, V. A. *Instabilities in Laser-Matter Interaction*; CRC Press: Moscow, 1995.

(4) Sipe, J. E.; Young, J. F.; Preston, J. S.; Vandriel, H. M. *Physical Review B* **1983**, *27*, 1141-1154.

(5) Young, J. F.; Preston, J. S.; Vandriel, H. M.; Sipe, J. E. *Physical Review B* **1983**, *27*, 1155-1172.

(6) Young, J. F.; Sipe, J. E.; Vandriel, H. M. *Physical Review B* **1984**, *30*, 2001-2015.

(7) Pedraza, A. J.; Fowlkes, J. D.; Guan, Y. F. *Applied Physics a-Materials Science & Processing* **2003**, *77*, 277-284.

(8) Brailovsky, A. B.; Gaponov, S. V.; Dorofeev, I. A.; Lutschin, V. I.; Semenov, V. E. *SPIE* **1990**, *1440*, 84-89.

(9) Landau, L. D.; Lifshitz, E. M. In *Fluid Mechanics*; Addison-Wesley: Reading M.A., 1959.

(10) Dolgaev, S. I.; Lavrishev, S. V.; Lyalin, A. A.; Simakin, A.; Voronov, V. V.; Shafeev, G. A. *Applied Physics a-Materials Science & Processing* **2001**, *73*, 177-181.

(11) Wood, R. F.; White, C. W.; Young, R. T. *Pulsed Laser Processing of Semiconductors*; Academic Press, Inc.: New York, 1984.

(12) Shen, M. Y.; Crouch, C. H.; Carey, J. E.; Younkin, R.; Mazur, E.; Sheehy, M.; Friend, C. M. *Applied Physics Letters* **2003**, *82*, 1715-1717.

(13) Sokolowski-Tinten, K.; Bialkowski, J.; Cavalleri, A.; von der Linde, D.; Oparin, A.; Meyer-ter-Vehn, J.; Anisimov, S. I. *Physical Review Letters* **1998**, *81*, 224-227.

(14) Chen, X. Y.; Lu, Y. F.; Cho, B. J.; Zeng, Y. P.; Zeng, J. N.; Wu, Y. H. *Applied Physics Letters* **2002**, *81*, 1344-1346.

(15) Lu, Y. F.; Choi, W. K.; Aoyagi, Y.; Kinomura, A.; Fujii, K. *Journal of Applied Physics* **1996**, *80*, 7052-7056.

(16) Cook, R. D.; Young, W. C. In *Advanced Mechanics of Materials*; MacMillan Publishing Company: New York, NY, 1985.

(17) Megson, T. H. G. In *Aircraft Structures for Engineering Students*; 2nd ed.; Halsted Press: New York, 1990.

(18) Porter; Easterling; Alloys, P. T. i. M. a., Ed.; Chapman and Hall: London, 1992.

(19) Wei, C. Y.; Cho, K. J.; Srivastava, D. *Physical Review B* **2003**, *67*, art. no.-115407.

(20) Bachilo, S. M.; Strano, M. S.; Kittrell, C.; Hauge, R. H.; Smalley, R. E.; Weisman, R. B. *Science* **2002**, *298*, 2361-2366.

(21) Dai, H. J. *Accounts of Chemical Research* **2002**, *35*, 1035-1044.

(22) Ouyang, M.; Huang, J. L.; Lieber, C. M. *Accounts of Chemical Research* **2002**, *35*, 1018-1025.

(23) Avouris, P. *Accounts of Chemical Research* **2002**, *35*, 1026-1034.

(24) Saito, R.; Dresselhaus, G.; Dresselhaus, M. S. *Physical Review B* **1996**, *53*, 2044-2050.

(25) Ando, T. *Semiconductor Science and Technology* **2000**, *15*, R13-R27.

(26) Ando, T.; Matsumura, H.; Nakanishi, T. *Physica B* **2002**, *323*, 44-50.

(27) Chico, L.; Crespi, V. H.; Benedict, L. X.; Louie, S. G.; Cohen, M. L. *Physical Review Letters* **1996**, *76*, 971-974.

(28) Chico, L.; Benedict, L. X.; Louie, S. G.; Cohen, M. L. *Physical Review B* **1996**, *54*, 2600-2606.

(29) Andriotis, A. N.; Menon, M.; Srivastava, D.; Chernozatonskii, L. *Physical Review B* **2002**, *65*, art. no.-165416.

(30) Li, J.; Papadopoulos, C.; Xu, J. *Nature* **1999**, *402*, 253-254.

(31) Papadopoulos, C.; Rakitin, A.; Li, J.; Vedeneev, A. S.; Xu, J. M. *Physical Review Letters* **2000**, *85*, 3476-3479.

(32) Paulson, S.; Helser, A.; Nardelli, M. *Science* **2000**, *290*, 1742-1744.

(33) Fuhrer, M. S.; Nygård, J.; Shih, L.; Forero, M.; Yoon, Y.-G.; Mazzoni, M. S. n. C.; Choi, H. J.; Ihm, J.; Louie, S. G.; Zettl, A.; McEuen, P. L. *Science* **2000**, *288*, 494-497.

(34) Buldum, A.; Lu, J. P. *Physical Review B* **2001**, *6316*, art. no.-161403.

(35) Yoon, Y. G.; Mazzoni, M. S. C.; Choi, H. J.; Ihm, J.; Louie, S. G. *Physical Review Letters* **2001**, *86*, 688-691.

(36) Balberg, I.; Binenbaum, N.; Wagner, N. *Physical Review Letters* **1984**, *52*, 1465-1468.

(37) Balberg, I.; Binenbaum, N. *Physical Review B* **1983**, *28*, 3799-3812.

(38) Scher, H.; Zallen, R. *Journal of Chemical Physics* **1970**, *53*, 3759-&.

(39) Kasap, S. O. *Electrical Engineering Materials and Devices*; McGraw-Hill: New York, 2000.

(40) Sheng, P.; Sichel, E. K.; Gittleman, J. I. *Physical Review Letters* **1978**, *40*, 1197-1200.

(41) Sheng, P. *Physical Review B* **1980**, *21*, 2180-2195.

(42) Hull, R. *Properties of Crystalline Silicon*; INSPEC: London, 1999.

(43) Brunco, D. P.; Kittl, J. A.; Otis, C. E.; Goodwin, P. M.; Thompson, M. O.; Aziz, M. J. **1993**, *64*, 2615-2623.

(44) Hoglund, D. E.; Thompson, M. O.; Aziz, M. J. **1998**, *58*, 189-199.

(45) Singh, R. K.; Gilbert, D. R.; Viatella, J. *Materials Science and Engineering B-Solid State Materials for Advanced Technology* **1996**, *40*, 89-95.

(46) Wood, R. F.; Geist, G. A.; Liu, C. L. **1996**, *53*, 15863-15870.

(47) Larson, B.; Tischler, J.; Mills, D. *Journal of Materials Research* **1986**, *1*, 144-154.

(48) Ivlev, G. D.; Gatskevich, E. I. *Applied Surface Science* **1999**, *143*, 265-271.

(49) Ansell, S.; Krishnan, S.; Felten, J. J.; Price, D. L. *Journal of Physics-Condensed Matter* **1998**, *10*, L73-L78.

(50) Jakse, N.; Hennet, L.; Price, D. L.; Krishnan, S.; Key, T.; Artacho, E.; Glorieux, B.; Pasturel, A.; Saboungi, M. L. *Applied Physics Letters* **2003**, *83*, 4734-4736.

(51) Kadiri, Y.; Jakse, N.; Wax, J. F.; Bretonnet, J. L. *Journal of Non-Crystalline Solids* **2002**, *312*, 143-147.

(52) Sastry, S.; Angell, C. A. *Nature Materials* **2003**, *2*, 739-743.

(53) Stich, I.; Parrinello, M.; Holender, J. M. *Physical Review Letters* **1996**, *76*, 2077-2080.

(54) Waseda, Y.; Shinoda, K.; Sugiyama, K.; Takeda, S.; Terashima, K.; Toguri, J. M. *Japanese Journal of Applied Physics Part 1-Regular Papers Short Notes & Review Papers* **1995**, *34*, 4124-4128.

(55) Beatty, K. M.; Jackson, K. A. *Journal of Crystal Growth* **2000**, *211*, 13-17.

(56) Her, T. H.; Finlay, R. J.; Wu, C.; Deliwala, S.; Mazur, E. *Applied Physics Letters* **1998**, *73*, 1673-1675.

(57) Ren, H.; Ma, R.; Li, X.; Chen, J.; Yang, H.; Gong, Q. *International Journal of Mass Spectroscopy* **2004**, *235*, 117-122.

(58) Mansano, R. D.; Verdonck, P.; Maciel, H. S.; Massi, M. *Thin Solid Films* **1999**, *343*, 378-380.

(59) Pedraza, A. J.; Fowlkes, J. D.; Jesse, S.; Mao, C.; Lowndes, D. H. *Applied Surface Science* **2000**, *168*, 251-257.

(60) Geohegan, D. B. In *Pulsed Laser Deposition of Thin Films*; Chrisey, D. B., Hubler, G. K., Eds.; Wiley: New York, 1994.

(61) Geohegan, D. B. *Applied Physics Letters* **1992**, *60*, 2732-2734.

(62) Zeldovich, Y. B.; Raizer, Y. P. *Physics of Shock Waves and High Temperature Hydrodynamics Phenomena*; Academic Press: New York, 1996.

(63) Geohegan, D. B.; Schittenhelm, H.; Fan, X.; Pennycook, S. J.; Puretzky, A. A.; Guillorn, M. A.; Blom, D. A.; Joy, D. C. *Applied Physics Letters* **2001**, *78*, 3307-3309.

(64) Britt, P. F.; Viswanathan, S.; Ivanov, I. N.; Puretzky, A. A.; Lance, M. J.; Geohegan, D. B. American Physical Society March Meeting, Austin, TX, 2003.

(65) Seiler, H. *Journal of Applied Physics* **1983**, *54*, R1-R18.

(66) Chung, M. S.; Everhart, T. E. *Journal of Applied Physics* **1974**, *45*, 707-709.

(67) Lebedev, N. N.; Skal'skaya, I. P.; Uflyand, Y. S. *Problems in Mathematical Physics*; Pergamon: Oxford, 1966.

(68) Kalinin, S. V.; Jesse, S.; Shin, J.; Baddorf, A. P.; Guillorn, M. A.; Geohegan, D. B. *Nanotechnology* **2004**, *15*, 907-912.

APPENDIX

1.1 Description of Evaporation Instability

Evaporation Instability in Silicon,
from: 'Instabilities in Laser-Matter Interaction', Anisimov, 1995

First find the critical time for evaporation:

Properties of silicon:

$T_{vap} := 3.173 \times 10^3 \cdot K$

$H_{fusion} := 50.2 \cdot 10^3 \cdot \frac{J}{mol}$

$H_{vapor} := 359 \cdot 10^3 \cdot \frac{J}{mol}$

$W_{atomic} := 28.0855 \frac{gm}{mol}$

$N_a := 6.02 \cdot 10^{23} \cdot \frac{1}{mol}$

Laser Conditions

$P \equiv 2 \cdot \frac{J}{cm^2}$ energy density of pulse

$t_{pulse} := 25 \cdot ns$ time of pulse

$I := \frac{P}{t_{pulse}}$ Intensity

$I = 8 \times 10^7 \frac{W}{cm^2}$

$M := \frac{W_{atomic}}{N_a}$ atomic mass

$k_b := 1.38 \cdot 10^{-23} \cdot \frac{J}{K}$ Boltzmann's

$L_v := \frac{H_{vapor} - H_{fusion}}{W_{atomic}}$ latent heat of evaporation

$V_o := 2000 \frac{m}{s}$ speed of sound

$A := .65$ absorbtivity

$\rho := 2.53 \frac{gm}{cm^3}$ density

$c_p := 25.61 \cdot \frac{J}{mol \cdot K} \cdot \frac{1}{W_{atomic}}$ heat capacity

$\kappa = 20 \frac{J}{m \cdot s \cdot K}$ Conductivity of Liquid Si

Coupled Equations per Anisimov:

$$A \cdot I = V_s \cdot \rho \cdot \left(L_v + c \cdot T_s\right)$$

$$V_s = V_o \cdot exp\left(\frac{-U}{T_s}\right)$$

$$U := \frac{M \cdot L_v}{k_b}$$

We can find the temperature T_S and velocity V_S of the interface in the coupled equations above using a root finder and using a two equations above and a root finder:

$$f(T_S) := \left[V_O \cdot e^{\frac{-U}{T_S}} - \left[-A \cdot \frac{I}{\left(-\rho \cdot L_v - \rho \cdot c_p \cdot T_S\right)} \right] \right]$$

$$T_S := root\left(f(T_S), T_S\right)$$

$$T_S = 7228.236\,\mathrm{K}$$

$$V_S := V_O \cdot e^{\frac{-U}{T_S}}$$

$$V_S = 11.687\,\mathrm{ms}^{-1}$$

Calculate the critical time for the onset of evaporation:

$$\chi := \frac{\kappa}{c_p \cdot \rho}$$

$$\chi = 8.669 \times 10^{-6}\,\mathrm{m}^2\,\mathrm{s}^{-1}$$

$$t_c := \frac{\chi}{V_S^2}$$

$$t_c = 63.473\,ns$$

$$W_{atomic} := 28.0855 \frac{gm}{mol}$$

$$H_{fusion} := 50.2 \cdot 10^3 \cdot \frac{J}{mol}$$

$$L_m := \frac{H_{fusion}}{W_{atomic}}$$

$$\tau := t_{pulse}$$

Distance evaporated

$$\left(t_{pulse} - t_c\right) \cdot V_S = -449.629\,nm$$

Since the critical time for evaporation to begin exceeds the pulse width of the laser, under these laser conditions, Si will not undergo enough evaporation.

Dispersion relation for instability in evaporation front:

$\delta := 800 \cdot nm$ skin depth

$\mu := 2 \cdot \delta^{-1}$

$\beta := \frac{V_s}{\mu \cdot \chi}$

$\beta = 0.539$

$p := \frac{\rho \cdot \chi \cdot \mu \cdot L_o \cdot c_p \cdot M}{k_b \cdot A \cdot I}$

$p = 0.439$

$\sigma := 8.061 \cdot 10^{-7} \cdot \frac{N}{\mu m}$

$d := 2.36 \cdot angstrom$ interatomic spacing

$L_o := 1.35 \cdot 10^{3} \cdot \frac{kJ}{kg}$ rough estimate

$\Lambda := \frac{\sigma \cdot \mu}{\rho \cdot L_o}$ $\Lambda = 0.001$

$\Theta_s(\zeta) = B_1 \cdot e^{-\zeta} + B_2 \cdot e^{-\beta \cdot \zeta}$

$\Theta_o = \Theta_s(0) = B_1 + B_2$

$B_1 := (\beta - 1)^{-1}$

$B_2 := \frac{-\rho \cdot \chi \cdot \mu \cdot L_o}{A \cdot I} - \frac{B_1}{\beta}$

$\Theta_o := B_1 + B_2$

$\Theta_o = 1.712$

$\Theta'_s(0) = -B_1 \cdot exp(-\zeta) - B_2 \cdot \beta \cdot exp(-\beta \cdot \zeta)$

$\Theta'_o = \Theta'_s(0) = -B_1 - B_2 \cdot \beta$

$\lambda := \frac{\rho \cdot \chi \cdot \mu \cdot L_o}{A \cdot I}$

$\Theta'_o := (-B_1 - B_2 \cdot \beta)$

$\Theta'_o = 0.077$

The dispersion relation is given by these two parametric equations where $\gamma(\alpha)$ is the rate of instability growth and $k(\alpha)$ is the wave number of the perturbation.

$$\gamma(\alpha) = \frac{\alpha - \beta}{\beta} \cdot \frac{\Theta'_o - (\alpha - \beta + 1)^{-1} - \alpha \cdot \Lambda \cdot (\alpha \cdot \Theta_o - \Theta'_o)}{\alpha \cdot \Theta_o \cdot (\Theta_o \cdot p^{-1} - \Lambda \cdot \beta) + \lambda \cdot \beta \cdot (1 - \lambda \cdot \beta)} \qquad \text{eq 5.11}$$

$k(\alpha)^2 = \alpha \cdot (\alpha - \beta) - \beta^2 \cdot \gamma(\alpha)$

$wavelength(\alpha) = \frac{2 \cdot \pi}{k(\alpha)}$

The parametric equations above can be simplified to:

$$\gamma(k) := \left(\frac{p}{\beta \cdot \Theta_o^{\,2}}\right) \cdot \left[\Theta'_o - (k+1)^{-1} - k^2 \cdot \Lambda \cdot \Theta_o\right]$$

An evaporation instability will grow if $\gamma(k) > 0$.

For our laser conditions, perturbation growth rate is always negative

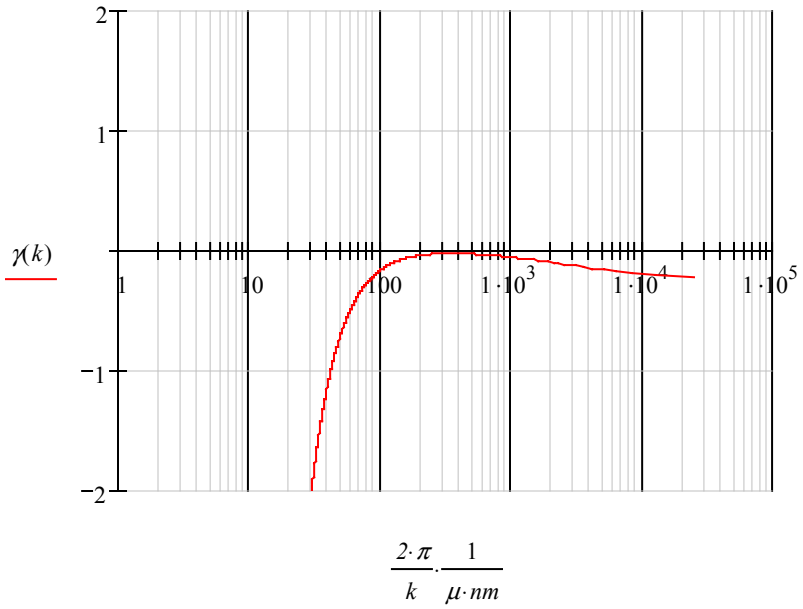

1.2 Description of Plume-Wave Interaction

Plume-Capillary Wave Interaction,
from: 'Formation of large scale relief on target surface under multiple pulsed action of laser radiation', Brailovsky 1990

The pressure in a wave from a sinusoidal surface with shape:

$$\xi = \xi_I \cdot exp(i \cdot k \cdot r)$$

is given by:

$$P = -\rho_o \cdot V_o^{\,2} \cdot \beta \cdot k \cdot \xi$$

$$\beta = \left(1 - M^2\right)^{\frac{-1}{2}}$$

$$M = \frac{V_o}{c}$$

where:
V_o = velocity of plasma from an undisturbed surface
ρ_o = density of plasma from an undisturbed surface
c = speed of sound
M = Mach number
k = wave number
P = pressure variation above a perturbed surface

The dispersion relation for a capillary wave absent of a pressure field is:

$$\omega = \sqrt{\left(\frac{\sigma \cdot k^3}{\rho_L}\right) \cdot tanh(k \cdot h)}$$

where:
σ = surface tension of liquid
ρ_L = density of liquid
h = depth of liquid

If the effect of the pressure wave is taken into account, the following dispersion relation is derived

$$\omega^2 = \frac{1}{\rho_L} \cdot \left(-\rho_o \cdot V_o^{\,2} \cdot \beta \cdot k^2 + \sigma \cdot k^3\right) \cdot tanh(k \cdot h)$$

The equation for the optimal wavelength is given by:

$$\lambda_{opt} = \frac{8 \cdot \pi \cdot \sigma \cdot \sqrt{1 - M^2}}{3 \cdot \sigma \cdot M^2}$$

1.3 Fowler-Nordheim Equation

Fowler-Nordheim Tunneling Equation

The tunneling current is given by the simplified fowler-nordheim equation:

$$J(V_a) = q \cdot n \cdot v_R \cdot exp\left[\frac{-E_c(V_a)}{E(V_a)}\right] \qquad J(V_a, T) = q \cdot n \cdot v_R \cdot exp\left[\frac{T_1}{T + T_o} \cdot \frac{-E_c(V_a)}{E(V_a)}\right]$$

Where

$v_R = \sqrt{\frac{k_b \cdot T}{2 \cdot \pi \cdot m_e}}$ - is the Richardson Velocity which estimates the average velocity of electrons perpendicular to the surface

$E_c = \frac{4 \cdot \pi \cdot \sqrt{2 \cdot m_e \cdot \Phi_{eff}(E)} \cdot \Phi}{q \cdot h}$ - is the critical field for tunneling

$\Phi_{eff} = \Phi - \sqrt{\frac{q^3 \cdot E}{4 \cdot \pi \cdot \varepsilon_o}}$ - is the effective work function of the metal which has been adjusted from the original work function to account for the effects of the applied field.

$E_{plate}(V_a) = \frac{V_a}{w \cdot \kappa}$ -is the electric field within a dielelctric between two flat plates for a given applied voltage and seperation distance.

$E_{cyl}(V_a) = \frac{V_a}{\kappa \cdot r \cdot ln\left(\frac{a + w}{a}\right)}$ -is the electric field within a dielelctric between two cylindrical plates for a given applied voltage, inner and outer radii, at any distance within the dielectric.

$I = J \cdot A_c$ -is the current through a barrier with a given cross-sectional area

$R = \frac{V_a}{I} = \frac{V_a}{J \cdot A_c}$ -Since this eqaution will be used within circuit analysis, it is advantageous to reexpress the Fowler-Nordheim equation as the voltage dependent resistance of the barrier.

q - is the electron charge
n - is the density of electrons in the metal
E - is the applied electric feild
h - is Planck's constant
k_b - is boltzman's constant
m_e - is the mass of an electron
T - is temperature
V_a - is the applied voltage across the barrier
κ - is the dielectric constant for the polymer
w - is the thickness of the barrier
r - is the distance from the center of two concentric cylinder plates
a - is the radius of the inner cylindric plate
A_c - is the cross-sectional area of the of the barrier

Combining the equations above gives:

$$I\left(V_a, w, A_c\right) = q \cdot n \cdot A_c \cdot \sqrt{\frac{k_b \cdot T}{2 \cdot \pi \cdot m_e}} \cdot exp\left[\frac{-4 \cdot \pi \cdot w \cdot \kappa \cdot \Phi}{q \cdot \left|V_a\right| \cdot h} \cdot \sqrt{2 \cdot m_e \cdot \left(\Phi - \sqrt{\frac{q^3 \cdot \left|V_a\right|}{4 \cdot \pi \cdot \varepsilon_o \cdot w}}\right)}\right] \cdot \frac{\left|V_a\right|}{V_a}$$

We can also include thermal fluctuation corrections as a pre-factor in the exponential:

$$I\left(V_a\right) = q \cdot n \cdot v_R \cdot A_c \cdot exp\left[\frac{-T_1}{T + T_o} \cdot \left(\frac{E_a\left(V_a\right)}{E_c\left(V_a\right)} - 1\right)\right]$$

1.4 Cone Solidification Derivation

Solidification of a Cone

Initially the cross section of the liquid-vapor interface is defined by a line.

$$y(x) = m \cdot x + b$$

Where m is the initial slope. However slope will change as x changes

$$y(x) = y' \cdot x$$

$$y(x) = x \cdot y'(x) - r \cdot y'_o$$

$$x = \frac{(y(x) - b)}{y'(x)}$$

$$V = \pi \cdot \Delta y(x) \cdot x^2$$

$$y'(x) = \frac{\Delta y(x)}{\Delta x}$$

$$V = \pi \cdot y'(x) \cdot \Delta x \cdot x^2$$

$$y_o(x) = x \cdot y'_o - r \cdot y'_o$$

$$y'_o := -.1$$

$$r := 10$$

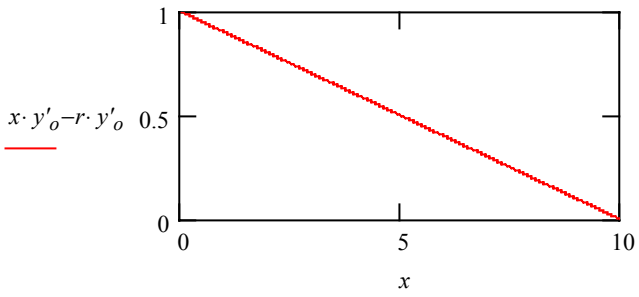

The slope will change with each step upward because atoms will be subtracted from the liquid state. It is required that total number of atoms stays the same throughout the process.

The number of atoms is the liquid state which exist in the region about to be solidified is given below. Because x is the independent variable in this derivation, we have to express the advance of the solid-liquid interface Δy in terms of Δx. This
is done by substituting $\Delta y = y'(x) \cdot \Delta x$.

$$M_L = \eta_L \cdot \pi \cdot y' \cdot \Delta x \cdot x^2$$

η_L is the volumetric atomic density of the liquid (atoms/volume),

h_L is the height of an atomic layer of liquid atoms

Some care has to be taken when expressing the number of solid atoms which will actually fill this region. There is a specific ratio of the vertical distance and the surface area that a solid atom takes up due to crystal structure at that face. If we consider density of atoms in only a volumetric sense then:

$$M_s = \frac{\kappa_s}{h_s} \cdot \Delta y \cdot \pi \cdot x^2 = \eta_s \cdot y' \cdot \Delta x \cdot \pi \cdot x^2$$

Crystallographic information does not fit naturally into this continuum approach. But we can try to artificially force it by considering that Δy for the liquid is different than Δy for the solid. For instance, a layer of atoms in the liquid is shorter than a layer of atoms in the solid for a Si(110)), but the surface density of atoms in the solid is larger than that for the liquid. The information on surface density has to separated from information on atomic step height. We can impose a different Δy for the solid.

$$\Delta y_S = \Delta y \cdot \frac{h_S}{h_L}$$

The number of atoms solidified Δy advance is then:

$$M_S = \eta_S \cdot \Delta y_S \cdot \pi \cdot x^2 = \frac{\kappa_S}{h_S} \cdot \Delta y_S \cdot \pi \cdot x^2 = \frac{\kappa_S}{h_S} \cdot \left(\Delta y \cdot \frac{h_S}{h_l} \right) \cdot \pi \cdot x^2 = \frac{\kappa_S}{h_l} \cdot y' \cdot \Delta x \cdot \pi \cdot x^2$$

This can be thought of in this sense, if Δy was equal to ,then we would have the right number of atoms for the advance of one atomic layer. This can be thought of another way as well. We know that the heights of the atomic layers are different. We can not consider that now, so we will assumer that they are the same and we are left then to express density only in terms of surface density. We can not in reality advance less than one atomic layer in the solid, so the fix is added to give the continuum expressions the proper quantized character. The change in the volume of liquid as a consequence of solidification is given below. This now looks like we are only considering surface atomic densities (κ), but we will reintroduce the height difference again later in the derivation to make everything proper.

$$\Delta V = \frac{-M_S}{\eta_l} = \left(\frac{-\kappa_S}{h_l} \cdot y' \cdot \Delta x \cdot \pi \cdot x^2 \right) \cdot \frac{1}{\eta_l} = \frac{-\kappa_S}{\kappa_l} \cdot y' \cdot \Delta x \cdot \pi \cdot x^2$$

The change in volume can be expressed in geometric terms as well as the slope and base of the cone change due to solidification. In this it is assumed that the liquid portion will continue to be a cone albeit one with a different ratio of base to height.

The volume of the liquid cone before solidification is:

$$V_1 = \frac{\pi}{3}\cdot y'(x)\cdot x^3$$

The volume of the liquid cone after Δy has solidified is:

$$V_2 = \frac{\pi}{3}\cdot y'(x+\Delta x)\cdot(x+\Delta x)^3$$

The change in the volume of liquid is

$$\Delta V = V_2 - V_1 = \left[\frac{\pi}{3}\cdot y'(x+\Delta x)\cdot(x+\Delta x)^3\right] - \frac{\pi}{3}\cdot y'(x)\cdot x^3$$

Equate this to the ΔV equation above

$$\frac{-\kappa_s\cdot y'\cdot\Delta x\cdot\pi\cdot x^2}{\kappa_L} = \left[\frac{1}{3}\cdot\pi\cdot y'(x+\Delta x)\cdot(x+\Delta x)^3\right] - \frac{1}{3}\cdot\pi\cdot y'(x)\cdot x^3$$

Solve for $y'(x+\Delta x)$ to find the new slope in terms of information of previous slope

$$y'(x+\Delta x) = -y'(x)\cdot x^2\cdot\frac{\left(3\cdot\kappa_s\cdot\Delta x - x\cdot\kappa_L\right)}{\left[\kappa_L\cdot(x-\Delta x)^3\right]}$$

So, now looking at the definition of a derivative

$$g'(x) = \lim_{\Delta x\to 0}\frac{g(x+\Delta x)-g(x)}{\Delta x}$$

Applying this to the equation for change in slope, we have

$$y''(x) = \lim_{\Delta x\to 0}\frac{y'(x+\Delta x)-y'(x)}{\Delta x}$$

$$y''(x) = \lim_{\Delta x\to 0}\frac{-y'(x)\cdot x^2\cdot\frac{\left(3\cdot\kappa_s\cdot\Delta x - x\cdot\kappa_L\right)}{\left[\kappa_L\cdot(x-\Delta x)^3\right]} - y'(x)}{\Delta x}$$

Use L'Hospitals rule to find the limit:

$$y''(x) = \lim_{\Delta x \to 0} \frac{d}{d\Delta x}\left[-y'(x)\cdot x^2 \cdot \frac{\left(3\cdot \kappa_s \cdot \Delta x - x\cdot \kappa_L\right)}{\left[\kappa_L \cdot \left(x - \Delta x\right)^3\right]} - y'(x)\right]$$

$$y''(x) = 3\cdot \frac{\left(\kappa_s - \kappa_L\right)}{\kappa_L}\cdot \frac{y'(x)}{x}$$

This is our differential equation which describes the shape of the solidified cone. Next, solve to find y(x).

Solving the differential equation by method of substitution:

$$y''\cdot x = q\cdot y' \qquad q = 3\cdot\left(\frac{\kappa_s - \kappa_L}{\kappa_L}\right)$$

substitute $v = y'$:

$$v'\cdot x = q\cdot v$$

$$x\cdot \frac{d}{dx} v = q\cdot v$$

$$\int \frac{1}{v}\, dv = \int \frac{q}{x}\, dx$$

$$ln(v) = q\cdot ln(x) + c_1$$

$$v = x^q \cdot exp\left(c_1\right) = c\cdot x^q$$

re-substitute $v = y'$:

$$y' = x^q \cdot c$$

$$y = \int x^q \cdot c\, dx$$

$$y(x) = \frac{x^{(q+1)}}{(q+1)}\cdot c + d$$

Solve for c and d from initial conditions. We know the orignal radius (r) and slope of the liquid cone (y'(r))

$$y(r) = 0 \qquad y'(r) = y'_o$$

$$\frac{d}{dx}y(x) = \frac{d}{dx}\left[\frac{x^{(q+1)}}{(q+1)}\cdot c + d\right] = x^q \cdot c$$

$$\frac{d}{dx}y(r) = y'_o = r^q \cdot c$$

solve for c:

$$c = \frac{y'_o}{\left(r^q\right)}$$

substitute and solve for d:

$$y(r) = 0 = \frac{x^{(q+1)}}{(q+1)}\cdot\frac{y'_f}{\left(r^q\right)} + d$$

$$d = \frac{-r}{(q+1)}\cdot y'_r$$

insert these into y(x)

$$y(x) = \frac{x^{(q+1)}}{(q+1)}\cdot\frac{y'_o}{\left(r^q\right)} + \frac{-r}{(q+1)}\cdot y'_o = \frac{y'_o \cdot x}{(q+1)}\cdot\left[\left(\frac{r}{x}\right)^{(-q)} - \frac{r}{x}\right]$$

We can check this solution in a few important ways to make sure that it is correct. The first is to make sure that it is a solution to the differential equation.

$$y(x) = \frac{y'_o \cdot x}{(q+1)}\cdot\left[\left(\frac{r}{x}\right)^{(-q)} - \frac{r}{x}\right]$$

$$y'(x) = \frac{d}{dx}\frac{y'_o \cdot x}{(q+1)} \cdot \left[\left(\frac{r}{x}\right)^{(-q)} - \frac{r}{x}\right] = \left(\frac{1}{x} \cdot r\right)^{(-q)} \cdot y'_o$$

$$y''(x) = \frac{d^2}{dx^2}\frac{y'_o \cdot x}{(q+1)} \cdot \left[\left(\frac{r}{x}\right)^{(-q)} - \frac{r}{x}\right] = \frac{1}{x} \cdot q \cdot \left(\frac{1}{x} \cdot r\right)^{(-q)} \cdot y'_o$$

by comparing first and second derivatives of y(x) we indeed find that:

$$y'' \cdot \frac{x}{q} = y'$$

$$y'' \cdot x = q \cdot y'$$

the equation checks out.

We now have to reconsider the difference in height between a solidified layer of solid and a liquid atomic layer. If we do this, the equation describing the solidified shape is now:

$$y(x) = \frac{h_S}{h_L} \cdot \frac{y'_o \cdot x}{(q+1)} \cdot \left[\left(\frac{r}{x}\right)^{(-q)} - \frac{r}{x}\right] \qquad \text{where:} \qquad q = 3 \cdot \left(\frac{\kappa_S - \kappa_L}{\kappa_L}\right)$$

It is also necessary to check that mass is conserved. We can find the revolved volume of the function y(x).

$$V = \int_0^r 2 \cdot \pi \cdot x \cdot f(x)\, dx$$

$$V = \int_0^r 2 \cdot \pi \cdot x \cdot \left[\frac{h_S}{h_L} \cdot \frac{y'_o \cdot x}{(q+1)} \cdot \left[\left(\frac{r}{x}\right)^{(-q)} - \frac{r}{x}\right]\right] dx$$

$$V = -\pi \cdot h_S \cdot \frac{y'_o}{\left[(q+3) \cdot \left[h_L \cdot (q+1)\right]\right]} \cdot \lim_{x \to 0^+} r \cdot x^2 \cdot q + r^3 \cdot q - 2 \cdot x^3 \cdot \left(\frac{r}{x}\right)^{(-q)} + 3 \cdot r \cdot x^2 + r^3$$

in taking the limit we find:

$$V = -\pi \cdot h_s \cdot \frac{y'_o}{\left[(q+3)\cdot\left[h_L\cdot(q+1)\right]\right]} \cdot \lim_{x \to 0^+} 0 + r^3 \cdot q - 0 + 0 + r^3$$

$$V = -y'_o \cdot h_s \cdot \pi \cdot \frac{r^3}{\left[(q+3)\cdot h_L\right]}$$

substitute the definition of q:

$$V = y'_o \cdot h_s \cdot \pi \cdot \frac{r^3}{\left[\left[3\cdot\left(\frac{\kappa_s - \kappa_L}{\kappa_L}\right) + 3\right]\cdot h_L\right]}$$

$$V = \frac{1}{3}\cdot y'_o \cdot \pi \cdot r^3 \cdot \frac{\kappa_L \cdot h_s}{h_L \cdot \kappa_s}$$

we also know that

$$h_L = \frac{\kappa_L}{\eta_L} \qquad h_s = \frac{\kappa_s}{\eta_s}$$

substituting these give

$$V = \frac{-1}{3}\cdot y'_o \cdot \pi r^3 \cdot \frac{\eta_L}{\eta_s}$$

This is just the equation for the volume of the original liquid cone with a factor considering density change due to phase change. So, conservation of mass works out as well.

1.5 Derivation of a Sinusoid Solidifying

Here are the equations for slope. These look a little cleaner and I think it should be easy to apply what was done for cones to sinusoids. We know the slope now, we know the next slope, we can build a differential equation from this. Finding the f-factors may be somewhat troublesome.

$$\frac{d}{dx}g_0(x) = -a\cdot sin(\upsilon\cdot x)\cdot\upsilon$$

$$\frac{d}{dx}g_1(x) = -a\cdot f_1\cdot sin(\upsilon\cdot x)\cdot\upsilon$$

$$\frac{d}{dx}g_2(x) = -a\cdot f_2\cdot f_1\cdot sin(\upsilon\cdot x)\cdot\upsilon$$

$$\frac{d}{dx}g_3(x) = -a\cdot f_3\cdot f_2\cdot f_1\cdot sin(\upsilon\cdot x)\cdot\upsilon$$

or

$$\frac{d}{dx}g_3(x) = f_3\cdot\left(\frac{d}{dx}g_2(x)\right)$$

or

$$g'_3(x) = f_3\cdot g'_2(x)$$

or

$$g'_{n+1}(x) = f_{n+1}\cdot g'_n(x)$$

f is the ratio between the volume of the liquid before solidification of the elemental volume and afterwards. This means that we have to know the volume before and the volume afterward.
The volume of the revolved sinusoid can be found by integration:

$$y_n(x) = a\cdot f_n\cdot\left(cos(\upsilon\cdot x) - cos\left(\upsilon\cdot x_t\right)\right)$$

$$V_n = \int_0^{x_t} 2\cdot\pi\cdot x\cdot y_n(x)\,dx$$

$$V_n = \int_0^{x_t} 2\cdot\pi\cdot x\cdot\left[a\cdot f_n\cdot\left(cos(\upsilon\cdot x) - cos\left(\upsilon\cdot x_t\right)\right)\right]dx$$

$$V_n = \frac{\pi \cdot a \cdot f_n}{\upsilon^2} \cdot \left[2 \cdot \upsilon \cdot x_t \cdot \sin\left(\upsilon \cdot x_t \right) - \cos\left(\upsilon \cdot x_t \right) \cdot \left(\upsilon^2 \cdot {x_t}^2 - 2 \right) - 2 \right]$$

Remember, we have already advanced Δx and Δy, we are only interested in the volume change above the S-L interface due to the difference in surface atomic density. This means that is the same in both cases. There is a new slope and a new amplitude. Wavelength is the same and x_t and y_i are the same. As in the case of the cone, the change in volume is:

$$\Delta V\left(y', \Delta x, \kappa_s, \kappa_L \right) = \frac{M_s}{\eta_L} = \frac{\kappa_s}{\kappa_L} \cdot \Delta y \cdot \pi \cdot x^2 = \frac{\kappa_s}{\kappa_L} \cdot y' \cdot \Delta x \cdot \pi \cdot x^2$$

$$V\left(x_t \right) = \frac{\pi \cdot a}{\upsilon^2} \cdot \left[2 \cdot \upsilon \cdot x_t \cdot \sin\left(\upsilon \cdot x_t \right) - \cos\left(\upsilon \cdot x_t \right) \cdot \left(\upsilon^2 \cdot {x_t}^2 - 2 \right) - 2 \right]$$

The volume before solidification is:

$$V_1 = \frac{\pi \cdot a \cdot f_1}{\upsilon^2} \cdot \left[2 \cdot \upsilon \cdot x_t \cdot \sin\left(\upsilon \cdot x_t \right) - \cos\left(\upsilon \cdot x_t \right) \cdot \left(\upsilon^2 \cdot {x_t}^2 - 2 \right) - 2 \right]$$

The volume after solidification is:

$$V_2 = \frac{\pi \cdot a \cdot f_2}{\upsilon^2} \cdot \left[2 \cdot \upsilon \cdot x_t \cdot \sin\left(\upsilon \cdot x_t \right) - \cos\left(\upsilon \cdot x_t \right) \cdot \left(\upsilon^2 \cdot {x_t}^2 - 2 \right) - 2 \right]$$

The change in volume is:

$$\Delta V = V_2 - V_1$$

But we do not really care about the change in volume, but rather *ratio* of change of volume f.

$$f_{n+1} = \frac{V_1}{V_2} = \frac{V_1}{V_1 + \Delta V} = \frac{f_n \cdot V\left(x_t \right)}{f_n \cdot V\left(x_t \right) + \Delta V\left(y', \Delta x, \kappa_s, \kappa_L \right)}$$

$$g_{n+1}(x) = \left(g_n(x) - g_n\left(x_t \right) \right) \cdot f_{n+1} + g_n\left(x_t \right)$$

$$g'_{n+1}(x) = f_{n+1} \cdot g'_n(x)$$

$$\Delta V\left(y', \Delta x, \kappa_s, \kappa_L \right) = \frac{\kappa_s}{\kappa_L} \cdot \Delta y \cdot \pi \cdot x^2 = \frac{\kappa_s}{\kappa_L} \cdot y' \cdot \Delta x \cdot \pi \cdot x^2$$

Should this equation be written in terms of f, or g, or y? Should we write this in terms of two coupled differential equations?

OK, we are looking for the equation that will give the final shape of the solid. This is the equation which traces the trajectory of the SLV point. So, what we want is. This is what we are looking for. y and g are the same thing. we can use f to unite the equations maybe. The ratio of volumes is equal to the ratio of slopes.

$$\frac{f_n \cdot V(x_t)}{f_n \cdot V(x_t) + \Delta V(y'_n, \Delta x, \kappa_s, \kappa_L)} = \frac{y'_{n+1}}{y'_n}$$

Change of variables:

$u = x_t \qquad v = y_i$

$v = v(u)$

$\Delta v = v(u + \Delta u) - v(u) = v' \cdot \Delta u$

$v'_1 = v'(u)$

$v'_2 = v'(u + \Delta u)$

$\Delta V = V_2 - V_1$

$V_2 = \Delta V + V_2$

the ratio of slopes is equal to the ratio of volumes

$$\frac{v'_2}{v'_1} = \frac{V_2}{V_1}$$

now we don't know V.1 exactly, but we think we can get it from knowing the volume and shape of the original liquid. I think that this is where the problem lies. We are leaving out a Δu somewhere

$$V_1 = V_0(x_t) \cdot \frac{v'_1}{v'_0(x_t)}$$

in that same vein

$$V_2 = V_0 \cdot \frac{v'_2}{v'_0}$$

but aha!, this is at a different x, so this is not the same V.0 at used in V.1

$$V_2 = V_0(x_t + \Delta x) \cdot \frac{v'_2}{v'_0(x_t + \Delta x)}$$

ΔV is then:

$$\Delta V = V_2 - V_1$$

$$\Delta V = V_0(x_t + \Delta x) \cdot \frac{v'_2}{v'_0(x_t + \Delta x)} - V_0(x_t) \cdot \frac{v'_1}{v'_0(x_t)}$$

Solving for the new slope gives:

$$v'_2 = v'_0(x_t + \Delta x) \cdot \frac{\Delta V \cdot v'_0(x_t) + V_0(x_t) \cdot v'_1}{V_0(x_t + \Delta x) \cdot v'_0(x_t)} \qquad \text{where} \qquad \Delta V = \frac{\kappa_s}{\kappa_L} \cdot v'_1 \cdot \Delta u \cdot \pi \cdot u^2$$

This is the general setup for the problem

$$v'' = \lim_{\Delta u \to 0} \frac{v'_2 - v'}{\Delta u}$$

$$v'_2 = v'_0(x_t + \Delta x) \cdot \frac{G \cdot v' \cdot \Delta u \cdot \pi \cdot u^2 \cdot v'_0(x_t) + V_0(x_t) \cdot v'}{V_0(x_t + \Delta x) \cdot v'_0(x_t)}$$

$$v'' = \lim_{\Delta u \to 0} \frac{v'_0(x + \Delta x) \cdot \frac{G \cdot v' \cdot \Delta u \cdot \pi \cdot u^2 \cdot v'_0(x) + V_0(x) \cdot v'}{V_0(x + \Delta x) \cdot v'_0(x)} - v'}{\Delta u}$$

$$v_0(u) = a \cdot (\cos(\upsilon \cdot u) + 1) \qquad v_0(u + \Delta u) = a \cdot [\cos[\upsilon \cdot (u + \Delta u)] + 1]$$

$$v'_0(u) = -a \cdot \upsilon \cdot \sin(\upsilon \cdot u) \qquad v'_0(u + \Delta u) = -a \cdot \upsilon \cdot \sin[\upsilon \cdot (u + \Delta u)]$$

$$V_0(u) = \pi \cdot \frac{a}{\upsilon^2} \cdot \left[2 \cdot \upsilon \cdot u \cdot \sin(\upsilon \cdot u) - \cos(\upsilon \cdot u) \cdot \left(\upsilon^2 \cdot u^2 - 2\right) - 2\right]$$

$$V_0(u+\Delta u) = \pi\cdot\frac{a}{v^2}\cdot\left[2\cdot v\cdot(u+\Delta u)\cdot sin[v\cdot(u+\Delta u)] - cos[v\cdot(u+\Delta u)]\cdot\left[v^2\cdot(u+\Delta u)^2-2\right]-2\right]$$

$$v'_2 = v'_0(u+\Delta u)\cdot\frac{G\cdot v'\cdot\Delta u\cdot\pi\cdot u^2\cdot v'_0(u)+V_0(u)\cdot v'}{V_0(u+\Delta u)\cdot v'_0(u)}$$

$$v'_2 = \frac{-a\cdot v\cdot sin[v\cdot(u+\Delta u)]\cdot\left[\begin{array}{l} G\cdot v'\cdot\Delta u\cdot\pi\cdot u^2\cdot(-a\cdot v\cdot sin(v\cdot u))\ \ldots \\ +\pi\cdot\frac{a}{v^2}\cdot\left[2\cdot v\cdot u\cdot sin(v\cdot u)-cos(v\cdot u)\cdot\left(v^2\cdot u^2-2\right)-2\right]\cdot v'\end{array}\right]}{\pi\cdot\frac{a}{v^2}\cdot\left[2\cdot v\cdot(u+\Delta u)\cdot sin[v\cdot(u+\Delta u)]-cos[v\cdot(u+\Delta u)]\cdot\left[v^2\cdot(u+\Delta u)^2-2\right]-2\right]\cdot(-a\cdot v\cdot sin(v\cdot u))}$$

$$v'' = \lim_{\Delta u\to 0}\frac{v'_2-v'}{\Delta u}$$

$$v'' = -v'\cdot v\cdot\frac{-v^2\cdot G\cdot u^2+v^2\cdot cos(v\cdot u)^2\cdot G\cdot u^2+2\cdot cos(v\cdot u)\cdot v\cdot u\cdot sin(v\cdot u)+2\cdot cos(v\cdot u)^2-2\cdot cos(v\cdot u)-v^2\cdot u^2}{-2\cdot v\cdot u+2\cdot cos(v\cdot u)^2\cdot v\cdot u+sin(v\cdot u)\cdot cos(v\cdot u)\cdot v^2\cdot u^2-2\cdot sin(v\cdot u)\cdot cos(v\cdot u)+2\cdot sin(v\cdot u)}$$

This is the differential equation defining this system

Numerical Solution to Sinusoid Solidification, Si(110)

$\kappa_s := \kappa_{110}$ $\quad \kappa_L = 7.164 \times 10^{18} \frac{1}{m^2}$ $\quad h_s := h_{110}$

$G := \frac{-\kappa_s}{\kappa_L}$ $\quad a := .1$ $\quad \lambda := 20$ $\quad \upsilon := \frac{2 \cdot \pi}{\lambda}$

$u_0 := \frac{\lambda}{2}$ $\quad v_0 := v(u_0)$ $\quad v'_0 := v'(u_0)$

$u_f := 0.001$ $\quad v_0 = 0$ $\quad v'_0 = 0$

---

initial condition: $v_n := \begin{pmatrix} v_0 \\ v'_0 \end{pmatrix}$

$$D(u,v) := \begin{pmatrix} v_1 \\ -v_1 \cdot \upsilon \cdot \dfrac{-\upsilon^2 \cdot G \cdot u^2 + \upsilon^2 \cdot \cos(\upsilon \cdot u)^2 \cdot G \cdot u^2 + 2 \cdot \cos(\upsilon \cdot u) \cdot \upsilon \cdot u \cdot \sin(\upsilon \cdot u) + 2 \cdot \cos(\upsilon \cdot u)^2 - 2 \cdot \cos(\upsilon \cdot u) - \upsilon^2 \cdot u^2}{-2 \cdot \upsilon \cdot u + 2 \cdot \cos(\upsilon \cdot u)^2 \cdot \upsilon \cdot u + \sin(\upsilon \cdot u) \cdot \cos(\upsilon \cdot u) \cdot \upsilon^2 \cdot u^2 - 2 \cdot \sin(\upsilon \cdot u) \cdot \cos(\upsilon \cdot u) + 2 \cdot \sin(\upsilon \cdot u)} \end{pmatrix}$$

$Z := rkfixed(v_n, u_0, u_f, N, D)$

$U := Z^{\langle 0 \rangle}$ $\quad V := Z^{\langle 1 \rangle} \cdot \frac{h_s}{h_L}$ $\quad \frac{V_N}{2 \cdot a} = 0.813$

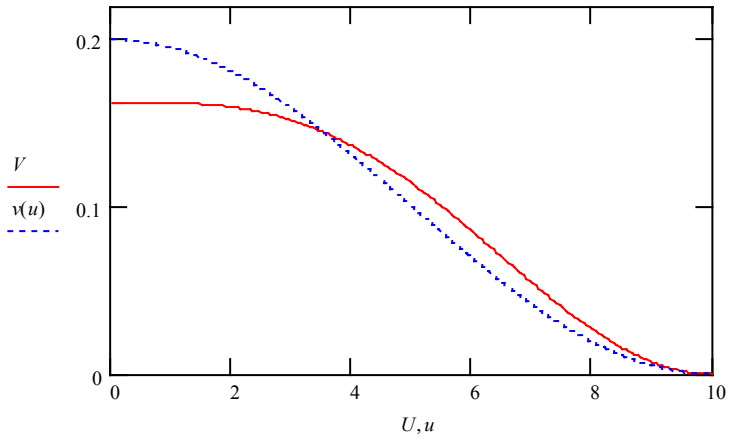

Numerical Solution to Sinusoid Solidification, Si(100)

$\kappa_s := \kappa_{100}$ $\quad \kappa_L = 7.164 \times 10^{18} \frac{1}{\mathrm{m}^2}$ $\quad h_s := h_{100}$

$G := \frac{-\kappa_s}{\kappa_L}$ $\quad G = -0.947$

$u_0 := \frac{\lambda}{2}$ $\quad v_0 := v(u_0)$ $\quad v'_0 := v'(u_0)$

$u_f := .001$ $\quad v_0 = 0$ $\quad v'_0 = 0$

---

initial condition: $v_n := \begin{pmatrix} v_0 \\ v'_0 \end{pmatrix}$

$$D(u,v) := \begin{pmatrix} v_1 \\ -v_1 \cdot v \cdot \dfrac{-v^2 \cdot G \cdot u^2 + v^2 \cdot \cos(v \cdot u)^2 \cdot G \cdot u^2 + 2 \cdot \cos(v \cdot u) \cdot v \cdot u \cdot \sin(v \cdot u) + 2 \cdot \cos(v \cdot u)^2 - 2 \cdot \cos(v \cdot u) - v^2 \cdot u^2}{-2 \cdot v \cdot u + 2 \cdot \cos(v \cdot u)^2 \cdot v \cdot u + \sin(v \cdot u) \cdot \cos(v \cdot u) \cdot v^2 \cdot u^2 - 2 \cdot \sin(v \cdot u) \cdot \cos(v \cdot u) + 2 \cdot \sin(v \cdot u)} \end{pmatrix}$$

$Z := rkfixed(v_n, u_0, u_f, N, D)$

$U := Z^{\langle 0 \rangle}$ $\quad V := Z^{\langle 1 \rangle} \cdot \frac{h_s}{h_L}$ $\quad \frac{V_N}{2 \cdot a} = 1.166$

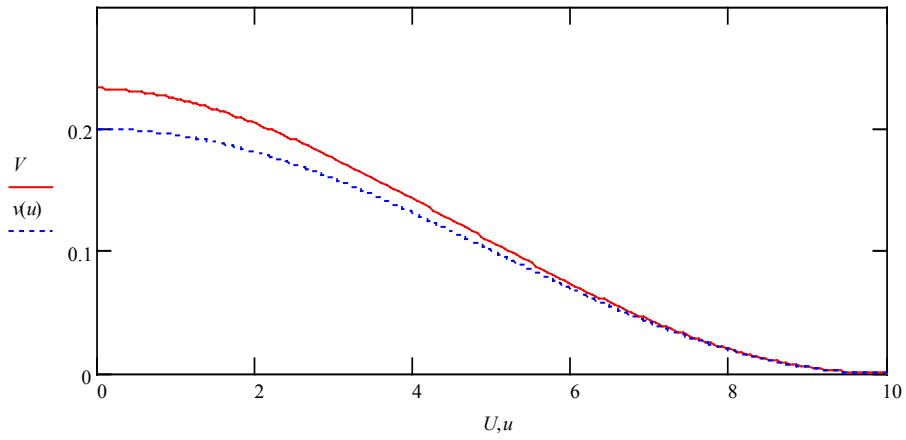

1.6 Description of Laser Melting Simulation

The heat diffusion equation is given below. ρ is the density, c is the specific heat, Qm is is heat of formation, and k is the thermal conductivity.

$$\rho c \frac{\partial T}{\partial t} = \nabla(k \nabla T) + Q_m \frac{d}{dt} solid + P(y,t)$$

Two sources of heat drive the system. One is latent heat of formation resulting from phase change. The other is the laser and is represented by a bulk heating term P(y,t).

$$P(y,t) = \alpha(1-R) I_0(t) e^{-\alpha y}$$

R is the reflectivity, and α is the absorption coefficient. The expression $I_0(t)$ is the incident laser power represented as a Gaussian function in time which decays exponentially as is penetrates into the surface. I_o is shown below. Units are in W/m^2.

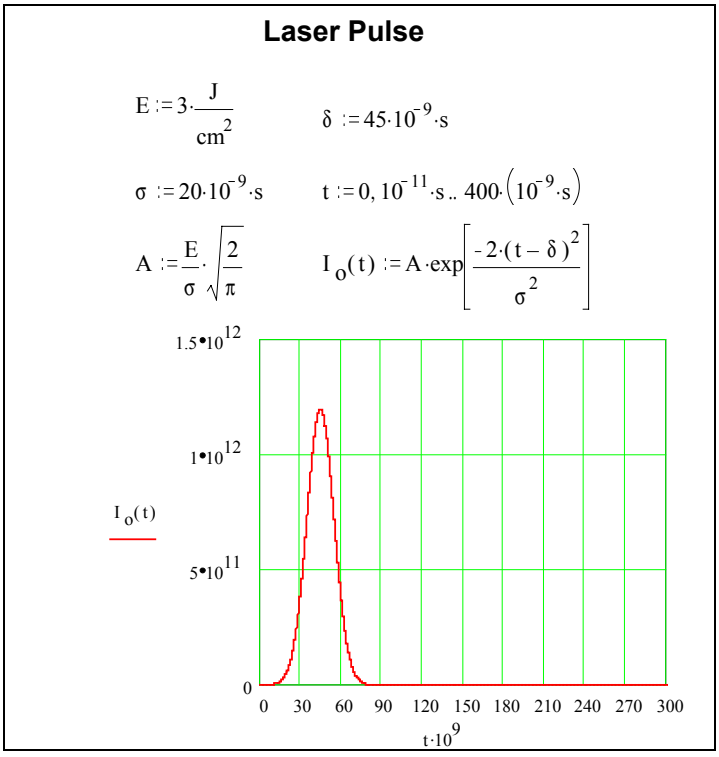

Density, conductivity, and heat capacity vary with temperature, and they all have an abrupt change across a phase change. We have chosen to represent the abrupt change with the continuous function arctan(…T). These are plotted below.

Density

$T := 0 .. 3000$

$T_m := 1687$

$$\rho(T) := \frac{\operatorname{atan}(T - T_m)}{5 \cdot \pi} + 2.43$$

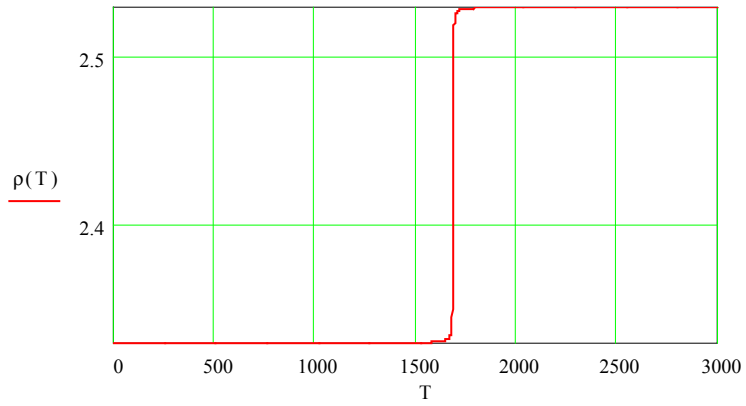

Thermal Conductivity

$sp := 1$

$T_m := 1687$

$$k(T) := \left(2.25 - .004 \cdot T + 2.78 \cdot 10^{-6} \cdot T^2 - 7.79 \cdot 10^{-10} \cdot T^3 + 8.04 \cdot 10^{-14} \cdot T^4\right) + \left[\left(\operatorname{atan}\left(\frac{T - T_m}{sp}\right) \cdot \frac{0.28}{\pi}\right) + 1.142\right]$$

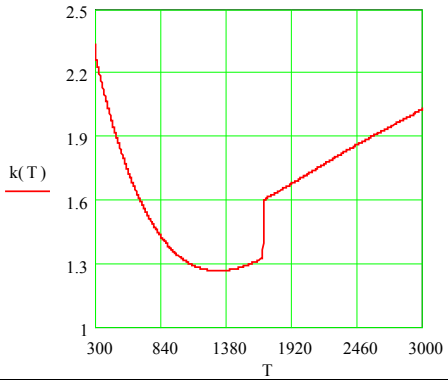

Heat Capacity

$$c_p(T) := 0.79 - 2.51 \cdot 10^{-4} \cdot T + 5.93 \cdot 10^{-7} \cdot T^2 - 2.83 \cdot 10^{-10} \cdot T^3 + 4.1 \cdot 10^{-14} \cdot T^4$$

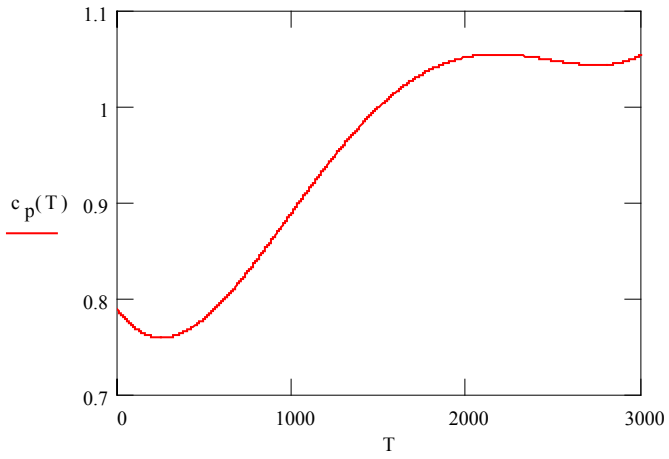

Laser Melting model parameters

Parameter	Symbols in FlexPDE	Material	Value and references
Density	rho	c-Si	2.32
ρ (g/cm^3)		*l*-Si	2.52
Melt latent	Qm	c-Si	4535.95
(J/cm^3)			
Melting	Tm		1685
Temperature(K)			
Thermal	lambda	c-Si: T<1200K	$1523.7*T^{-1.226}$
conductivity		T≥1200K	$9*T^{-0.502}$
(w/cm.K)		*l*-Si	$0.5+2.93x10^{-4}(T-T_M)$
Specific heat	cp	c-Si	$0.695*\exp(2.375x10^{-4}T)$
(J/g.K)		*l*-Si	1.0465
Reflectivity	Ref		0.66
Absorption	Absor		$1.7x10^6$
(cm^{-1})			
Width of the	w		$0.1x10^{-4}$
domain (cm)			
Height of the	h		$50x10^{-4}$
domain (cm)			
Energy density	E		3
(J/cm^2)			
Pulse width	D		$25x10^{-9}$
(s)			
Pulse delay	Dela		$45x10^{-9}$
(s)			
Maximum pulse	A		E/D*(2/PI)^0.5=$1.197x10^8$
amplitude			
(W/cm^2)			
Incident laser	I0		$A*\exp[\frac{-2*(t-Dela)^2}{D^2}]$
power (W/cm^2)			
Heat source	P		Absor*(1-Ref)*I0*exp(-Absor*y)

1.7 FlexPDE Code for Laser Melting

FlexPDE code for laser melting simulation

```
{
 This problem shows the application of FlexPDE to the laser melting of silicon.
}

TITLE
  'Laser Melting'
COORDINATES
   cartesian('x','y')

SELECT
! errlim = 1E-4
!  cubic
  smoothinit
  gridlimit = 3
regrid=off

VARIABLES
  temp(range=3000)
  solid(range=1)
DEFINITIONS
  Qm= 4536                  { latent heat }
  Tm= 1687                    { Melting temperature }
  T0= 4                     { Melting interval +- T0 }

  Tinit
  sinit

  lammain=4.0559-0.014648*temp+2.541e-5*temp^2-2.4507e-8*temp^3+1.3684e-11*temp^4-4.361e-
15*temp^5+7.351e-19*temp^6-5.0801e-23*temp^7
  lamadd=arctan((temp-1687)/1)*0.284111/PI+0.1421
  lambda =lammain+lamadd {w/cm.k}
  rho= 2.42 + ARCTAN((temp-1687)/1)*0.2/PI                { Density g/cm3 }
  cp = 0.78572-2.51e-4*temp+5.93e-7*temp^2-2.83e-10*temp^3+4.1e-14*temp^4      { heat capacity J/g.k}
  E= 1.8{Energy density J/cm2}
  D=25e-9 {Pulse width s}
  Dela=45e-9 {pulse Delay s}
  A= E/D*(2/PI)^0.5 {max pulse amplitude, W/cm^2}
  I0= A*exp(-2*(t-Dela)^2/D^2)  {incident laser power, W/cm^2}
  Absor=arctan((1687-temp)/1)*190000/PI+1655000 {Absorption coefficient cm-1}
  Ref=0.6691-3.1255e-5*temp+8.5224e-8*temp^2-5.71e-11*temp^3+1.222e-14*temp^4+1.31e-
18*temp^5-8.4e-22*temp^6+8.51e-26*temp^7 {Reflectivity}
  P=Absor*(1-Ref)*I0*exp(-Absor*y)  {Heat generation function- another source of heat}
  w = .05e-4 { width of the domain, cm}
  h =  25e-4 {height of the domain.cm}

INITIAL VALUES
   temp=Tinit
   solid =  0.5*erfc((tinit-Tm)/T0)

EQUATIONS
```

```
  rho*cp*dt(temp) - div(lambda*grad(temp))  = P  +  Qm*1e9*(0.5*erfc((temp-Tm)/T0) - solid)
  dt(solid) - 1e-6*div(grad(solid)) =  1e9*(0.5*erfc((temp-Tm)/T0) - solid)

BOUNDARIES
 region 1
   Tinit=300
    sinit=1
   start(0,0)
   natural(temp)=0 line to (w,0)
   natural(temp)=0 line to (w,h)
   natural(temp)=0 line to (0,h)
   natural(temp)=0 line to finish
 feature
    start(0,h/250)  line to (w,h/250)

TIME  0 by 1e-9 to 650e-9

MONITORS
   for cycle=1
  { elevation(temp) from(w/2,0) to (w/2,h) {range=(300,4000)}
   elevation(solid) from(w/2,0) to (w/2,h) }
{contour(temp)}
{contour(solid)}
{contour(rho)}
{contour(cp)}
{contour(Qm)}
{contour(P)}

PLOTS
  for t= 0 by 10e-9 to 300e-9 by 1e-9 to endtime
  { for t=50e-9 by 1e-9 to 60e-9}
   {elevation(solid) from(w/2,0) to (w/2,h/1)}
   elevation(temp) from(w/2,0) to (w/2,h/1) {range=(300,4000)}
{   contour(temp)painted range=(300,4000)  }

HISTORIES
   history(solid)   at (w/2,0) export format "#t#b#1"  file = "E_18_To300_s.txt"
   history(temp)   at (w/2,0) export format "#t#b#1"  file = "E_18_To300_t.txt"
   history(temp) at (w/2,h)
```

1.8 Matlab Code for Model for Surface Structure Evolution

```
%surface_evolution.m
%this program uses both height and deviation from a sin wave to detmine the
%best wavelength fof growth

clear
plotreq = 0; %request to watch end stage solidification
plot_5 = 1; %results of capillary and thermal effects
plot_66 = 1; figure(66); clf %results of solidication

%material constants

Tm = 1687;                          %melting temperature (K)
T = Tm-0;
Wa = 28.0855;                       % atomic weight (gm/mol)
Na = 6.022142*10^23;                 % avagadro's number (atoms/mol)
rhoL= T*(-6.2508^-4)+3.713;         %density of the liquid phase (g/cm^3)
aSi = 2.3613*10^-6*T+0.54219;       %unit cell edge length at T, (nm)
rhoS = 8*Wa/Na*((aSi*10^-7)^(-3));          %density of solid Si at T, (gm/cm^3)
D = 0.18;                                   % thermal diffusivity (cm^2/s)
sigma = 740;                              %surface tension (mN/m) = (g/s^2)
Gz = 25;                                   %thermal gradient in liquid (K/um)
surface = 100;

if (surface == 111)
   h = 1;
   k =  1;
   l  =  1;
   del = 0; %deviation from the (hkl) normal
   nu = 0;  %precession about the (hkl) normal
   D = D;
   sigma = sigma;
end

if (surface == 100)
   h = 1;
   k =  1;
   l  =  1;
   del = 0; %deviation from the (hkl) normal
   nu = 0;  %precession about the (hkl) normal
   D = D;
   sigma = sigma;
end

%the following function returns the epitaxial layer height (h4), and the
%area of the footprint (A4), in terms of the unit cell edge length for
%tetrahedrally bonded atoms given a certain direction
[h4,A4] = tetra_surf_density(h,k,l,del,nu);
hS = aSi*h4;  %Average eptixial height of the solid phase (nm)
hL = .28; %Average eptixial height of the liquid phase (nm)

tmelt = 300;  %melt time (ns)
```

```
hmelt = 1;     %melt depth (um)
i = 0;

for tmelt = 450 : 50 :  800  %melt time (ns)
   i = i + 1;

   smin = 45; %min wavelength (um)
   sstep = 1;  % wavelength increment (um)
   smax = 65; % max wavelength (um)

   count = 0;
   %define the initial shape of the surface, the solid-vapor interface
   for s = smin : sstep : smax;                    %wavelength (um)

      count = count + 1;
      Xo = 0 : .01 : s/2;          %distance along the surface (um)
      A_SV = .05;                  %amplitude of the LV interface (um)
      SVo = A_SV*(cos(2*pi*Xo/s) + 1);
      SVoo = SVo;

      for cycle = 1 : 1

         %the following function returns the shape of the SL and LV interfaces
         %after a given melt time
         [Xf,SL1,LV1]  =  capillary_thermal_effects(Xo,SVo,tmelt,hmelt,rhoL,D,sigma);

         %the additional effect of faceting is included if dealing with the
         %(111) surface
         if (surface == 111)
            tf = tmelt*2/3; %solidification lasts for about 2/3 of the total melt time
            A_SL  = max(SL1)/2;
            L_SL = 2*max(Xf);
            [ Xf, SL15] = facet_function(Xf,tf,A_SL,L_SL,Gz);
         end

         if (plot_5 == 1 )
            figure(5)
            clf
            plot(Xo,SL1,'g')
            hold on
            %plot(Xo,SL15,'r')
            plot(Xo,LV1,'k')
            drawnow
         end

         %the following function returns the shape of the SV interface resulting
         %from the solidification of liquid pools on the surface
         [Xo,SV2] = end_stage_solidification(Xo,LV1,SL1,hS,hL,rhoS,rhoL,plotreq);
         SV2 = SV2 -min(SV2);

         if ( plot_66 == 1)
            clf
            figure(66)
            plot(Xo,SV2,'r')
```

```
            hold on
            plot(Xo,SVoo)
            drawnow
          end

          statmat(count,:) = [ count s SV2(10) ];
          SVo = SV2;  %update cycle

        end
    end
      %spline fit to results to interpolate highest growth;

    lambda = smin : (smax - smin)/1000 : smax;
    growth = interp1(statmat(:,2),statmat(:,3),lambda,'cubic');

    figure(67)
    clf
    plot(statmat(:,2),statmat(:,3))
    hold on
    plot(lambda,growth,'r')

    growth_max = max(growth);
    lambda_star =  lambda( find( growth_max == growth ));
    growth_factor = (growth_max - SVoo(10))/SVoo(10);

    lambda_mat(i,:)  = [ tmelt lambda_star ]

end %end for tmelt

% end of calculation alarm
while ( 1 == 1)
    x = 0 : 1 :2000;
    y = .2*sin(2*pi*x/4000).*(sin(x) + sin(6/3*x) + sin(9/3*x));
    y2 = .2*sin(2*pi*x/4000).*(sin(x) + sin(6/3*x) + sin(9/3*x));
    sound([ y'  y2'],4000)
    pause(2)
end
```

1.9 Function for Simulating Thermal and Capillary Effects

```
function   [Xf,SLf,LVf]  =  capillary_thermal_effects(Xo,SLo,tmelt,hmelt,rhoL,D,sigma)

warning off MATLAB:divideByZero
% this function finds the shape of a SL interface which has been acted upon
% by thermal diffusion.

%this function computes the fourier transform of the intial shape, then
%computes the new amplitude of each of the frequency components in the
%fourier transform, then takes the inverse transform to determine the new
%shape

%(Xo,SLo) are the points defining the solid-liquid interface (um)
%tm is the melt time (ns)

Xoo = Xo;
tm = tmelt*10^-9; %conversion for melt time, (ns) -> (s)
hm = hmelt*10^-4;  % conversion for melt depth (um) -> (cm)
Xo = Xo*10^-4; %conversion for wavelength (um) -> (cm)
%D = 0.184; % thermal diffusivity (cm^2/s)
%sigma = 740; %surface tension (mN/m) = (g/s^2)
vis = 8*10^-4/rhoL;  %viscocity (N*s/m^2)

%plot request
plot1 = 0; %initial interface
plot2 = 0; %FFT of initial interface
plot3 = 0; %initial and final interface

%interpolate the data so that there are 2^n points to help
%improve speed of fft calculation

killnan = find( isnan(SLo) == 1 );
if ( isempty(killnan) == 0 )
   disp('NaN found in capillary_thermal_effects')
   break
end

SLo(killnan) = [ ];
Xo(killnan) = [ ];


npts = 2^7-1;
x = 0 : max(Xo)/npts : max(Xo);
y = interp1(Xo,SLo,x,'linear','extrap');

%create a mirror image of the interface
xm = -reverse(x);
ym = reverse(y);

x = [ xm x ];
y = [ ym y ];
```

```
%repeat the interface several times to form a wave pattern
nrepeat = 6;
for i = 1: nrepeat
   y = [ y y ];
end
x2 = length(y)/length(x)*min(x) + ( max(x) - min(x) )/(length(x)) : ( max(x) - min(x) )/(length(x)) : length(y)/length(x)*max(x);
x = x2;

%take the fourier transform of the wave
Fy = fft(y);
Fy = fftshift(Fy);

%cut the fft plot in half
Fy( 1 : length(Fy)/2) = [ ];

%scale the data to frequency
Fw = 0  :  1/(2^nrepeat)   :  (length(Fy) -1)/(2^nrepeat);

%scale the data to wavelength
Fs = 1./Fw*max(Xo)*2;

%send the transform through a filter based on the
%thermal diffusivity
SL_filter = exp(-(2*pi./Fs).^2*D*tm); %amplitude of SL interface after tm
SL_filter_Fy = Fy.*SL_filter;

%send the transform through a filter based on the
%capillary wave equation which includes damping
w = sqrt ( sigma/rhoL*(2*pi./Fs).^3.*tanh(2*pi*hm./Fs)); %frequency of wave from dispersion relation(Hz)
gamma = 2*vis*10*w*sqrt( rhoL/sigma/hm);  %damping coefficent(Hz)
LV_filter = exp(-gamma*tm).*cos( w*tm );
LV_filter_Fy = Fy.*LV_filter;

%create a mirror image of the SL and LV filtered transform
m = zeros(size(Fy));
for i = 1 : length(SL_filter_Fy)
   mSL(i) =  SL_filter_Fy(length(SL_filter_Fy)+1-i);
   mLV(i) =  LV_filter_Fy(length(LV_filter_Fy)+1-i);
end
SL_filter_Fy = [ mSL SL_filter_Fy ];
LV_filter_Fy = [ mLV LV_filter_Fy ];

%take the inverse fourier transform
SLf = abs(ifft(SL_filter_Fy));
LVf = abs(ifft(LV_filter_Fy));

%cut and scale to fit input
SLf = SLf((npts+1):(npts+1)*2);
LVf = LVf((npts+1):(npts+1)*2);
Xf = 0  :  max(Xo)/(npts+1) : max(Xo);
SLf = interp1(Xf,SLf,Xo);
```

```
LVf = interp1(Xf,LVf,Xo);
SLf = SLf - min(SLf);
LVf = LVf - min(LVf);
Xf = 0 : max(Xoo)/(length(SLf)-1) : max(Xoo);

%plotting
if (plot1 == 1)
   figure(1)
   clf
   plot(x(1:4*(npts+1)),y(1:4*(npts+1)),'r')
   hold on
end

if (plot2 == 1)
   figure(41)
   clf
   plot(Fw,abs(Fy))
   hold on
   plot(Fw,abs(Fy),'r.')
end

if (plot3 == 1)
   figure(42)
   clf
   plot(Xf,SLf,'r')
   hold
   plot(Xo,SLo)
end
```

1.10 Function for Determining Faceting Effects

```
function [ xo, zf ] = facet_function(xo,tf,A,L,Gz)
warning off MATLAB:divideByZero
%function to find the final shape of the 111 SL interface after
%solidification

%x = vector of points defining the x-axis of the interface (um)
%tf = time for solidification (ns)
%A = amplitude of initial surface (um)
%L = wavelength of initial surface (um)
%Gz = thermal gradient in liquid ( K/um)

%A = .1;    %amplitude of the sin wave (um)
%L = 20;   %wavelength (um)
%Gz = 250;   %vertical thermal gradient (K/um)

sf = 7.2; % scaling factor for silicon
Jx = 0.3*sf; %speed factor for lateral motion (m/s/K)
F = 8.4*10^26; %nucleation rate (nucleus/m^2/s)
h = 3.13*10^-10; %height of a layer (m)
d = 100;
T111 = -23;

plot_1 = 0;
plot_2 = 0;
plot_3 = 0;

%find the lateral position of moving ledges as a function of time
%Postion on the interface
xi_min = .1;
xi_max = L/2;
xi_int = 50;
xi_step = (xi_max - xi_min)/xi_int;
xi = xi_min : xi_step : xi_max;
xi_0 = xi;
xi_tip = 0;
zi = -(A * cos( 2 *pi *xi/L + pi)  - A);
zi_0 = zi;
zi_tip = -(A * cos( 2 *pi *xi_tip/L + pi)  - A);

ns = 10^-9;
tprev = 0;

if ( plot_2 == 1)
   figure(2)
   clf
   hold on
end

i = 0;
for t = 0 : tf/100*ns : tf*ns;
   i = i + 1;
```

```
    %the temperature at this position is given by the thermal field
    Ti = (A*cos( 2 *pi *xi/L +pi)  - A)*Gz + zi*Gz  + T111;
    Ti = max(Ti,T111);
    Ti_tip =  (A*cos( 2 *pi *xi_tip/L +pi)  - A)*Gz + zi_tip*Gz  + T111; %temperature at the crest

    %the z- and x- velocities at this point are
    Vzi = -h*sf*(F*exp(-140./abs(Ti)).*(2*Jx*Ti).^2).^(1/3).*sign(Ti); %vertical velocity  (m/s)
    Vzi_tip = -h*sf*(F*exp(-140./abs(Ti)).*(2*Jx*Ti_tip).^2).^(1/3).*sign(Ti_tip);  %velocity of the crest =
avg. vertical interface velocity
    Vzi = Vzi - Vzi_tip; %find vertical velocity relative speed of the interface
    Vxi = -Jx*Ti.*sign(xi); %lateral velocity  (m/s)

    %the position of this point after time t is
    del_z = Vzi*(t-tprev)*10^6;   %vertical displacement (um)
    del_x = Vxi*(t-tprev)*10^6;   %lateral displacement (um)

    zi2 = zi + del_z;
    xi2 = xi + del_x;

    if (plot_2 == 1)
       for j = 1 : length(xi)
          plot([ xi(j) xi2(j)],[zi(j) zi2(j)])
       end
    end

    % update values
    tprev = t;
    xi_prev = xi;
    zi_prev = zi;
    xi = xi2;
    zi = zi2;

    if(plot_2 == 1)
       plot(xi,zi,'r')
       axis([ 0 L/2 -inf inf ])
    end

    %reconfigure results so that they share the same x-axis
    u = 1;
    Xi = xi_min : xi_step/10 : xi_max+u;

    remove = find( (xi < xi_min) |   (xi > xi_max+u));
    xi(remove) = [ ];
    zi(remove) = [ ];
    if (length(xi) > 2 )
       Zi = interp1(xi,zi,Xi,'linear');
       remove = find(  Xi > xi_max );
       Zi(remove)= [ ];
       Xi(remove) = [ ];
       Zi = [ zi_tip Zi ];
       Xi = [ 0 Xi ];
       zi_map(i,:) = Zi;
    end
end
```

```
outline = max(zi_map);
Xi = xi_min :  (xi_max - xi_min)/(length(outline)-1) : xi_max;
zf = interp1(Xi,outline,xo,'linear','extrap');
zf = zf - min(zf);

if(plot_2 == 1)
   plot(Xi,outline,'g')
end

if(plot_3 == 1)
   figure(3)
   clf
   plot(Xi,outline,'r')
   hold
   plot(xi_0,zi_0)
end

%_____________________________________________________________
%plot of thermal field

if (plot_1 == 1)
   zmin = 0;
   zmax = 2*A*1.1;
   i = 0;
   for x = -L/2 : L/d/2 : L/2;
      i = i + 1;
      j = 0;
      for z = zmin : (zmax-zmin)/d : zmax;
         j = j + 1;
         T(j,i) = (A*cos( 2 *pi *x/L +pi)  - A)*Gz + z*Gz  + T111;
         T(j,i) = max(T(j,i),T111);
      end
   end
   x = -L : L/d : L;
   z = zmin : (zmax-zmin)/d : zmax;
   Ti_Line = -(A * cos( 2 *pi *x/L + pi)  - A);
   % temperature field
   if (plot_1 == 1)
      figure(1)
      clf
      surf(x,z,T)
      shading flat
      colormap(bone)
      hold on
      contour3(x,z,T,[ T111 T111],'r');
      contour3(x,z,T,[ 0 0],'k');
      %fill([ -L, x, L] ,[ 0, Ti_Line, 0],[ .5 .5 .7])
      colorbar
      axis([ -inf inf zmin zmax -inf inf  ])
      view([ 0 90])
   end
end
```

1.11 Function for Modeling End-Stage Solidification

```
function [Xf,SVf] = end_stage_solidification(Xo,LVo,SLo,hS,hL,rhoS,rhoL,plotreq)

%this function calculates the the final solid shape for the initial
%solid-liquid (SL) and liquid-vapor (LV) interface shapes.
%(Xo,LVo) is a series of points defining the initial liquid-vapor interface (um)
%(Xo,SLo) is a series of points defining the inital solid-liquid interface (um)
%Xo is measured from 0 to half the wavelength of the surface wave (um)
%LVi and SLi must be equal where Xi is a maximum
%hS is the height of a solid atomic layer (nm)
%hL is the height of a liquid atomic layer (nm)
%rhoS is the volumetric density of the solid (gm/cm^3)
%rhoL is the volumetric density of the liquid (gm/cm^3)

Wa = 28.0855;               % atomic weight of Si (gm/mol)
Na = 6.022142*10^23;    % avagadro's number (atoms/mol)
new_shape = [ 0 0 ];

%surface atomic density
etaS = rhoS*Na/Wa/10^21; %molten volumetric atomic density (atoms/nm^3)
etaL = rhoL*Na/Wa/10^21; %molten volumetric atomic density (atoms/nm^3

kS = etaS*hS;
kL = etaL*hL;

steps = 1000; %number of steps in the solidification process

incr = hL/1000;    % increment of solidification per iteration (um)

%establish the location where the interfaces first meet

startpos = find (  min(LVo - (SLo-1) ) == (LVo - (SLo-1)) );

%move interfaces into contact
LVo = LVo - LVo(startpos);
SLo = SLo - SLo(startpos);

%let any extraneous regions be part of the new
%shape as they are
LV_outer = LVo(startpos:length(LVo));
SL_outer = SLo(startpos:length(SLo));
Xo_outer = Xo(startpos:length(Xo));
new_shape(1:length(Xo_outer),:) = [ reverse(Xo_outer') reverse(LV_outer') ];

%define inner regions which will solidify
LV = LVo(1:startpos);
SL = SLo(1:startpos);
x = Xo(1:startpos);
xstep = max(x)/length(x);
xslv = max(x);
yslv = 0;
```

```
cond = 1;
i = length(Xo_outer);

%_____________________________________________________________________________
while ( cond == 1 )
   i = i + 1;
   %advance the SL interface upward
   SL = SL + incr;
      %Find the new SLV point using cubic interpolation
   SV = (LV - SL); %distance between the LV and SL interfaces
      xslv_old = xslv;
   yslv_old = yslv;
      if ( length(SV) > 1 )
      if ( SV(1) > 0 )
         %interplolate to find new points on the SLV interface
         xslv = interp1(SV,x,0,'linear','extrap');
         yslv = interp1(x,LV,xslv,'linear','extrap');

         if(xslv > 2* xstep)

            resizecond = 1;
            xbif_index = 0;
            xbif = 0;
            LV_bif = 0;
            %check for and eliminate bifurcation in solidification
            if ( ((xslv_old - xslv) > 1) & xslv > 2*xstep )
               xbif_index = min (find(SV < .001 & SV > -.001) );
               xbif_index = xbif_index : length(x);
               xbif = x(xbif_index);
               LVbif = LV(xbif_index);
               x(xbif_index) = [ ];
               LV(xbif_index) = [ ];
               SL(xbif_index) = [ ];
               %SL = SL - SL(length(SL)) + LV(length(SL)) - 2*hL/1000 ;
               %plot(xbif,LVbif,'m')
               xslv = min(xbif);
               yslv = max(LVbif);
               new_shape(i:i+length(xbif)-1,:) = [ reverse(xbif') reverse(LVbif') ];
               i = i + length(xbif_index)-1;
               resizecond = 0;
               %pause

            end

            %figure(13)
            %plot(new_shape(:,1),new_shape(:,2),'r')
            %pause
            %figure(12)

            %Calculate the area of the solid-liquid interface
            %redefine the interface
            xi = x;%0 : xstep : xslv;
            yi = SL;%SL(1:length(xi));
```

```
zi = LV;%LV(1:length(xi));
xi = [ xi xslv ];
yi = [ yi yslv]; %height of the SL interface
zi = [ zi yslv]; %height of the LV interface
L = length(xi);

c = xi(1:L-1);
d = xi(2:L);
f = yi(1:L-1);
g = yi(2:L);
m = zi(1:L-1);
n = zi(2:L);

S_kernal = pi*(c+d).*sqrt( (f-g).^2 + (d-c).^2 ); %surface area of a frustrum
SSL = sum(S_kernal); %total surface area of a the SL interface

%find the volume of the liquid
V_kernal_LV = 1/3*pi*(m-n).*(c.^2 + c.*d + d.^2);
V_kernal_SL = 1/3*pi*(f-g).*(c.^2 + c.*d + d.^2);
V = sum(V_kernal_LV) -  sum(V_kernal_SL);

%The number of atoms which are added to the liquid as an epitaxial layer solidifies
del_atoms = SSL*(kL-kS)*10^6;

%The change in liquid volume is then (um^3)
del_V = del_atoms*Wa/rhoL/Na*(10^12);

%The new volume of the liquid is
V_2 = V + del_V;

%The new shape of the new LV interface is then
LV_2 = (LV - SL)*V_2/V + SL;
LV = LV_2;

%The liquid layer which has solidified will now have a different
%height. The SL and LV layers need to be shifted by this amount
SL = SL + (hS - hL)/1000;
LV = LV + (hS - hL)/1000;

plotfreq = 20;
if(plotreq == 1)
   if ( round(i/plotfreq) == (i/plotfreq) )
      figure(12)
      clf
      hold on
      plot(x,LV,'b')
      plot(-x,LV,'b')
      plot(xslv,yslv,'g')
      plot(x,SL,'r')
      plot(-x,SL,'r')
      plot(Xo,LVo,'k')
      plot(-Xo,LVo,'k')
      plot(new_shape(:,1),new_shape(:,2),'g')
      plot(-new_shape(:,1),new_shape(:,2),'g')
```

```
                axis([ -inf inf 0 inf ])
                drawnow
            end
        end
         new_shape(i,:) = [ xslv yslv ];

        if (resizecond == 1)
            %resize the interfaces
            xr = 0 : xslv/1000 : xslv;
            SL = interp1(x,SL,xr,'linear','extrap');
            LV = interp1(x,LV,xr,'linear','extrap');
            x = xr;
        end

        % else
        %cond = 0;
        %xslv = 0;
        %yslv = yslv + hS/1000;
        %new_shape(i,:) = [ xslv yslv ];
        %end
      else % xslv > 2*xstep
        cond = 0;
      end

    else % SV(1) > 0
      cond = 0;

    end
  else %( length(SV) > 1 )
    cond = 0;
  end

end

%Prepare output
%spline fit the final shape so that the x-axis spacing is the same
new_shape(i:i+length(LV)-1,:) = [ reverse(x') reverse(LV') ];
killspikes = find(abs (diff(new_shape(:,2))) > .005 );
new_shape(killspikes+1,:) = [ ];
new_shape(length(new_shape),:) = [ ];
Xf = Xo;
new_shape(:,1) = reverse(new_shape(:,1));
new_shape(:,2) = reverse(new_shape(:,2));
d = 1 : 2 : length(new_shape);
new_shape(d,:) = [ ];
SVf = interp1(new_shape(:,1),new_shape(:,2),Xo,'linear','extrap');
if ( find( isnan(SVf) == 1 ) > 0 )
  disp('generated NaN in end_stage')
  break
end
```

1.12 Function for Determining the Atomic Density of Silicon

```
function   [h4,A4] = tetra_surf_density(h,k,l,del,nu)

%this program calculates the hieght and footprint of
%tetrahedrons for the purpose of determining surface atomic density

%given an initial direction given by (h,k,l) vector, and then deviation
%from that direction (del) and then precession around the (hkl) vector

%h4 is the height of the rotated tetrahedron
%A4 is the surface area of the shadow cast by the rotated tetrahedron
%onto surface of interest

%surface_density_cubes_tetras.m

%euler angles of rotation
phi0 = atan2( k,(h + eps));
theta0 = atan2( sqrt( h^2 + k^2 ),(l + eps));

del_phi = del*pi/180*sin(nu*pi/180);
del_theta = del*pi/180*cos(nu*pi/180);

phi = phi0 +del_phi;
theta = theta0 +del_theta;

%rotation matrices
Rz = [ cos(phi) -sin(phi) 0 ; sin(phi) cos(phi) 0 ; 0 0 1 ]; %rotation matrix around z-axis
Rx = [ 1 0 0 ; 0 cos(theta) -sin(theta) ; 0 sin(theta) cos(theta) ]; %rotation matrix around x-axis
RR = Rx*Rz;

%_____________________________________________________
%tetrahedron calculations

%points defining the tetrahedron
p4 = .5*[ 0 0 0 ; 1 0 1; 1 1 0 ; 0 1 1 ]';

%rotate the tetrahedron in the same manner as the cube
q4 = ( RR*p4)';

%the maximum vertical extents define the hieght of the tetrahedron
h4 = max( q4(:,3) ) - min ( q4(:,3) );

order_mat = [ 1 2 3 1 ; 1 2 4 1; 1 3 4 1; 2 3 4 2 ];

% plot shadow of tetrahedron
if (0 == 1)
   figure(2)
   clf
   for i = 1 : 4
      plot( q4(order_mat(i,:),1) , q4(order_mat(i,:),2)   )
      hold on
```

```
   end
end

%find the area of the tetrahedron
A4 = 0;
for i = 1 : 4  %number of faces
   x = q4(order_mat(i,:),1) ;
   y = q4(order_mat(i,:),2) ;
   Atri = 0;
   for j = 1 : 3 %number of corners per face
      Atri = 1/2*( x(j)*y(j+1) - x(j+1)*y(j) ) + Atri;
   end
   A4 = abs(Atri) + A4;
end
A4 = A4/2;

%_____________________________________________________
```

1.13 Matlab Ray-Tracing Program

```
%light_focussing_wave_surface.m
%this program determines the path of light reflected from
%a wavy surface
clear
figure(1)
clf

anglesun = 90*pi/180;
na = 1; %index of refraction of air
nump = 800;
minp = -10;
maxp = 10;
mrefnummax =2; %number of reflections
xposmin = -10; %positions of incident traces
xposstep = .02;
xposmax = 10;
pintpos = 1; %initial condition for previous point of intersection
plt = 0;     %request plot (1 = yes) (0 = no)
plot_1 = 0; % request for ray_tracing plot
plot_2 = 0; %request for linear intensity plots
plot_3 = 0; %request for intensity map
plot_4 = 1; %request for contour of intensity map
mrefnum = 1; %count of multiple reflection (initial state)
blur = .01;
%points defining surface of silicon

f = 40
amps = 2.82;
for amp = 3.2: .1 :3.2
   f = f + 1;

   pxc = -10: .1 : 10;
   pyc = -amp*cos(pxc/10*pi);
   a = -10; %left extent of plot
   b = 10;  %right extent of plot
   c = -4;   %bottom extent of plot
   d = 4;  %top extent of plot

   spline_points = 100;  % number of points in horizontal direction
   y_meter_min  = c ;   %min position for intensity measurements
   y_meter_max = d;    %max position for intensity measurements
   y_meter_step =    (y_meter_max - y_meter_min ) / (spline_points);       %vertical step for intensity
measurements


   %convert curve to a spline
   %in order to space the points evenly
   xi = minp : (abs(maxp)+abs(minp))/nump : maxp;
   yc1 = spline(pxc,pyc,xi);
   %leave only necessary part of curve
   yc1 = yc1(1:nump/2+1);
```

```
xc1 = xi(1:nump/2+1);

%create mirror image to complete curve
xi = minp : (abs(maxp)+abs(minp))/nump : maxp;
yc2 = spline(-pxc,pyc,xi);
%leave only necessary part of curve
yc2 = yc2(nump/2+2:nump+1);
xc2 = xi(nump/2+2:nump+1);

%combine two halves to complete shape
xc = [ xc1 xc2 ];
yc = [ yc1 yc2 ];

%calculate first derivative of curve
slopec = diff(yc)./diff(xc);
slopec = spline(xc(1:nump),slopec,xc);


i = 0;
for y_meter = y_meter_min : y_meter_step : y_meter_max
   y_meter
   i = i + 1;

   j = 1;
   for xpos = xposmin : xposstep : xposmax %xpos is the approximate xlocation for incident light ray

      %incident light ray
      xl = minp : ( maxp  -  minp )/nump : maxp;
      m1 = tan(anglesun);
      b1 = (-1-m1*xpos)*ones(size(xl));
      iyl = m1*xl + b1;
      %plot(xl,iyl,'r')

      pangleref = anglesun;

      for mrefnum = 1 : mrefnummax

         %determing the reflected beam
         [ryl,intpos,angleref,angleinc,brk,m2,b2]                                    =
reflectfun_2(iyl,xc,yc,slopec,pangleref,pintpos,plt,mrefnum,nump);

         if (brk == 1)
            %disp('ray termination')
            break
         end %end for break condition

         if (plot_1 == 1)
            figure(1)
            cl = [ 'y' 'k' 'y' 'g' 'c' 'b' 'k' 'b' 'm' 'y' 'g' 'c' 'b' 'k' ];
            plot(xc,ryl,cl(mrefnum))
         end


         %find intersection of light meter and reflected beam
```

```
    if (mrefnum > 0)
       x_meter = (y_meter - b2)/m2;
       if ( plot_1 == 1)
          figure(1)
          %plot(x_meter,y_meter,'r.')
       end
       %build a vector of data on the position of the intersection
       %between the reflected beam and the meter
       meter_vec(j) = [ x_meter ];
    end

    %remove irrelevant portions of rays

    if (mrefnum > 1)
       if ( yc(pintpos) > yc(intpos) )
          iyl( find( iyl > yc(pintpos) )) = inf;
          iyl( find( iyl < yc(intpos) )) = inf;
       else
          iyl( find( iyl < yc(pintpos) )) = inf;
          iyl( find( iyl > yc(intpos) )) = inf;
       end  %end conditional yc(pintpos) > ....

       if (plot_1 == 1)
          figure(1)
          cl = [ 'y' 'k' 'y' 'g' 'c' 'b' 'k' 'b' 'm' 'y' 'g' 'c' 'b' 'k' ];
          plot(xc,iyl,cl(mrefnum))
       end

       %draw silicon
       if (plot_1 == 1)
          figure(1)
          plot(xc,yc,'k')
          axis([ a b c d])
          %grid
          hold on
       end

    end  %end conditional mrefnum >1 ...

    %update values for next iteration
    piyl = iyl;
    iyl = ryl;
    ppintpos = pintpos;
    pintpos = intpos;
    pangleref = angleref;

    %generate a statistics matrix to store information about location
    %of light incidence, angle of incidence, and reflection number

    statmat(j,1:5) = [j xpos mrefnum intpos angleinc];
    j = j+1; %index for statistics matrix

end  %mrefnum
```

```
end  %end for loop for xpos


% build a matrix of intensities
meter_length = length(meter_vec);
% it is first necessary to re-arrange the points of intersection in an
% increasing order
swap = 1;
while ( swap > 0 )
   swap = 0;
   for u = 1 : meter_length - 1;
      if ( meter_vec(u+1) < meter_vec(u) )
         dummy = meter_vec(u+1);
         meter_vec(u+1) = meter_vec(u);
         meter_vec(u) = dummy;
         swap = swap + 1;
      end
   end
end

if ( 1 == 1 )
   %take a moving average and wrap around from left to right
   n = 10 ; % number of points on either side to average over
   dmet = diff(meter_vec);
   Lm = length(dmet);
   dmet_a = [ dmet(Lm - n: Lm)  , dmet , dmet(1:n-1) ];

   Lm = length(dmet_a);
   for k = n+1 : Lm - n
      dmet1(k-n) = sum( dmet_a(k-n:k+n) )/ (2*n+1);
   end

   dmet3 = dmet1;
   Lm = length(dmet);
end
for m = 1 : meter_length-1
   line_pos(m) = ( meter_vec(m) + meter_vec(m+1) )/2;
end

incident_intensity = length(line_pos)/(b-a); %incident intensity

% a measure of the intensity across the meter at a given height
refl_coef = .66;
line_int = (1./dmet3)/incident_intensity*refl_coef + 1;
%line_int = line_int/sum(line_int)*length(line_int);

% build a spline of the data
XX = a : (b-a)/spline_points : b;
YY = interp1( line_pos, line_int , XX, 'linear','extrap');
%YY = interp1( line_pos, line_int , XX, 'spline');

if (plot_2 == 1)
   figure(2)
   plot(line_pos, line_int)
```

```
        hold on
        plot(line_pos, line_int,'r.')
        plot(XX, YY, 'g')
      end

      meter_mat(i,:) = YY;

    end % for y_meter

      %draw silicon
    if (plot_1 == 1)
      figure(1)
      plot(xc,yc,'k')
      axis([ a b c d])
      %grid
      hold on
      fill([ a xc b ], [ c yc c ], [0 0 1 ])
    end

    figure(12)
    x_mesh = XX;
    y_mesh = y_meter_min : y_meter_step : y_meter_max;

    %remove data below surface
    yc2 = spline(xc,yc,x_mesh)
    xc2 = x_mesh;
    meter_mat2 = meter_mat;
    [ umax vmax ] = size(meter_mat);

    if(1 == 1)
    for u = 1 : umax
      for v = 1 : vmax

        if ( y_mesh(v) < yc2(u)- 2*y_meter_step )
          meter_mat2(v,u) = NaN;
        end
      end
    end
end

    meter_mat = meter_mat2;

    if (plot_3 == 1)
      figure(3)
      clf
      surf(x_mesh,y_mesh,-meter_mat+min(min(meter_mat)))
      shading interp
      colormap('gray')
      axis ([ a b y_meter_min y_meter_max -inf inf ])
      view(0,90)
      hold on
      fill([ a xc b ], [ c yc c ], [.75 .75 .75 ])

      max_int = max(max(meter_mat));
```

```
      [ y_pos x_pos ] = find ( meter_mat == max_int )
      plot( x_mesh(x_pos), y_mesh(y_pos), 'r.')
      plot( x_mesh(x_pos), y_mesh(y_pos), 'ro')
      dtext = y_mesh(y_pos);
      dtext = round ( 10 * dtext ) /10;
      itext = round ( 10 * max_int) /10;
      text( x_mesh(x_pos)+.5, y_mesh(y_pos),...
         [ '( d = ' num2str(dtext) ' , I = ' num2str(itext) ' )' ],...
         'fontname','times','fontsize',14,'color','k')

      text( -9.9,c/2, ['amplitude = ' num2str(amp) ],'fontname','times','fontsize',14,'color','k')

   end

   if (plot_4 == 1)
      figure(4)
      clf
      thing = [ 1.7 2  3 9*max(max(meter_mat2)) max(max(meter_mat2))  ];
      meter_mat = meter_mat2;
      [cs,h] = contour(x_mesh,y_mesh,meter_mat2, thing,'b');
      clabel(cs,h,'labelspacing',200,'fontname','times','rotation',0,'color','k');
      axis ([ a b y_meter_min y_meter_max ])
      hold on

      max_int = max(max(meter_mat));
      [ y_pos x_pos ] = find ( meter_mat == max_int )
      plot( x_mesh(x_pos), y_mesh(y_pos), 'r.')
      plot( x_mesh(x_pos), y_mesh(y_pos), 'ro')
      dtext = y_mesh(y_pos);
      dtext = round ( 10 * dtext ) /10;
      itext = round ( 10 * max_int) /10;
      text( x_mesh(x_pos)+2, y_mesh(y_pos),...
         [ '(d=' num2str(dtext) ', I=' num2str(itext) ')' ],...
         'fontname','times','fontsize',14,'color','k')
           text( -9.9,c/2, ['amplitude = ' num2str(amp) ],'fontname','times','fontsize',14,'color','k')

      surf(x_mesh,y_mesh,(-meter_mat+min(min(meter_mat)))/10)
      shading interp
      colormap('gray')
      axis ([ a b y_meter_min y_meter_max -inf inf ])
      view(0,90)

      fill([ a xc b ], [ c yc c ], [.75  .75 .75 ])
   end

  %print -dtiff -zbuffer -r300

end %for amp
```

1.14 Function Used in Ray-Tracing Program

```
function[ryl,intpos,angleref,angleinc,brk] = reflectfun(iyl,xc,yc,slopec,anglesun,pintpos,plt,mrefnum,nump)

%_____________________________________________________________________
%iyl = points tracing incident light
%xc = x values for reflecting curve
%yc = y vlaues for reflecting curve
%pintx = previous x intersection point
%pinty = previous y intersction point
%plt = plot query for intersection point, 1 = yes, anything else = no
%mrefnum = integer indicating which multiple intersection value this is

%ryl = y values for reflected ray
%intx = new x intersection point
%inty = new y intersection point
%_____________________________________________________________________


%omit origin of reflected light (previous intersection point)
iyl(max(1,pintpos-1) : min(nump,pintpos+1)) = inf;
%omit anything above the intersection point on first reflection
     if (mrefnum == 2)
        iyl( find( iyl > yc(pintpos) )) = inf;
     end %end mrefnum ==1

%do this by brute force, find smallest difference
%between light ray vector and curve
dely = abs(yc - iyl);
mindely = min(dely);
intpos= find( dely == mindely );
intpos= intpos(1);

%find slope at intersection point
slopei = slopec(intpos);
anglec = atan(slopei);
anglenorm = anglec + pi/2;
angleinc = anglesun - anglenorm;

%find first reflected ray
angleref =  anglenorm - angleinc;
m2 = tan(angleref);
b2 = yc(intpos) - m2*xc(intpos);
ryl = m2*xc + b2;
intx = xc(intpos);
inty = yc(intpos);

%conditional statement which sends a break loop signal
%if the light ray will does not intersect anything, 1 = break, 0= no break
brk = 0;
```

```
if ( abs(intpos-pintpos) < 3 )
   brk = 1;
   plt = 0;
end


if (plt == 1)
   c = [ 'r' 'm' 'y' 'g' 'c' 'b' 'k'];
   plot(xc(intpos),yc(intpos),[c(mrefnum) 'o'])
end
```

VITA

Stephen Jesse was born in Boulder, Colorado on December 05, 1973. He graduated from Hendersonville High School in Hendersonville, Tennessee in 1992 and entered the engineering program at the University of Tennessee, Knoxville that same year. He completed the requirements for a Bachelor degree in mechanical engineering in 1996. In 2000 he completed his Master's of Science degree in mechanical engineering. Stephen is currently working with Dr. Anthony Pedraza and Dr. David Geohegan continuing research in laser matter interaction and nano-composites.